8-26-2011 12:00 AM

Photocatalytic Degradation of Phenolic Compounds in Water: Irradiation and Kinetic Modeling

Jesus Moreira del Rio
The University of Western Ontario

Supervisor
de Lasa, Hugo
The University of Western Ontario

Follow this and additional works at: https://ir.lib.uwo.ca/etd

Part of the Catalysis and Reaction Engineering Commons

PHOTOCATALYTIC DEGRADATION OF PHENOLIC COMPOUNDS IN WATER: IRRADIATION AND KINETIC MODELING

(Spine title: **Photocatalytic Oxidation of Phenols: Radiation and Kinetics**)

(Thesis format: Monograph)

by

Jesus Moreira del Rio

Graduate Program in Chemical and Biochemical Engineering

A thesis submitted in partial fulfillment
of the requirements for the degree of

Doctor of Philosophy

The School of Graduate and Postdoctoral Studies

The University of Western Ontario
London, Ontario, Canada

THE UNIVERSITY OF WESTERN ONTARIO
School of Graduate and Postdoctoral Studies

CERTIFICATE OF EXAMINATION

Supervisor   Examiners

_____   _____
Dr. Hugo de Lasa   Dr. Ajay K. Ray

Supervisory Committee

                                                  _____
                                                  Dr. Shahzad Barghi
_____

                                                  _____
                                                  Dr. Andy X. Sun
_____

                                                  _____
                                                  Dr. Madjid Mohseni

The thesis by

Jesus <u>Moreira del Rio</u>

entitled:

**PHOTOCATALYTIC DEGRADATION OF PHENOLIC COMPOUNDS
IN WATER: IRRADIACION AND KINETIC MODELING**

is accepted in partial fulfillment of the
requirements for the degree of
Doctor of Philosophy

_____   _____
        Date   Chair of the Thesis Examination Board

ii

Abstract

Scaling up a photoreactor requires both knowledge of optical properties of the slurry medium and an established kinetic model. Measuring the scattering and absorption coefficients of particles suspended in water involves the use of specialized optical equipment, as well as the partial solution of the radiative transfer equation (RTE). In addition, modeling of the radiation field in photoreactors with complicated geometries offers special challenges.

On the other hand, most of the kinetic models (KM) for phenol photodegradation reported in the literature were obtained for a single organic chemical species only. In fact, neglecting all the intermediate species generated during the photoreaction, is a common oversimplification that limits the KM application. As a result, once the radiation and kinetic models fully established, energy efficiencies can be obtained.

In this PhD dissertation, the photocatalytic degradation of phenol over four different TiO_2 catalysts is studied. It is proven that phenol yields hydroquinone, catechol, benzoquinone, and acetic and formic acids as main intermediate species.

The radiation field inside photocatalytic reactors is predicted by solving the RTE. From the solution of the RTE, the local volumetric rate of energy absorption (*LVREA*) is also calculated. The radiation field inside an annular photoreactor is simulated using the Monte Carlo (MC) method for different TiO_2 suspensions in water. All simulations are performed by using both the spectral distribution, and the wavelength-averaged scattering and absorption coefficients.

The Henyey-Greenstein phase function is adopted to represent forward, isotropic and backward scattering modes. It is assumed that the UV lamp reflects the back-scattered photons by the slurried medium. It is proven, photo-absorption rates, using MC simulations and spectral distribution of the optical coefficients, agree closely with experimental observations from a macroscopic balance (MB). It is also found that the scattering mode of the probability density function, is not a critical factor for a consistent representation of the radiation field.

When solving the RTE, two optical parameters are needed: (1) the absorption and scattering coefficients, and (2) the phase function. In this research work, the MC method, along with an optimization technique, is shown to be effective in predicting the wavelength-averaged absorption and scattering coefficients for different TiO_2 powders. To accomplish this, the *LVREA* and the transmitted radiation (P_t) in the photoreactor are determined by using a MB. The optimized coefficients are calculated ensuring that they comply with a number of physical constrains, falling in between bounds established via independent criteria.

The optimization technique is demonstrated by finding the absorption and scattering coefficients for different semiconductors that best fit the experimental values from the MB. The objective function in this optimization is given by the least-squared error for the *LVREA*. A photocatalyst is synthesized and its optical properties determined by the proposed method. This approach is a general and promising one; not being restricted to reactors of concentric geometry, specific semiconductors and/or particular photocatalytic reactor unit scale.

Based on the proposed intermediate reactions, a phenomenological based unified kinetic model is proposed for describing the obtained experimental observations in phenol photodegradation. This Langmuir-Hinshelwood (L-H) kinetic model is based on a "Series-Parallel" reaction network. This reaction model is found to be applicable to the various TiO_2 photocatalyst in the present study.

This unified kinetic network is based on the identified and quantified chemical species in the photoconversion of phenol and its intermediates. In order to minimize the number of optimized parameters, the adsorption constants of the different intermediate species on the different catalysts configuration, are obtained experimentally. It is shown that the unified kinetic model requires a number of significant assumptions to be effective; avoiding overparametization. As a result, the unified kinetic model is adapted for each specific TiO_2 photocatalyst under study.These different models adequately describe the experimental results. It is shown that this approach results in good and objective parameter estimates in the L-H kinetic model, which is typically applied to photocatalytic reactors.

Finally, two efficiency factors, the quantum yield and the photochemical and thermodynamic efficiency factor, are obtained, in this PhD dissertation. These factors are based on the kinetic model proposed and the radiation being absorbed by the photocatalyst particles. The

efficiency calculations consider stoichiometric relationships involving observable chemical species and $OH^\bullet$ groups. The obtained efficiency factors point toward a high degree of photon utilization and, as a result, the value of photocatalysis and Photo-CREC-Water reactors for the conversion of organic pollutants in water is confirmed.

Keywords

Acknowledgments

My sincere gratitude goes to Dr. Hugo de Lasa for being an outstanding advisor and excellent professor. His high quality standards, constant encouragement, and invaluable suggestions made my PhD program and thesis successful.

I would like to thank The National Council of Science and Technology in Mexico (CONACyT-México) for the scholarship that allowed me to pursue my PhD at UWO.

My sincere thanks go to Ying Zhang for helping me understand the different principles of a variety of analytical techniques. She provided valuable insights on mass spectrometry and HPLC analysis. I also thank José Muñoz and Pastor Solano for their technical support in the lab.

I specially thank Professor Benito Serrano for his constructive comments on this thesis, for his words of wisdom, and most importantly, for his friendship.

I am grateful to the graduate assistance in the department of Chemical and Biochemical Engineering; Joanna and April. Their invaluable help and assistance were always critical for the successful completion of my PhD program.

I also wish to thank to my friends: Bhavik (special recognition), Pablo, Jazmin and Carmen for helping me get through the difficult times, for all the emotional support, camaraderie, entertainment and caring they provided. I also acknowledge Aarón for all the emotional and moral support. Thank you Aarón for making me believe in me when I did not.

Lastly and most importantly, this work is dedicated to my parents, Jesús Moreira Leyva and Teresa del Río Hernández, whose love, encouragement and moral example have been critical in my life. I would not have reached this point in my life it if had not been for them. Also, this thesis is dedicated to my brother and sisters, Ladislao, Rosy, Magdalena, and Ana Teresa, who have played an important role in my life.

Table of Contents

List of Tables

List of Figures

List of Appendices

Nomenclature

A_{ads} electron acceptor

$\beta_1, \beta_2, \beta_3$ empirical constants

β_{cat} specific extinction coefficients, $\text{cm}^2 \text{ g}^{-1}$

β_{L} lamp decay coefficient, min^{-1}

β_{p} extinction coefficient of Pyrex material, cm^{-1}

C   concentration, mol. l^{-1}

$\vec{C}$ vector of concentrations

$\vec{C}_0$ vector of initial concentrations

C_{cat} catalyst concentration, $\text{g } l^{-1}$

C_{e} concentration in the liquid phase at equilibrium (mg-C l^{-1})

d_{a} agglomerate mean diameter, nm

D_{ads} electron donor

$\Delta H_{OH^{\bullet}}$ enthalpy of OH radical formation, joule mol^{-1}

d_p primary particle diameter, nm

d_{pr} primary particle diameter range, nm

E_{bg} Energy band gap, eV

ε_{cat} true extinction coefficient, $l \text{ g}^{-1}$

e^{-}_{cb} electron located in the conduction band

ex,ey,ez   direction cosines

G total incident radiation, einstein $\text{m}^{-2} \text{ s}^{-1}$

g   g parameter in H-G phase function

h^{+}_{vb} hole left in the valence band

I	radiation intensity, einstein m^{-2} s^{-1} sr^{-1}
I	intermediate produced during a photoreaction
j	emission term in the RTE
k	apparent constants, min^{-1}
$\vec{k}$	vector of predicted parameters
κ^*	specific absorption coefficient, m^{-1}
K^A	adsorption constant of component, mg-C^{-1} L
k^I	intrinsic kinetic constant, min^{-1}
k^k	reaction kinetic constant, mol gcat^{-1} min^{-1}
l	length of the photon flight, m
LS	least square
λ_{bg}	wavelength needed for TiO_2 excitation, nm
λ_{Ebg}	minimum wavelength for the electron-hole excitation, nm
M_{cat}	weight of the TiO_2 catalyst, g
mgC	milligrams of carbon
N	number of moles
N_E	number of experiments
OC$_{inter}$	TOC profiles from HPLC results
$P\big|_{C\to 0^+}$	photons transmitted when the cat concentration approaches to zero einstein s^{-1}
P(a)	absorption criterion
P(l)	Probability that the photon travels a distance l
p(Ω–Ω')	Phase Function for scattering in RTE
Pa	rate of absorbed photons, einstein s^{-1}

$P_{\text{a-wall}}$ rate of photons absorbed by the inner Pyrex glass, einstein s^{-1}

P_{bs} rate of back-scattered photons exiting the system, einstein s^{-1}

LVREA   Local Volumetric Rate of Energy Absorption, einstein s^{-1} m^{-3}

LVREA$_{\text{exp}}$ experimental Local Volumetric Rate of Energy Absorption, einstein s^{-1} m^{-3}

P_{fs} rate of forward-scattered radiation, einstein s^{-1}

P_{i} rate of photons reaching the reactor inner surface, einstein s^{-1}

P_{ns} rate of transmitted non-scattered radiation, einstein s^{-1}

P_{o} rate of photons emitted b the BL lamp, einstein s^{-1}

ppm-C   parts per million of carbon in the organic species

ppm-C$_0$ parts per million of carbon in the organic species, initial concentration

P_{t} rate of transmitted photons, einstein s^{-1}

P_{ts} rate of forward-scattering radiation, einstein s^{-1}

$q(\lambda,\theta,z)$ net radiative flux over the lamp emission spectrum, μW cm^{-2}

Q_{abs} radiation absorbed by the photocatalyst, j

Q_{e} amount of compound per unit weight, mg-C gcat^{-1}

q_{λ} lamp output power, μW cm^{-2}

Q_{max} max amount of absorbed compound per unit weight at equilibrium

Q_{used} fraction of energy used to produce OH$^{\bullet}$, j

r   radial coordinate

r   reaction rate, mol gcat^{-1} min^{-1}

$R1..6$ random numbers

$r_{\text{OH, T}}$ total rare of reaction of OH$^{\bullet}$

$r_{\text{TOC,0}}$ degradation rate of TOC, mg-C min^{-1} l^{-1}

s linear coordinate along the direction Ω, m

S	organic substrate
σ^*	specific extinction coefficient, m^{-1}
S_a	catalyst surface area, m^{-2}
t	time, min
T	transpose
u	stoichiometric coefficient
$\vec{u}$	vector of measured variables
V	volume of reactor, L
V_{CSTR}	volume of the tank, L
V_{PFR}	volume of the annular section in the reactor, L
W_{cat}	catalyst loading , $g\ m^{-3}$
W_{cat}	mass of the solid catalyst, g
W_{irr}	weight or irradiated catalyst, g
x,y,z	Cartesian coordinates, m
$\hat{y}$	vector of experimental observation
$\vec{y}$	vector of predicted values

Acronyms

1,4-BQ	benzoquinone
AcAc	acetic acid
AOP	advanced oxidation process
BL lamp	Black Light Lamp
CI	confidence intervals
DO	discrete ordinate

DP 25   TiO$_2$ Degussa P25

FoAc   formic acid

FV   finite volume

GC/MS   gas chromatography with mass spectroscopy

H-G   Henyey-Greenstein

HPLC   high performance liquid chromatography

KM   kinetic models

L-H   Langmuir-Hinshelwood

LuAc   lumped terms of carboxylic acids

MB   macroscopic balance

MC   Monte Carlo

MRB   macroscopic radiation balance

ODE   ordinary differential equation

o-DHB   ortho-dihydroxybenzene or catechol

OxAc   oxalic acid

p-DHB   para-dihydroxybenzene or hydroquinone

PTEF   Photochemical Thermodynamic Efficiency Factor

QY   quantum yield

RN   reaction network

RTE   Radiative Transfer Equation

SSR   squared sum of residuals

TOC   total organic carbon

UV   ultra violet

Greek Symbols

β extinction coefficient, m^{-1}

ϕ azimuth angle

κ absorption coefficient, m^{-1}

λ wavelength of radiation, m

θ zenith angle

σ scattering coefficient, m^{-1}

Ω solid angle, steradian

Subscripts and Superscripts

λ indicates dependence on wavelength

*   denotes specific values

e   denotes emission of light

i, j   denotes component i and j

Chapter 1
Introduction

1 Introduction

Water pollution is one of the main threats and challenges that humanity faces today. Everyday human activities introduce contaminant substances and wastes into rivers, lakes, groundwater aquifers and oceans. This contamination modifies the environmental water quality, producing large quantities of water that are unsuitable for various uses, including human consumption. Common water pollutants include: textile dye; herbicides and pesticides; alkanes; haloalkanes; aliphatic compounds; alcohols; carboxylic acids; aromatic compounds; detergents and surfactants; agro waste like insecticides, pesticides and herbicides (Bahnemann, 2004; Vidal 1998); inorganic compounds like heavy metals, such as mercury, cadmium, silver, nickel, lead; noxious gases; and pathogens like bacteria fungi and viruses (Vinu and Madras 2010). Both organic and inorganic contaminants can be found in ground water wells and surface waters; these residues can cause adverse effects to the environment and to human health.

Many of the contaminants are so toxic that they can cause health problems in humans at trace levels. Water pollution also reduces the available amount of freshwater resources for both people, and ecosystems. Freshwater scarcity is already a reality in many developing countries. The United Nations, for instance, predicts that two-thirds of the world's population will live in water-scarce regions by 2025 (Ganoulis 2009). The increase in water demand by the growing world population and the overuse of water, together with water pollution and climate change, are the main reasons for water scarcity.

To alleviate the problem, contaminated water needs to be treated and re-used. The treatment of contaminated water is based on various mechanical, biological, physical, and chemical processes. After filtration and elimination of particles in suspension (primary treatments), biological treatment is ideal (secondary treatments). Unfortunately, there are certain products, called bio-recalcitrant (non-biodegradable), for which much more effective non-reactive systems, such as air stripping, adsorption on granulated activated carbon, incineration, ozone and oxidation (tertiary treatments), are needed. These processes aim to

treat wastewaters, and therefore improve water quality, but some of these technologies (such as adsorption and filtration) merely concentrate the pollutants by transferring them to other phases. The next problem, then, becomes how to properly disposal of the new pollutant-rich streams. Therefore, management of toxic chemicals with strict environmental legislation, drives the development of clean and green processes, to eliminate the pollutants before they are disposed into the environment. Furthermore, for these processes to be effective, complete mineralization and degradation of all organic and inorganic contaminants from water and wastewater, are required.

The strong potential of tertiary treatments called Advanced Oxidation Processes (AOPs) for bio-recalcitrant wastewater treatment is universally recognized today, and many researchers around the world are devoting their efforts to the development of these processes (Malato and Blanco 2004; Franch et al., 2004). Although they make use of different reaction systems, AOPs are all characterized by the same chemical feature: the production of hydroxyl radicals ($OH^\bullet$). A useful attribute of the hydroxyl radicals is their very low selectivity. These radicals can virtually destroy any organic contaminant present in water. They can even destroy pollutants that are not amenable to biological treatments, which are all characterized by high chemical stability and difficulty to be completely mineralized (Andreozzi et al. 1999).

In order to apply a decontamination technique to these cases, it is necessary to adopt reactive systems much more effective than those adopted in conventional purification processes. Among AOPs, heterogeneous photocatalysis has confirmed its efficiency in degrading a wide range of organic contaminants into CO_2, water and some readily biodegradable mineral acid (Chong et al., 2010). Moreover, photocatalysis is not restricted to water purification only, as it is also used in air purification, self cleaning surfaces, among others (Herrmann 1999).

Over the past few decades, photocatalysis has been the subject of extensive research in the removal of contaminants in air and water streams (de Lasa et al., 2005). Several features, such as ambient operating conditions, complete destruction of parents and their intermediate compounds, and relatively low operating cost, have confirmed its applicability to water treatment. Photocatalysis processes make use of solid semiconductors that are activated with UV light. The most common photocatalyst is the TiO_2 (Ray et al., 2000). So far, the application of the TiO_2 mediated photoreactions for water treatment is still experiencing a

series of technical challenges: (1) separation of TiO_2 catalyst after water treatment is considered the major obstacle (Chong et al., 2010); (2) catalyst development with a strong absorption in the visible spectrum region (Colmenares et al., 2006); (3) understanding the theory behind common reactor operation parameters, such as light intensity distribution inside photocatalytic reactors; and (4) addressing mathematical inconsistencies commonly found in the kinetic modeling.

The rate of degradation in photocatalysis is directly dependant on the radiation intensity. This step is the single most important factor distinguishing photocatalytic reactors from the conventional thermally activated ones (Pareek et al. 2003). The radiation field inside a photoreactor is obtained by solving the RTE. Application of this approach is recent (Cassano et al., 1995) in photocatalytic systems. The optical properties of the slurry medium (water + TiO_2); namely, the absorption coefficient (κ), the scattering coefficient (σ) and the phase function, play an important role in the overall design of the photoreactor. Therefore, the values for the scattering and absorption coefficients, as well as the expression for the phase function, need to be established for a rigorous design and in scaling-up applications of photoreactors. These values are required to evaluate the amount of radiation being absorbed by the catalyst, which will lead to the determination of the photonic efficiencies in the rector (Marugán et al., 2006). Experimental evaluation of the effective optical properties for a particular fluid-particle system is generally very time-demanding and requires the use of complex actinometric or spectrophotometric techniques (Imoberdorf et al. 2008). Therefore, a numerical approach would be a desirable alternative to reduce time, cost and method complexity for the measurement of such properties.

Most of the photomineralization kinetics over TiO_2 surface involves only a single constituent model compound. However, due to the non-selective nature of the hydroxyl radicals produced in the photocatalytic process, numerous intermediate species are formed before complete mineralization into CO_2 and H_2O is reached. Neglecting this phenomenon is a common oversimplification in the kinetic modeling of different organic model compounds (Chong et al., 2010). Even in recent reviews of TiO_2 mediated reactions, the kinetic modeling is treated only for the single model compound (Vinu and Madras 2010; Gaya et al., 2008). Some good work on the kinetic modeling of phenol photodegradation for multiple components was published by our research group (de Lasa 2009; Ortiz-Gomez et al., 2008

and 2007). Their model was based on the L-H kinetics. Nonetheless, this model contains certain limitations, such as (1) high cross-correlation among kinetic and adsorption coefficients, (2) the model was proposed only for one type of TiO_2 catalyst, DP 25, (3) adsorption constants of the different organic compounds on TiO_2 were not discussed. These adsorption constants were restricted to the same value for the different intermediate species, and (4) total organic profiles were not included in the model. In this instance, the total organic concentration of model and intermediate compounds can be represented collectively in the total organic carbon (TOC) profiles. This will yield an in-depth and complete understanding of the photomineralization kinetics.

As mentioned earlier, most of the kinetic models proposed in the literature deal with a single model compound. The method of the initial rate has been the customary approach to estimate the kinetic parameters in photocatalytic processes (Bellobono et al. 2009 and 2008; Laoufi et al., 2008; Selvam et al., 2007; Sivalingam et al., 2004; Mehrvar et al. 2000; Xu and Langford 2000; Chen at al., 1997; Tatti et al. 1997; Rota et al. 1996; Trillas et al. 1992). Nevertheless, this model fails in systems with more than one reacting species, which is typically found in photocatalysis. Furthermore, this method includes substantial issues that limit its application. It has a significant lack of reproducibility given the subjective nature of the procedure. These limitations are further discussed in Chapter 3.

Therefore, there is a need for a unified kinetic modeling approach that incorporates not only the model compound, but also the other detectable intermediate species. This general kinetic model should be able to predict concentration profiles of organic compounds for different TiO_2 catalysts. The model needs to be based on experimental degradation profiles, with the experimental values for the adsorption constants determined independently. The proposed approach should allow decoupling kinetic and adsorption parameter determination minimizing the cross-correlation among parameters. It is anticipated this unified kinetic model should also be able to predict the experimental TOC profiles in the photodegradation of organic compounds.

The radiation field inside the photoreactor affects the overall performance of the photocatalytic system. This field needs to be established inside the photoreactor so that fully illuminated conditions are ensured during the operation of a photoreactor. In modeling the

radiation field, the role of the phase function needs to be investigated in order to understand the behaviour of light inside the slurry medium. The role of the lamp should also be studied. The final objective is, then, to determine both absorption and scattering coefficients, and to calculate the radiation being absorbed by the different TiO_2 photo catalysts and various photocatalyst loadings. Understanding the radiation filed, and the amount of light being used in the photocatalytic process, allows determining reactor photo-efficiencies.

Phenol has been used as a model pollutant to evaluate the performance of many photoreactor designs and photocatalyst activities (Tryba et al., 2006; Salaices et al., 2004). In addition, phenol and its derivatives are well known for their acute toxicity and bio-recalcitrant nature. These compounds are present in wastewater from many industrial processes. They have been detected in urban and agricultural waste (Ahmed et al., 2010) around the world. Exposure to phenol is related to severe illnesses such as leukemia and some serious human organ malfunctions.

A comprehensive identification and quantification of aromatic and carboxylic acids in phenol photodegradation allows the formulation of a general unified reaction network (RN). This permits further development and simplification of a kinetic model applicable for a particular photocatalyst. The expected kinetic model should incorporate the oxidation intermediates that are kinetically significant. In this respect, the role of iron ions is investigated in the photocatalytic decomposition of phenol on DP 25 and Anatase form TiO_2 photocatalysts. Determination of the adsorption constants for the different intermediate species participating in the photodegradation of phenol allows reducing the number of optimized parameters needed in the kinetic modeling. To our knowledge, the experimental determination of the adsorption constants for different phenolic hydroxylated compounds has not been performed. Furthermore, experimental values for these constants have not been incorporated into this type of L-H kinetic model.

Finally, with the results obtained from the radiation and kinetic models, a comprehensive method for predicting energy efficiencies is applied. This method accounts for all the $OH^{\bullet}$ radical species needed by phenol and its intermediates throughout the photoreaction. This method also involves the irradiation absorbed by the catalyst, and the energy needed to produce the $OH^{\bullet}$ groups. In this PhD dissertation, the radiation field inside an annular

photoreactor is obtained from experimental data and by solving the RTE using MC methods. Also, the problems in the kinetic model, explained earlier in this Chapter are overcome by applying a phenomenological unified kinetic model for different TiO_2 photocatalysts. Lastly, in this dissertation, efficiency assessments are done for different TiO_2 photocatalysts. This thesis is divided in the following chapters:

Chapter 2 of this thesis outlines the main objectives of the research project and the major areas investigated. Chapter 3 summarizes the literature survey relevant to the area of research. Chapter 4 describes the experimental methods and materials used in this study. Analytical equipment, as well as the experimental procedures, are also reported in detail.

Chapter 5-Part I reports results and discussions concerning the experimental determination and modeling of the radiation field in the annular photoreactor. The approaches used to determine the scattering and absorption coefficients for different TiO_2, the role of the lamp and the phase function employed in the modeling are also reviewed.

Chapter 6-Part II deals with the oxidation of phenol at optimum experimental conditions. The identification and quantification results for phenol, hydroquinone, catechol, benzoquinone, and formic and acetic acids are reported. This Chapter also presents the results on the isotherms adsorptions for phenol and its intermediates and for different TiO_2 photocatalysts. Finally, this chapter closes with the development of a unified general reaction network for the photocatalytic oxidation of phenol and its intermediates.

Chapter 7 Part III describes the kinetic models considered for the different photocatalysts. The models are validated with experimental data, and its confidence intervals and cross-correlation coefficients are reported. In these kinetic models, the experimental obtained adsorption constants are utilized to reduce cross-correlation among parameters.

Chapter 8 reports the determination of the photochemical and thermodynamic efficiency factor and the quantum yield for the reaction schemes obtained in Chapter 7. Results of the radiation absorbed by the photocatalysts obtained in Chapter 5 are used in the energy efficiency assessments. Finally, Chapter 9 reports conclusions and recommendation for future work.

Chapter 2
Scope

2   Main Objective

This PhD dissertation seeks gaining understanding of the radiation field and of the kinetics of the photocatalytic degradation of phenol in water. More specifically, the purpose of the study is to elucidate the behavior of UV light inside a photoreactor by means of experimental and theoretical measurements of the optical properties for different photocatalysts. The final goal of this research is to establish a unified kinetic network for phenol photocatalytic degradation. This unified reaction network is applied to the kinetic modeling of phenol degradation on different TiO_2 photocatalysts and can considerably help in the evaluation of energy efficiency in photocatalytic reactor. Phenol is selected as a model compound given its refractory nature in water and its impact on human health associated with its consumption.

Therefore, the following specific objectives for this research include the following:

(1)   Experimental determination of the radiation field distribution inside a slurry photoreactor by means of measuring the experimental LVREA with a macroscopic radiation balance.

(2)   Development and implementation of a MC based algorithm for the simulation of the radiation field inside a photoreactor for three commercial TiO_2 photocatalysts whose optical properties are given, i.e. absorption and scattering coefficients. The aim of this MC method is to numerically determine the LVREA for the photocatalysts inside the photoreactor.

(3)   Implementation of an optimization procedure, using MC simulations of the radiation field, in order to numerically determine optical properties for different TiO_2 catalysts.

(4)   Preparation of a TiO_2 photocatalyst by hydrolysis of titanium isopropoxide (IV) and numerical determine its optical properties.

(5)   Development of reaction runs in the Photo-CREC Water-II for the photo-oxidation of phenol and its reaction intermediates. The planned experimental runs are intended to examine the effect of different TiO_2 photocatalysts at optimum operation conditions in our reaction set up.

(6)   Development and validation of a general reaction network and a unified kinetic reaction model for phenol photodegradation. To this end, quantification and identification of intermediates compounds in phenol degradation are done by using HPLC and GC/MS analytical techniques. When developing the kinetic model, experiments at different levels of initial concentrations of phenol are examined.

(7)   Kinetic parameter estimation based on a L-H mechanism. This model presents high correlation among kinetic and adsorption constants leading to multiple solutions for the optimized parameters. Hence and to reduce parameter cross-correlation, independent determination of the adsorption constants for phenol and its different intermediates is done experimentally.

(8)   Determination of the energy efficiency in the photocatalytic unit using thermodynamic principles and quantum yields once the UV radiation and kinetic models are established.

Chapter 3
Literature Review

3 Introduction

This chapter presents a critical literature survey on photocatalysis; its fundamentals and applications. Moreover, the technical literature specifically related to the objectives of this PhD thesis is covered in detail. In this respect, a review on radiation and kinetic modeling is reported. As well, different reactor configurations and present challenges in photocatalysis are considered. Lastly, this chapter closes with some alternative applications of photocatalysis other than water remediation.

3.1 Heterogeneous Photocatalysis: its Fundamentals

Water scarcity and quality are some of the problems humanity faces. Some regions of the world currently have little or no access to clean water. In addition, rapid industrialization, population growth, and the large number of contaminants entering the water supply from human activities, contribute to exacerbate this problem. Many health problems are associated with the lack of fresh and clean water. It has been reported that 1.2 billion people lack access to drinking water. Almost 3 billion people have scarce or no access to sanitation technologies. Additionally, millions of people die annually from illnesses related to contaminated water (Malato et al., 2009). Producing safe drinking water is perhaps the most important issue in water industry. Drinking water; polluted with pesticides, herbicides, and recalcitrant organic compounds, and lack of sanitation, is responsible for the death of more than 5000 children every day; and more than one billion people lack access to water with low levels of contaminants.

Conventional treatments of water and decontamination could solve many of these problems. However, these methods are often operationally intensive and generate residual streams containing the removed pollutants. The problem now becomes to property disposed these contaminant-rich streams, this adds up the global contamination problem. In order to resolve and suppress water pollution, development of advanced technologies with low operation costs and high efficiency for the complete destruction of contaminants is desired.

In this respect, Advanced Oxidation Processes (AOPs) have emerged as promising water treatment technologies for the complete destruction of organic contaminants in water (Thiruvenkatachari et al, 2008; Bahnemann 2004). AOPs for the removal of bio-recalcitrant compounds in wastewater are universally recognized today, and many researchers around the world are devoting their efforts to the development and improvement of these processes (Franch et al., 2004). Although they make use of different reaction systems, AOPs are all characterized by the same chemical feature, the production of hydroxyl radicals ($OH^{\bullet}$). This radical is an extremely powerful and non-selective oxidant, which is capable of oxidizing the majority of organic compounds very quickly (Navarro et al. 2005).

Heterogeneous photocatalysis is a tertiary water treatment process belonging to the AOPs. Photocatalytic reactions are the result of the interaction of photons having the appropriate wavelength with a solid semiconductor (Fujishima et al., 2008; Linsebigler et al., 1995).

The general mechanism of photocatalysis is shown in Figure 1. When the impinging light has energy equal to, or greater than the semiconductor bandgap, radiation is absorbed and electrons are moved from the valence band to the conduction band giving rise to the formation of electron-hole pairs (Cassano et al., 2000). These separated charges walk randomly to the surface of the catalyst. When they reach the semiconductor surface they can recombine, get trapped in a metastable surface state, or participate in successive reactions. The holes react directly with an electron donor (D_{ads}) or with water to produce $OH^{\bullet}$ radicals. The electron reduces the adsorbed oxygen or reacts with an electron acceptor (A_{ads}). These oxidative-reductive reactions can totally mineralize and transform organic compounds into water, carbon dioxide and some mineral acids. The mechanism described above could be represented by the following equations (Navio et al., 1996; Lengrini et al., 1993; Hoffman et al, 1995; Litter 1999):

$$\text{Semiconductor} \xrightarrow{h\nu} e_{eb}^{-} + h_{vb}^{+} \tag{1}$$

$$S \rightarrow I \rightarrow CO_2 + H_2O \tag{2}$$

$$h_{vb}^{+} + OH_{ads}^{-} \rightarrow OH_{ads}^{\bullet} \tag{3}$$
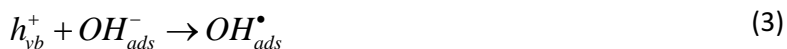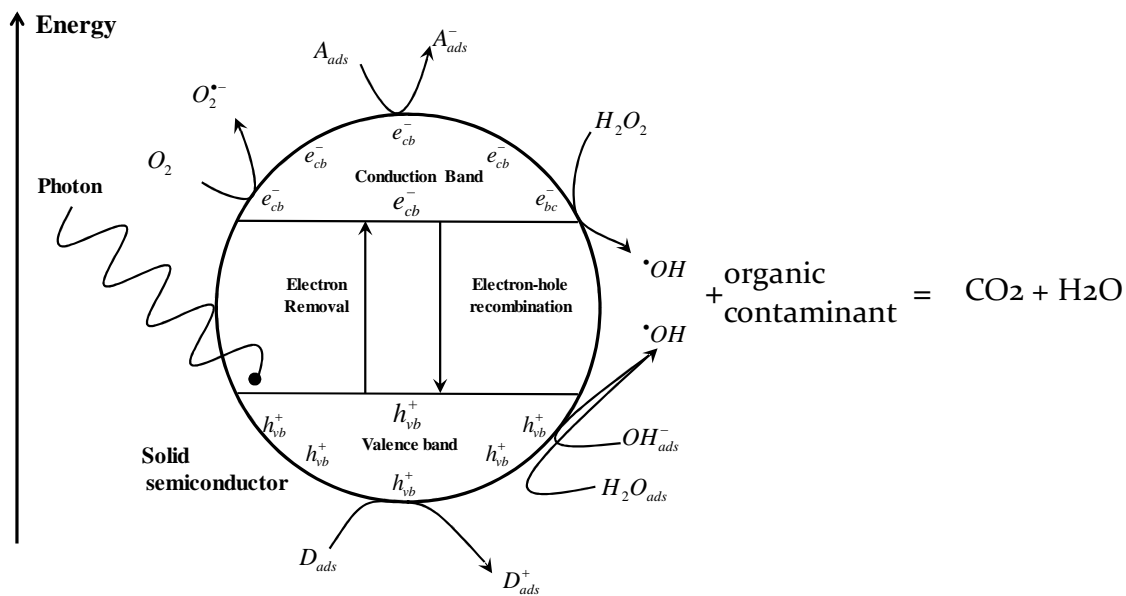
Figure 1 Principle mechanism of photocatalysis

Some adsorbed substrate can be directly oxidized by electron transfer:

$$h_{vb}^{+} + D_{ads} \rightarrow D_{ads}^{+} \tag{4}$$

$$OH_{ads}^{\bullet} + D_{ads} \rightarrow D_{oxid} \tag{5}$$

$$e_{cb}^{-} + A_{ads} \rightarrow A_{ads}^{-} \tag{6}$$
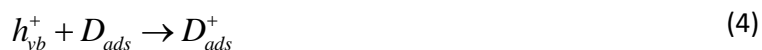
The considerable reducing power of formed electrons allows them to reduce some metals and dissolved oxygen with the formation of the superoxide radical ion $O_2^{\bullet-}$, whereas remaining holes are capable of oxidizing adsorbed H_2O or OH^- to reactive $OH^{\bullet}$ radicals

$$e_{cb}^{-} + O_{2ads} + H^{+} \rightarrow HO_2^{\bullet} \leftrightarrow O_2^{\bullet-} + H^{+} \tag{7}$$

$$HO_2^{\bullet} + e_{cb}^{-} + H^{+} \rightarrow H_2O \tag{8}$$

$$2HO_2^{\bullet} \rightarrow H_2O_2 + O_2 \tag{9}$$

$$H_2O_2 + O_2^{\bullet-} \rightarrow HO^{\bullet} + O_2 + OH^{-} \tag{10}$$

$$H_2O_2 + h\nu \rightarrow 2HO^{\bullet} \tag{11}$$

$$H_2O_2 + e_{cb}^- \rightarrow OH^{\bullet} + OH^- \tag{12}$$
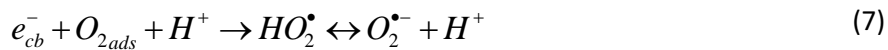
From Eqs. (1) to (12), the production of hydroxyl radicals is apparent. This powerful oxidant is a short-lived, extremely potent oxidizing agent, capable of oxidizing organic compounds present in water (Zaleska 2008). The oxidative pathway leads, in many cases, to complete mineralization of an organic substrate to CO_2, H_2O, and in some cases, an inorganic acid. This also leads to the generation of intermediate hydroxylated species before complete mineralization is achieved.

The energy required for the electron excitation depends on the particular characteristics of the semiconductors. The minimum wavelength necessary for the photo-excitation (λ_{Ebg}) depends on the bandgap of the photocatalyst. Table 1 gives band gap energies for some popular semiconductors.

Table 1 Bandgap energy and λ_{Ebg} of various photocatalysts (Bhatkhande et al., 2001)

Photocatalyst	Bandgap (eV)	λ_{bg}	Photocatalyst	Bandgap (eV)	λ_{bg}
Si	1.1	1127	α-Fe_2O_3	3.1	400
WSe_2	1.2	1033	ZnO	3.2	388
Fe_2O_3	2.2	564	TiO_2 (Anatase)	3.2	388
CdS	2.4	517	$SrTiO_3$	3.4	365
WO_3	2.7	459	SnO_2	3.5	354
TiO_2 (rutile)	3.0	413	ZnS	3.7	335

Many semiconductors have been tested so far as photocatalysts, although only TiO_2 in the anatase form seems to have the most interesting required attributes; such as high stability, good performance and low cost (Fujishima and Zhang 2006).

In this respect, the photodecomposition power of TiO_2, for a wide variety of organic compounds present in water, has been reported in the literature (Ahmed et al. 2011). Among the semiconductor photocatalysts tested, Degussa P25 (DP 25) TiO_2 has been proven to be the most active catalyst (Zhou et al. 2006). However, its wide band gap energy (3.0 eV for rutile and 3.2 eV for anatase) means that only 5% of solar spectrum could be used as light source in an industrial application (Colmenares et al. 2006; Karvinene and Lamminmäki 2003). Therefore, to use visible sunlight, which composes the largest part of solar radiation (Fujishima et al., 2007), a photocatalyst TiO_2 with strong absorption in the visible region should be developed.

To improve the response of TiO_2 in the visible light, surface modification has been applied. Three main benefits are the result of these structural changes (Litter and Navio 1996):

(1) Inhibiting the electron-hole recombination by increasing the charge separation and, therefore, the efficiency of the photocatalytic process.
(2) Increasing the wavelength response range (i.e. excitation of wide band gap semiconductors by visible light).
(3) Changing the selectivity or yield of a particular product.

Surface sensitization of TiO_2, with a number of organic dyes, extends the sensitivity of TiO_2 into the visible region. This can be accomplished by injecting electrons from an excited level of the dye into the TiO_2 conduction band.

Also, and in order to modify the electronic structure, advanced ion implantation techniques could be applied. For instance, it has been reported that Cr, V, Fe and Ni shifted smoothly the response of TiO_2 in the visible region (Kitano et al., 2007). The narrowing of the band gap was attributed to the metal substitution of Ti ions in the TiO_2 lattice. Nonetheless, there is considerable controversy about this matter. Some investigators report that doping of ions, such as V^{5+}, Cu^{2+}, Fe^{3+}, and W^{6+} in TiO_2 increases its photoactivity, whereas others have shown that Co^{3+} and Al^{3+} and doping can reduce photoactivity (Vinu and Madras 2010). Some other results concluded that Fe-TiO_2 catalytic activity decreased over time in the photodegradation of ethanol (Arana et al., 2004). It has been hypothesized that those different results are due to the diverse preparation methods used in the doped-TiO_2 catalysts (Arana et al., 2003). Another benefit of ion doping is that it changes the lifetime of electron-hole

separation and adsorption characteristic of the original TiO_2 solid (Wilke and Breuer 1999). By increasing the lifetime of the separated charges, the catalyst activity is increased as well.

More research on TiO_2 catalyst modifications will be forthcoming in the next decades. This research will aim to produce a catalyst capable of generating hydroxyl radicals with visible irradiation. These new photocatalysts will need to be cheap, biologically and chemically inert, insoluble under most conditions, photostable, and nontoxic in order to compete with the current most active TiO_2 Degussa P25 catalyst.

In an annular slurry photoreactor, the efficiency of purification, hence the overall degradation rate, is determined by the UV radiation distribution within the illuminated space (Pareek 2005). The first step in photocatalysis is always the adsorption of light by the solid semiconductor, generating; then, the e^-/h^+ pairs that produce the hydroxyl radicals. As a result, the rate of initiation in any photocatalytic process is intimately related to the radiation intensity inside the photoreactor. The light intensity distribution inside the reactor should not be the rate determining step. Therefore, it is desired to have a well-illuminated reactor with no dark zones. Nonetheless; due to the nature of the TiO_2 catalyst, scattering of light within the photocatalytic reactor makes the design procedure even more complex (Pareek et al. 2003). In this respect, for design purposes, studying the rate of energy absorption in the photoreactor is important. Three parameters should be obtained from the radiation field modeling: (1) the local volumetric rate of energy absorption (Marugán et al., 2006), (2) the optimal photocatalyst concentration ensuring maximum radiation absorption and no dark zones within the reactor (Moreira et al. 2010), and (3) the phase function that better describes the interaction of TiO_2 particles with light (Cabrera et al. 1996).

3.2   Radiation Studies in Photocatalytic Reactors

The photocatalytic reaction can take place if the light source used in the process has enough energy to promote TiO_2 excitation. Therefore, an accurate estimation of light intensity distribution is critical in the design and rating of photoreactors (Pareek et al., 2008). This task involves the estimation of the LVREA. Experimentally, the LVREA could be determined by different methods. The simplest one is chemical actinometry, which gives high values for the LVREA, because it assumes that the reacting medium absorbs all photons reaching the inner reactor wall. Salaices et al. (2001 and 2002) proposed an alternative experimental method for

the evaluation of the rate of photon absorption inside an annular photoreactor. This method uses radiometric measurements, along with a macroscopic radiation balance (MRB), to determine the radiation absorbed by the solid catalyst, as well as the forward and backward scattering radiation and the extinction coefficients.

The LVREA can also be obtained by numerically solving RTE (Pasquali et al., 1996). The difficulty of the exact calculation of radiative transfer in absorbing and scattering media has led to the development of approximate solutions for the RTE (Carvalho and Farias 1998). The most common numerical methods for finding the solution to the RTE are the Discrete Ordinate method (DO), the Finite Volume method (FV); which is in fact, a conservative variant of the DO method, and the MC method (Pareek and Adesina 2004).

Stochastic simulation methods, such as MC method, are preferred over deterministic methods for finding the LVREA for complicated geometries (Changrani and Raupp 1999). It has been stated that a statistical approach to assess the absorbing and scattering phenomena in heterogeneous systems is the most effective tool (Yokota et al., 1999). Although the discrete and finite volume methods are extensively applied in solving the RTE, application of these methods for complicated reactor geometries is very difficult.

3.2.1 Experimental Evaluation of Photon Absorption in an Annular Photoreactor

Experimentally, the rate of light adsorption is performed by doing a MRB around the catalyst suspension as described in Figure 2

$$P_a = P_i - P_t - P_{bs} \tag{13}$$

where P_a is the rate of absorbed photons, P_i is the rate of photons reaching the reactor inner surface, P_{bs} is the rate of back-scattered photons exiting the system, and P_t is the rate of transmitted photons in einsteins s^{-1}.

The various terms in Eq. (13) are estimated as follows:

(a) P_i is estimated from the rate of photons emitted by the black light lamp (P_o) minus the rate of photons absorbed by the inner Pyrex glass ($P_{a\text{-}wall}$):

$$P_i = P_o - P_{a-wall} \qquad (14)$$
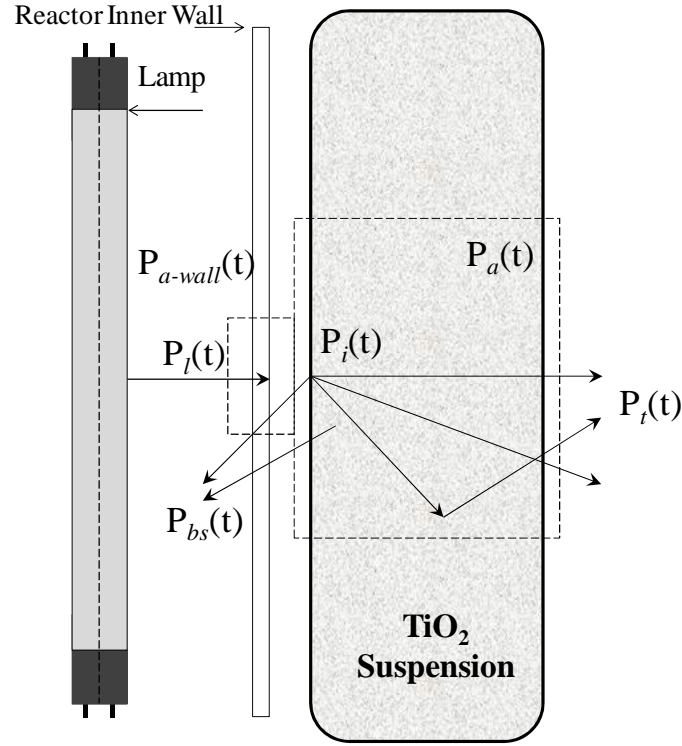
Figure 2 Schematic representation of the Macroscopic Radiation Balance in the Photo-CREC Water-II (Adapted from Salaices et al., 2002).

The rate of photons emitted by the lamp can be determined from radiometric measurements and from the lamp emission spectrum. When measuring the total radiation emitted by the lamp, the following equation is applied to get the total radiation,

$$P_o = \int_{\lambda_1}^{\lambda_2} \int_0^L \int_0^{2\pi} q(\theta, z, \lambda) r\, d\theta\, dz\, d\lambda \qquad (15)$$

where $q(\theta,z,\lambda)$ is the radiative flux obtained from the spectrometric measurements in W m^{-2} at every wavelength of the emission spectrum, r is the radial coordinate in m, z is the axial coordinate in m. The emission spectrum of the lamp will be presented in future sections of this thesis.

$P_{a\text{-}wall}$ is estimated from transmission measurements through the inner Pyrex tube. Results will be presented in following chapters.

(b) P_{bs} is approximated from the difference between P_i and the rate of photons transmitted when the catalyst concentration approaches zero (Augugliaro et al., 1991; Schiavello et al., 1991; Salaices et al. 2002):

$$P_{bs} = P_i - P\big|_{C \to 0^+} \tag{16}$$

(c) P_t is the addition of the transmitted nonscattered radiation (P_{ns}) and the forward-scattering radiation (P_{fs}).

$$P_t = P_{ns} + P_{fs} \tag{17}$$

One should mention that P_{fs} and P_{ns} can be estimated by using polished-aluminum tube collimators, which account for the combined transmitted nonscattered radiation and forward-scattering radiation (P_t), and black collimators, which account only for the transmitted non-scattered radiation respectively (P_{ns}), as explained by Salaices et al., 2002. Hence, P_t is directly measured at each window position in the reactor, using the polished aluminum collimator. Determination for each term in the MRB will be explained in section 5.1.

3.2.2   Numerical Evaluation of the LVREA

The application of the radiative transfer equation (RTE) to photocatalytic processes can be done by making a radiation balance across a thin slab (shown in Figure 3). The resulting equation may be expressed as (Pareek et al., 2008 and 2003; Marugan et al., 2006; Brandi et al., 2003; Martin et al., 1996):

$$
\begin{aligned}
\frac{dI_\lambda(s,\Omega)}{ds} &= -\kappa_\lambda I_\lambda(s,\Omega) - \sigma_\lambda I_\lambda(s,\Omega) \\
&+ j_\lambda^e(s) + \frac{1}{4\pi}\sigma_\lambda \int_{4\pi} p(\Omega' \to \Omega) I_\lambda(s,\Omega') d\Omega'
\end{aligned} \tag{18}
$$

where I_λ is the spectral specific intensity of radiation having a wavelength λ (einstein m^{-2} s^{-1} sr^{-1}), κ_λ is the absorption coefficient (m^{-1}), σ_λ is the scattering coefficient (m^{-1}) of the participating media, and p($\Omega' \to \Omega$) is the phase function for the in-scattering of photons.

The first term on the right hand side of Eq. (18) represents the loss of photons due to absorption, the second term considers the loss of radiation due to out-scattering, the third term accounts for emission of light due to temperature effects and the fourth term shows the gain in radiation due to in-scattering.
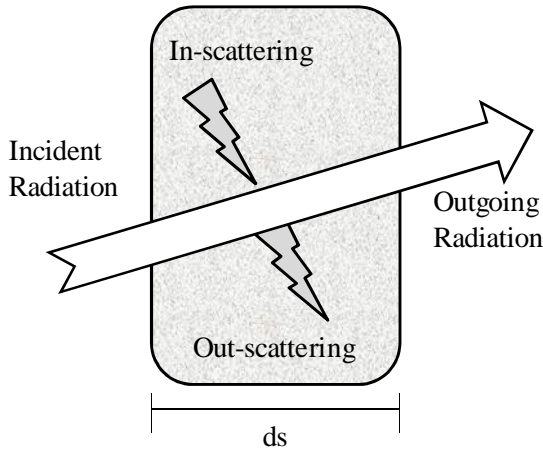
Figure 3 Radiation balance in a slab in the photoreactor

Integration of this partial-integro-differential equation requires at least one boundary condition, at the point of radiation entrance to the reactor volume. This can be provided by an appropriate lamp emission model.

The radiation balance presented here is normally made with the following assumptions (Romero et al, 1997):

    (a) Scattering occurs, but every scattering is independent of each other. This assumption is valid for low concentration of TiO_2 in water, which is typical in photocatalysis.

    (b) Scattering is elastic; the loss of radiation only occurs through absorption by the TiO_2 particles and out-scattering. Similarly, the gain in radiation is by emission and in-scattering.

Due to photocatalysis being carried out at low temperatures, the emission term can be neglected. If it is considered that the sum of κ_λ and σ_λ is called the extinction coefficient β_λ, Eq. (18) could therefore be rearranged to give:

$$\frac{dI_\lambda(s,\Omega)}{ds} = -\beta_\lambda I_\lambda(s,\Omega) + \frac{1}{4\pi}\sigma_\lambda \int_{4\pi} p(\Omega' \rightarrow \Omega) I_\lambda(s,\Omega') d\Omega' \tag{19}$$

If the local incident radiation at any point from all the directions is given by:

$$G_\lambda(x, y, z) = \int_{\Omega=0}^{\Omega=4\pi} I_\lambda(s,\Omega) d\Omega \tag{20}$$

Then the LVREA at any point can be represented as:

$$LVREA(x, y, z) = \kappa_\lambda G_\lambda(x, y, z) \tag{21}$$

The absorption threshold for TiO_2 depends on the energy bandgap. For anatase, the bandgap is 3.2 eV, and those photons with a wavelength less than or equal to the band gap energy $(\lambda_{Ebg} = 390\,nm)$ promote excitation of electrons in the semiconductor particles. Therefore, the total LVREA is given by:

$$LVREA = \sum_{\lambda \leq \lambda_{bg}} E_{l,\lambda}(x, y, z) = \sum_{\lambda \leq \lambda_{bg}} \kappa_\lambda G_\lambda(x, y, z) \tag{22}$$

In order to find the solution of the RTE, two optical parameters for the different TiO_2 catalyst are needed: the absorption and scattering coefficients and the distribution function for photon scattering or the phase function of the slurred media.

3.2.2.1   Optical Properties of TiO_2 Powders

Since the values for the κ_λ and σ_λ coefficients for titania powders depend on the wavelength of the light source, Eq. (19) needs to be solved for every individual wavelength of the radiation source. In most cases, this complicates the solution of the RTE, not only because it requires extensive use of computer memory, but also because the determination of absorption and scattering coefficients is not a trivial exercise. Therefore, in the calculations presented in

this study, the wavelength-averaged values of the absorption and scattering coefficients will also be considered.

Theoretical determination of the absorption and scattering coefficients can, to some extent, be achieved; however, it is hard to utilize a theoretical approach to calculate these two values. Conventional spectrometric measurements can only allow the determination of the extinction coefficient by a simple extinctance measurement with the black collimators (see section 5.1.3). Several studies in the literature have evaluated the absorption and scattering coefficients for DP 25, Anatase, and Hombikat UV-100 (Romero et al., 2003; Cabrera et al., 1996). These authors used an experimental approach that renders separate values of the absorption coefficients. They used independent measurements with a cell-spaced total diffuse reflectance equipment, which allows the determination of all the radiation that is coming out from the sample cell. The values for the specific scattering and absorption coefficients are reported in Figure 4 and Figure 5 respectively, as a function of wavelength.

For polychromatic radiation, the wavelength-averaged values for three of the different photocatalysts used (DP 25, Anatase and Hombikat UV-100) is easily calculated over the useful spectrum of the incident radiation with the following formulas (Toepfer et al., 2006):

$$\kappa^* = \frac{\int_{\lambda_{\min}}^{\lambda_{\max}} \kappa_\lambda^* q_\lambda d\lambda}{\int_{\lambda_{\min}}^{\lambda_{\max}} q_\lambda d\lambda} \tag{23}$$

$$\sigma^* = \frac{\int_{\lambda_{\min}}^{\lambda_{\max}} \sigma_\lambda^* q_\lambda d\lambda}{\int_{\lambda_{\min}}^{\lambda_{\max}} q_\lambda d\lambda} \tag{24}$$
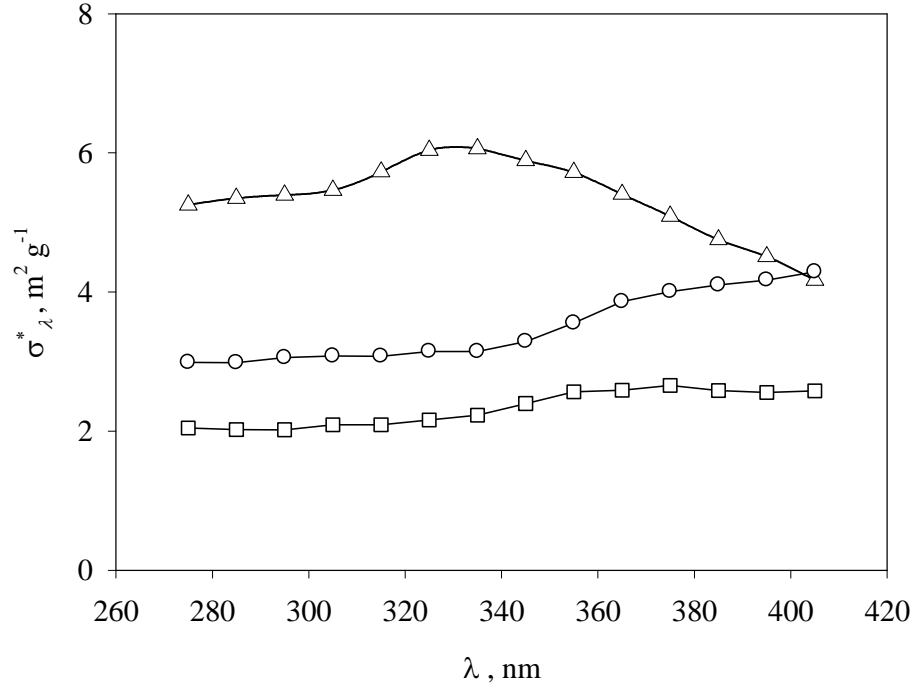
Figure 4 Specific Scattering coefficient, (Δ) DP 25, (○) Anatase, and (□) Hombikat UV-100.
(Adapted from Romero et al., 2003 and Cabrera et al., 1996)

λ_{min} and λ_{max} are the minimum and maximum wavelength of the incident radiation from the BL-lamp (310-410 nm), q_λ is the radiation intensity at wavelength λ, and κ^* and σ^* are the specific absorption and extinction coefficients reported in Figure 4 and Figure 5.

Although some experimental values for the optical properties of some TiO_2 materials have been reported in the literature, the development of new TiO_2 based photocatalysts requires that the optical properties for these materials be accurately determined. Therefore, developing an easy to apply methodology for the assessment of optical properties for different solid materials, is of outmost importance.
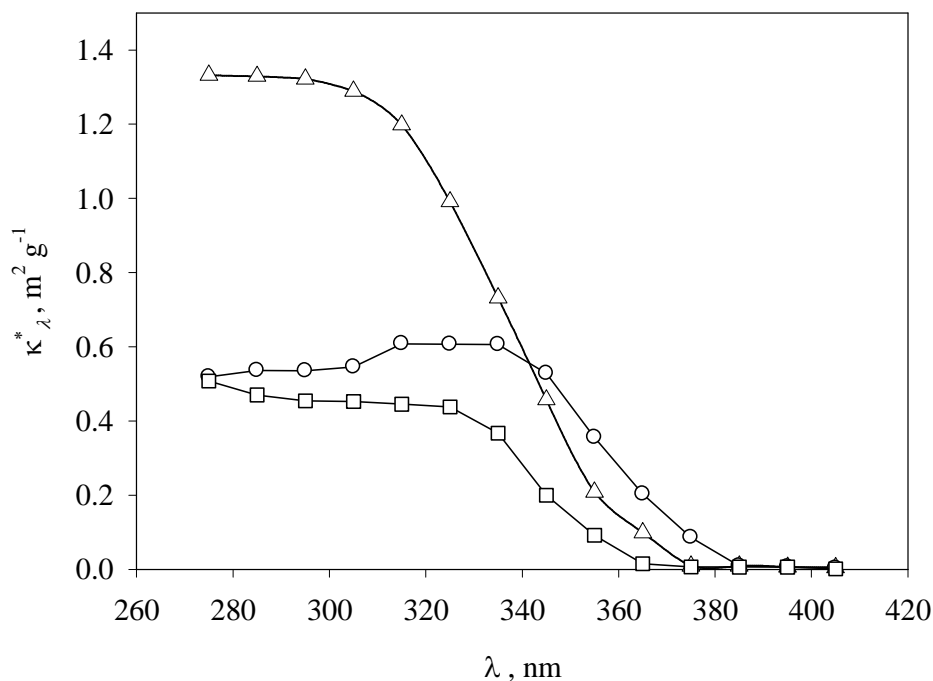
Figure 5 Specific absorption coefficient, (Δ) DP 25, (○) Anatase, and (□) Hombikat UV-100. (Adapted from Romero et al., 2003 and Cabrera et al., 1996)

3.2.2.2　Monte Carlo Simulations

The LVREA distribution can be determined in any computational domain by solving the RTE. Several issues have to be addressed before this can be accomplished. First, the optical properties of the reaction medium (i.e. absorption and scattering coefficients and the phase function) have to be known (Pareek et al., 2008). Second, the boundary conditions (light being received by the radiation source) have to be precisely established. In MC simulations, individual photons (or bundles of photons) are traced from their creation until the photons are either absorbed or scattered from the system.

The RTE is an integro-differential equation that describes the light intensity distribution in a photoreactor. For homogeneous photoreaction systems, an analytical solution for the RTE is feasible (Yokota et al., 1999). For a heterogeneous medium; however, and given solid particles cause scattering and light absorption, an analytical solution is only possible under simplified assumptions (Colina-Marquez et al., 2009; Brucato et al., 2006; Li Puma et al., 2007). Furthermore, due to the heterogeneous nature of TiO_2 particles, scattering occurs according to mechanisms that are quite different from those in multiphase gas-liquid systems.

In photocatalytic systems, the light intensity distribution in a photoreactor is a function of: (a) lamp type, (b) reactor geometry, (c) type of catalyst, (d) catalyst concentration, (e) particle agglomeration size, (f) the nature of the reactor walls (highly reflecting reactor walls, specular and diffuse reflecting walls, non-reflecting walls), (g) flow rate, (h) pH, (i) recycle flow rate, and (j) radiation wavelength (Pareek et al. 2003;Salaices et al., 2002).Therefore, a numerical solution of the RTE seems to be a viable alternative.

The MC method is a statistical method, which is based on following the trajectories and fates of photons inside the absorbing reactor volume, until the photons are either absorbed by the solid particles, the reactor walls, or outside-scattered by the slurred media (Yokota et al., 1999; Pareek et al., 2003). Emission, reflection and absorption are determined at each point in the reactor by a random event. The optical properties of the media, as well as the phase function, determine the probability distribution functions for each event played in MC method. The number of photons emitted from the light source's surface is related to the emitting power of the radiation source. Once a photon is emitted by the light source, it may be absorbed by the semiconductor particle (determined by a random choice based on the absorption coefficient). If the photon is absorbed, a new photon is emitted with a new randomly chosen direction (based on the scattering coefficient of the media). If, however, the photon is not absorbed in the reacting space, the photon will reach a wall. Once the photon reaches this point, its fate will be given by the nature of the rector walls (reflecting or absorbing walls).

The MC method has been successfully employed in solving the RTE in photocatalytic reactors. Different MC simulations for radiation modelling could be considered depending on the underlying hypotheses. Pasquali et al. (1996) used MC method to find a two dimensional radiation field inside an annular reactor with a coaxial central lamp. They studied the effect of the optical thickness and concluded that in order to exploit the reactor volume effectively, the value for the LVREA inside the annular section should be sufficiently large at every point within the reactor. This LVREA value depends mainly in the amount of TiO_2 concentration used, and that it is desirable to have a catalyst with low values for the albedo.

The MC method has also been applied in an annular packed-bed photoreactor. Changrani and Raupp (1999) used two different methods for simulating the photon transport inside a

photoreactor packed with alumina reticulated foam. In the first approach, the photon flight is determined by a predefined reticulate structure. In the second approach, a random porous structure is generated as the photons fly inside it. These two approaches yielded almost identical results. The fates of the photons inside the packed annular section were determined by using the optical properties of the medium, absorption and extinction coefficients. The effect of the role of the lamp in MC methods has not been studied in the literature. The fate of photons that are back reflected to the lamp remains unclear.

The MC method can easily be used for any complex geometry. However, a large enough sample of photons must be followed, so that the solution has statistical significance. Ideally, the number of events played in MC should be the total number of photons which the light source is emitting. Nevertheless, fewer events need to be played, so that the extensive computer time is not required to obtain simulation results with low statistical error.

Pareek et al (2008) presented a MC approach for predicting the radiation field inside a 3D space. In this work, a detailed description of the MC method is explained for an isocratic phase function. These authors divided the reaction space into small cubic cells. From the information of points of absorptions, predictions for the LVREA were made. The most interesting conclusion about this work was that simulations of 6×10^{19} photons were obtained by forming packets of photons. 6×10^{11} photons were grouped to give 10^8 packets of photons, which is the number of events played in MC simulations. Yokota et al. (1999), for example, considered 10^5 events in a MC simulation for the prediction of light intensity decay in a heterogeneous medium.

In photocatalysis, there is multiple scattering involved due to the topography of TiO_2 particles. The parameter describing the scattering mode in Eq. (18) is the phase function $p(\Omega' \rightarrow \Omega)$. This parameter gives the probability that a photon will be scattered from the direction Ω' to the direction Ω. Therefore, the selection of the phase function is an important step in any calculation where multiple scattering is involved.

Computing the new directions of the scattered photons is perhaps the most challenging task in solving the RTE, requiring a large amount of computer time (Binzoni et al., 2003).Thus, complicated phase functions require a large computation time, leading to inefficient

simulations. In an established scattering problem; however, the phase function is given, not chosen. Therefore, it is customary to use a phase function that preserves the main characteristics of the real phase function, while at the same time, rendering manageable computation of the scattering angles (Satuf et al., 2007).

The Henyey-Greenstein (HG) phase function seems to be an appropriate choice. This is a one parameter function that is able to reproduce a wide range of scattering probability density functions (Marugan et al., 2006). Moreover, most of the studies presented in the literature on MC simulations adopted isocratic phase functions (Pareek et al 2008, Pasquali et al 1996). It has been stated that the H-G phase function approximation provides adequate results when the scattering phenomena is close to isotropic (Bai et al., 2011).

The H-G phase function is represented by the following equation:

$$p_{HG}(\theta) = \frac{1}{4\pi} \frac{1 - g^2}{\left(1 + g^2 - 2g\cos(\theta)\right)^{3/2}}$$

(25)

where θ is the scattering angle and g is the asymmetry factor of the scattered radiation distribution. The H-G phase function is determined by the g parameter. The g parameter varies smoothly from -1 to +1. In this way, the H-G phase function considers completely backward to a completely forward phase function form. When $g = 0$, it represents an isotropic phase function (Satuf et al., 2005). Figure 6 shows the probability distribution functions versus the scattering angle θ in polar coordinates for different g values. The figure shows that the phase function can model backward, forward and isocratic phase functions with a simple mathematical expression. Therefore, different values for g are enough to describe different phase functions with a high degree of accuracy (Satuf et al., 2005).
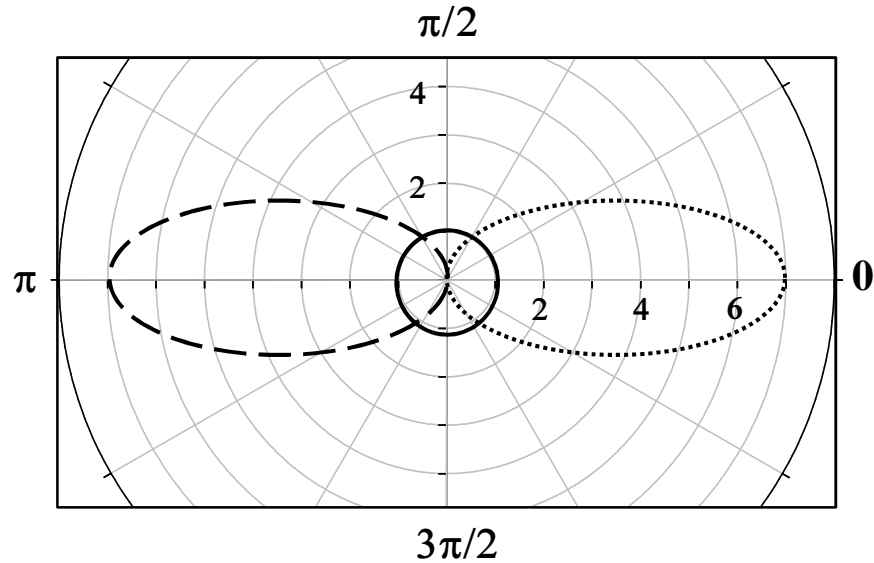
Figure 6 P_{HG} for (solid line) *g = 0*, (broken line) *g = -0.5*, and (dotter line) *g = +0.5*

MC simulations of photon interactions employ random numbers to choose points of emission, optical depths, scattering angles, absorption and scattering probabilities. Since all these random numbers are generated by a set of algorithms in a computer, no output is truly random. Therefore; in order to produce sequences of numbers that pass a suitable randomness test, an algorithm has to be developed. The RAND function in MATLAB provides an excellent and an easy way to generate pseudorandom numbers for MC simulations (Pareek et al., 2008). This function (with a period of $(2^{19937}-1)/2$) easily exceeds any of the computational number of simulation steps**.**

Once all the optical properties of the medium are well established, the phase function is selected and the radiation source is well characterized, MC method can easily be applied to solve the RTE. The mathematical steps and considerations of the MC method need to be established before solving the problem.

3.3 Kinetic Studies of Photocatalytic Degradation of Organic Pollutants in Water

Most of the kinetic studies of organic compounds on TiO_2 catalysts presented in the technical literature, deal with a single model organic compound. However; it has been shown that during photodegradation of organic compounds, several intermediate compounds are formed

(Ortiz-Gomez et al., 2008; Fujishima et al., 2000). While a kinetic model with a single component might fit well the experimental data, neglecting the intermediate compounds and the total organic profiles to complete mineralization, is a common error in portraying the photodegradation kinetics (Chong et al. 2010). In this respect, kinetic models for the oxidation of organic model compounds have been mainly obtained on the initial rates method. These kinetic models fail to consider the intermediate compounds normally formed during a photoreaction.

Depending on the degree of complexity in the kinetic model, two approaches can be taken when modeling phenol photodegradation. First, the organic concentration of all the species participating could be expressed together in the TOC profiles. This will lead to a simpler kinetic modeling with an in-depth understanding on the photodegradation kinetics. Second, a kinetic model based on the L-H equations provides a tool for describing the behaviour of the model compound, as well as the intermediate species formed during the photoreaction (Hernandez-Alonso et al., 2002). L-H model provides the values for the kinetic constants for each of the heterogeneous reactions contributing to phenol oxidation after a kinetic parameter optimization evaluation is performed.

Thus, on the basis of the above, two approaches will be discussed. The first one considers a simplified kinetics. The second approach consists of a more rigorous approach involving a L-H kinetics with several organic chemical species.

Concentration profiles for the model compound and its intermediate species are considered in a kinetic model by applying non-linear regression analysis to a combined set of all the experimental data. This will result in a parameter estimation that is objective and more accurate, within the mechanistic limitations of the assumed kinetics.

3.3.1   Conventional Langmuir Isotherm

It has been reported that the pH plays a major role in the adsorption of organic molecules on solids, particularly when the adsorbant is TiO_2 (Bekkouche et al., 2004). It has also been reported in the same study that the optimum adsorption of phenol occurs at a pH value between 5 and 6. In strong acidic solutions, the adsorption of phenol is lower. This is explained by the fact that at low pH, the molecule of phenol is non-dissociated (neutral). The

TiO$_2$ surface is also neutral at lower pH values (TiOH). In conclusion, adsorption of phenol is favoured around the isoelectric point of TiO$_2$. One should mention that in the experimental evaluation of adsorption constants of different compounds on TiO$_2$, it is important to keep the same experimental conditions as those used in the degradation experiments: pH, flow rate, air rate supply and temperature.

The classical model of Langmuir isotherm gives a good description of the adsorption of phenol and its intermediates on TiO$_2$ at equilibrium (Cai et al. 2003). The well known expression of the Langmuir model is given by the following equation:

$$Q_e = \frac{Q_{max} K_i^A C_e}{\left(1 + K_i^A C_e\right)} \tag{26}$$

where Q$_e$ (mg-C g$_{cat}^{-1}$) and C$_e$ (mg-C l^{-1}) are the amount of compound per unit weight and the concentration in the liquid phase at equilibrium, respectively. Q$_{max}$ (mg-C g$_{cat}^{-1}$) is the maximum amount of organic compound adsorbed that forms a monolayer on the TiO$_2$ powder and K$_i^A$ (mg-C^{-1} l) is the adsorption constant of component i. This constant related the affinity of the compounds to the binding sites in the TiO$_2$ catalyst.

In order to find K$_i^A$ and Q$_{max}$ from experimental data, the expression shown in Eq. (26) needs to be rearranged. On linearization the equation it becomes:

$$\frac{1}{Q_e} = \frac{1}{Q_{max}} + \frac{1}{Q_{max} K_i^A} \frac{1}{C_e} \tag{27}$$

From the slope and the intercept of Eq. (27), the calculation of the two Langmuir parameters could be obtained when experimental data of C$_e$ and Q$_e$ is available.

This approach has been used for different authors (Bekkouche et al., 2004; Ksibi et al. 2003). All of them concluded that phenol, hydroquinone and hydroxylated phenolic compounds, and carboxylic acids are weakly adsorbed on TiO$_2$ surface and that adsorption equilibrium is obtained after 30 minutes.

3.3.2   Approximation Mmethods for Kinetic Modeling

The complexity of the kinetic modeling in photocatalytic reactions is caused by the fact that the TOC profiles are a sum parameter that includes many sub products that undergo diverse reactions (Ortiz-Gomez et al., 2008). Therefore, many different equations are needed to describe the physical process. From a practical point of view, total organic carbon (TOC) profiles appear to be of zero order; and hence, it will be easy to handle them in a kinetic modeling. The degradation rate of TOC could be referred to as the maximum degradation rate since it dictates the degree of total mineralization.

An approximate kinetic solution, having an analytical form of an L-G equation, can be applied to the experimental TOC profiles. This equation is given as follows (Chong et al. 2010; Malato et al. 2009; Minero et al. 1996):

$$r_{TOC,0} = -\frac{d[TOC]_0}{dt} = \frac{\beta_1[TOC]}{\beta_2 + \beta_3[TOC]} \tag{28}$$

β_1, β_2 and, β_3 are empirical constants. [TOC] is the concentration profile of TOC in ppm-C when phenol is degraded in a photocatalytic process, $r_{TOC,0}$ is the degradation rate of TOC in mg-C min$^{-1}l^{-1}$. Eq. (28) can be rearranged and the following expression is obtained:

$$\frac{1}{r_{TOC,0}} = \frac{\beta_3}{\beta_1} + \frac{\beta_2}{\beta_1}\frac{1}{[TOC]_0} \tag{29}$$

By using the experimental TOC profiles at different initial concentrations, values for the initial rate can be calculated. From the intercept and the slope obtained, one can calculate the ratio of the different β numbers as shown below.

$$\frac{\beta_3}{\beta_1} = \text{intercept} \quad \text{and} \quad \frac{\beta_2}{\beta_1} = \text{slope} \tag{30}$$

Using these values, the experimental TOC profiles can be fitted with Eq.(31).

$$\frac{\beta_2}{\beta_1}\left[\ln\left(\frac{[TOC]_0}{[TOC]}\right)\right] + \frac{\beta_3}{\beta_1}[[TOC]_0 - [TOC]] = t \tag{31}$$

Hence, values for the empirical constants can be found from this procedure. The above equation also allows the prediction of TOC degradation as a function of time and initial concentration of TOC. In following chapters, this methodology will be applied.

3.3.3 Langmuir-Hinshelwood Isotherms for Multicomponent System in Photocatalysis

In photocatalytic processes, the interaction of the organic compounds with the semiconductor surface plays a major role (Robert et al. 2000). Adsorption of these compounds on the catalyst's surface is a prerequisite for a high efficient process. It is also known that photocatalytic reactions can be modeled using a Langmuir-Hinshelwood (L-H) rate equation. Therefore; for a multicomponent system in photocatalysis, a set of differential equations, based on the L-H model, can be developed. These equations describe the formation and disappearance of the model compounds as well as their intermediate species. Due to the immediate decomposition of the model compound into CO_2 and other intermediates, influence of these compounds has to be considered on the L-H rate equations and this, even if their adsorption onto TiO_2 surface is weak (Xu and Langford 2000). Therefore; the following assumptions are considered in developing the kinetic model: (a) model compound and its intermediates adsorb on the catalyst surface; hence, the reaction is surface mediated, (b) final product CO_2 is not adsorbed by the TiO_2, (c) the reaction system is in dynamic equilibrium (Chong et al. 2010), (d) photolysis is neglected as it has a little effect in the model compound and intermediate degradation. If these assumptions are valid, the reaction steps only involve adsorption surface sites, organic molecules and its intermediates, electron-hole pairs and the reactive oxygen species.

The general form the L-H equation for photocatalytic reactions is given by (Montoya et al. 2009; Laoufi et al. 2008; Brosillion et al. 2008; Gora et al. 2006;Chan et al. 2001; Mehrvar et al. 2000):

$$r_i = \frac{k_i^k K_i^A C_i}{1 + \sum_{j=1}^{n} K_j^A C_j} \tag{32}$$

where subscript *i* refers to component "*i*", r_i is the reaction rate (mol g_{cat}^{-1} min^{-1}), k^k_i is the reaction kinetic constant (mol g_{cat}^{-1} min^{-1}), K^A_i is the absorption constant (mol^{-1} l), and C_i is the concentration of the participating species (mol. l^{-1}). "*j*" is the subscript denoting each component of the *n* chemical species.

When a rector is operated in a batch mode as is the case of Photo-CREC Water II a balance equation for each component "*i*" can be expressed as follows:

$$r_i = \frac{1}{W}\frac{dN_i}{dt} = \frac{V}{W}\frac{dN_i/V}{dt} = \frac{V}{W}\frac{dC_i}{dt}$$ (33)

with W being the mass of the solid catalyst (g_{cat}), V is the reactor volume (*l*), N_i is the number of moles *i* (mol) and *t* is the time (min).

Substituting Eq. (33) into Eq. (32), the reaction rate for each chemical species in the contest of the slurry reaction unit can be obtained:

$$\frac{dC_i}{dt} = \frac{\frac{V}{W}k^k_i K^A_i C_i}{1+\sum_{j=1}^{n}K^A_j C_j}$$ (34)

This last equation can also be expressed as:

$$\frac{dC_i}{dt} = \frac{k_i C_i}{1+\sum_{j=1}^{n}K^A_j C_j}$$ (35)

with k_i being:

$$k_i = \frac{W}{V}k^k_i K^A_i$$ (36)

The rate constants in Eq. (35) represent apparent constants in min^{-1}. The intrinsic kinetic constant can be calculated using the following relationship (Wolfrum et al. 1992):

$$k_i^I = \frac{V_{CSTR} + V_{PFR}}{V_{PFR}} \tag{37}$$

where V_{CSTR} is the volume of the tank and V_{PFR} is the volume of the photoreactor in l.

From the discussion presented above, it can be concluded that for every component participating in the reaction scheme, an equation with the form of Eq. (35) can be obtained to represent the photocatalytic oxidation of the model compound and its intermediates. Several kinetic and adsorption parameters need to be numerically estimated. One limitation of the L-H model is that for a large number of chemical species, a large number of kinetic and adsorption parameters will need to be optimized. This could lead to models with high cross correlation. This could be solved to some extend by experimentally finding the adsorption constants of the participating components.

3.3.4   Parameter Estimation Problem

The formulation of the differential equations based on L-H model is equally important to the actual solution of the problem of parameter estimation. Parameter estimation of the kinetic constants is done by fitting the mathematical model to the experimental data. The mathematical model with the best parameter estimate is used to predict the behavior of a reacting system, where that model is assumed to describe the physical process. The L-G model, for multiple reactants, is formed by a set of ordinary differential equations (ODE). The set of ODE cannot be solved analytically; hence the optimization process needs an algorithm that calls for the iterative integration of the set of ODEs that minimizes an objective function (Englezos et al. 2001).

If a dynamic system described by a set of ODEs of the L-H form is considered; then, the ODEs cannot be solved analytically. Hence, in these situations the model can be written in the following form (Englezos et al. 2001; Constantinides et al. 1999).

$$\frac{d\vec{C}(t)}{dt} = f\left(\vec{C}(t), \vec{u}, \vec{k}\right), \quad \vec{C}(0) = \vec{C}_0 \tag{38}$$

$$y(t) = AC(t) \tag{39}$$

where

$\vec{k} = [k_1, k_2, ..., k_p]^T$ is a p-dimensional vector of parameters whose numerical values are unknown;

$\vec{C} = [C_1, C_2, ..., C_n]^T$ is an n-dimensional vector of state variables;

$\vec{C}_0 = [C_{10}, C_{20}, ..., C_{n0}]^T$ is an n-dimensional vector of initial conditions for the state variables. These variables are precisely known from experimental measurements.

$\vec{u} = [u_1, u_2, ..., u_r]^T$ is an r-dimensional vector of measured variables.

$\vec{y} = [y_1, y_2, ..., y_m]^T$ is an m-dimensional output vector i.e., the set of variables that are measured experimentally; and

A is the m × n observation matrix which indicates the state variables that are measured experimentally.

The kinetic parameters should be estimated by minimizing the least square (LS) objective function. The objective function is a suitable measure of the overall departure of the model calculated values from experimental measurements. For a system of ODEs, the objective function is given by:

$$SSR = \sum_{i=1}^{N} \left[\hat{y} - \vec{y}(t_t - \vec{k}) \right]^T \left[\hat{y} - \vec{y}(t_t - \vec{k}) \right] \tag{40}$$

where $\hat{y} - \vec{y}(t_t - \vec{k})$ is the residual of the ith measurement defined as the difference between the measured value, $\hat{y}$, and the calculated value using the model and the estimated parameters $\vec{y}(t_t - \vec{k})$;

When data from more than one experiment is used in the parameter estimation, the objective function becomes:

$$SSR = \sum_{j=1}^{N_E} \sum_{i=1}^{N} \left[\hat{y} - \vec{y}\left(t_t - \vec{k}\right) \right]^T \left[\hat{y} - \vec{y}\left(t_t - \vec{k}\right) \right] \tag{41}$$

N_E denotes the number of experiments

The main objective in estimating kinetic parameters is to obtain values for the kinetic and adsorption constants with low 95% confidence intervals (CI) and low to moderate cross-correlation among optimized coefficients.

3.4 Photocatalytic Reactors

The development and design of water and air treatment systems based on heterogeneous photocatalysis is an area of great technical importance (de Lasa et al., 2005). The design of a highly efficient photocatalytic system is of vital interest and one of the most desirable, yet challenging goals in the research of photocatalytic reactors. An important obstacle in the development of an efficient reactor is the establishment of effective reactor designs for intermediate and large-scale use, as demanded by industrial and commercial use. To achieve a successful implementation, several reactor design parameters must be optimized; such as, photoreactor geometry, the type of photocatalyst and its concentration, utilization of radiated energy, operating conditions, etc.

3.4.1 Photoreactor Configurations

Photocatalytic reactors for water treatment can be classified according to their design characteristics; the majority of them fall under the following next categories (de Lasa et al., 2005; Mukherjee and Ray 1999):

a) State of the TiO_2 catalyst: slurry reactors or rector with immobilized photocatalyst.

b) Type of irradiation: photoreactors can be irradiated using: artificial UV light, UV polychromatic lamps or solar radiation.

c) Position of the irradiation source: immersed light source, external light source and distributed light sources such as reflectors or optical fibers.

The majority of the reactors patented are a variation of the slurry reactor and the classical annular reactor of immersion or the external-type. Slurry reactors present larger photocatalytic activity when compared to reactors with an immobilized catalyst (de Lasa et al., 2005). Most of the kinetic studies presented in the literature deal only with experimental data produced in slurry photoreactors. Immobilization of the catalyst generally reduces the overall performance of the photoreactor due to the mass transfer limitations and less catalyst irradiated area (Mukherjee and Ray 1999). Table 2 summarizes the advantages and disadvantages of slurry and immobilized photocatalytic reactors as reported by (de Lasa et al., 2005; Mukherjee and Ray 1999).

Table 2 Suspended versus immobilized photocatalytic systems

Slurry Reactors	Immobilized reactors
Advantages.	Advantages.
● Fairly uniform catalyst distribution	●Continuous operation
	●Improved removal of organic material from water phase while using a support with adsorption properties
●High photocatalytic surface area to reactor volume ratio	
	●No need for an additional catalyst separation operation
● Limited mass transfer	
●Minimum catalyst fouling effects due to the possible continuous removal and catalyst replacement	
●Well mix particle suspension	
●Low pressure drop through the reactor	Disadvantages
	●Low light utilization efficiencies due the light scattering by immobilized photocatalyst.
	●Restricted processing capacities due to possible mass transfer limitations.
Disadvantages	●Possible catalyst deactivation and catalyst wash out.
●Requires post-process filtration	
●Difficult to assess light scattering and absorption in the particle suspended medium	

In the case of photocatalytic reactor with solar irradiation, most of the reactor's designs are TiO$_2$ slurry reactors (de Lasa et al., 2005). The implementation of solar photocatalytic reactors needs special attention in the design of solar thermal collectors, given the important characteristics shared by these units. There are; however, specific constrains for the design of

solar photocatalytic reactors; for instance, the need of expensive UV transparent materials. Solar photocatalytic reactors can operate in continuous and discontinuous mode.

Malato Rodriguez et al., 1996 studied the degradation of several real wastewater samples at the Plataforma Solar de Almeria (Spain) applying a solar photocatalytic reactor. They proved the feasibility of solar photocatalytic detoxification with added oxidants for the treatment of industrial effluents with organic loads of hundreds of ppm. They studied a solar slurry photocatalytic reactor with TiO_2 as a catalyst in two different configurations; compound parabolic concentrating reactor and parabolic trough system. Their results showed that the degradation of industrial waste water can be treated with heterogeneous photocatalysis within the range of medium or low concentration on TOC loads.

3.4.1.1   Operating Conditions in Photocatalysis

The degradation rates of organic compounds in photocatalysis are highly dependent on a number of the operation parameters. These parameters summarized as follows (Chong et al., 2010):

1. TiO_2 Loading: the amount of TiO_2 is directly proportional to the overall photocatalytic reaction rate. This also depends on the reactor geometry and state of catalyst in the system (either fixed or slurry catalyst). The photoreactor should be operated at a catalyst concentration that ensures efficient photons absorption and does not create dark zones within the reactor.

2. pH: this variable depends on the isoelectric point or the surface charge of the photocatalyst used. For TiO_2, the point of zero charge lays in the pH range of 4.5-7.0.

3. Temperature: this variable has little or no effect on the photocatalytic reaction rate. However, it was shown that an increase in photocatalytic reaction temperature (>80 °C) promoted the recombination of electron hole charges (Gaya et al., 2008). Moreover; temperatures below 80 °C actually favour adsorption of contaminants on the TiO_2 surface, resulting in getting kinetics following the of L-H model.

4. Dissolved oxygen: oxygen is an electron scavenger in the photocatalytic process; hence, providing continuous oxygen to the system ensures that the reaction limiting step is not the lack of oxygen.

5. Contaminants and their loadings: under same operating conditions, different initial concentrations of organic compounds will require different irradiation time to achieve complete mineralization. Excessively high concentration of organic substances could saturate the TiO_2 surface and block the UV light reaching the catalyst's surface.

6. Light Wavelength: UV light used in the process needs to have sufficient energy to promote electron hole formation. For TiO_2, the activation threshold occurs at 388 nm. Therefore, UV light with $\lambda < 388$ nm is required for the activation of the catalyst.

7. Light Intensity: A linear dependency of the photocatalytic reaction rate on radiant flux changes to a square-root dependency above certain threshold value. Zeroth order dependency is found at really high radiation intensities.

3.4.1.2 Photoreactor Modeling

Photocatalytic reactions have a very distinctive characteristic: the reaction is activated by light absorption; and consequently, the radiation distribution inside the photoreactor must be obtained. Therefore, the geometry of a photoreactor is much more important than in thermal reactors due to the light propagation inside the reacting zone. An important limitation in the radiation modeling is placed by the pre-established shapes and sizes of the different radiation sources.

Designing a photoreactor starts by selecting its geometry; the light source will be a decisive factor in doing so. Once the geometry has been selected, mass balances has to be performed. These mass balances allow calculating the intrinsic reaction rate, independent of the reactor shape and configuration. Ideally, this reaction rate should be obtained experimentally with the proper degradation experiments. At this stage, the reaction mechanism (or kinetic network) should be known so that the proper rate expressions are obtained. The radiation field inside the reactor needs to be determined, since the activation of the catalyst only occurs when light is present in the system.

Design and scale-up of photoreactors, as well as kinetic studies of photocatalytic systems always requires that the LVREA inside the reactor is known. Fortunately, methods are now available for the correct evaluation of true photon absorption rates in the most commonly used cylindrical reactor geometries (Alfano et al., 2000). However, the solution of the complete radiation transmitted equation is not a simple task (Cassano et al., 2000). In any event, successful modeling and design photoreactors is a combined exercise considering both kinetics and radiation modeling.

3.4.1.3   Photoreactor Efficiencies

Efficiency determinations in photocatalytic reactors allow for a comparison between experimental results obtained from different laboratories and under different experimental conditions (Salaices et al., 2002). Several efficiency definitions are available in the technical literature.

The most frequent parameter is the quantum yield (Sun et al., 1996), which relates the radicals produced on the catalyst surface during the primary reaction processes per absorbed photon. Serrano et al. (1997) also proposed a photochemical thermodynamic efficiency factor (*PTEF*). This parameter relates the energy needed to produce OH$^{\bullet}$ radicals over the irradiated energy absorbed by the photocatalyst. In either case; efficiency determination involves the same key variable, the rate of photons absorbed by the photocatalyst. Hence, it is important to accurately determine this parameter.

3.5   Application of Photocatalytic Processes

Due to the multidisciplinary nature of TiO_2 photocatalysis, numerous researchers have devoted studying photocatalysis and its applications. TiO_2 photocatalysis is classified into many different subjects: (1) reaction kinetics and mechanisms, (2) reactor design and engineering, (3) material synthesis and modification, (4) surface and colloid chemistry, (5) photoelectrochemistry, (6) charge recombination and transfer dynamics, and (7) thin film and coating fabrication (Choi 2006). Thanks to the interdisciplinary nature of TiO_2-related research and the diversity of its applications, TiO_2 is certainly one of the most frequently and thoroughly studied materials in the world. Applications for TiO_2 photocatalysis are

summarized in Table 3. This table was built from data presented in the literature (Fujishima et al. 2008 and 2007; Choi 2006; Diebold 2003).

Table 3 Summary applications for TiO_2 photocatalysis

Application	Category	Examples
Water Purification	Wastewater treatments	Decontamination of river water, ground water, lakes, industrial wastewaters, airport and agricultural wastewater, pool water, fish feeding tanks, water disinfection, oil spill remediation, killing microorganisms and pathogens in water, etc.
Air Purification	Indoor air cleaners Outdoor air purifiers	Room air cleaners, air conditioning, tunnel and buildings air purification, deodorization and disinfection of indoor air, air cleaning units for refrigerators, etc.
Self-cleaning surfaces	Materials for residential and offices	Window blinds, exterior tiles, kitchen and bathroom components, plastic surfaces, traffic signs and reflectors, tent materials, building windows, spray coating for cars, indoor lamp covers, etc.
Self-sterilizing surfaces	Hospitals	Titles and coatings to cover floor and walls in operating rooms, hospital uniforms, public restrooms, pet-breeding rooms.
Photocatalytic metal corrosion prevention	Automotive	Metal corrosion prevention using TiO_2 photo anodes, photocatalytic coating of TiO_2 on metal surface for corrosion prevention, etc.
Photocatalytic lithography	Others	Development of alternative lithographic process utilizing photocatalysis.
Water splitting	Energy	Water splitting for the production of hydrogen from water using photocatalysis.

As presented in the above table, applications of TiO_2 photocatalysis are very diverse. The principles of photocatalytic reactions taking place on the surface of TiO_2 can be applied to the development of many different technologies. Degradation of pollutants in water, air, and even solid phases, and the production of hydrogen from water, are among the most studied areas of TiO_2 photocatalysis.

3.6 Conclusions

The following are the conclusions of this chapter:

(a) Photocatalysis is a potential solution for complete mineralization of organic compounds present in water. This technology can also be applied in air treatment, production of materials with self-cleaning properties, and production of hydrogen from water.

(b) Experimental determination of optical properties in photocatalytic reactors is still a difficult task and this despite the vast information regarding methods for modeling the radiation field inside those reactor units. The optical properties of the TiO_2-water medium need to be obtained in order to solve the RTE.

(c) The MC method is a viable alternative for solving the RTE. However, studies on different phase functions, as well as the effect of the lamp in the modeling are still needed.

(d) Most kinetic studies in the literature deal with simple approaches and single chemical species. However the photocatalytic degradation of organic pollutants should involve not only the model reactant species but various intermediates. Thus, kinetic modeling of photocatalysis reactions is still area worthy of investigation. In particular, the L-H model seems to be a viable alternative for generalized kinetics applicable to a plurality of semiconductors.

(e) Give all the above, this PhD thesis intends to contribute to the numerical determination of optical properties in TiO_2 slurries as well as photocatalytic reaction kinetics involving the various chemical species present.

Chapter 4
Experimental Methods

4 Introduction

This chapter describes the experimental apparatus employed in this PhD research project. The reactants; and the analytical techniques for model pollutant and reaction intermediates identification and quantification are also presented. Lastly; the technique for catalyst preparation and characterization, as well as the experimental procedure employed, is discussed.

4.1 Reactor Setup

The photocatalytic degradation of phenol over various TiO_2 catalysts was carried out in an annular photocatalytic reactor. A schematic representation of the photo reactor is shown in Figure 7. This reactor is called the Photo-CREC-Water II and it is constituted by the following components: (1) 15-W black light lamp or (BL lamp), (2) Pyrex glass inner tube with diameter of 3.58 cm, (3) replaceable Pyrex inner tube with diameter of 5.6 cm, (4) silica windows, (5) black polyethylene outer tube, (6) stirred tank, (7) centrifugal pump, (8) air injector and, (9) sampling port.

Seven 1.1-cm diameter circular windows, made of fused silica, are equally spaced along the reactor's outer cylinder wall to allow radiation transmission measurements. The external cylinder, represented by number 5 in Figure 7, was made of non-reflecting black polyethylene in order to eliminate the reflected radiation from reaching the inner surface wall. The lamp used in the photoreactor is a 15-W 1.33-cm radius, 41.3-cm length, black-light UV lamp. It is positioned symmetrically inside the inner tube of the reactor. A typical radiation spectrum of this type of lamp is given in Figure 8. The characteristics of the lamp are presented in Table 4 along with a summary for the dimensions of the photo reactor. The reactor is equipped with a four-point distributor injector at the entrance. This injector ensures uniform and intense mixing. The four injection points are located on the top section of the reactor at 90°-radial and 45°-azimuthal positions. The pump allows a recirculation flow rate of 16 l min^{-1}. The inner Pyrex reactor tube was selected based on its transmittance. As shown

in Figure 9, this material has good UV transmission properties, allowing for more than 90% of the UV radiation longer than 315 nm.
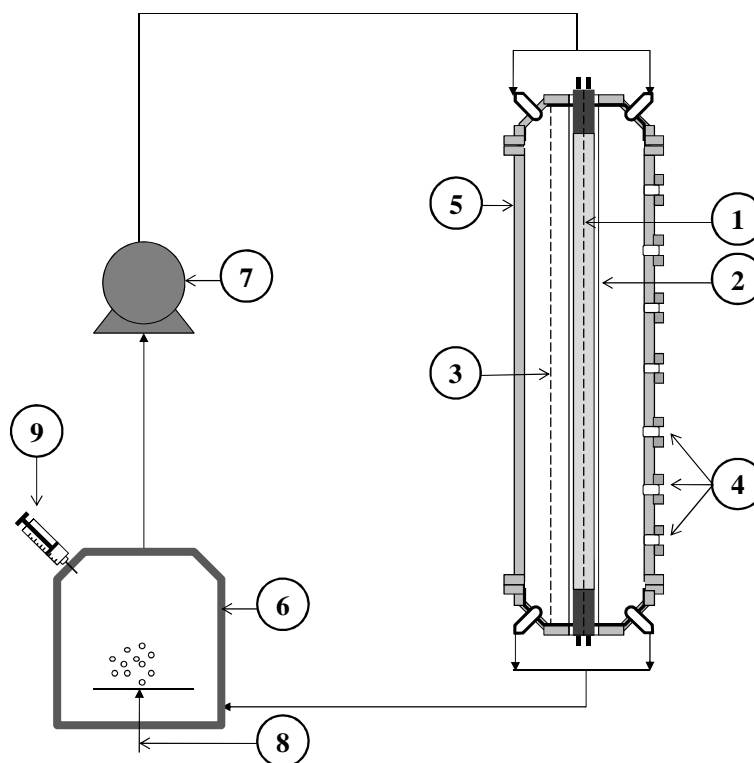
Figure 7 Schematic representation of the Photo-CREC Water-II reactor

Table 4 Dimensions for the photocatalytic reactor and lamp characteristics

Component	Parameter	Value
Annular reactor	internal radius	1.76 cm
	external radius	4.44 cm
	height	44.5 cm
	internal Pyrex glass thickness	0.23 cm
	Illuminated Reactor Volume	2.5 l
Black Blue Light Lamp	input power	15 W
(UVP-XX-15BLB)	output power	4 W
	length	41.3 cm
	radius	1.33 cm
	emission range	300 - 420 nm
	emission rate	1.1910×10^{-5} einsteins s^{-1}

43
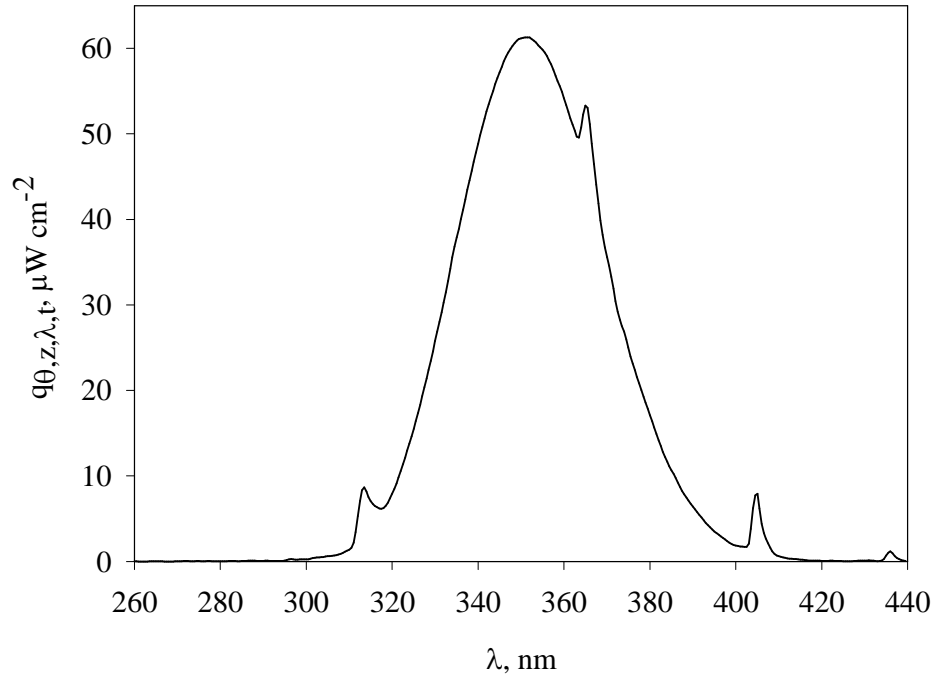
Figure 8 Typical radiative flux spectra for a black light lamp
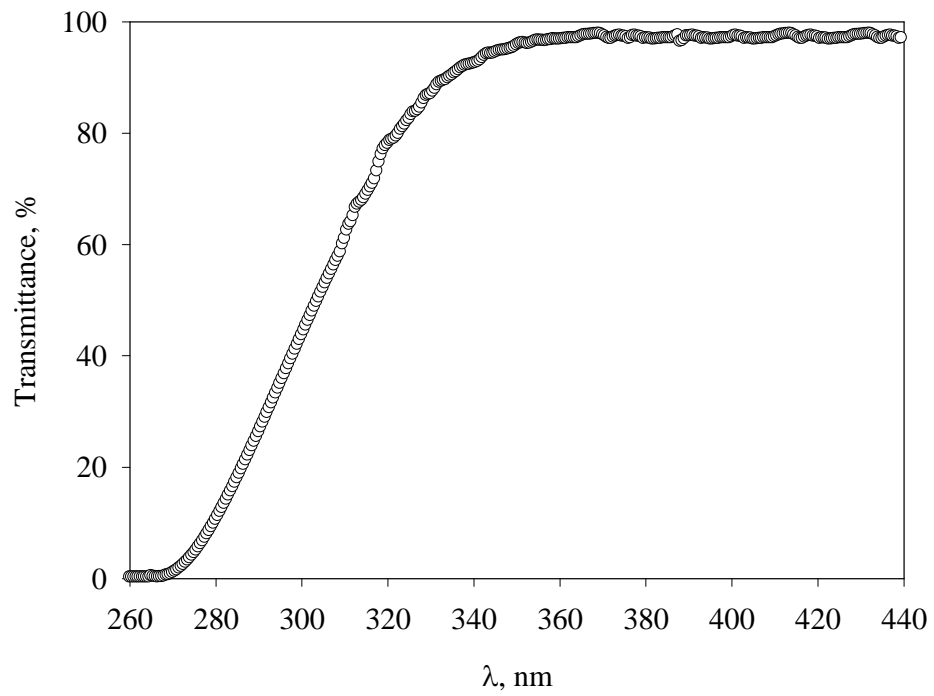
Figure 9 Transmittance as a function of wavelength for the inner Pyrex glass

4.2 Reactants

For this study, the following reactants were used, as received, without any further treatment: a) phenol 99+% (Sigma-Aldrich Lot 0001446411), b) catechol ≥99% (Sigma-Aldrich Lot 10021AA), c) hydroquinone 99% (Sigma-Aldrich Lot 0001446411), d) p-benzoquinone (Fluka Lot 0001333985), e) resorcinol 99+% (Sigma-Aldrich Lot MKBB5334), f) oxalic acid 99+% (Aldrich Lot 241172-50G), g) formic acid (Fluka Lot BCBB9543), h) ortho-phosphoric acid 85% (Fluka Lot DCB0522), i) maleic acid (Fluka Lot 0001451383), j) fumaric acid 99+% (Sigma-Aldrich Lot MKBB7131), k) H_2SO_4 (Caledon, Lot 100602), l) HCl (Sigma-Aldrich Lot 01050DJ), m) 2-propanol ≥99% (Sigma-Aldrich Lot 56096EK), n) titanium (IV) isopropoxide 97% (Aldrich Lot 07009DJ), o) dichloromethane (Caledon Lot 72672), p) sodium sulfate (Caledon Lot 73205, methanol HPLC grade (Caledon Lot 70930) and, q) $FeSO_4x7H_2O$ (J.T. Baker, Lot Y40470).

Table 5 and Table 6 show the names, acronyms and chemical structure of the aromatic and carboxylic acids compounds used in the present study.

Three TiO_2 photocatalysts were used for the photoconversion experiments. These catalysts include Degussa P25 (Evonik Degussa Corporation Lot 4168012489), Anatase >99% (Aldrich Chemicals Lot 23,203-2) and, Hombikat UV-100 (Sachtleben Chemicals)

4.3 Substrate Analysis

4.3.1   Identification of Intermediate Species by GC/MS

Identification of intermediate species in the phenol photodegradation was performed by using a variation of the EPA method 8270D, with the preparation technique 3580. This method identifies semi-volatile organic compounds in water by gas chromatography/mass spectrometry (GC/MS).

Table 5 Names, acronyms and chemical structure for the aromatic compounds employed in this study
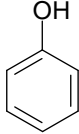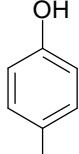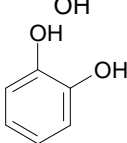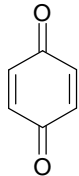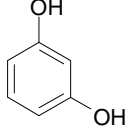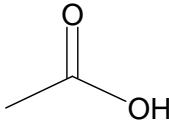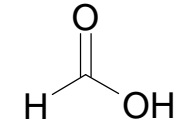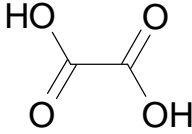
Name	Acronym	Chemical Structure
Phenol	Phenol	
para-dihydroxybenzene (Hydroquinone)	p-DHB	
ortho-dihydroxybenzene (Catechol)	o-DHB	
1,4,-Benzoquinone (p-Benzoquinone)	1,4-BQ	
Resorcinol	Resorcinol	

Table 6 Names, acronyms and chemical structure for the acids employed in this study

Name	Acronym	Chemical Structure
Acetic acid	AcAc	
Formic Acid	FoAc	
Oxalic Acid	OxAc	

The method consists of extracting the possible intermediate species in water by using an organic solvent. This technique is summarized as follows:

(a)　For an initial concentration of 20 ppm of C in phenol, a sample of 25 ml is taken from the photoreactor after 3 hours of reaction time. This sample is transferred into a separation funnel.

(b)　10 ml of dichloromethane (CH_2Cl_2, pesticide quality or equivalent) is measured and immediately transferred to the separation funnel.

(c)　The funnel is shaken for 5 minutes; pressure should be released every 30 seconds by opening the separation funnel from the top cap.

(d)　The organic phase is separated from the funnel and put in a 25 ml crystal vial.

(e)　1 g of sodium sulfate, previously purified by heating it at 400 °C for three hours in a furnace and cooled down in a desiccator for one hour, is added to the sample and shaken for 2 minutes. The sodium sulfate traps the micro drops of water present in the sample.

(f)　The extracted sample is filtered with a pipette through glass wool and is placed in a vial. 1 μL of this sample is injected into an Agilent 5973 Network GC system with a Mass selective detector.

For the GC/MS analysis, an Agilent 19091z-205 350 max HP-1 capillary column of 50 m x 200 μm x 0.5 μm nominal was used. The inlet injection temperature was fixed at 310 °C with a split ratio of 1:30. Helium was used as the carrier gas at a flow rate of 67.5 ml min^{-1}. Temperature of the MS detector was fixed at 320 °C. Samples were run for 35 minutes.

4.3.2   Quantification of Model Pollutant and Intermediate Species

The quantification analysis of aromatic components were performed in a Shimadzu High Performance Liquid Chromatograph prominence LC 20AB with an autosampler SIL-20AC.HT and a column oven CTO-0AC with a Diode Array detector SPD-M20A. An Altima HP C18 column (5 μ 150 mm x 4.6 mm, Lot 50198212) and a mobile phase of methanol and water (miliQ water) 67/33 % v/v at a flow rate of 0.5 ml min^{-1}, were used. The temperature of the column oven was kept at 25 °C throughout all the analysis. The

wavelength of analyses for phenol, p-DHB, o-DHB and 1,4-BQ were done at 270, 290, 275 and, 255 nm respectively. Injection volume for all samples was 10 μL.

Quantification of the two major carboxylic acids detected (acetic and formic) was done in a Waters 1525 binary pump HPLC, with a 2487 dual λ Absorbance detector equipped with a Waters 717 plus Autosampler. A Supelco C-61H column (30 cm x 7.8 mm, Lot 043010) and a mobile phase of 0.1% phosphoric acid at a flow rate of 0.5 ml and a wavelength of 210 nm was employed for the separation in the HPLC system. The injection volume of all the samples was 10 μL at 25 °C. For all the photocatalytic degradation experiments, the total organic carbon was also analyzed using a Shimadzu TOC-V$_{CPH}$, equipped with an ASI-V autosampler.

4.3.3 Catalysts Characterization

The catalyst surface areas (S$_a$) were measured using a Micrometritics Chemisorption Controller ASAP 2010. The TiO$_2$ samples were degassed for 120 minutes at 300 °C. After degassing the samples, N$_2$ was contacted with the catalyst sample immersed in liquid N$_2$. The amount of N$_2$ adsorbed at the operating temperature was used to estimate the total catalyst surface area. Particle size distribution of the TiO$_2$ catalysts was performed by a Brookhaven Instruments ZetaPALS Zeta potential analyzer. For size measurements, samples were diluted in MiliQ water and measured for at least 120 s.

XRD analyses were performed on a Rigaku rotating-anode X-Ray Diffractometer employing CoKa radiation. Monochromation was achieved by using a curved crystal, diffracted beam, graphite monochromater. The instrument was operated at 45kV and 160mA, using the normal scan rate of 10° two-theta per minute. X-rays were collimated using 1° divergent and scatter slits, and a 0.15-mm receiving slit. Sample scans were completed at a rate of 10 degree/minute.

4.4   Experimental Procedure

4.4.1   Radiation Inside the Photoreactor

The photoreactor unit described in Figure 7 contains seven circular windows (S1-UV grade fused silica, 0.32 cm-thickness x 2.54 cm-diameter). These windows are equally spaced along the reactor outer cylinder wall. They allow radiation transmission measurements through the annular section of the reactor. Radiation transmission through the different TiO_2 catalysts at different concentrations was measured on a StellarNet EPP2000C-25 LT16 spectrometer. For the radiation measurements, UV-opaque and inner polished collimators were attached to the reactors windows to limit the amount, and the angle, of the radiation transmission through the catalyst suspensions. UV-opaque collimators (2.3 cm-length x 1 cm –diameter, angle view of 44.4°) were used to determine the extinction coefficients since their non-reflecting surface minimizes the forward-scattering radiation reaching the detector. Aluminum polished collimators (2.3 cm-length x 1 cm –diameter. Angle view of 160°) allowed the assessment of the total transmitted radiation throughout the slurred medium. Figure 10 shows a view of the black and inner-polished collimator tubes used when determining the extinction coefficient in the photoreactor. The view angles for each of these two collimator tubes are also reported. Figure 11 shows a detailed view of the sensor collimator arrangement.

Titanium dioxide suspensions for radiation transmission measurements in the photoreactor were prepared with distilled water. Before any measurement, the reactor was thoroughly washed to ensure that no foreign particles were present during any measurement. The radiation transmission was measured first for an empty reactor with and without the internal tube, in order to measure the transparency of the internal Pyrex tube. The next step was to fill out the reactor with both 6 liters of distilled water and; then, adjust the pH of the solution at 3.7 ± 0.1 with H_2SO_4. After that, the TiO_2 concentration was increased from 0 to 0.3 $g\ l^{-1}$, for every catalyst concentration, the radiation transmission in the seven windows was measured. When building the radiation transmission profiles, measurements for windows 2 through 6 were averaged. Windows 1 and 7 were not considered because the radiation transmission was low.
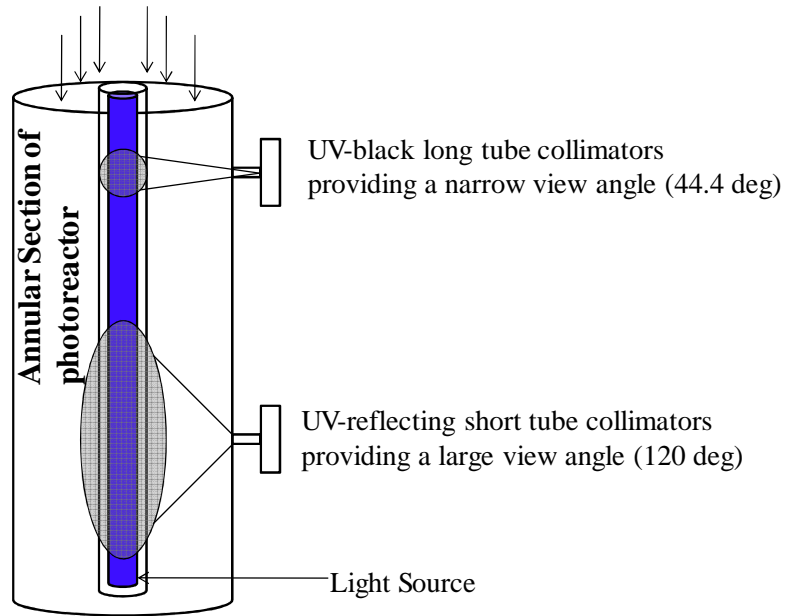
Figure 10 Detection cones representing the angle of included rays for black collimators tube and UV-reflecting short tube collimators (adapted from de Lasa et al. 2005).
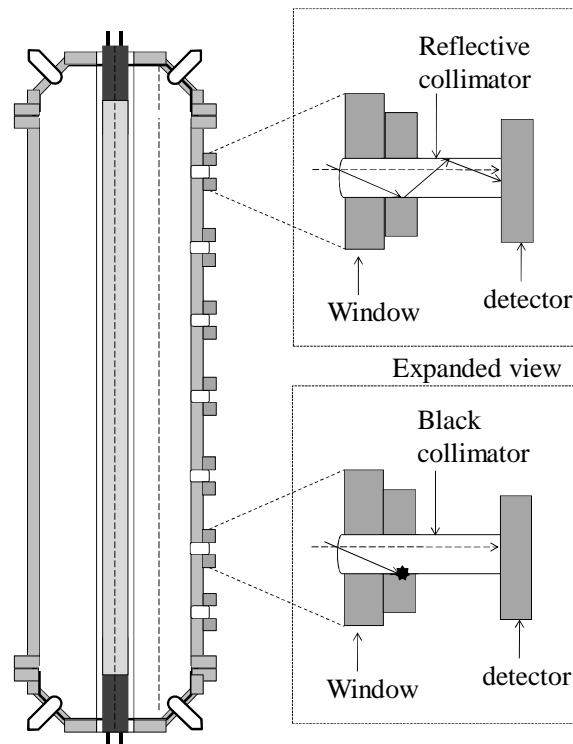
Figure 11 Detailed view of the sensor collimator arrangement

4.4.2   Sol-Gel TiO$_2$ Catalyst Preparation

The synthesized TiO$_2$ catalyst; hereafter referred to as Sol-Gel Cat, was prepared from the hydrolysis of titanium (IV) isopropoxide. The following procedure was implemented:

(a)   20 ml of miliQ water were mixed in 100 ml of 2-propanol inside a 500 ml beaker. This solution is referred as Solution A.

(b)   100 ml of 2-propanol are put in a 250 ml beaker, then, 10 ml of titanium isopropoxide are carefully added to this solution while keeping a vigorous magnetic stirring. This solution is referred as Solution B.

(c)   Solution B is slowly added drop wise to Solution A, vigorous stirring is kept during the entire procedure.

(d)   The final solution is sealed and kept with magnetic stirring for 2 hours.

(e)   The gel formed is aged for 120 hours and it is then dried for 12 hours, at 80 °C, inside an electric oven.

(f)   The final powder is grinded and calcined at 580 °C for two hours with a heating ramp of 5 °C per minute.

(g)   The final TiO$_2$ powder is labeled Sol-Gel Cat.

4.4.3   Photoconversion Experiments

Phenol was the model compound employed in the photoconversion experiments. The abundance of experimental results, based on phenol as a model compound, makes the use of this contaminant very valuable for comparison purposes. Although, phenol has been extensively used as a model compound in many studies, on a laboratory scale, there are still several issues such as the phenol striping and identification of intermediate species.

As proven in the experimental section, phenol is not stripped to detectable extents by the airflow circulated in the forms of bubbles throughout the slurry TiO$_2$ suspension. Identification of chemical species is an area that deserves special attention when analyzing experimental results

With this end, for every experimental run, the reactor system was cleaned thoroughly with clean water and washed with distilled water in order to remove any particles present from previous experimental runs. Desired initial concentrations for the different experiments were

prepared from a stock solution of 2400 ppm of C in phenol. In all the experiments, the reactor was prefilled with de-ionized water, the pump was set to 16 l min^{-1} and the airflow set to 6 l min^{-1}. When filling the reactor with water, the pH was adjusted to 3.7 ±0.1, using H_2SO_4 solution on an Orion 2 star pH meter. Before adding the desired amount of TiO_2 (0.15 g l^{-1}), the reactor was kept running for five minutes; after this time a reference sample was taken. Next, the photocatalyst TiO_2, which had been previously dissolved in 100 ml of water, was added to the mixture. The final volume of the reacting solution was 6 liters with the desire phenol concentration (10-30 ppm of C).

Before turning the UV lamp "on" and starting the reactor irradiation, phenol was allowed to be in contact with the catalyst for 30 minutes. During this period, henceforth referred to as the dark period, the reaction media was pumped around the system in order to reach adsorption equilibrium of phenol on the catalyst. After this period, another sample was taken. The lamp was then turned "on" and the timer was reset to zero to start irradiation period. The operating conditions (airflow, recirculation flow rate, catalyst concentration) were kept constant, except for the pH, which was not adjusted after the reaction started. All the experiments were carried out at a temperature of 30 ±1 °C. Samples were taken every 30 minutes until the model compound and the detectable intermediate species were photo-converted to concentrations below 1% of the initial concentrations. Each sample was filtered using PTFE filters (Mandel, 0.2 μm) before being analyzed on the HPLC and TOC. In the experiments with Fe^{3+} ions, the Fe^{3+} solutions were premixed with the TiO_2 in 100 ml for 30 minutes. Optimum concentrations of 5 ppm of Fe^{3+} were used in all the experiments.

4.4.4   Adsorption of Phenol and its Intermediates on TiO_2

Experiments of adsorption of phenol and its intermediates on the different TiO_2 were conducted in the Photo-CREC Water II reactor at a temperature of 30 ±1 °C. Operating conditions for the reactor were the same as in the photodegradation experiments. First, the reactor was filled with 6 liters of water at certain contaminant initial concentration (10, 20, 30, 40 and, 50 ppm-C in the contaminant). One sample was taken at this point in order to measure the actual concentration of the species (C_0). Then, 0.15 g l^{-1} of the respective TiO_2 catalysts was added to the solution. The reacting solution, with the catalyst, was left running for one hour in order to reach adsorption equilibrium. After this period of time, a sample was

taken in order to measure the concentration in the liquid at equilibrium (C_e). With these two concentration values, the adsorption capacity at equilibrium time will be determined with the following formula:

$$Q_e = \frac{(C_0 - C_e)V}{M_{cat}} \qquad (42)$$

where C_o and C_e are the initial and equilibrium concentrations of the adsorbate respectively (mg l^{-1}). V is the total volume of the solution (l), and M_{cat} is the mass of the TiO_2 catalyst. In this manner, the adsorption isotherm for phenol and its intermediates was built for all the catalysts studied. The effect of Fe^{3+} ions on the adsorption of the different species was studied for DP 25 and Sol-Gel Cat. The general procedure for determining the adsorption isotherms was the same; however, 5 ppm of Fe^{3+} were added to the solution before the catalysts were weighed and added to the solutions in the reactor.

When separating the TiO_2 particles from the liquid phase, using a centrifuge was the best option. When filtering the samples through PTFE filters, equilibrium concentrations were really scattered and no reproducibility was achieved.

4.5 Conclusions

This chapter reports the equipment configuration (reactor, spetroradiomenter, aluminum and UV-opaque collimators); analytical techniques for phenol and its intermediates' identification and quantification (GC/MS, HPLC, TOC). Experimental procedures for radiation measurements; as well as photodegradation experiments, are fully described. It is found that establishing the analytical methods and the experimental procedures is essential for achieving the goals of this PhD dissertation

Chapter 5
Results and Discussion Part I: Radiation Modeling in the Photo-CREC Water II Photoreactor

5   Introduction

This chapter presents the experimental evaluation of the radiation being absorbed by four different TiO_2 catalysts (DP 25, Anatase, Hombikat UV-100 and Sol-Gel Cat) by using Macroscopic Radiation Balance (MB). The MB allows determination of radiation being absorbed by the catalyst, radiation transmission throughout the reactor at different catalyst concentrations, and evaluation of the extinction coefficients using black collimators tubes. Then, modeling of the radiation field in the Photo-CREC Water II reactor is developed using a Monte Carlo method (MC). The purpose of the MC method is to calculate the radiation being absorbed by the catalysts at different concentrations. Experimental and simulation results are compared. Lastly, an optimization method is presented in order to numerically determine the absorption and scattering coefficients for of the titania samples and the synthesized TiO_2.

Before presenting the simulations for the radiation being absorbed by the photocatalysts, the physical properties for the TiO_2 photocatalysts employed in this work are reported inTable 7. The primary crystal size, d_{pr} was determined from the XRD measurements and the method presented by Bakardjieva et al., (2005).

Table 7 Physical properties of various TiO_2 samples used in the present study

Catalyst	S_a $m^2 g^{-1}$	d_{pr} nm	d_a nm	*Composition*[*]
DP 25	47.4	35 (A), 20 (R)	477	80% A, 20% R
Anatase	12.6	47	316	99% A
Hombikat UV-100	252	10	1009	99 % A
Sol-Gel Cat	57.4	18 (A), 25 (R)	318	94% A, 6% R

* A refers to anatase phase and R refers to rutile phase

Agglomerate external surface area (S_a) is reported in the first column of table. Hombikat UV-100 is the catalyst with the largest agglomerate surface area and the smallest primary particle size (d_{pr}). Sol-Gel Cat also presents small d_{pr}. Concerning the particle agglomerate size (d_a) for the solids dispersed in water, all the samples exhibit a significant degree of agglomeration. Hombikat UV-100 forms larger agglomerates than the rest of the TiO_2 samples. The last column in Table 7 reports the structural composition for the powders used. Anatase is the predominant phase in all cases; although, DP 25 and Sol-Gel Cat contain rutile phase as well.

5.1   Determination of the Absorption of Photons by a Macroscopic Balance

The MB already reported in the literature review section is applied in this chapter to obtain the experimental LVREA for the different photocatalyst studied. Each parameter involved in the MB will be discussed separately.

5.1.1   Radiation Emission by the UV Lamp

The first step in determining the radiation being absorbed by the TiO_2 photocatalysts is to characterize the light source. Figure 12 reports a typical radiation flux along the axial position of the BL-Lamp. This Figure shows quite a symmetrical distribution along the axial coordinate. Previous studies (Salaices-Arredondo 2002) reported that similar lamps with more than 1000 hours of operation might present asymmetric radiation emission in the axial direction. Figure 13 illustrates an asymmetric axial distribution of BL-lamp used for 1200 h. For the photodegradation experiments, six different lamps displaying only symmetric radiation distribution were used in order to avoid asymmetric radiation profiles in the photodegradation experiments.

It can be observed from Figure 12 that in the central region from 10 to 36 cm axial length, the radiation profile develops with essentially no changes of the radiation levels. This is the region of the reactor where the radiation measurements are more reliable.
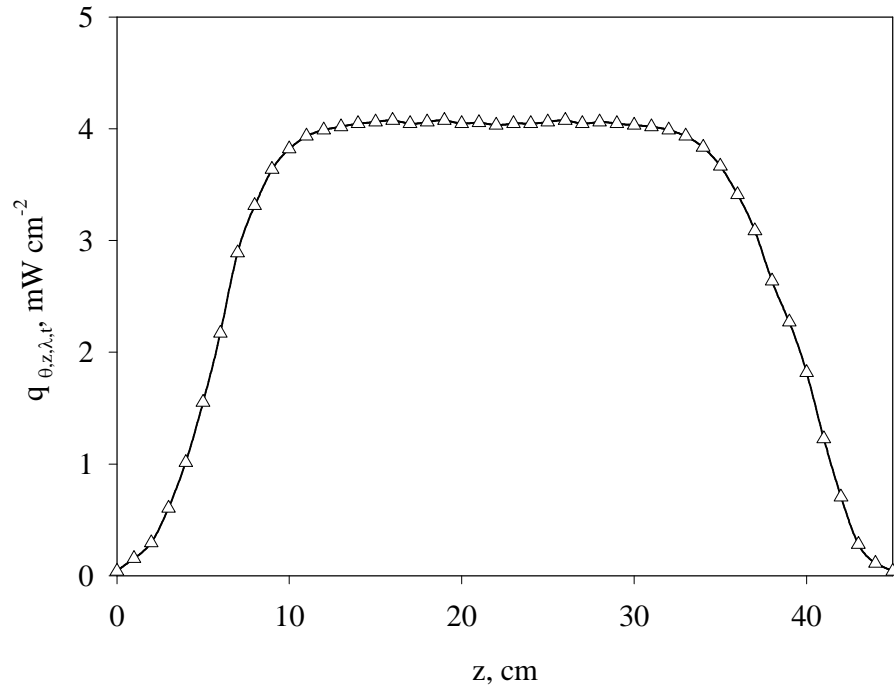
Figure 12 Typical BL lamp axial radiation flux measured at 3.1 cm from the reactor axis

Consequently, it is postulated that measurements in this region will be performed neglecting the end effects of the lamp. This will be explained in more detail in further sections. The decay of the lamp emission was assessed for one particular lamp with utilization time of more than 1000 hours with an exponential lamp decay model of the following form:

$$P_0 = P_{0i} \exp(-\beta_L t) \tag{43}$$

where P_0 is the lamp emission rate in mW cm^{-2}; P_{0i} is the initial lamp emission rate (mW cm^{-2}); β_L is the lamp decay coefficient and t is the time in hours.

Figure 14 reports the emission decay of the studied lamp as well as the best fit for the model in Eq. (43). A value of 5.89×10^{-4} h^{-1} was found for the lamp decay coefficient.
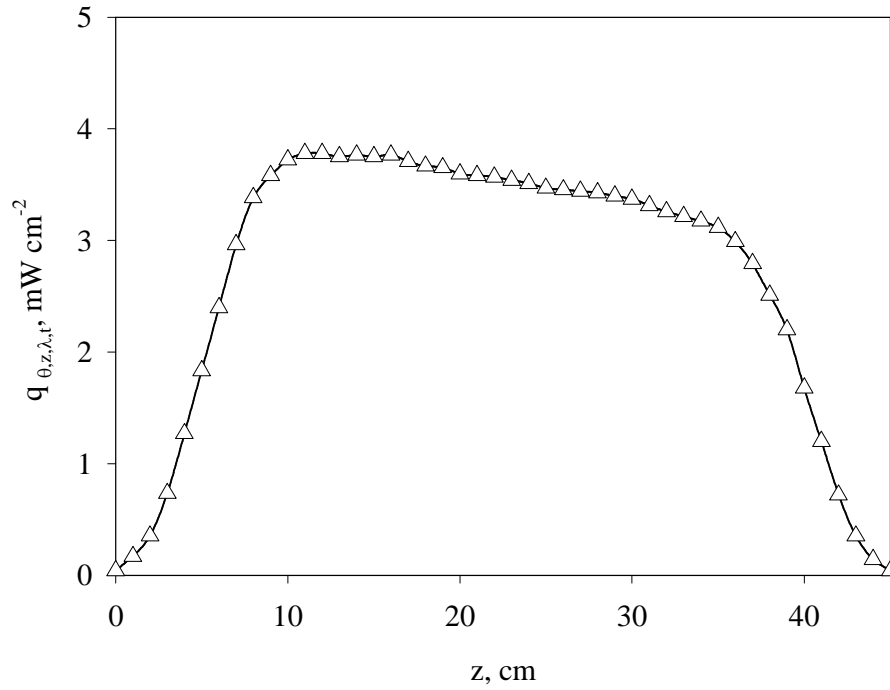
Figure 13 Typical BL lamp asymmetrical axial radiation flux for lamps used more than 1000 hours
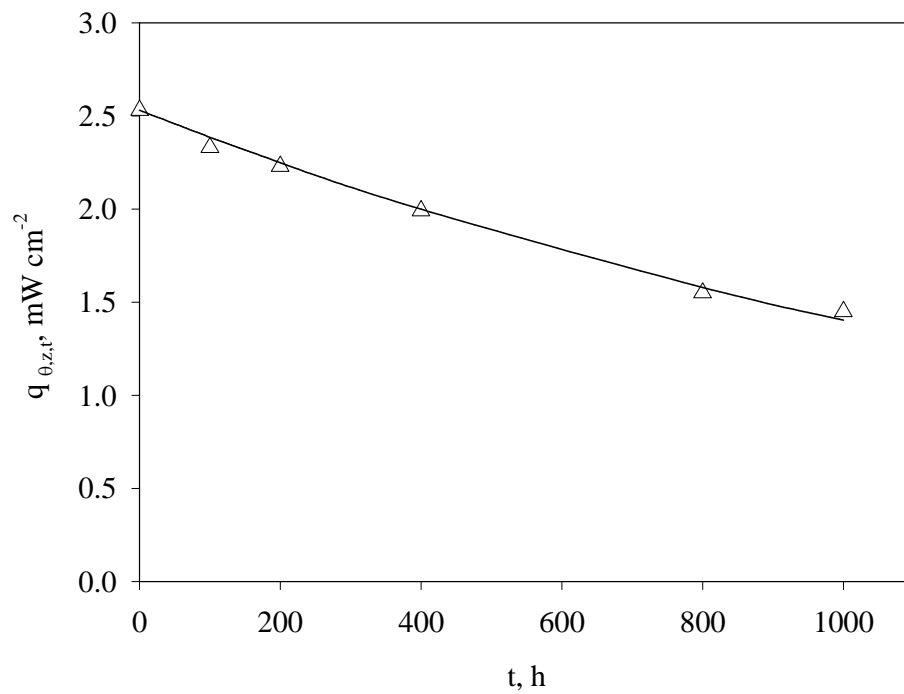
Figure 14 Exponential decay function for a BL-Lamp. (Δ) Experimental values measured at 6.85 cm from the lamp axis (—) model presented in Eq. (43)

Although decay in the emission power in the BL-Lamp exists, the emission spectrum remains constant with lamp utilization (results not shown here). Therefore, the lamp power decay is equivalent to the decay in the emission of photons by the lamp. These findings are consistent with the ones reported by Salaices-Arredondo 2002. In this study, four different TiO_2 were used and Fe^{3+} ions in solution were also studied for DP 25 and the Sol-Gel Cat. Hence, six different BL lamps were utilized in the photodegradation experiments. For the photoconversion experiments, the lamps were used no more than 100 hours. This ensures constant emission of photons throughout the experiments.

The spectrum of Lamp A is reported in Figure 15. Light measurements were made at 5.8 cm from the lamp axis and 22.2 cm axial position. The figure shows that the BL lamp emits mainly in the range of 310-410 nm with three peaks at 312, 365 and 405 nm. In this figure the λ_{Ebg} for TiO_2 is also reported. Wavelengths larger than λ_{Ebg} do not promote electron hole generation (388 nm).
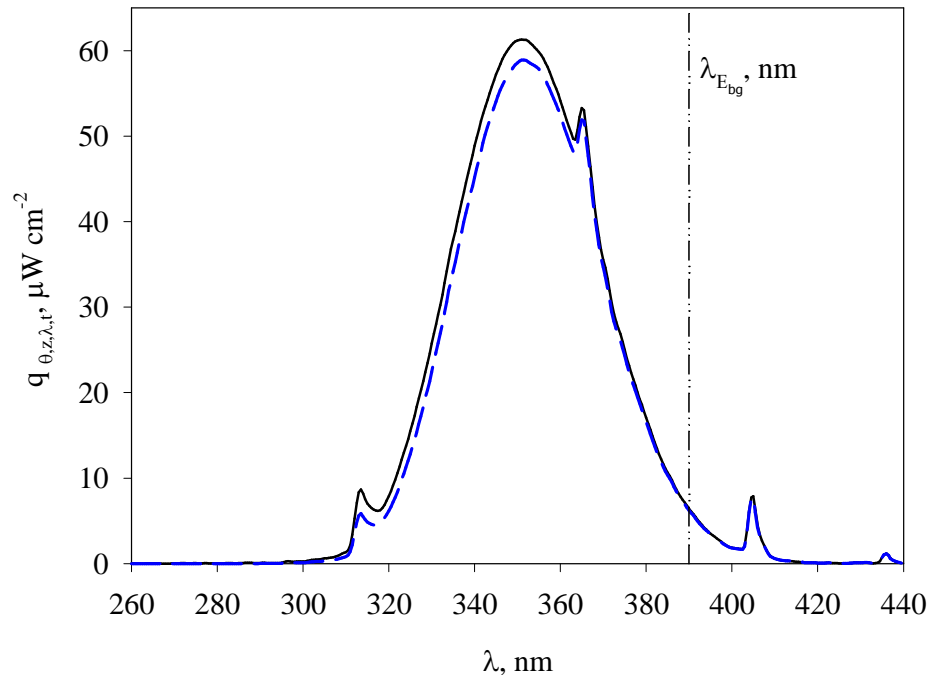
Figure 15 (——) Emission spectra of the Lamp A and (– – –) spectra variation through the inner Pyrex glass

Each point of Figure 15 represents the radiative flux integrated over the wavelength spectrum

$$P_0 = \int_{\lambda_1}^{\lambda_2} q_{\theta,z,t} d\lambda \qquad (44)$$

Thus, the rate of emission of photons by the lamp P_o, is estimated by using Eq. (44) and the lamp spectrum in Figure 15. The estimated values for the six lamps used in this study are reported in Table 8. This table includes the lamp emission power at $t = 0$ in einsteins s^{-1} and in watts. The table also includes the lamp efficiency, η_l, with respect to the nominal power reported by the manufacturer (15 W). All the lamps utilized in the photodegradation experiments presented efficiencies lower than 30%.

Table 8 Emission rates for the different lamps used in this study

Lamp	Po (einstein s^{-1})	Wo (W)	η_l (%)
A	1.1910×10^{-5}	4.03	26.9
B	1.1446×10^{-5}	4.01	26.7
C	1.1830×10^{-5}	4.11	27.4
D	1.2121×10^{-5}	3.94	26.2
E	1.1620×10^{-5}	3.94	26.2
F	1.2340×10^{-5}	4.18	27.9

5.1.2 Rate of Absorption of Photons by the Pyrex Glass and Photons Entering the Annular Section of the Photo-CREC Water II

The rate of photons being absorbed by the Pyrex glass is easily estimated by measuring the transparency of this material. The extinction coefficient of the Pyrex material (β_p) is estimated using Beer's Law. The change of this coefficient with respect to wavelength is sketched in Figure 16. It can be seen from the Figure that the extinction coefficient decreases rapidly with the wavelength reaching a value of <0.5 cm^{-1} for wavelengths above 320 nm. It was also shown in Figure 9 that transmittance of light by the inner Pyrex wall is more than 90% for wavelengths longer than 320 nm. Therefore, the glass material is essentially transparent to these wavelengths.

In Figure 15, the variation spectrum through the 0.23-cm-thinckness Pyrex glass is presented. In this respect, the spectrum of Lamp A remains almost unchanged after crossing the Pyrex wall, with a slight change in intensity. Hence, the rate of absorption in the Pyrex glass is estimated for all the lamps by using the variation spectra and Eq. (44).
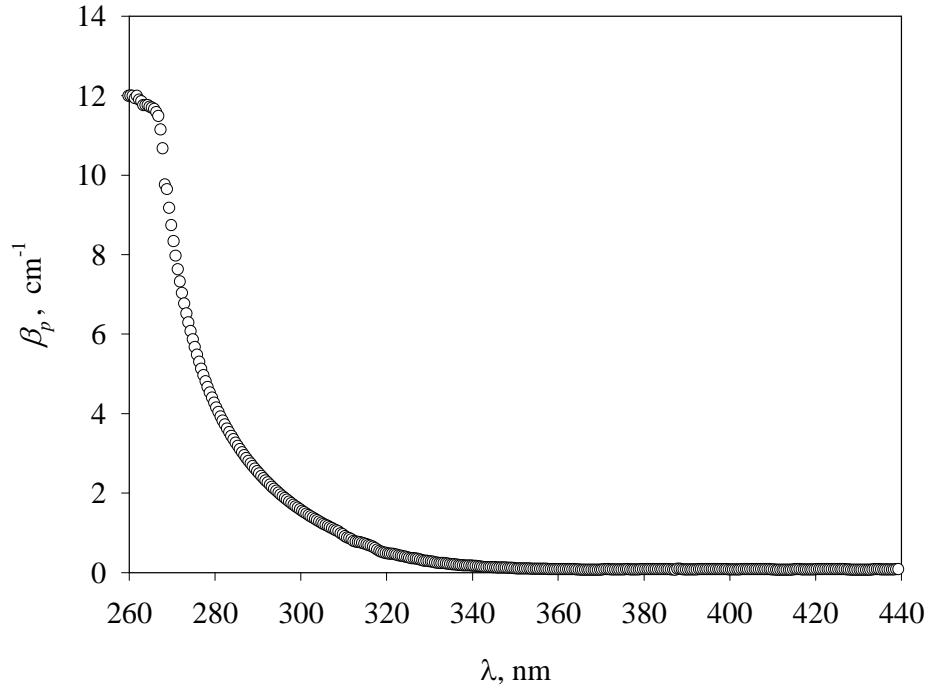
Figure 16 Extinction coefficient of the Pyrex glass

Table 9 Energy distribution for the inner Pyrex glass

Lamp	P_i (einstein s^{-1})	W_i (W)	$P_{a\text{-wall}}$ (einstein s^{-1})	$W_{a\text{-wall}}$ (W)	P_i/P_0 (%)	P_{awall}/P_0 (%)
A	1.1210×10^{-5}	3.79	7.003×10^{-7}	0.25	94.1	5.9
B	1.0782×10^{-5}	3.64	6.638×10^{-7}	0.23	94.2	5.8
C	1.1085×10^{-5}	3.75	7.453×10^{-7}	0.26	93.7	6.3
D	1.1467×10^{-5}	3.87	6.545×10^{-7}	0.23	94.6	5.4
E	1.0888×10^{-5}	3.68	7.321×10^{-7}	0.26	93.7	6.3
F	1.1661×10^{-5}	3.94	6.787×10^{-7}	0.24	94.5	5.5

Once the $P_{a\text{-wall}}$ term is experimentally determined, the radiation entering the annular section in the reactor is calculated by using Eq. (14). Table 9 summarizes these values. In this table, the fraction of light entering the annular section is also presented with respect to the emission intensity of the lamp.

5.1.3 Transmission of Photons in the Annular Section in the Photo-CREC Water II Photoreactor

The second parameter needed to calculate the light absorbed by the different TiO_2 catalysts is the transmitted radiation, P_t. This parameter is determined from radiometric measurements of the radiation transmission through the different flowing catalyst suspensions at the reactor's windows. As expressed in Eq. (17), the total transmitted radiation is measured by using the polished-aluminum collimator at 6.85 cm from the lamp axis.
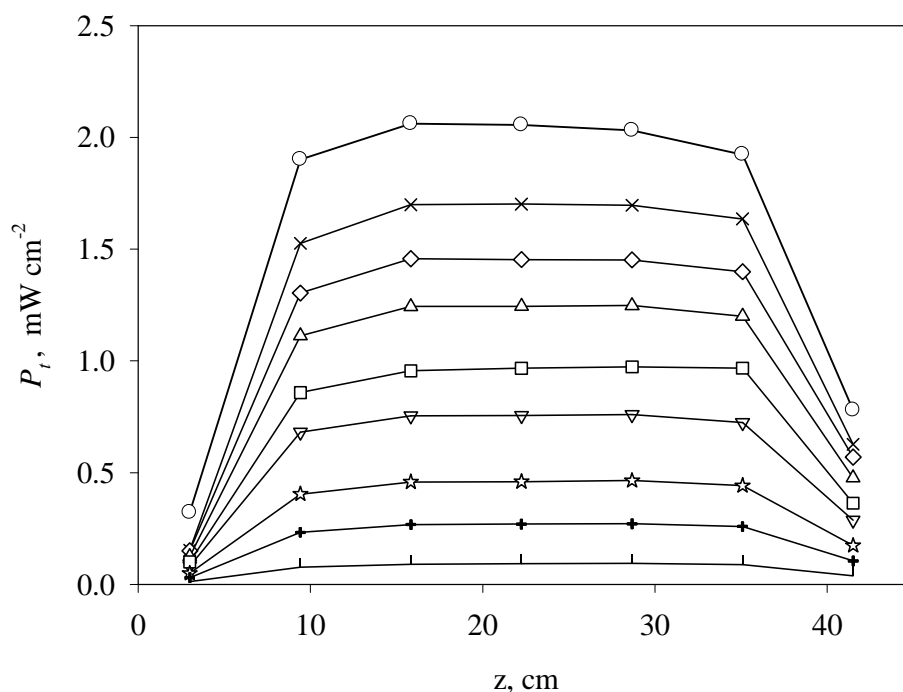
Figure 17 Axial distribution of the radiation transmission in the photoreactor when TiO_2 DP 25 and aluminum collimator are used. ($\circ$) 0, ($\times$) 2, ($\Diamond$) 6, ($\triangle$) 10, ($\square$)15, ($\triangledown$) 20, ($\star$) 30, (+) 50 and (|) 90 mg l^{-1}

The transmitted radiation along the axial position in the reactor is measured at the different window positions. Figure 17 displays typical profiles for the transmitted radiation at the different window positions in the photoreactor. These values were found for TiO_2 DP 25 at a flow rate of 16 l min^{-1}.

In the central region of the reactor, the radiation profiles remain constant. This is the region were all the radiation transmission measurements are done. For all the measurements, an average of windows 2-6 is taken, and the end effects are neglected. Similar results are obtained when the UV-opaque collimators are used. An example of this profile is presented in Figure 18 when an UV-opaque collimator at 13.74 cm from the lamp axis is used.
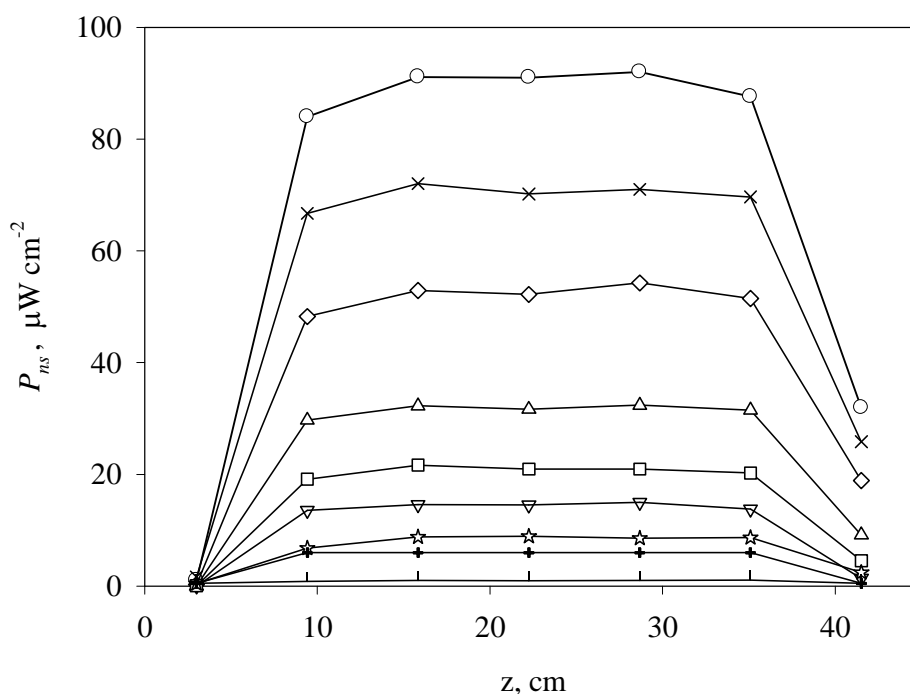
Figure 18 Axial distribution of the radiation transmission in the photoreactor when TiO_2 DP 25 and black collimator are used. ($\circ$) 0, ($\times$) 2, ($\Diamond$) 6, (Δ) 10, ($\Box$)15, (∇) 20, ($\star$) 30, (+) 50 and (|) 90 mg l^{-1}

Figure 19 shows the total radiation transmission throughout the annular section as a function of catalyst concentration for the four catalysts considered in this study. Results in this plot were obtained by using the polished collimators and an average reading of windows 2-6.

When the black collimators are used for the transmitted radiation measurements, the transmitted non-scattered radiation is the only one taken into consideration. This parameter is shown in the first term of the right hand side in Eq. (17). The profiles for these measurements are shown in Figure 20.
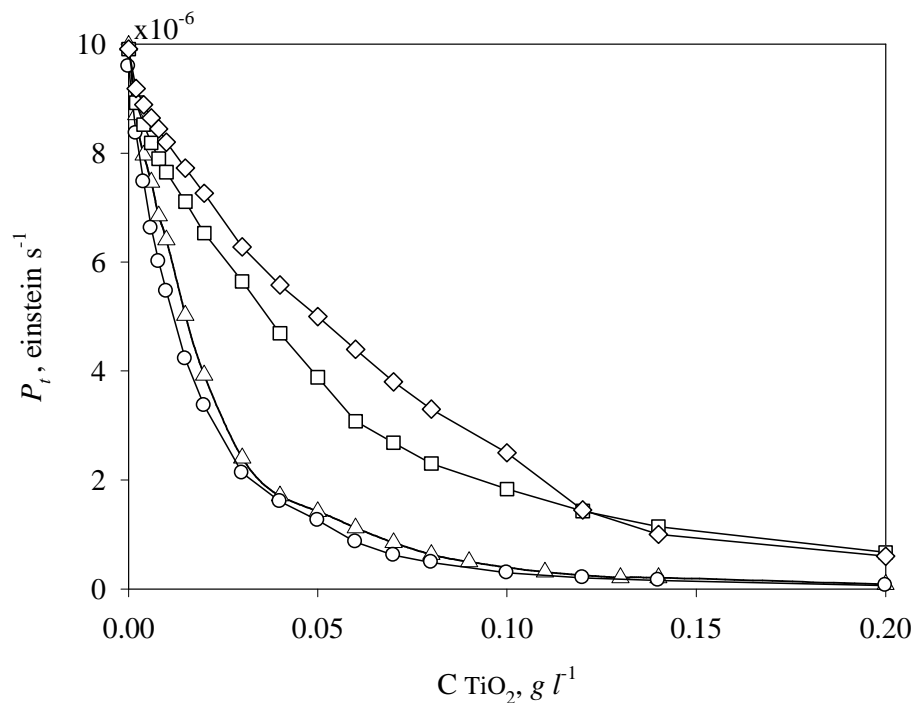
Figure 19 P_t vs. catalyst concentration expressed in einstein s^{-1} when aluminum collimator is used. (Δ) DP 25, ($\circ$) Anatase, ($\square$) Hombikat UV-100 and ($\Diamond$) Sol-Gel Cat
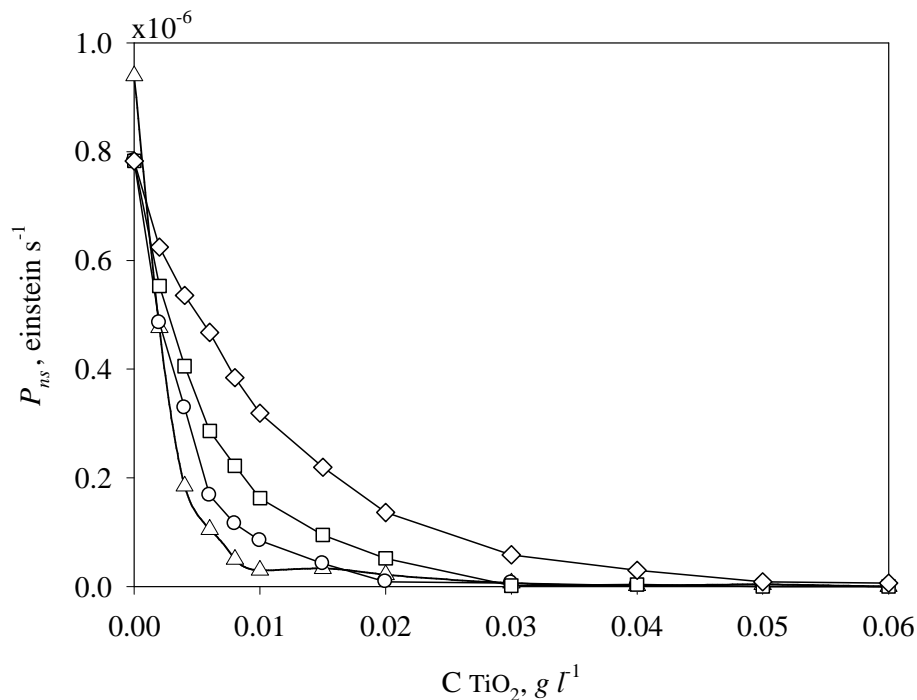
Figure 20 Transmitted non-scattered radiation vs. catalyst concentration expressed in einstein s^{-1}. ($\triangle$) DP 25, ($\circ$) Anatase, ($\square$) Hombikat UV-100 and ($\Diamond$) Sol-Gel Cat

The Beer-Lambert law was fitted to the average readings from windows 2 to 6 of the data presented in Figure 20 to obtain the true extinction coefficient for the different catalysts according to the following formula:

$$A = -\log\left(\frac{P_{ns}}{P_{ns0}}\right) = \varepsilon_{cat} C_{cat} \tag{45}$$

where A is the absorbance; P_{ns} is the transmitted non-scattered radiation in einstein s^{-1} at different catalyst concentrations; P_{ns0} is the transmitted non-scattered radiation in einstein s^{-1} at zero catalyst concentrations; ε_{cat} is the true extinction coefficient (L g^{-1}); and C$_{cat}$ is the catalyst concentration (g l^{-1}).

The results for this linearization are presented in Figure 21 for the total non-scattered transmitted radiation. Specific extinction coefficients, β_{cat} in units of cm^2 g^{-1}, are also reported in Table 10, with true and specific extinction coefficients being related with the following equation:

$$\beta_{cat} = \frac{\varepsilon_{cat}}{l} \tag{46}$$

where l is the path length where the photons of light travel, $l = 2.69$ cm for the photoreactor.
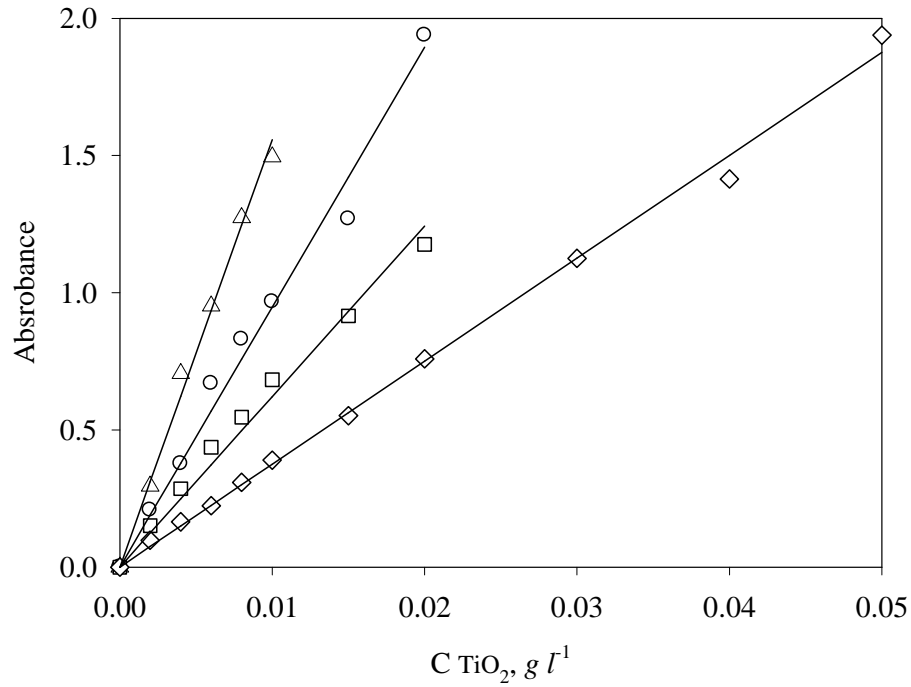
Figure 21 Linearization of Eq. (45) for the determination of the true extinction coefficient ε_{cat}. ($\triangle$) DP 25, ($\circ$) Anatase, ($\square$) Hombikat UV-100 and ($\Diamond$) Sol-Gel Cat

Table 10 True and specific extinction coefficients for the different catalysts

Catalyst	ε_{cat} (L g^{-1})	β_{cat} (cm^2 g^{-1})
DP 25	155.8	57903.3
Anatase	94.8	35228.3
Hombikat UV-100	62.2	23112.3
Sol-Gel Cat	37.5	13950.2

5.1.4   Rate of Back-scattered Photons Exiting the System

Salaices et al. 2001 and Salaices-Arredondo 2002 adopted two assumptions for the development of Eq. (16). This allows the determination of the rate of back-scattered photons in the photoreactor. The first assumption considers that a number of backscattering centers are located in a boundary layer close to the inner glass tube wall. The second assumption considers that there is a maximum number of scattering centers in this boundary layer, and once that number is reached, no additional centers occur. Using these two assumptions and Eq. (16), the rate of back-scattered photons is estimated for each catalyst.

5.1.5   Rate of Absorption of Photons and Experimental LVREA

So far, P_i, P_t, and P_{bs} have been determined. Therefore, the radiation being absorbed by the different catalysts can be calculated using Eq. (13). In the photodegradation experiments, a catalyst concentration of 0.15 g l^{-1} was employed for all the catalysts. Table 11 reports the values for all the parameters involved in the MRB for a catalyst concentration of 0.15 g l^{-1}.

Table 11 Parameters involved in the MRB at 0.15 g l^{-1} catalyst concentration

Catalyst	einstein s-1					
	P_0	P_a	P_i	P_t	P_{awall}	P_{bs}
DP 25	1.1910×10^{-5}	9.6781×10^{-6}	1.1210×10^{-5}	2.0630×10^{-7}	7.0030×10^{-7}	1.3253×10^{-6}
Anatase	1.1446×10^{-5}	8.9664×10^{-6}	1.0782×10^{-5}	1.5611×10^{-7}	6.6380×10^{-7}	1.6597×10^{-6}
Hombikat	1.1830×10^{-5}	9.8256×10^{-6}	1.1085×10^{-5}	1.1412×10^{-6}	7.4530×10^{-7}	1.1798×10^{-7}
Sol-Gel Cat	1.2121×10^{-5}	1.0360×10^{-5}	1.1467×10^{-5}	1.0000×10^{-6}	6.5450×10^{-7}	1.0621×10^{-6}

Once the radiation being absorbed by the catalyst was determined, the next step is to find the experimental local volumetric rate of energy absorption (LVREA_exp). This variable is easily found from the P_a variable applying the following relationship:

$$LVREA_{exp} = \frac{P_a}{V_R} \tag{47}$$

where V_R is the total volume of the photoreactor in m^3 and LVREA$_{exp}$ in einstein s^{-1} m^3. The LVREA$_{exp}$ for the four catalysts is sketched in Figure 22.
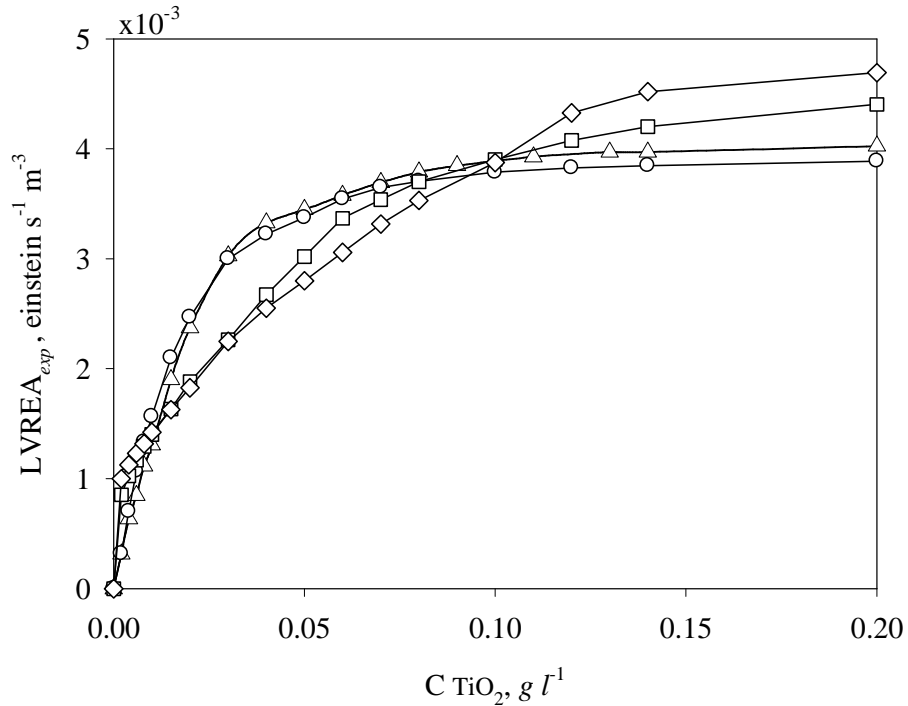
Figure 22 Experimental LVREA for (Δ) DP 25, ($\circ$) Anatase, ($\square$) Hombikat UV-100 and ($\Diamond$) Sol-Gel Cat inside the Photo-CREC Water II

For low catalyst concentrations, it is found that the DP 25 and Anatase catalysts absorb more light than Hombikat and Sol-Gel Cat. However, as the catalyst concentration increases, Hombikat and Sol-Gel Cat present a larger value of the *LVREA*. From these profiles, it can be seen that the absorption of light strongly depends on the catalysts used, which ultimately impacts the photodegradation rate. Values for the energy absorbed by the different catalysts will be used in Chapter 8 in order to calculate the reactor efficiency for the different catalysts employed in the photodegradation experiments.

5.2 Monte Carlo Simulations for the LVREA in the Photoreactor

In this section, MC simulations are performed to determine the LVREA for the Photo-CREC Water-II reactor for the different types of TiO$_2$ photocatalysts. In the simulation, four parameters are used: (i) an extinction coefficient, (ii) the probability of photon absorption,

(iii) the probability of backward scattering absorption by the internal Pyrex glass tube and (iv) the Henyey-Greenstein phase function describing the forward, isotropic and backward scattering. It is also assumed that the inner UV lamp reflects photons back-scattered by the TiO_2 suspension.

As well, an optimization method is employed to numerically find the absorption and scattering coefficients more adequate for the various photocatalysts used in the present study.

5.2.1   Optical Properties of TiO_2 Catalysts

Applying Eq. (23) and (24), with the spectrum presented in Figure 15 and the data in Figure 4 and Figure 5, the wavelength-averaged coefficients are calculated and reported in Table 12. Values for Sol-Gel Cat are not presented because this catalyst was synthesized in our laboratory and its optical properties are uknown.

Table 12 Experimental specific wavelength-averaged coefficients for different TiO_2

Catalyst	κ_λ^* (m^2 g^{-1})	σ_λ^* (m^2 g^{-1})
DP 25	0.6394	5.6077
Anatase	0.3957	3.1149
Hombikat	0.2747	2.3415

Given that the absorption and the scattering coefficients expressed in Eq. (18) are given in length^{-1} units, the specific averaged coefficients of Table 12 are converted into the adequate units using the following formula:

$$\kappa = \kappa_\lambda^* \, x \, W_{cat}$$
$$\sigma = \sigma_\lambda^* \, x \, W_{cat}$$

(48)

where κ and σ coefficients are given in m^{-1} and W_{cat} is the catalyst loading in g m^{-3}. The values presented in Eq. (48) are the ones used in finding the solution of the RTE.

5.2.2   Solution of the RTE Using Monte Carlo Method

The radiation scattering mechanism in a photocatalytic reactor starts when a photon is emitted from the lamp, travels a distance *l*, and then is either absorbed or scattered within the reacting medium. The generated photons interact with the reacting medium according to probabilistic interactions determined by the absorption and scattering coefficients (κ and σ) of the reacting medium, and also the phase function. The MC simulation begins with a given total energy input which is a function of the lamp used in the photocatalytic process.

The spectrum intensity of the lamp used in this study was previously reported. Table 8 showed the lamp emission rates and the emission rates reaching the reactor inner Pyrex glass. From this table, it can be seen that approximately 6 % of the emitted radiation by the lamps is absorbed by the inner Pyrex glass.

For the MC simulations performed in the Photo-CREC Water –II, the following model assumptions are adopted in this study:

(a) Emission of photons from the lamp surface is assumed to be uniform and directionally independent,

(b) Emission of photons from the lamp surface is considered to be a stochastic process,

(c) Photons emitted by the lamp have a defined probability to be absorbed by the inner Pyrex glass tube before entering the reacting medium. This probability is defined by the transparency of the Pyrex tube. The photons reflected to the lamp by the slurry medium have the same chances of being absorbed by the inner Pyrex tube,

(d) Photons scattered by the reacting medium are determined by the H-G phase function. Forward, isotropic and backward scattering are considered for the simulation, with photon reflection being assumed elastic,

(e)   Photons reaching the outer polyethylene reactor wall are considered absorbed by the reactor wall. As a result, these photons are counted as transmitted (i.e. its trajectory is terminated at the wall).

Assuming one photon is emitted in a random direction from the lamp surface, it enters the annular region of the reactor (illustrated in Figure 23), and it travels a distance l ($l \geq 0$) with a finite probability of arriving to a point "A" through the heterogeneous medium, without being scattered or absorbed. Once the photon reaches point A, there are two possibilities for the light ray (Pareek et al., 2008): (a) the photon is absorbed and thus, its course is arrested; (b) it is scattered according to the H-G phase function and its flight continues until this photon is either absorbed by a catalyst particle or reaches the reactor wall and its trajectory is terminated. On the other hand, if the photon is back-reflected towards the lamp, after travelling a distance l, the photon can be re-emitted at the same axial position but with different equatorial and angular angles.

For this simulation, experimental results were used to model the spectral distribution of the BL-lamp. The number of photons associated with each wavelength was experimentally determined for the range 300 nm $\leq \lambda \leq$ 410 nm using spectrometric measurements. The rate of photon emissions for every lamp used in this study are presented in Table 13. This experimental data is used as a starting point for the simulations. Once the number of photons is determined for every wavelength, their fate is traced using the MC simulations. In this way, the number of events considered in the MC calculations becomes dependent on the number of photons at every wavelength. Simulations are performed by using the averaged wavelength absorption and scattering coefficients (Eq. (48)), and also the spectral distribution of such coefficients as reported by Figure 4 and Figure 5.
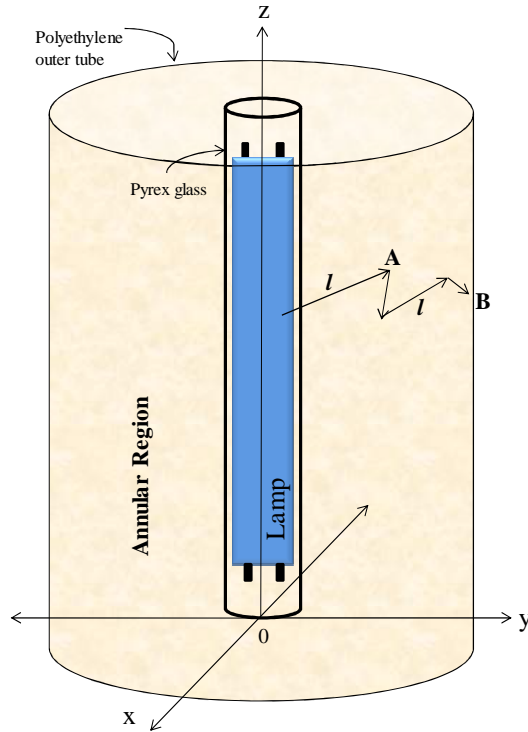
Figure 23 3D view of the annular region used for MC simulations

Table 13 Rate of photon emission for different UV lamps

Lamp	Po (einstein s^{-1})	Po (photons s^{-1})
A	1.1910×10^{-5}	7.172×10^{18}
B	1.1446×10^{-5}	6.893×10^{18}
C	1.1830×10^{-5}	7.124×10^{18}
D	1.2121×10^{-5}	7.299×10^{18}
E	1.1620×10^{-5}	6.998×10^{18}
F	1.2340×10^{-5}	7.431×10^{18}

5.2.3 Mathematical Steps in MC Simulations

The annular region presented in Figure 23 was divided into small cubic cells. Every time a photon is absorbed in a cubic cell, its value is saved in the corresponding cubic cell so that the LVREA can be calculated. The whole annular region is considered for the MC

simulation, using a coordinate system as described in Figure 23. The trajectories of the photons for every wavelength are traced using the following steps in the context of the MC simulation:

(1)   The photon emission location on the lamp surface is determined first by using two random numbers: R_1 ($R_1 < 1$) sets the location along the z coordinate (refer to Figure 24) $U(1.6\ cm,\ L+1.6\ cm)$ while R_2 ($R_2 < 1$) fixes its circumferential position $U(0,\ 2\pi)$.

(2)   Once the photon emission coordinates are set, the direction of the photon flight is established in spherical coordinates by two angular coordinates; the zenith (θ) and azimuth (ϕ) angles, by using the H-G phase function:

$$p_{HG}(\theta) = \frac{1}{4\pi} \frac{1-g^2}{\left(1+g^2-2g\cos(\theta)\right)^{3/2}} \tag{49}$$

The random event for which the zenith angle falls (with a probability density function given by Eq. (49)) for the [θ, $\theta +d\theta$] interval (Binzoni et al., 2003) is calculated by using a random number R uniformly distributed in the range [0,1] such that:

$$\int_{o}^{\theta} p_{HG}(\theta')d\theta' = R \tag{50}$$

To calculate the zenith angle, Eq.(50) has to be solved, in order to obtain a solution that expresses θ as a function of R, with this equation being solved numerically. However, this approach increases considerably the computation time in MC simulations. As an alternative, a probability density function can be conveniently found by slightly modifying Eq.(50) as (Binzoni et al., 2003):

$$\tilde{p}_{HG}(\cos(\theta)) = \frac{1}{2} \frac{1-g^2}{\left(1+g^2-2g\cos(\theta)\right)^{3/2}} \tag{51}$$
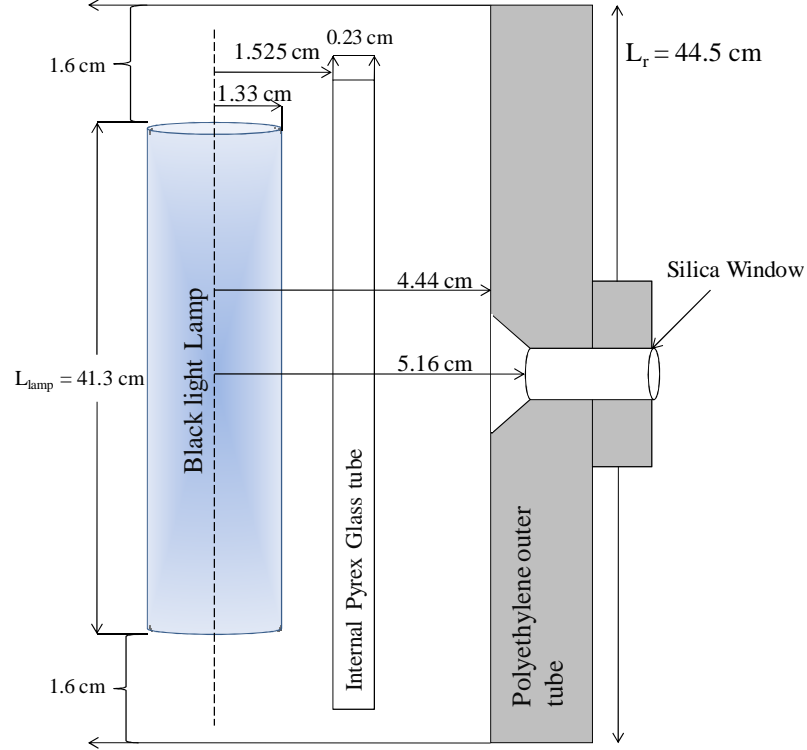
Figure 24 Dimensions for the Photo-CREC Water-II photoreactor

Therefore, a distribution for $\tilde{p}_{HG}(\cos(\theta))$ can be represented as,

$$\int_{-1}^{\cos(\theta)} \tilde{p}_{HG}(\cos(\theta'))d(\cos(\theta')) = R \tag{52}$$

With Eq. (52) having an exact analytical solution expressed by:

$$\cos(\theta) = \begin{cases} \dfrac{1}{2g}\left[1+g^2 - \left(\dfrac{1-g^2}{1-g+2gR}\right)^2\right], & \text{if } g \neq 0 \\ 2R-1, & \text{if } g = 0 \end{cases} \tag{53}$$

Two random numbers (R_3 and R_4) uniformly distributed in the range [0, 1] are generated to calculate the zenith and azimuth angles. When $cos(\theta)$ is calculated with Eq. (53) by using R_3, the zenith (latitude) angle for the photon flight direction is obtained by computing the $\theta = a\ cos((cos(\theta))$. For the azimuth angle, the same probability of reflection is assigned; therefore, the scattering angles are calculated as follows:

$$\theta = a\cos(\cos(\theta))$$
$$\phi = 2\pi R_4 \qquad (54)$$

In the simulations, different values for g were studied to include the different scattering modes. For isotropic scattering, $g = 0$ and Eq. (54) becomes:

$$\theta = a\cos(2R_3 - 1)$$
$$\phi = 2\pi R_4 \qquad (55)$$

(3)   Photons have a 6% probability of being absorbed by the inner Pyrex glass tube. This probability is determined by the transparency of the tube material (refer to Figure 8 and Table 9). If the photon is absorbed by the Pyrex glass, its trajectory is arrested and a new photon is generated (step 1). If at any time, the photon of light is back-scattered by the suspension towards the lamp, the photons again have a 6% probability of being absorbed by the Pyrex glass. If the photon is not absorbed by the inner Pyrex glass tube, it is considered lamp reflected at the same axial position, but with a different angle.

(4)   Once the photon emitted in the first steps enters the reaction zone, it travels a distance l without an interaction occurring along this path. Then, the next step is the evaluation of the photon flight length l. The probability of this event is given by (Pareek et al. 2008):

$$P(l) = e^{-\beta_\lambda l} \qquad (56)$$

where β_λ is the extinction coefficient of the medium. Therefore, the flight length l can be calculated by a random number R_5 ($R_5 < 1$) as follows:

$$l = -\frac{1}{\beta_\lambda}\ln(R_5) \qquad (57)$$

Yokota et al. (1999) present a slightly different definition for the free path length,

$$l = -\frac{1}{\beta_\lambda} \ln(1 - R_5) \qquad (58)$$

This definition; however, renders the same results for the simulation because $(1-R_5)$ is also a random number between 0 and 1.

If after traveling a distance l the photon is located in point "A", its Cartesian coordinates are simply determined by:

$$
\begin{aligned}
x_{new} &= x_{old} + e_x l \\
y_{new} &= y_{old} + e_y l \\
z_{new} &= z_{old} + e_z l
\end{aligned}
\qquad (59)
$$

where "old" refers to the previous location of the photons inside the reactor and "new" refers to the new location once the photon travels a distance l. The utilization of Cartesian coordinates for establishing photon location present computational advantages because a photon's direction is uniquely specified by the direction cosines (e_x, e_y, e_z), with respect to the coordinate axes (Changrani and Raupp 1999). Specific details for the determination of the direction cosines are presented in Appendix A.

(5)   If the position of the photon after traveling a distance l is inside the annular region, two possibilities can happen; either the photon is absorbed by the medium or it is scattered to a new location. This step involves the probability calculation of the photon being absorbed. For photons crossing in the reactor annulus, their fate is determined by an absorption criterion, which is the probability that the photon is scattered. This absorption criterion is given by (Changrani and Raupp 1999):

$$P(a) = \frac{\kappa_\lambda}{\beta_\lambda} = \frac{\kappa_\lambda}{\kappa_\lambda + \sigma_\lambda} \qquad (60)$$

Thus, another random number is generated ($R_6 < 1$), if $P(a) > R_6$; then the photon is absorbed and stored in the corresponding volume cell. At this point the photon

trajectory is terminated and the sequence of calculations is re-initiated for a new photon emitted by the lap surface (step 1). Otherwise, the photon is scattered and a new direction for the photon is established (step 2). However; if the photon of light is outside the outer polyethylene tube, the photon is allowed to escape as a forward scattered photon and is assumed to be absorbed by the non-reflecting wall. These mathematical steps are summarized in Figure 25.

In the MC simulations a large number of events must to be considered until the physical properties under investigation have small statistical fluctuations. Ideally, the number of events traced should be equal to the number of photons emitted by the lamp per unit time as presented in Table 13 (Pareek et al., 2008). However, this is a demanding computational process because the BL-lamps emit in the order of 10^{18} photons per second (10^{-5}einstein s^{-1}). For the simulations in this study, $\sim$7.2 10^{18} photons were accounted forming 10^{7} packets of photons, and as a result, events could be calculated using an Intel Core Duo PC (2 GHz).
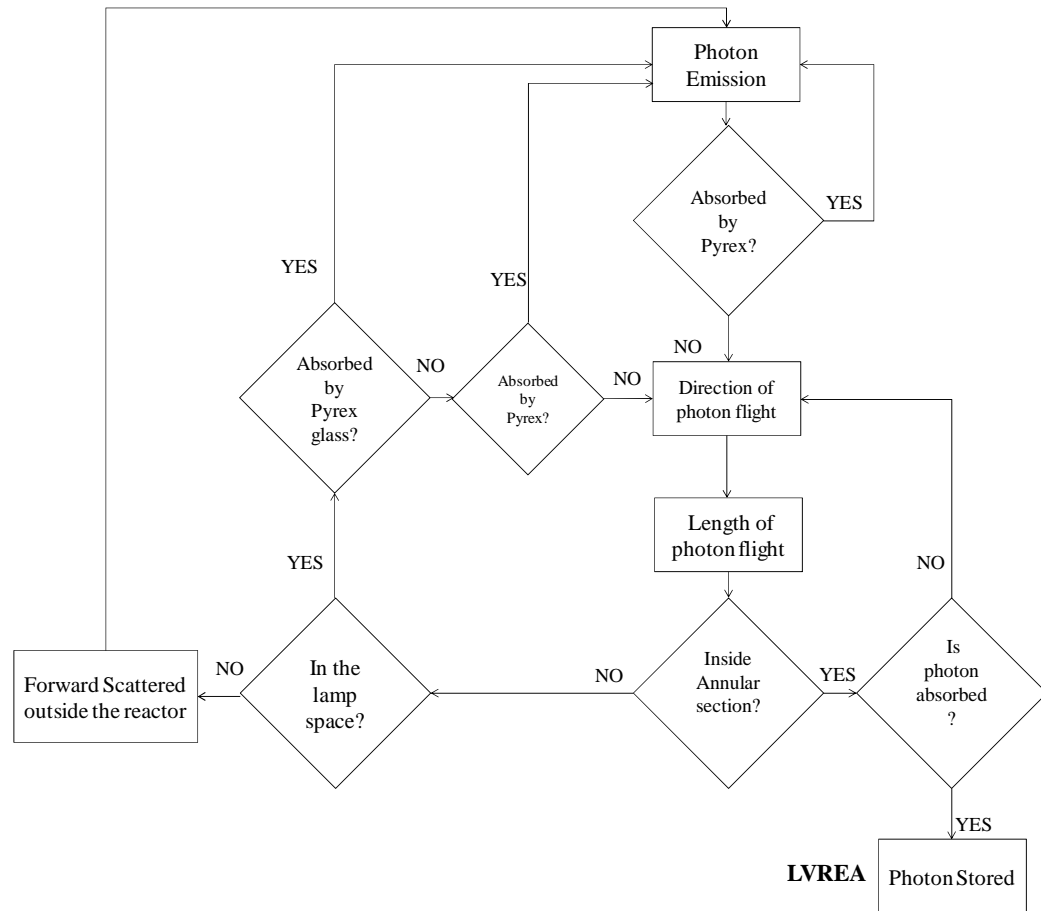
Figure 25 Algorithm for MC simulations

The RAND number generator in MATLAB was considered suitable for MC simulations of the LVREA. The reasons for selecting this algorithm were discussed in the Chapter 3. Thus; for the simulations presented in this study, MATLAB programs are developed to estimate the absorbed photons in the Photo-CREC Water-II reactor, with the RAND function being used for the generation of random numbers in all cases.

One proposed MC method simulation (Simulation 1) to predict the LVREA assumed that those photons that are back-scattered by the medium, and impinge on the lamp, are reflected at the same axial position, (i.e., there is no absorption of photons by the fluorescent BL lamp). On the other hand, another MC simulation assumed that photons reflected by the medium impinging on the lamp, were actually absorbed by the lamp (Simulation 2). For the above described simulations, the wavelength-averaged scattering and absorption coefficients

were used (Eq. (48)) and isotropic scattering was assumed. Eq. (54) was employed to calculate the reflecting angles for the photons inside the reactor (i.e. $g = 0$).

Radiation absorption experimental results and MC simulations for Simulation 1 are reported in Figure 26 for DP 25, Anatase, and Hombikat UV-100 catalysts. MC results for Simulation 2 are reported in Figure 27. The LVREA predictions presented in Figure 26 confirm that the use of wavelength-averaged parameters renders good prediction for the LVREA. However, the prediction for the LVREA is not very accurate for the case of Hombikat UV-100 catalyst. In Figure 26 one can notice an under estimation for the LVREA at low concentrations of TiO_2 Hombikat UV-100.

Given that "Simulation 1" provides a more realistic scenario, it is chosen for the evaluation of the LVREA in the Photo-CREC Water-II reactor. However, to assess the influence of the absorption and scattering coefficients, a "Simulation 3" was performed.

In simulation 3, the spectral distribution of the absorption and scattering coefficients were used as reported in Figure 4 and Figure 5. In this case, a polynomial equation was adjusted to the experimental values in order to determine the coefficients at the required wavelength in MC simulations. Figure 28 reports these results with isotropic scattering ($g = 0$) being assumed.

Comparing Figure 26 and Figure 28, one can conclude that by using the spectral distribution for the MC simulations, a more accurate prediction for the LVREA and the transmitted radiation inside the reactor is obtained; however, experimental determination of these coefficients for a large number of different wavelengths could be a burden process, requiring more computational time.
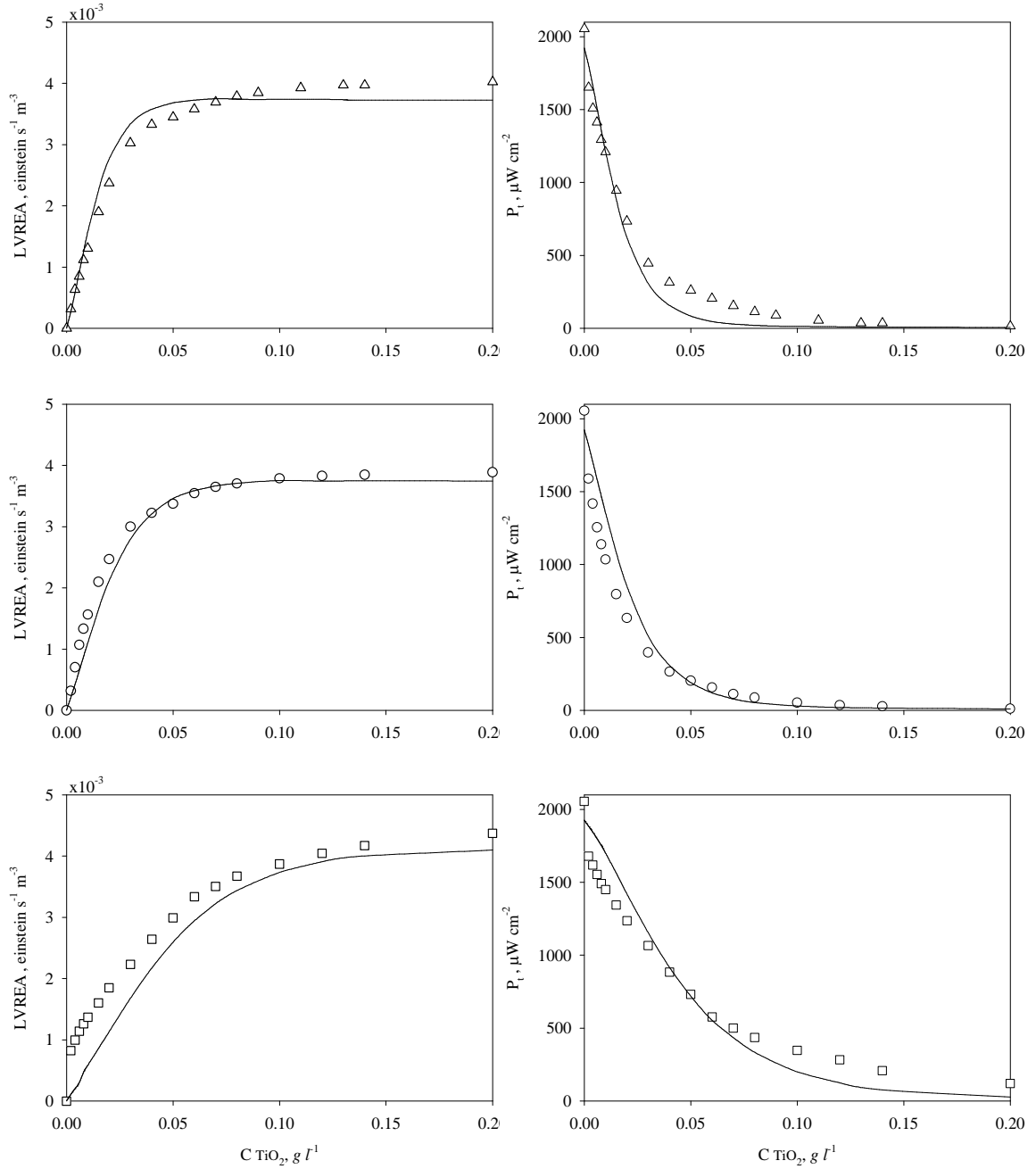
Figure 26 Experimental results for the LVREA and the transmitted radiation and comparison with "MC simulation 1". Experimental data: (Δ) DP 25, (○) Anatase, and (□) Hombikat UV-100 and (—) MC simulations
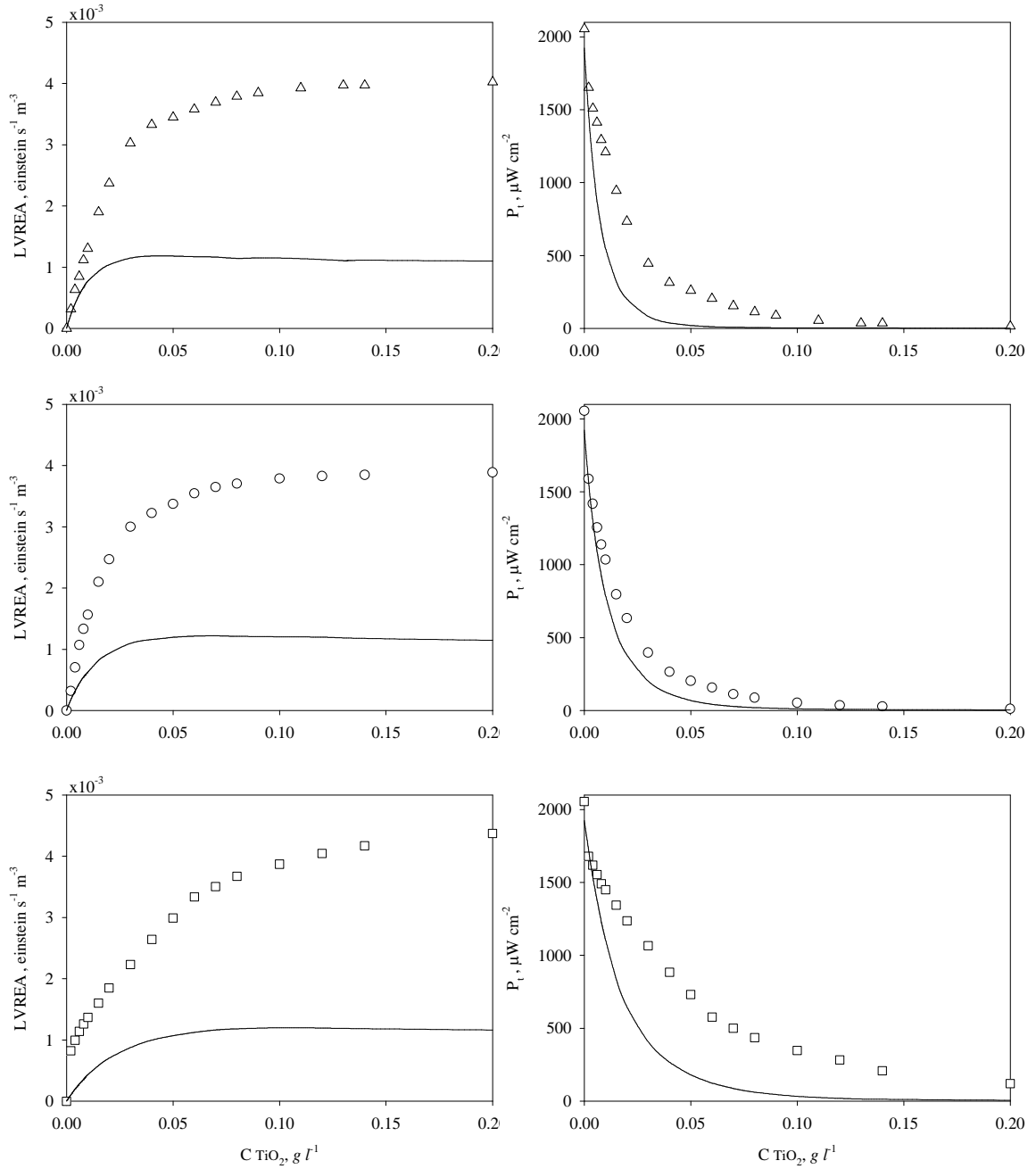
Figure 27 Experimental results for the LVREA and the transmitted radiation and comparison with "MC simulation 2". Experimental data: (Δ) DP 25, (○) Anatase, and (□) Hombikat UV-100 and (—) MC simulations
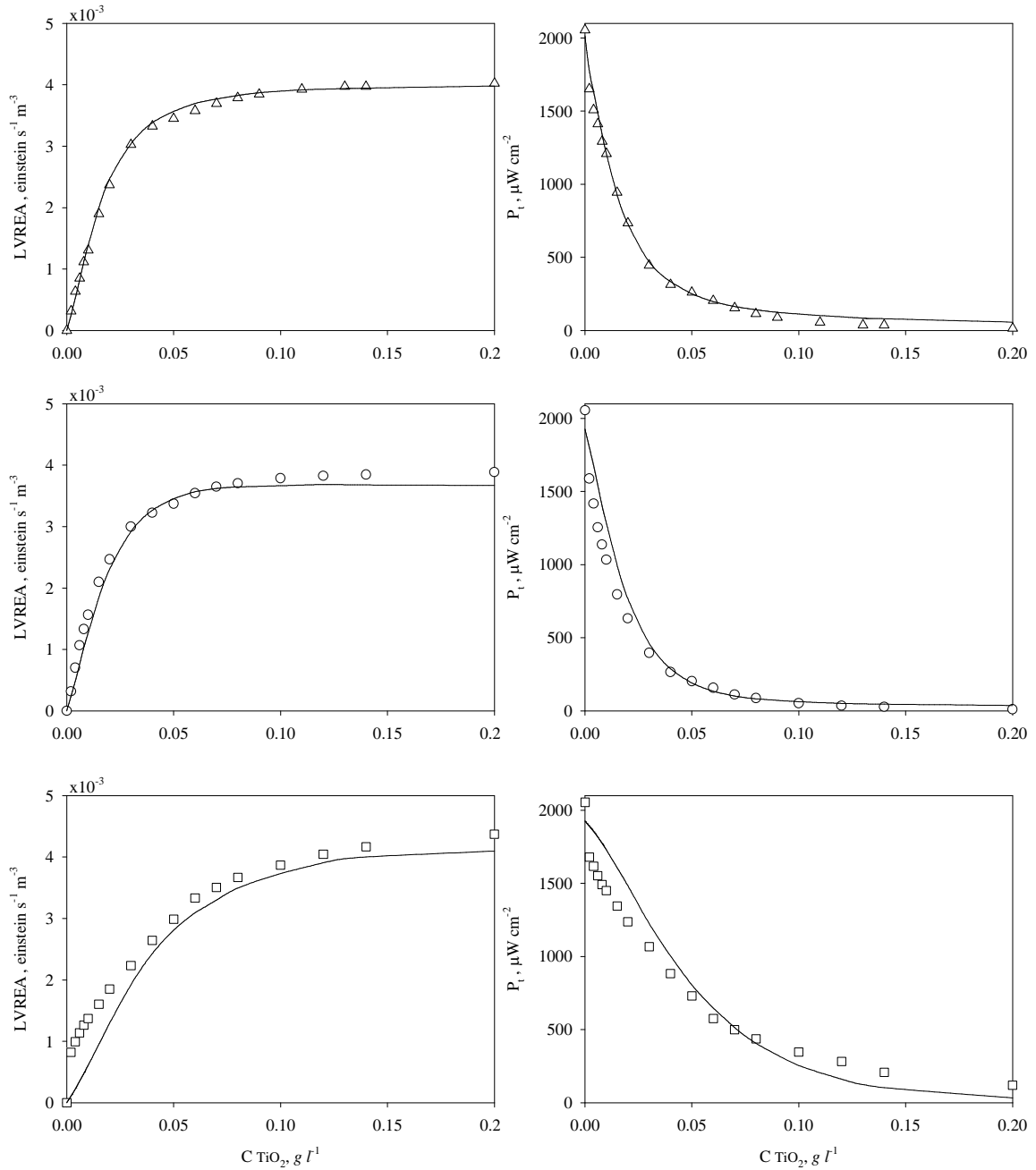
Figure 28 Experimental results for the LVREA, and the transmitted radiation and comparison with "MC simulation 3". Experimental data: (Δ) DP 25, (○) Anatase, and (□) Hombikat UV-100 and (—) MC simulations

Table 14 summarizes the errors from experimental data and MC Simulations 1, 2, and 3 adopting the isotropic scattering assumption. Knowing that "Simulation 3", which involves the spectral distribution of scattering and absorption coefficients, renders the smallest errors

for both LVREA and P_t, "Simulation 3" is proposed for further calculations to establish the significance of asymmetry factors. With this end, "Simulation 4" involving a variation of the asymmetry factor (see Eq. (53)), is implemented with this factor changing from a narrow forward peak ($g = 1$) to a narrow backward peak ($g = -1$). Results for different values of g are shown in Figure 29 for DP 25, whereas Table 15 presents the least square errors from experimental data for these simulations.

Table 14 Least square error calculation for MC simulations 1, 2 and, 3

Case	DP 25		Anatase		Hombikat UV-100	
	$LVREA_{error}$	$P_{t\ error}$	$LVREA_{error}$	$P_{t\ error}$	$LVREA_{error}$	$P_{t error}$
Simulation 1	8.762×10^{-7}	2.287×10^{5}	1.097×10^{-6}	6.250×10^{5}	5.272×10^{-6}	4.818×10^{5}
Simulation 2	7.573×10^{-5}	2.307×10^{6}	6.442×10^{-5}	4.006×10^{5}	6.526×10^{-5}	2.703×10^{6}
Simulation 3	8.339×10^{-8}	5.253×10^{4}	5.451×10^{-7}	4.112×10^{5}	4.103×10^{-6}	5.708×10^{5}

From Figure 29 and Table 15, it can be seen that the highest deviation from experimental values is found when $g = \pm 1$ (i.e. narrow forwardly directed peak and narrow backwardly directed peak scattering). For g values in the range $-0.8 < g < 0.8$, the differences from MC simulations and experimental values are not very large; less than 10% in all cases. These findings suggest that for the mentioned range of asymmetry factors, a precise evaluation of the mode of reflection of the scattered photons is not very critical for a good representation of the experimental values. Results reported in this study are in agreement with those found by Pasquali et al. (1996). These authors studied two different distribution density functions, isotropic and diffuse phase functions. They concluded that both phase functions render good modeling of the radiation field in an annular photoreactor.
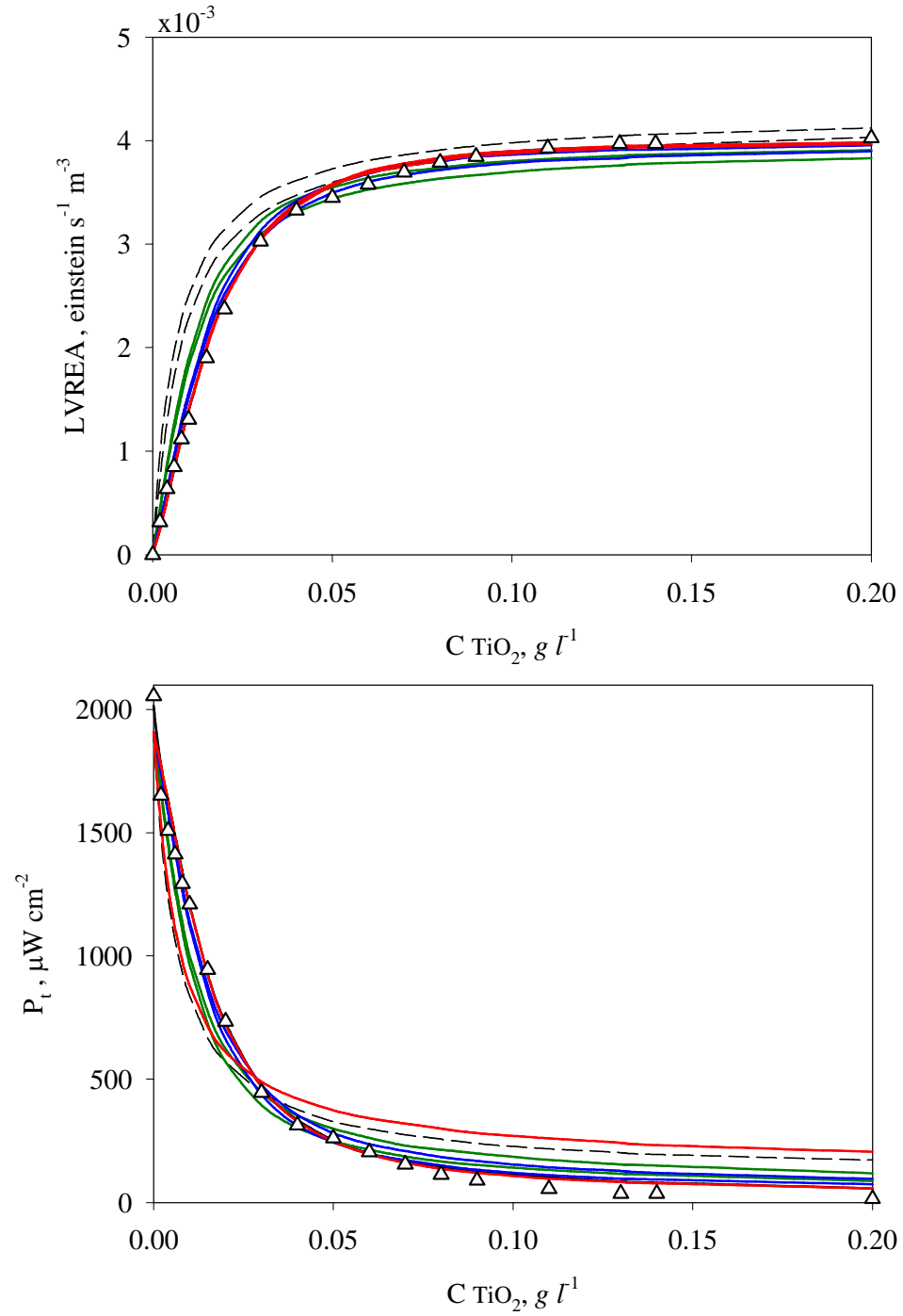
Figure 29 Asymmetry factor influence in MC simulation 4, (Δ) experimental results for DP 25, (- - -) g = 1, (- - -) g = -1, (green —) g = 0.8 and -0.8, (blue —) g = 0.5 and -0.5 and (red —) g = 0.1 and -0.1

Table 15 Least square error calculation for MC simulations at different g values

G	DP 25		Anatase	
	$LVREA_{error}$	$P_{t\ error}$	$LVREA_{error}$	$P_{t\ error}$
1	7.316×10^{-6}	1.749×10^{6}	1.009×10^{-5}	6.209×10^{5}
0.8	1.427×10^{-6}	9.867×10^{5}	5.937×10^{-7}	7.048×10^{4}
0.5	2.852×10^{-7}	4.893×10^{5}	$\mathit{2.265 \times 10^{-7}}$	$\mathit{2.173 \times 10^{5}}$
0.1	9.802×10^{-8}	3.240×10^{5}	$\mathit{5.142 \times 10^{-7}}$	$\mathit{3.913 \times 10^{5}}$
Isotropic	$\mathit{8.339 \times 10^{-8}}$	$\mathit{5.253 \times 10^{4}}$	5.451×10^{-7}	4.112×10^{5}
-0.1	$\mathit{7.601 \times 10^{-8}}$	$\mathit{3.017 \times 10^{5}}$	5.643×10^{-7}	4.088×10^{5}
-0.5	2.065×10^{-7}	4.099×10^{5}	3.584×10^{-7}	2.569×10^{5}
-0.8	1.156×10^{-6}	8.155×10^{5}	5.680×10^{-7}	7.337×10^{5}
-1	4.238×10^{-6}	1.536×10^{6}	4.794×10^{-6}	3.361×10^{5}

In the present study, the most accurate representation for the LVREA and *Pt* profiles were obtained with g = 0 (isotropic scattering), and g=-0.1 for DP 25, and with *g* = 0.1 for Anatase. Thus, the isotropic phase function can be used in MC simulations for both DP 25 and Aldrich catalysts. However, for Anatase, weak backward scattering mode produced better simulation results when compared to the experimental values. These findings differ from those reported by Satuf et al. (2005), who found that for DP 25, *g* varies from 0.6 to 0.4 and that for Aldrich, *g* varies from 0.8 to 0.4 for a wavelength range 295 to 405 nm.

In photocatalytic systems, the slurry system contains a countless number of irregular Titania particles. However; since TiO_2 aggregates, this creates smoother aggregate shapes. This explains the good results obtained in MC simulation with isotropic scattering averaging individual particle shapes (Modest, 2003).

Figure 30 shows the radial profiles for the LVREA at different photocatalyst concentrations for DP 25 for the isotropic scattering mode. Similar results are obtained for catalysts Anatase and Hombikat UV-100. It can be observed that the LVREA exhibits a quick uniform drop with the radial coordinate. One can also notice that in cases where the photocatalyst

concentration is high, the particles closer to the radiation source absorb most of the radiation entering the reactor.

Finally; one can also conclude that if a sufficiently high photocatalyst concentration is used, a close-to-the-wall highly irradiated zone with dark areas towards the reactor center line develops. Thus, there should be an "optimum photocatalyst concentration" which maximizes photodegradation in the photocatalytic reactor. This optimum photocatalyst concentration also provides an optimally irradiated condition inside the reactor without dark zones. Photocatalyst concentrations above this maximum show an essentially negligible effect on LVREA. According to Salaices et al. (2001), and in agreement with our MC simulations, this optimum photocatalyst concentration is achieved when $P_t = 0.2\% P_i$ in the photoreactor employed here. Furthermore, one can also notice that a great advantage of the MC simulations is that this "optimum photocatalyst concentration" can also be predicted by determining the LVREA at different catalyst concentrations.
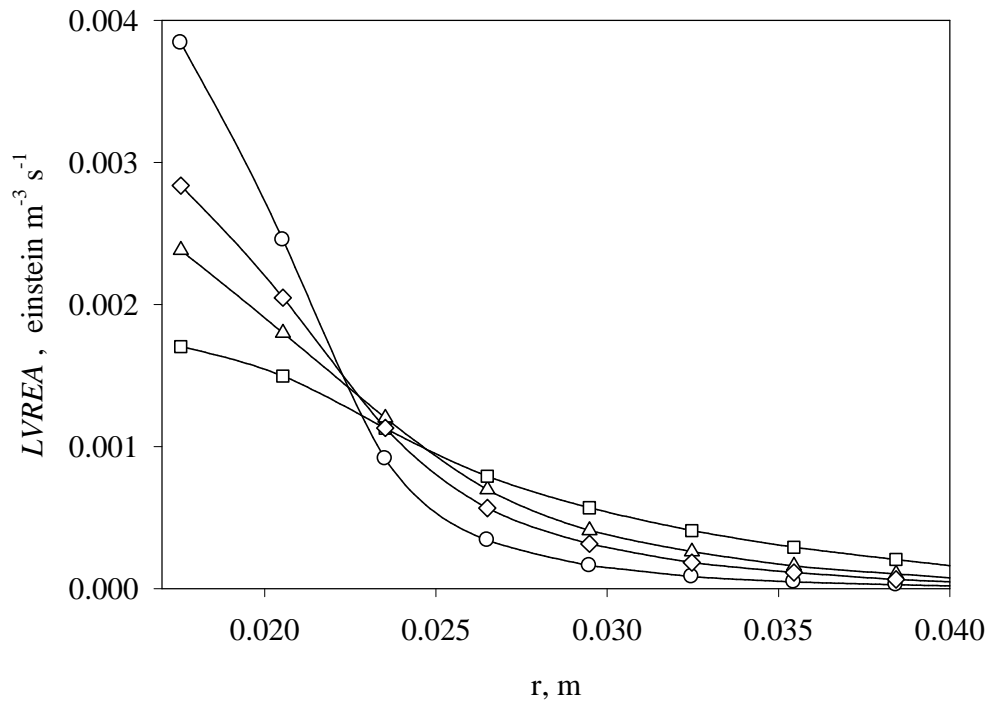
Figure 30 Radial profiles of LVREA for different DP 25 concentrations by MC. (○) 0.14, (◊) 0.09, (△) 0.07 and, (□) 0.04 g l^{-1}

Furthermore, one should expect that this "optimum photocatalyst concentration" is close to the one determined in photocatalytic reaction experiments. Figure 31a reports the LVREA profiles for different concentrations of DP 25. The arrow shows that the LVREA for $P_t = 0.2\% P_i$ is reached at 0.14 g l^{-1}. It is interesting to observe that in both cases the "optimum photocatalyst concentrations" are in agreement with the ones inferred from the overall reaction rate for phenol degradation, as shown in Figure 31b. It can be seen that the overall reaction rate reaches a maximum value of about 7.0 μmol-C l^{-1} min^{-1} for catalyst concentrations higher than 0.14 g l^{-1}.

As a result, one can conclude that the MC simulations are not only valuable to define the "optimum photocatalyst concentration" leading to optimum irradiation, but also an excellent tool to identify the operating conditions leading to a best possible photocatalytic rates for a given photocatalytic reactor configuration.

5.3 Prediction of Absorption and Scattering Coefficients Using MC Simulations in the Photo-CREC Water-II

In the previous section of this chapter, it was mentioned that the *LVREA* is found from the solution of the RTE. In order to numerically solve this equation, the absorption and scattering coefficients and the phase function should be known, as well as the boundary conditions (light being received by the radiation source). Under best scenario situations, the extinction coefficient (β_{cat}), which is the sum of the absorption coefficient (κ_{cat}) and the scattering coefficient (σ_{cat}), can be readily obtained from experimental measurements. In a heterogeneous medium, where absorption and scattering coexist, the extinction coefficient could be found by "extinctance" measurements ($-log[I/I_0]$) using a conventional spectrophotometer or black collimator tubes (refer to section 5.1.2, Eq. (45)). Thus, conventional spectrophotometry can be carried out in order to find the addition of both coefficients, which can be represented by the following equation:

$$\beta_{cat} = \kappa_{cat} + \sigma_{cat} \tag{61}$$
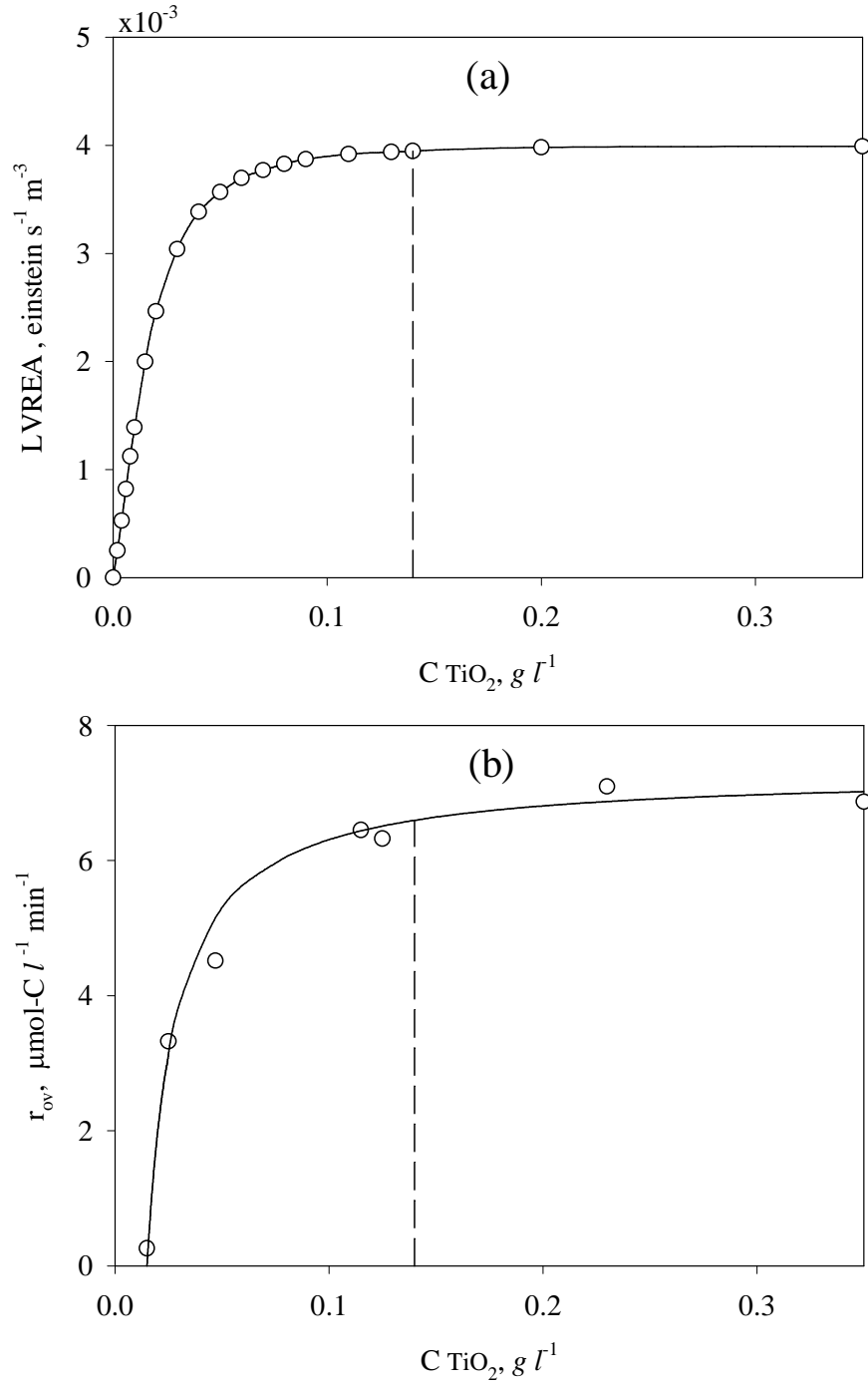
Figure 31 (a) LVREA inside the Photo-CREC Water-II as a function of DP 25 loading. (b) Overall reaction rate for phenol degradation versus DP 25 concentration (as presented by Salaices et al., 2001)

Although, the extinction coefficient is easy to evaluate (values are reported in Table 10), it does not provide sufficient information of the radiation distribution inside an annular slurry photoreactor. Therefore, it is necessary to obtain either the absorption or the scattering coefficients independently so that the absorption and scattering coefficients are fully established. Experimental measurements for evaluating the scattering and absorption coefficient of fluid-particle systems are generally very time demanding and may require the use of complex actinometric or spectrophotometric techniques (Imoberdorf et al., 2008).

In order to find the values for the absorption and scattering coefficient for the different catalysts used in this study, an alternative approach is reported to numerically evaluate the wavelength-averaged absorption and scattering coefficients. First, the *LVREA* and the transmitted radiation throughout the reactor are evaluated by using a macroscopic radiation balance. Extinction coefficients are evaluated using the MB and a black collimator of 2.3 cm long. Once these experimental parameters are determined, MC method is applied along with an optimization to find the absorption and scattering coefficients that best fit the experimental *LVREA* and P_t data. For the optimization, the experimental value for the extinction coefficient is considered to be the summation of the absorption and scattering coefficients (refer to Eq. (61)).

In order to compare the values for the coefficients found in this study, Table 16 presents the wavelength-averaged coefficients calculated from the values reported by Cabrera et al. (1996) and Eqs. (23) and (24) for three photocatalyst. Again, for MC simulations, the specific averaged coefficients have to be converted into the adequate units using Eq. (48).

Table 16 Experimental specific wavelength-averaged coefficients for different TiO_2

Catalyst	κ_{cat}^* $(m^2\ g^{-1})$	σ_{cat}^* $(m^2\ g^{-1})$	β_{cat}^* $(m^2\ g^{-1})$
DP 25	0.6394	5.6077	6.2471
Anatase	0.3957	3.1149	3.8106
Hombikat UV-100	0.2747	2.3415	2.6152

The calculation of both scattering and absorption coefficients (denotes as κ^*_{cat} and σ^*_{cat} in Eq. (48)) involves an optimization calculation where one starts with a pair of coefficients and searches the ones that better fit the experimental values for the *LVREA* and the P_t, obtained from a MB. Fitted coefficients shall be calculated using statistically based methods with small spans for the 95% confidence interval. This method of absorption and scattering coefficient calculation with optimization is described in Figure 32.

The optimization Toolbox "fminsearch" in Matlab is used in this study to find the best values for the coefficients. This optimization tool finds the minimum of a function specified by the user by using the derivative-free method. This function provides convergence criterion, which for this study, is defined as the summation of the least squared error for the *LVREA* and P_t. Ideally, the error should be defined as the summation of the error differences for *LVREA* and Pt as follows:

$$error = \sum \left(LVREA_{\exp}(W) - LVREA_{MC}(W)\right)^2 + \sum \left(P_t(W)_{\exp} - P_t(W)_{MC}\right)^2 \qquad (62)$$

where *LVREA*(*W*) and *Pt*(*W*) denotes values in watts , exp is for experimental values and MC denotes values found from MC simulations.

However, experimental P_t and *LVREA* are related according to Eq.(13). Hence, the error function needs to be redefined in order to avoid optimizing two dependent functions. Consequently, a new definition of error was defined as follows:

$$error_{LVREA} = \sum \left(LVREA_{\exp}(W) - LVREA_{MC}(W)\right)^2 \qquad (63)$$

$$error_{Pt} = + \sum \left(P_t(W)_{\exp} - P_t(W)_{MC}\right)^2 \qquad (64)$$

As a result, when the optimization is performed, either Eq. (63) or (64) can be used as the error definition. In our case, Eq. (63) is adopted for all calculations.
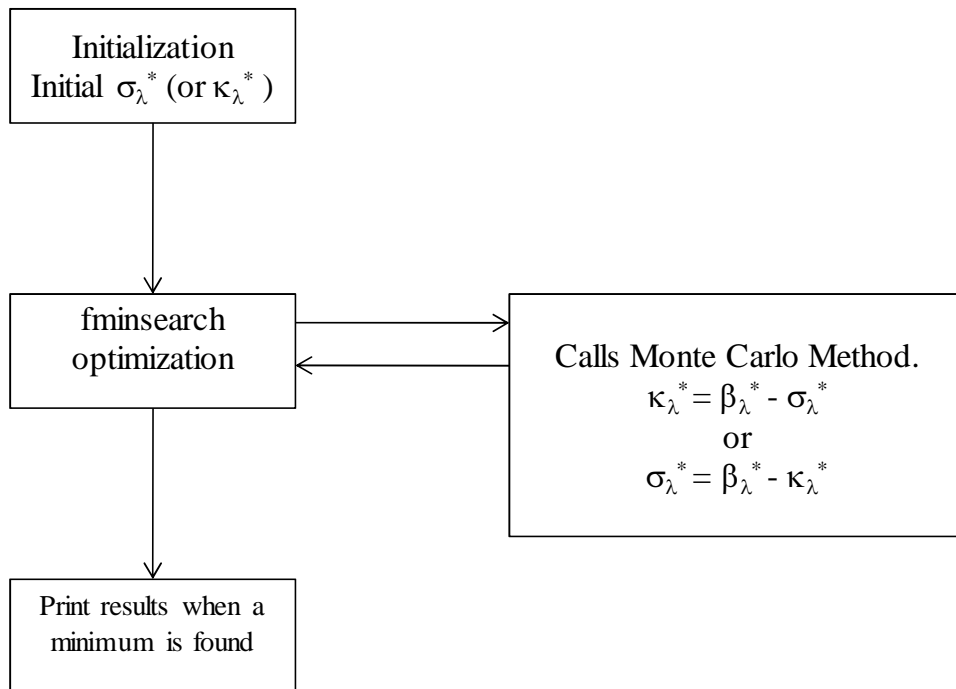
Figure 32 Optimization procedure in finding the specific absorption and scattering coefficients

During the optimization process, different pairs of the absorption and scattering coefficients might be found, satisfying the convergence criteria, which show the existence of local minima. Accordingly; and in order to develop a meaningful calculation, it is proposed in the present study to proceed as follows: a) the experimentally extinction coefficients are determined experimentally (i.e. β_{cat}), b) During the optimization procedure, if σ^{*}_{λ} is the optimized coefficient, then, the κ^{*}_{λ} coefficient is determined within the MC code by using Eq. (61) as follows:

$$\kappa^{*}_{\lambda} = \beta^{*}_{\lambda} - \sigma^{*}_{\lambda} \tag{65}$$

The optimization process starts with an initial guess for the adjusted coefficient; either κ^{*}_{λ} or σ^{*}_{λ}, half of the value of experimental extinction coefficient was used as an initial guess in all cases. Then, the optimization calls MC simulation which generates results for the *LVREA_{MC}* and P_{tMC}. Once these results are obtained, MC calculates the error expressed in Eq. (63). The error value is then returned to the optimization instruction, and the process continues until a minimum is found. At this point, the program stops and prints the results.

Solution for the determined coefficients should meet two different constrains: (a) coefficients have to be positive and (b) coefficients have to satisfy Eq. (61). These two physical constrains are considered when analyzing the optimized values found with fminsearch.

Results from the optimization, and the comparison with experimental results for the absorption and extinction coefficients, are reported in Table 17. This table also reports the error between experimental values and the optimized coefficients. From Table 17, one can see that the confidence intervals (CI) are smaller than 10% for all the cases. The low value for the CI validates the utilization of MC method for the prediction of optical coefficients in the Photo-CREC Water-II photoreactor.

Figure 33 displays the experimental data for the *LVREA* and P_t and the results found from MC simulations when the optimized coefficients are used in the calculations. Good agreement between experimental and predicted values is found for both cases, *LVREA* and P_t.

Table 17 Optimized κ_{cat}^* and σ_{cat}^* coefficients vs. experimental values

Catalyst	κ_{cat}^* (m^2 g^{-1})				σ_{cat}^* (m^2 g^{-1})			
	Exp.	Estimate	CI	error(%)[1]	Exp.	Estimate	CI	error(%)[1]
DP 25	0.6394	0.5771	0.052	9.74	5.6077	5.6700	0.037	1.11
Anatase	0.3957	0.4397	0.025	11.12	3.4149	3.3709	0.025	1.29
Hombikat	0.2747	0.2664	0.017	10.30	2.3415	2.3689	0.022	1.21
Sol-Gel Cat	ND	0.1438	0.006	-----	ND	1.2512	0.050	-----

[1] Represents the error with respect to experimental value. ND = not determined.
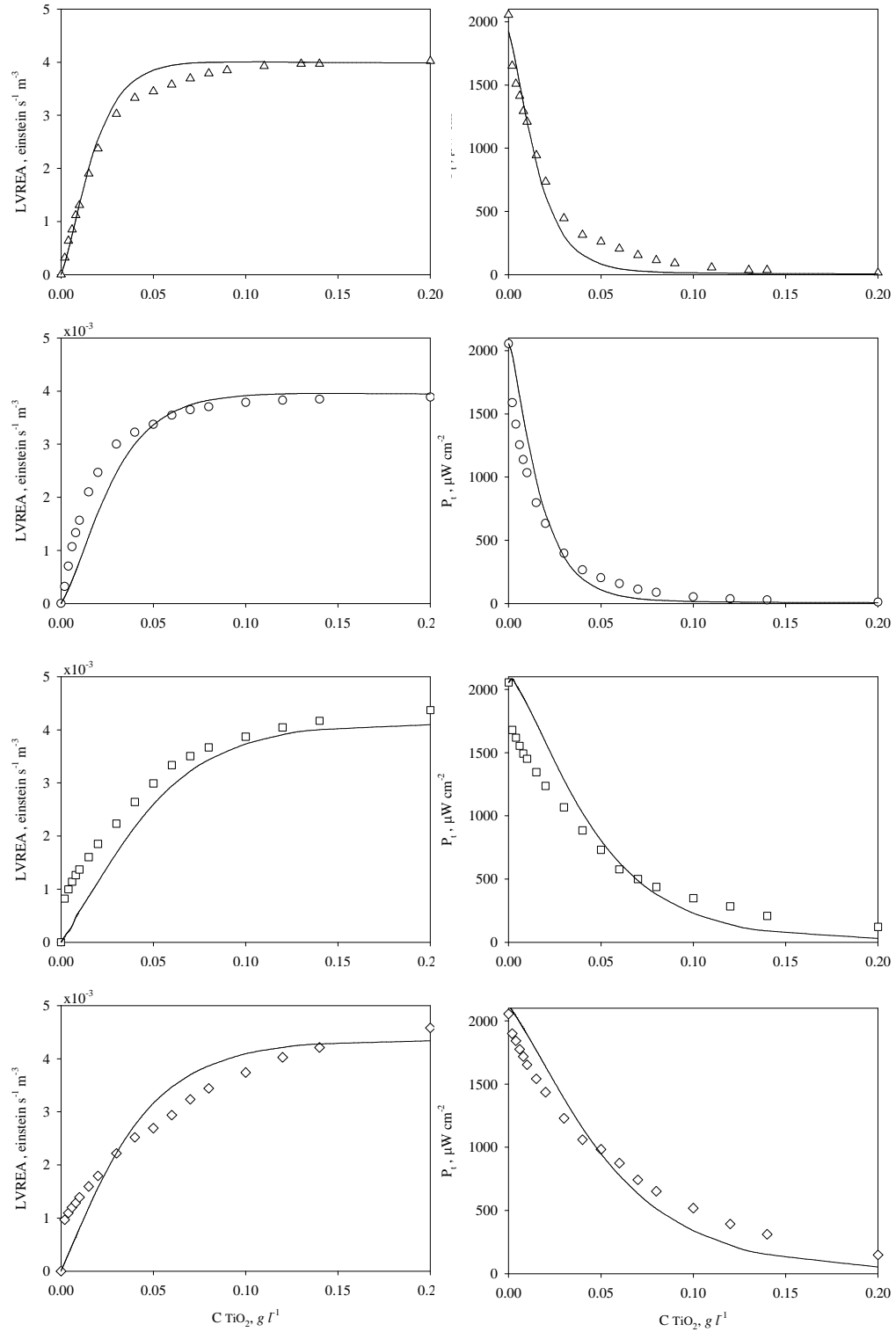
Figure 33 Experimental results for LVREA and P_t compared with MC simulations when the fitted absorption and scattering coefficients are used (Δ) DP 25, ($\circ$) Anatase, ($\square$) Hombikat UV-100 and, ($\Diamond$) Sol-Gel Cat

5.4 Conclusions

The following are the conclusions of this chapter:

(a)   MC based method can be employed to simulate the UV radiation field in an annular heterogeneous reactor for four different TiO_2 photocatalysts (DP 25, Anatase, Hombikat UV-100 and, Sol-Gel Cat). The MC method is an effective tool for solving the RTE, providing an easy to use and easy to apply alternative to circumvent the problems associated with analytical solutions. The MC simulations can be applied for virtually any reactor configuration or geometry allowing precise predictions of optimum catalyst concentrations and reactor designs.

(b)   The determination of absorption and scattering coefficients in photocatalytic reactors require an optimization procedure. This method involves the experimental determination of *LVREA*, P_t and extinctance in properly designed photocatalytic reactors with special black collimator tubes, such as is the case of Photo-CREC Water-II reactor.

(c)   The optimization calculation also requires MC simulations, allowing determination of both absorption and scattering coefficients. The determined κ^*_λ and σ^*_λ coefficients can be established complying with a number of constrains, as well as with narrow spans and low cross-correlation.

(d)   Spectroradiometric measurements in the Photo-CREC Water-II allow the determination of the radiation being absorbed by different TiO_2 catalysts. Other parameters involved in the MB are obtained with the help of inner polished and UV-opaque collimators. The MB allows determining the total radiation transmission, the non-scattered radiation transmission and the back-scattering radiation exiting the system.

(e)   UV-Opaque collimator minimizes the in-scattering and out-scattering collected by the detector allowing the determination of the extinction coefficients for the different TiO_2 catalysts.

(f)   MC simulations, with back-scattered photons reaching the BL-lamp and reflected with different angular and longitudinal angles, provide a more accurate result for the LVREA than when the lamp absorbs such photons. It is demonstrated that for isotropic scattering, spectral distribution for the absorption and scattering coefficients used in the MC simulations, provides an accurate evaluation of the LVREA. This solution is comparable with the one obtained when the averaged-wavelength absorption and scattering coefficients are used.

(g)   Narrow backward and forward peaks ($g = -1$ and $g = 1$, respectively) in the H-G phase function are not suitable for MC simulations. On the other hand, it is demonstrated that a g value close to zero provides good representation for the experimental LVREA. It is found that for the range $-0.8 < g < 0.8$, differences from MC simulations and experimental values are not very large; less than 10% in all cases. This suggests that the adoption of a specific phase function is not crucial for a good representation of the radiation field, provided it is kept in the $-0.8 < g < 0.8$ range. It is shown that by comparing the light absorption rates and the transmitted radiation from both experimental observations and the MC simulations that there is satisfactory agreement. Therefore, one can use the MC simulation as an effective tool in finding the LVREA for concentric photocatalytic reactors designed on the same principles as the Photo-CREC Water-II.

(h)   The LVREA reaches a maximum value for DP 25 concentration at the optimum photocatalyst concentration of $0.14\ g\ l^{-1}$. It is further demonstrated that this optimum catalyst concentration for reactor irradiation is in close agreement with the optimum value found while developing phenol photocatalytic degradation rates experiments.

Chapter 6
Results and Discussion Part II: Mineralization of Phenol and its Intermediates

6   Introduction

This chapter reports the photocatalytic degradation of phenol and its intermediates. Four different TiO_2 photocatalysts were used in the photodegradation experiments. The influence of Fe ions in solution was also studied while using DP 25 and Sol-Gel Cat TiO_2 photocatalysts. All the experiments were performed at optimum operational conditions previously found from other recent studies in the Photo CREC photoreactor unit (Ortiz-Gomez 2006 and Salaices-Arredondo 2002). Flow rate, air being supplied, radiation intensity, catalyst loading were kept constant for all the experiments. The pH of the reacting system; however, was set at the beginning of every experimental run at 3.7±0.1 with H_2SO_4.

The first section of this chapter includes the identification and quantification of the intermediate aromatic species and carboxylic acids involved in phenol photodegradation. The second section is devoted to report the degradation profiles for phenol, total organic carbon and reaction intermediates at different initial phenol concentrations. The final section in this chapter includes the study of adsorption of phenol and intermediate species on different TiO_2.

6.1   Detection of Intermediate Species in Phenol Photodegradation

Evidence of the reaction intermediates existence during photodegradation was obtained by using different analytical techniques. Total organic carbon (TOC) measurements were done using a TOC analyzer. TOC profiles show the extent of mineralization of phenol and its intermediates. Phenol and aromatic intermediates were quantified using a HPLC with a C18 column. Carboxylic acids were quantified employing a HPLC with a Supelco C-61H column. The conditions for all the analyses were discussed in the experimental methods section of this PhD dissertation. Detection of aromatic compounds was performed on a GC/MS by using the EPA method 8270D. Data for the identification of aromatic components are presented in Appendix B. It was found that the major aromatic compounds detected are three hydroxylated compounds, hydroquinone (o-DHB), catechol (p-DHB), resorcinol, and 1,4-

benzoquinone (1,4-BQ). These observed species are in agreement with previous findings reported by Salaices-Arredondo 2002; Ortiz-Gomez 2006 and 2008.

In this respect reviewing the technical literature, one can notice that many compounds are reported as intermediate species of phenol degradation on TiO_2 photocatalysts including hydroquinone, catechol, 1,4-benzoquinone, and resorcinol. These species are identified as potential hydroxylated intermediate compounds. Additionally, several carboxylic acids have been detected as intermediates, with the main ones being fumaric acid, maleic acid, oxalic acid, lactic acid, and formic acid (He et al., 2010; Vinu et al., 2010; Laoufi et al., 2008;Ortiz-Gomez et al., 2008 and 2006; Wang et al., 2005; Choor et al., 2004; Sobczynski et al., 2004).

Regarding phenol intermediate species present in a photoreaction, other studies also attempted to elucidate the reaction mechanism of phenol photodegradation by TiO_2 under UV light (Sobczynski et al., 2004). These authors found that during phenol degradation; in addition to phenol five hydroxylated aromatic compounds are present, including 1,4-benzoquinone and four aliphatic compounds. They concluded that catechol, hydroquinone and 1,4-benzoquinone were the three aromatic intermediates kinetically important and that their concentrations, along with that of phenol, should be known in the course of the photoreaction. Sobczynski et al., 2004 also reported a reaction mechanism for the photodegradation of phenol on TiO_2 and included acetic and formic acids as the main two carboxylic acids.

Figure 34 shows the concentration profiles for phenol and its intermediates when DP 25 catalyst is used at initial pH of 3.7. In this figure, 30 ppm-C was the initial concentration. The experimental TOC profiles are also reported, with TOC reporting the addition of carbon masses of various intermediate species, as observed with HPLC. It can be noticed that the curve representing the species mass addition agrees well with the experimental TOC curve. Hence, it can be speculated that the major intermediates species involved in the photodegradation were detected during the HPLC analysis.
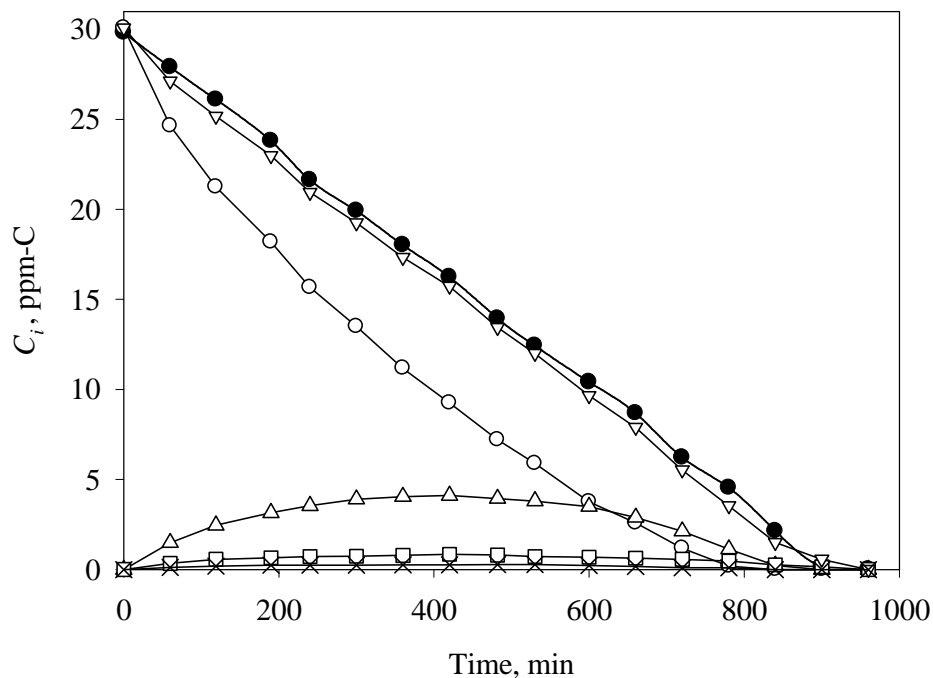
Figure 34 Concentration profiles for (○) phenol, (●) TOC, (Δ) p-DHB, (□) o-DHB, (×) 1,4-BQ and, (▽) species mass addition for DP 25

On the other hand, Figure 35 reports the intermediate concentration profiles for those other components detected and present during phenol degradation over DP 25.

It should also be mentioned that both hydroquinone and catechol were the two major aromatic intermediate species detected in phenol degradation on DP 25. Benzoquinone and resorcinol were also detected but at significantly lower concentrations. In addition, two major carboxylic acids were also quantified: formic and acetic acid. All these intermediates, aromatic and carboxylic compounds, were consistently detected when various TiO_2 catalysts were used in the degradation experiments. Results will be reported in detail in the upcoming sections of this PhD dissertation.
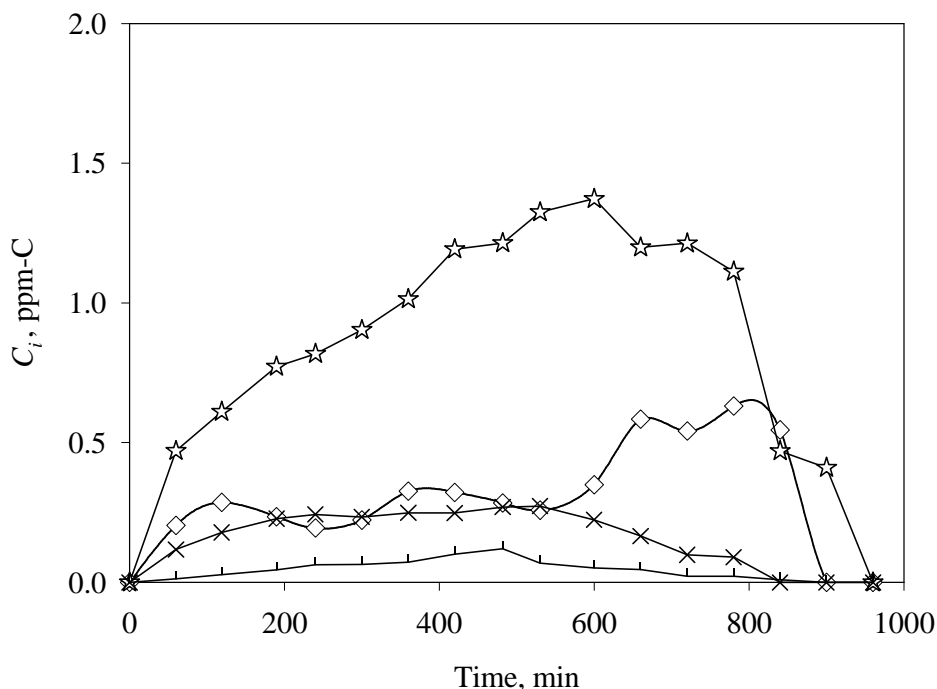
Figure 35 Concentration profiles for intermediates species present at lower concentrations during phenol photoconversion. (☆)Acetic acid, (◊) Formic acid and (×) 1,4-benzoquinone and (|)resorcinol

Once it was established that, in addition to phenol, another intermediate species are produced during the course of the photoreaction, it was concluded that their quantification was important. Therefore, for the photoreaction results; phenol, hydroquinone, catechol, benzoquinone, resorcinol, acetic acid and formic acid were analyzed by using the HPLC methods explained in the Chapter 4. Also, TOC was measured during the reaction time, in order to assess the extent of total mineralization of phenol.

6.2 Photocatalytic Oxidation of Phenol

This chapter reports experimental TOC plots for the different catalysts followed by phenol and reaction intermediates profiles. Four different catalysts were tested using the photodegradation of phenol. These catalysts are DP 25, Anatase, Hombikat UV-100 and Sol-Gel Cat. The influence of iron ions in the photodegradation of phenol was also studied for DP 25 and Sol-Gel Cat, which were the two catalysts with the highest phenol degradation rates. The optimum Fe^{3+} ions concentration used was 5 ppm (Ortiz-Gomez et al., 2008). For each catalyst, a different lamp was used in order to eliminate the potential influence of lamp

power decay, known to take place after more than 100 hours of utilization. Table 18 reports

the photocatalyst used, the lamp utilized and the initial power of each of the lamp.

Table 18: Catalysts tested for phenol photodegradation

Catalyst	Lamp	P_0 (einstein s^{-1})
DP 25	A	1.1910×10^{-5}
Anatase	B	1.1446×10^{-5}
Hombikat UV-100	C	1.1830×10^{-5}
Sol-Gel Cat	D	1.2121×10^{-5}
DP 25+Fe^{3+}	E	1.1620×10^{-5}
Sol-Gel Cat+Fe^{3+}	F	1.2340×10^{-5}
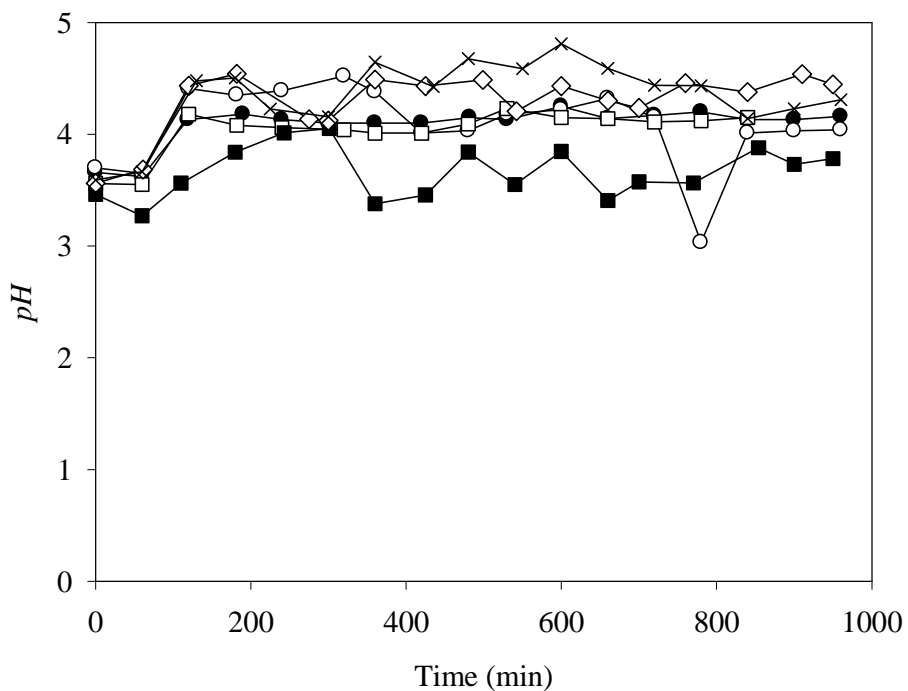
Figure 36 pH change for 30 ppm-C of phenol on (●) DP 25, (◊) Anatase, (×) Hombikat UV-100, (■) Sol-Gel Cat, (○) DP 25+Fe^{3+},and (□) Sol-Gel Cat+Fe^{3+}

For all of the catalysts tested, initial concentrations of 10, 20, and 30 ppm-C in phenol were considered as initial substrate concentrations. This was required to have enough experimental data for kinetic modeling. As described in the experimental section, for all the experiments, the pH of the solution was initially adjusted to 3.7 with H_2SO_4. Figure 36 presents the evolution of pH for the all the catalysts employed in the experiments, for an initial concentration of 30 ppm-C in phenol.

For all the catalysts employed, a slight increase in pH was observed during the first 100 minutes of reaction. After that, an apparent plateau was reached with essentially no further change in the pH of the reacting solution. This allowed us to neglect the pH effect in the degradation rate of phenol and to establish the effect with the photocatalyst type used.

Thus, once pH and lamp power decay were controlled, the next step was the quantification of intermediate species during phenol photocatalytic conversion for different photocatalysts. These results will be presented in the following sections of this chapter.

6.2.1   Degussa P25

A first set of experiments was performed by employing DP 25. This TiO_2 powder has shown the highest photocatalytic activity and it has been used often as a standard photocatalyst (Rengifo et al., 2009). Figure 37d reports the TOC and phenol profiles for different initial phenol concentrations at different irradiation times. One can notice that the TOC decay curve displays a close to zero-order reaction kinetics.
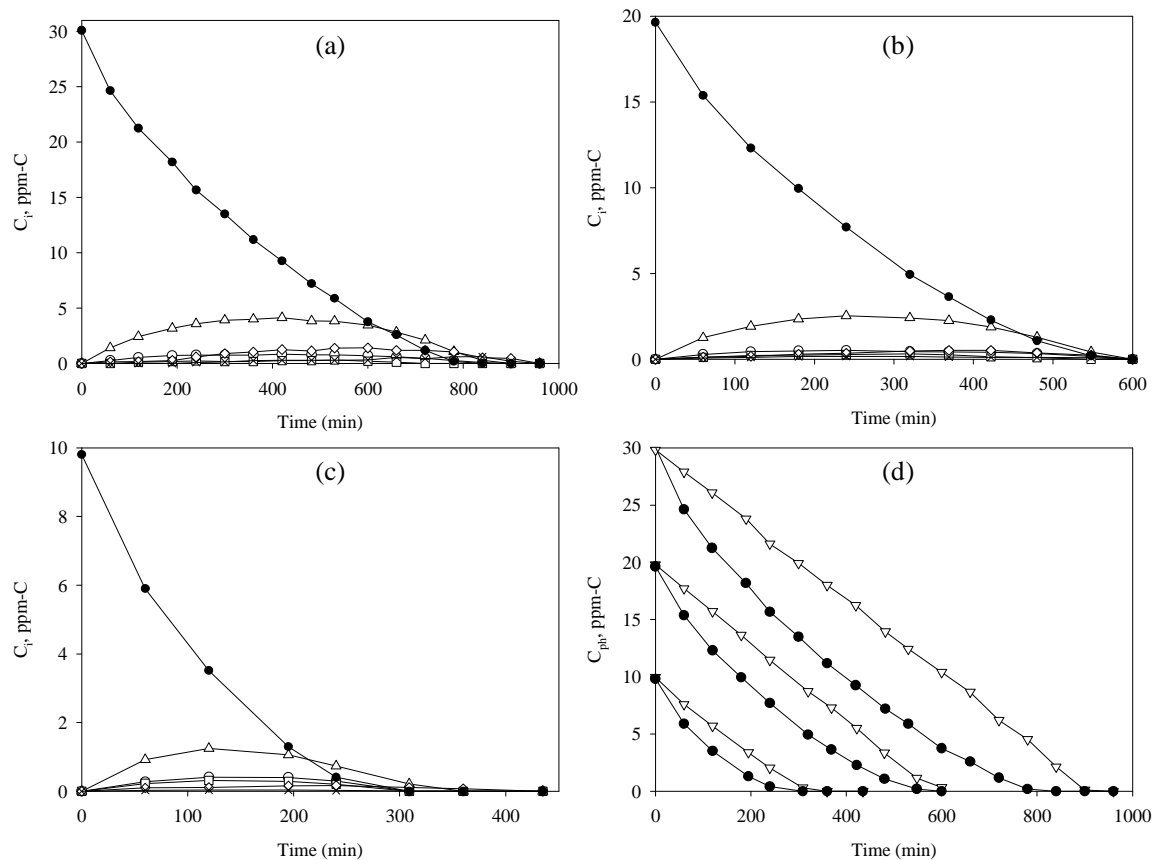
Figure 37 Concentration profiles during phenol photodegradation on DP 25. (•) phenol, (▽) TOC, (△) hydroquinone, (○) catechol, (□) benzoquinone, (◊) acetic acid and (×) formic acid. (a) 30 ppmC, (b) 20 ppmC, (c) 10 ppm-C, and (d) comparison of TOC and phenol profiles

Figure 37 a, b, and c show phenol and detected intermediate species during phenol degradation over DP 25 at different initial phenol concentrations. Three major aromatic intermediate species were observed: hydroquinone, catechol and benzoquinone. In addition two carboxylic acids were also quantified: acetic and formic acids. In this case, resorcinol was detected at very low concentrations only. Therefore, resorcinol is considered not to be required in the kinetic analysis for DP 25.

Figure 38 Concentration profiles of phenol photoconversion intermediate species at several initial concentrations on DP 25: (Δ) hydroquinone, (○) catechol, (□) benzoquinone, (◊) acetic acid, and (×) formic acid. (a) 30 ppmC, (b) 20 ppmC, (c) 10 ppmC, and (d) comparison of hydroquinone profiles

Figure 38 a, b, and c report the concentration profiles of phenol oxidation intermediates at different initial concentrations. Figure 38c shows a comparison of hydroquinone profiles, which is the intermediate oxygenated species produced at highest concentrations.

6.2.2   Anatase

Figure 39 provides a comparison between phenol and TOC decay profiles. It can be seen that Anatase behaves differently than DP 25 when it comes to total mineralization. The TOC profiles in Anataseseem to decay very slowly, as shown by Figure 39c, indicating a controlling step or the production of an intermediate more resistant to the photodegradation.

Identification of phenol intermediates again was performed for the case of Anatase. Results showed that hydroquinone, catechol and benzoquinone were produced during phenol photodegradation. No other intermediates were found by using the technique described in the experimental section. From the results above however, one can speculate about the production of an unknown oxygenated intermediate. One can notice that while for phenol and its intermediates there is total degradation, the TOC profiles display a slow and incomplete mineralization.
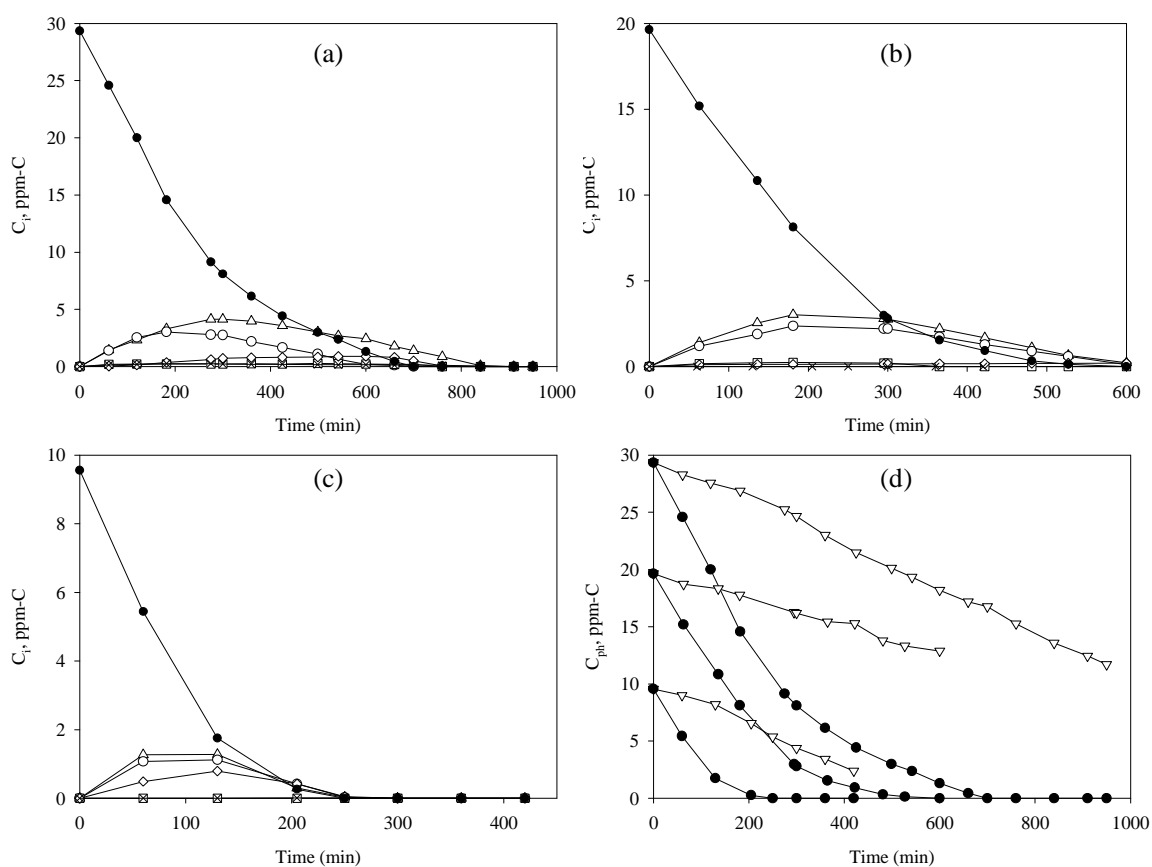
Figure 39 Concentration profiles during phenol photodegradation on Anatase. (●) phenol, (▽) TOC, (△) hydroquinone, (○) catechol, (□) benzoquinone, (◊) acetic acid and (×) formic acid. (a) 30 ppmC, (b) 20 ppmC, (c) 10 ppm-C, and (d) comparison of TOC and phenol profiles

Figure 40 provides a detailed description of the different intermediates produced at different initial concentrations. For the case of Anatase, hydroquinone and catechol are formed in higher concentrations. No significant amounts of formic acid were detected and the concentration of benzoquinone could be considered negligible.
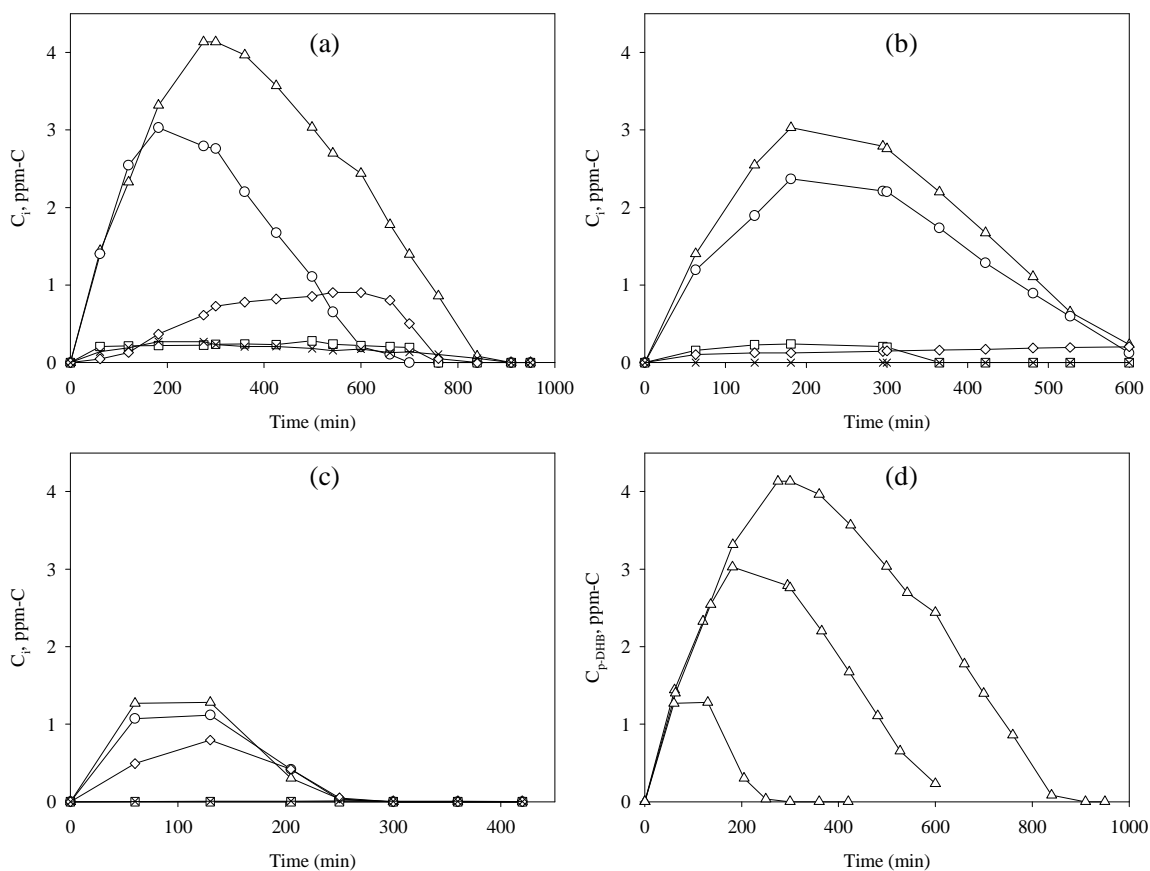
Figure 40 Concentration profiles of phenol photoconversion intermediate species at several initial concentrations on Anatase: ($\triangle$) hydroquinone, ($\circ$) catechol, ($\square$) benzoquinone, ($\diamond$) acetic acid, and ($\times$) formic acid. (a) 30 ppmC, (b) 20 ppmC, (c) 10 ppmC, and (d) comparison of hydroquinone profiles

Figure 41 shows a comparison between the experimental TOC and the addition of carbon masses of the various intermediate species, as observed with HPLC. It can be noticed that the curve representing mass addition does not agree with the experimental TOC. Hence, other non-identified intermediate or intermediates are present during phenol degradation when using Anataseas a photocatalyst. These unknown intermediate/intermediates could not be

identified using GC/MS, with this photocatalyst being the only one presenting such a behavior, as well as the lowest activity among the studied photocatalysts.
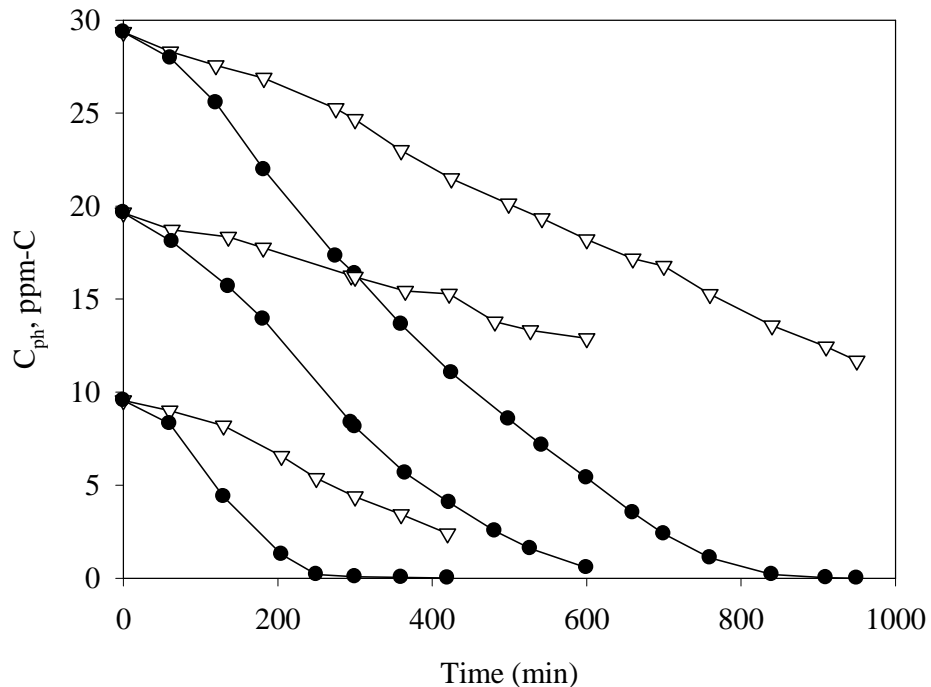
Figure 41 Concentration profiles for ($\triangledown$) experimental TOC and ($\bullet$) species mass addition of the quantified intermediates species for phenol photoconversion using Anatase

6.2.3   Hombikat UV-100

Figure 42 shows phenol and phenol reaction intermediates photodegradation using Hombikat UV-100. Total mineralization was not achieved during the 600 minutes of irradiation. There were, as reported in Figure 43, significant changes of intermediates produced: a) catechol was not detected, b) benzoquinone was formed at higher concentration than when using either DP 25 or Anatase, c) formic acid was the only carboxylic intermediate found.

In summary; for Hombikat UV-100, hydroquinone, benzoquinone and formic acid were the only intermediates formed. The addition of these intermediates species and phenol (see Figure 44) yields curves close to TOC profiles. It can, as a result, be hypothesized that all species were adequately quantified during photoconversion using Hombikat UV-100.
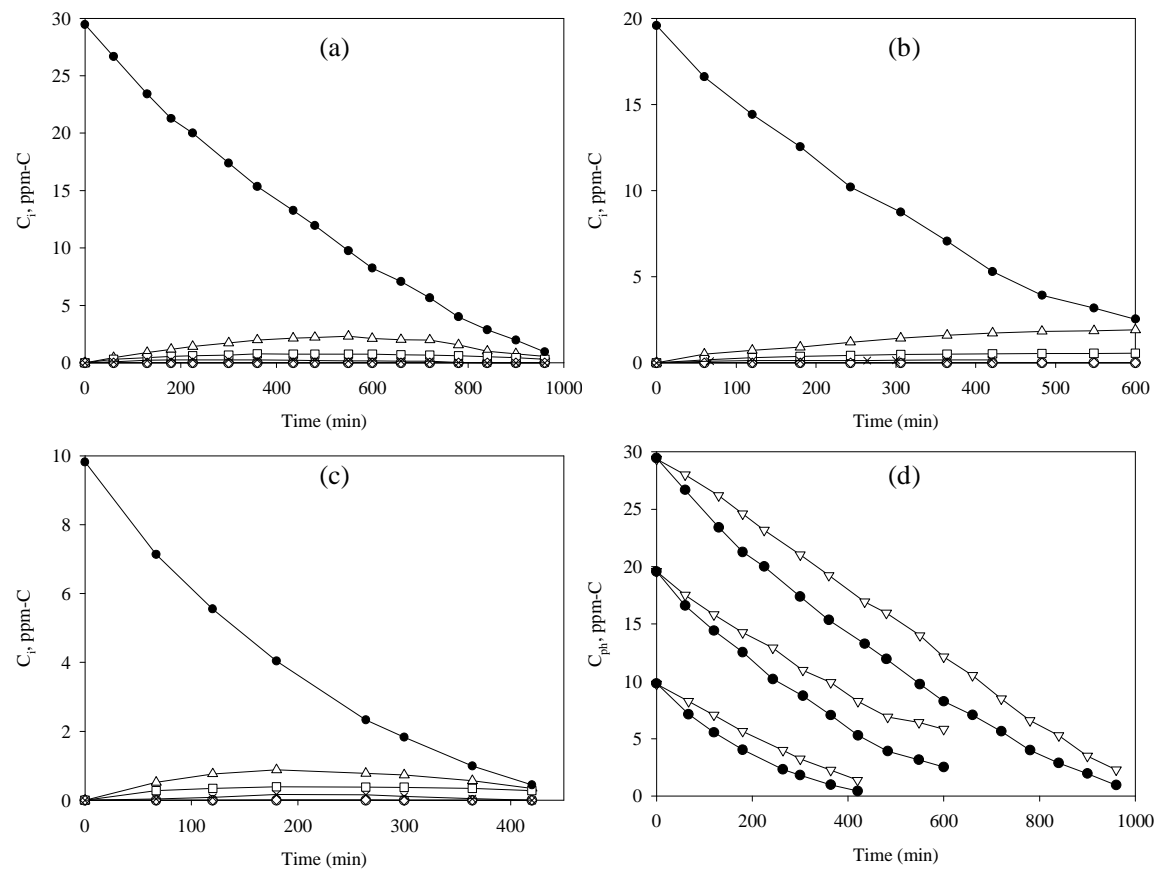
Figure 42 Concentration profiles during phenol photodegradation using Hombikat UV-100. (•) phenol, ($\triangledown$) TOC, ($\triangle$) hydroquinone, ($\circ$) catechol, ($\square$) benzoquinone, ($\lozenge$) acetic acid and ($\times$) formic acid. (a) 30 ppmC, (b) 20 ppmC, (c) 10 ppm-C, and (d) comparison of TOC and phenol profiles
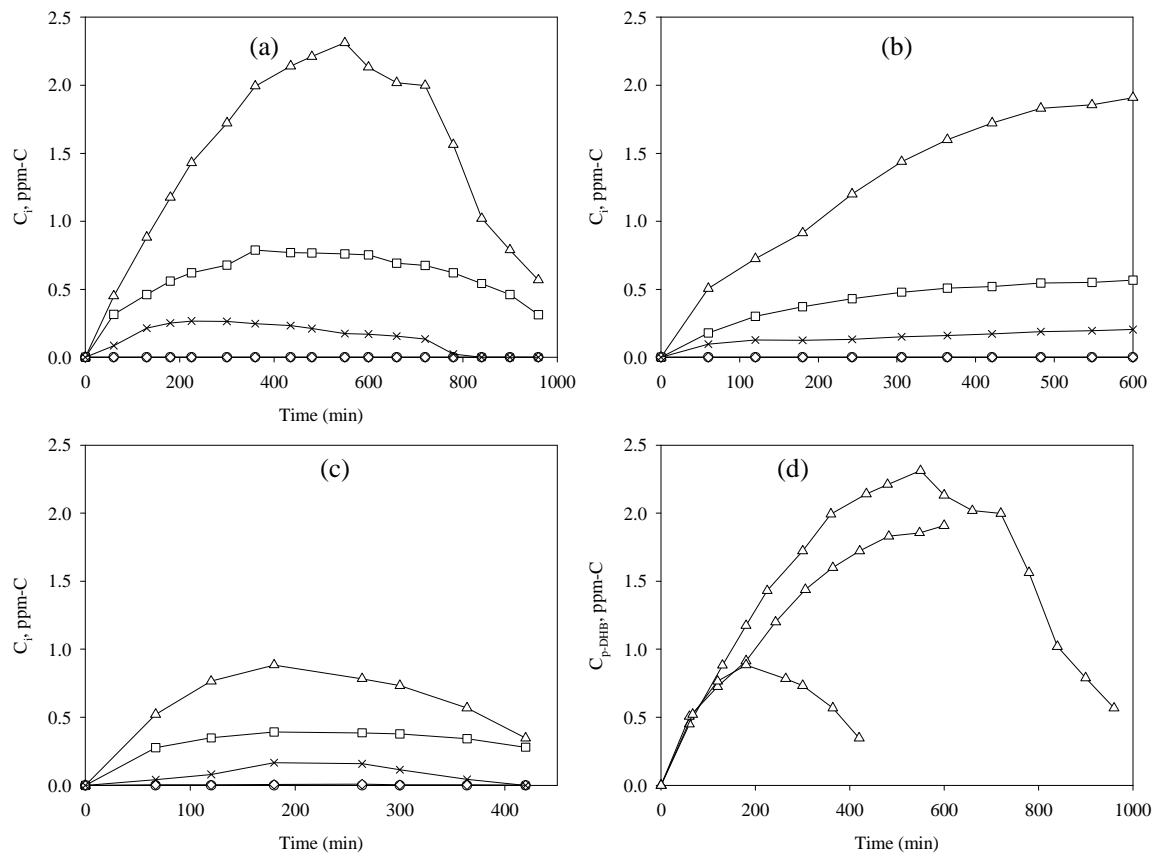
Figure 43 Concentration profiles of phenol photoconversion intermediate species at several initial concentrations on Hombikat UV-100: (Δ) hydroquinone, ($\square$) benzoquinone, ($\Diamond$) acetic acid, and ($\times$) formic acid. (a) 30 ppmC, (b) 20 ppmC, (c) 10 ppmC, and (d) comparison of hydroquinone profiles

Figure 44 Concentration profiles for ($\triangledown$) experimental TOC and ($\bullet$) species mass addition of the quantified intermediates for phenol photoconversion using Hombikat UV-100

6.2.4   Sol-Gel Cat

Figure 45 reports the photo degradation of phenol at different initial concentrations using Sol-Gel Cat. Figure 46 shows the various compounds produced during the photoreaction as follows: a) hydroquinone is again the major intermediate, b) catechol and benzoquinone are detected in lower concentrations however, c) acetic and formic acids are the carboxylic acids present.
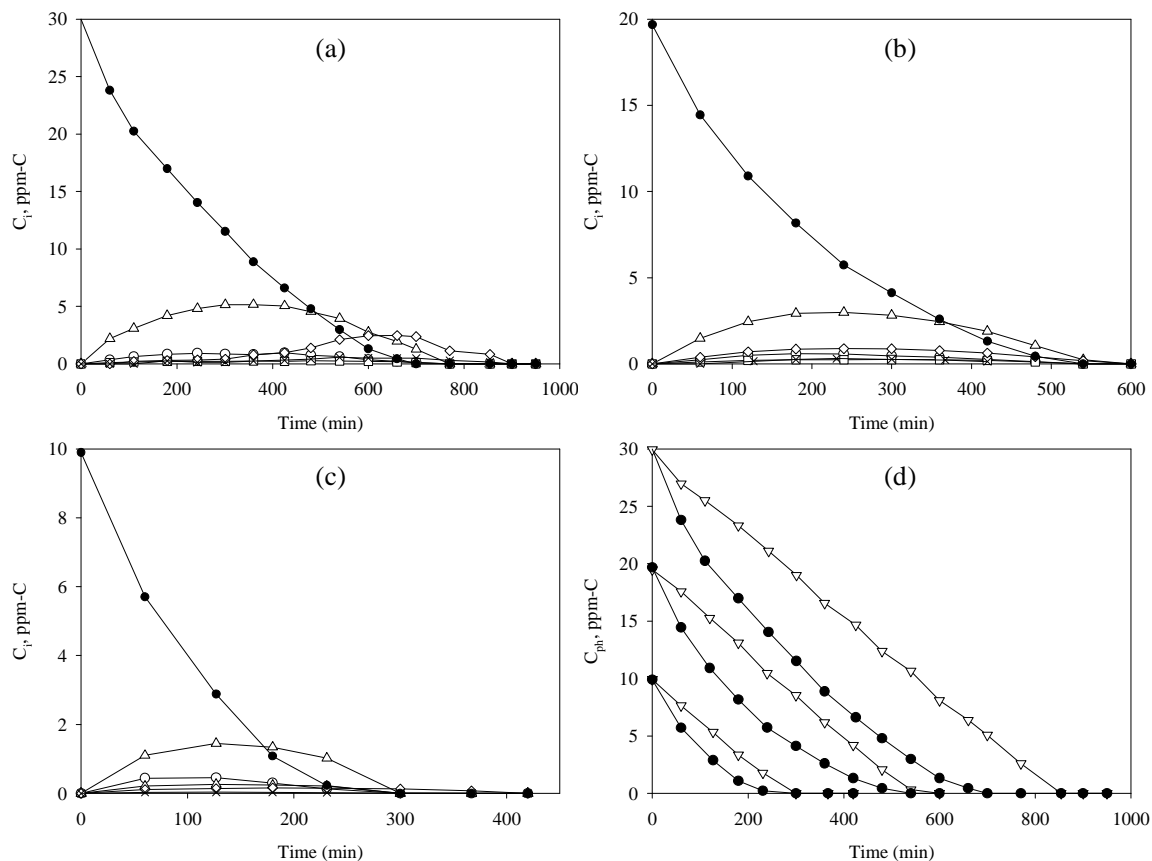
Figure 45 Concentration profiles during phenol photodegradation using Sol-Gel Cat. (●) phenol, (∇) TOC, ($\triangle$) hydroquinone, (○) catechol, (□) benzoquinone, (◊) acetic acid and (×) formic acid. (a) 30 ppmC, (b) 20 ppmC, (c) 10 ppm-C, and (d) comparison of TOC and phenol profiles

Comparison between TOC and the addition of the intermediate species masses, as detected with HPLC, is reported in Figure 47. It can be noticed that data agrees well during the first irradiation period, indicating that most of the species formed were quantified. Nevertheless; following the initial irradiation period, the curved reporting mass addition remains consistently below the TOC. This difference could be assigned to the following: (a) intermediate species neither detected nor quantified by HPLC or GC/MS and (b) adsorption of detected and undetected intermediates. The later of these two possibilities seems an unlikely one, given phenol and intermediate do not adsorb strongly on TiO_2.
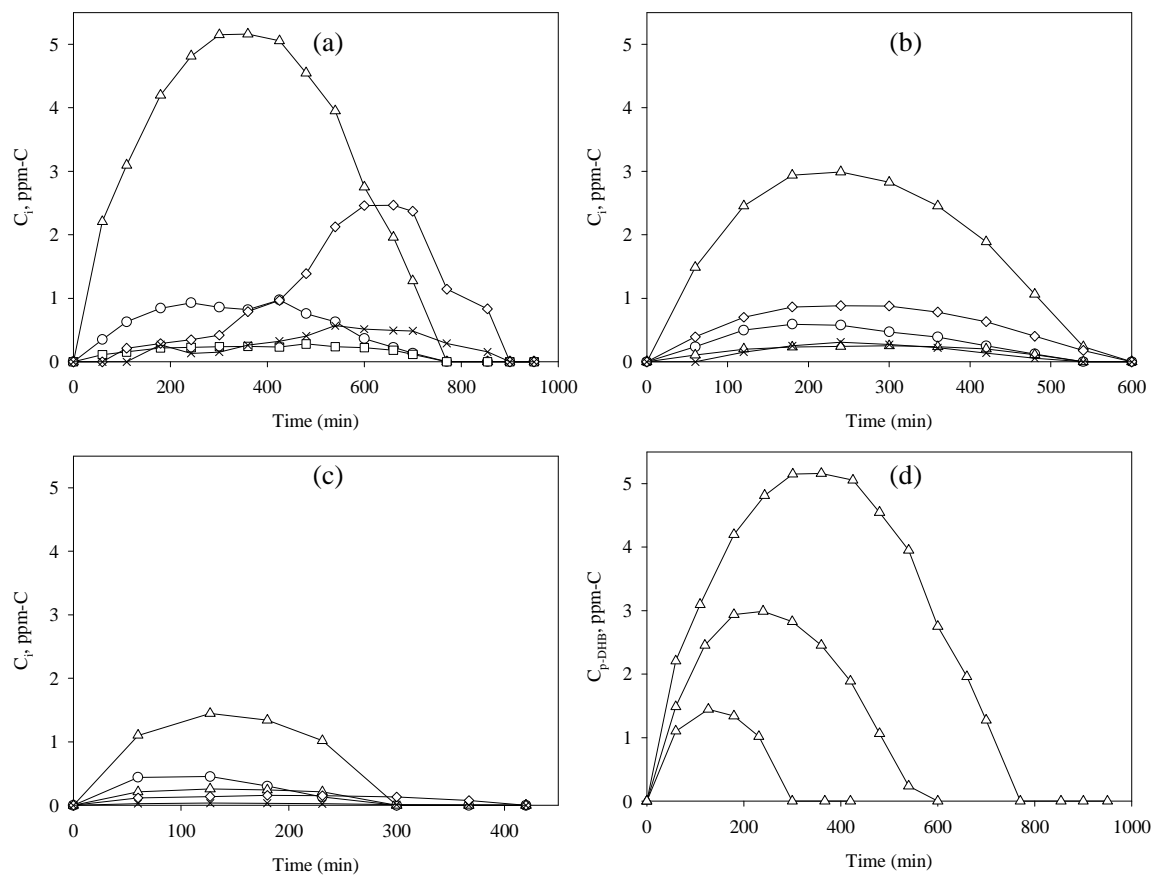
Figure 46 Concentration profiles of phenol photoconversion intermediate species at several initial concentrations on Sol-Gel Cat: (Δ) hydroquinone, (○) catechol, (□) benzoquinone, (◊) acetic acid, and (×) formic acid. (a) 30 ppmC, (b) 20 ppmC, (c) 10 ppmC, and (d) comparison of hydroquinone profiles
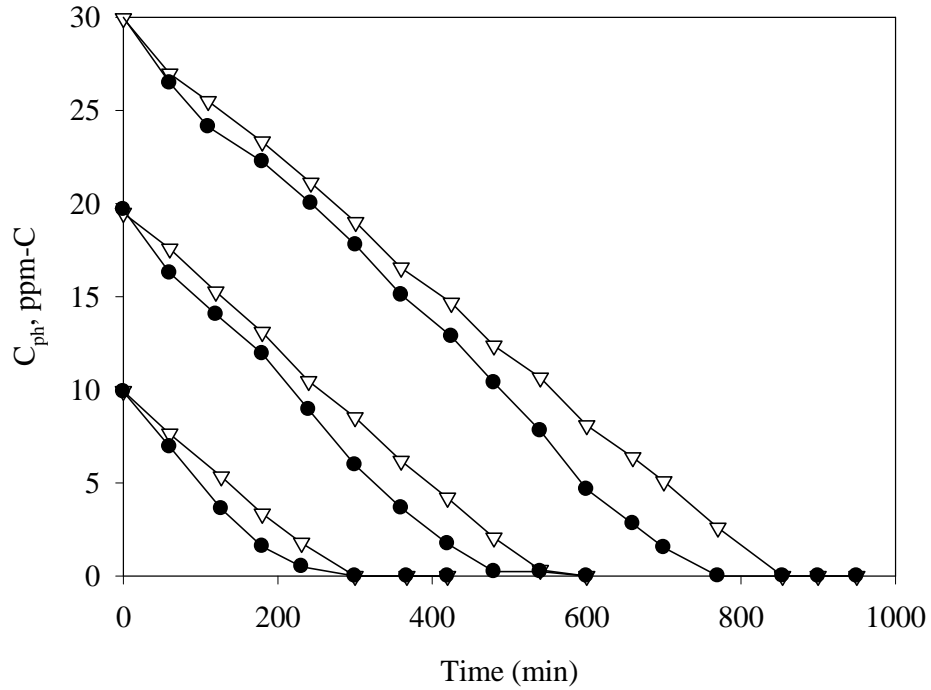
Figure 47 Concentration profiles for ($\triangledown$) experimental TOC and ($\bullet$) species mass addition of the quantified intermediates for phenol photoconversion on Sol-Gel Cat

In summary, four TiO_2 samples were studied experimentally. All experiments were performed at the same experimental conditions and at the same catalyst concentration of 0.15 g l^{-1}. The photodegradation of phenol over the different TiO_2 catalysts is reported in Figure 48. Phenol profiles for these same experimental results are presented in Figure 49. The fastest phenol degradation was achieved by Anatase. However, phenol mineralization did not show complete degradation of the organic intermediate compounds generated during the photoreaction. Measurements of TOC were essential in determining the complete removal or organic contaminants in water. As it can be observed in the two figures mentioned above, the fastest TOC depletion was achieved using Sol-Gel Cat. DP 25 also showed a significant photocatalytic activity, with Anatase being the catalyst with lower activity for total mineralization.
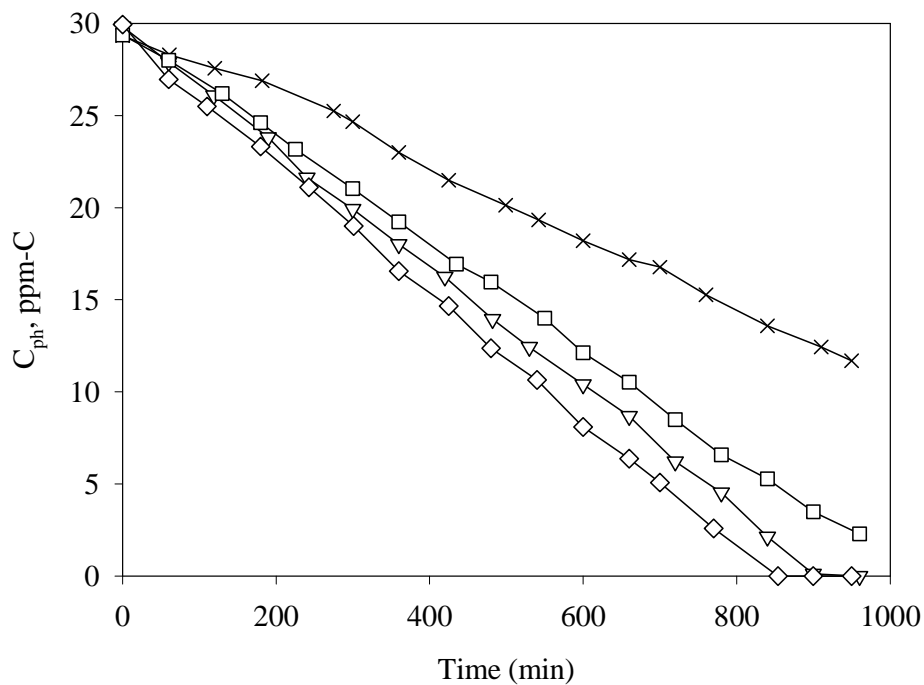
Figure 48 TOC profiles for phenol photodegradation over several TiO$_2$ samples: ($\triangledown$)DP 25, ($\times$) Anatase, ($\square$) Hombikat UV-100, ($\lozenge$) Sol-Gel Cat
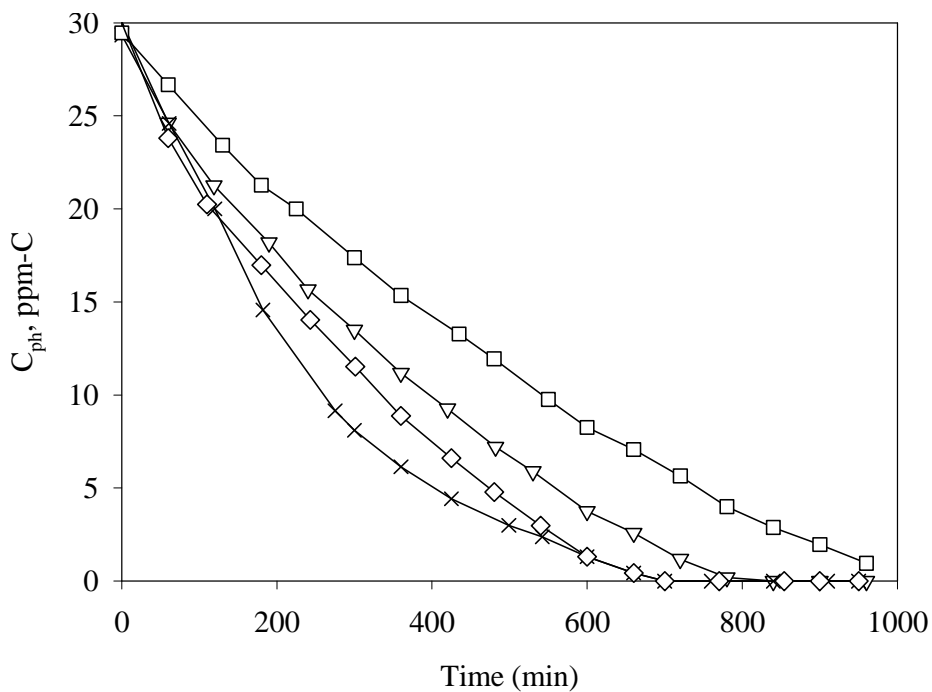
Figure 49 Phenol photoconversion profiles over several TiO$_2$ samples: ($\triangledown$) DP 25, ($\times$) Anatase, ($\square$) Hombikat UV-100, ($\lozenge$) Sol-Gel Cat

Following this first set of experiments, the two catalysts displaying the best photocatalytic properties (DP 25 and Sol-Gel Cat) were selected for further research regarding the influence of iron ions the photocatalytic activity.

6.3   Effect of Fe^{3+} Ions on Phenol Photocatalysis

This section reports the effect of Fe ions on the rate of photocatalytic oxidation and mineralization of phenol and its reaction intermediates. Ortiz-Gomez 2006 studied the influence of Fe ions in solution. $FeSO_4x7H_2O$ was utilized as an iron ions source at an observed optimum 5ppm Fe^{3+} ion concentration. This author concluded that Fe cations have a strong influence on the phenol photocatalytic reactions. High ions concentrations lead to a decrease in the mineralization rates, while low contents promoted a significant increase. It was found that 5 ppm of Fe^{3+} rendered the highest phenol oxidation rate. Ortiz-Gomez 2006 also demonstrated that ferric ions Fe^{3+} and ferrous ions Fe^{2+} promoted the same enhancement in the photodegradation. It was postulated that the increase in the photoactivity on the TiO_2 catalyst was due to a facilitated electron transfer to the electron scavengers. This process occurs through a continuous oxidation-reduction cycle of the Fe cations adsorbed onto the catalyst surface.

In Figure 50, the effect of 5 ppm of ferric ions is demonstrated for the oxidation of phenol at several initial concentrations on DP 25. Figure 51 reports the effect of Fe ions in the total phenol mineralization. It can be observed that the addition of 5 ppm of Fe^{3+} to the reaction solution promotes a higher photodegradation rate that when DP 25 is used alone at a pH of 3.7.

It can also be noticed that the effect of Fe ions lasted throughout the reaction and its effect does not fade away with time. The intermediate species produced during phenol degradation on DP 25 with 5 ppm of Fe^{3+} are reported in Figure 52. When compared with DP 25 alone, the presence of iron ions yielded larger concentration of hydroquinone. Catechol and acetic acid were also formed in higher concentrations and this when compared with the profiles found with DP 25 alone.
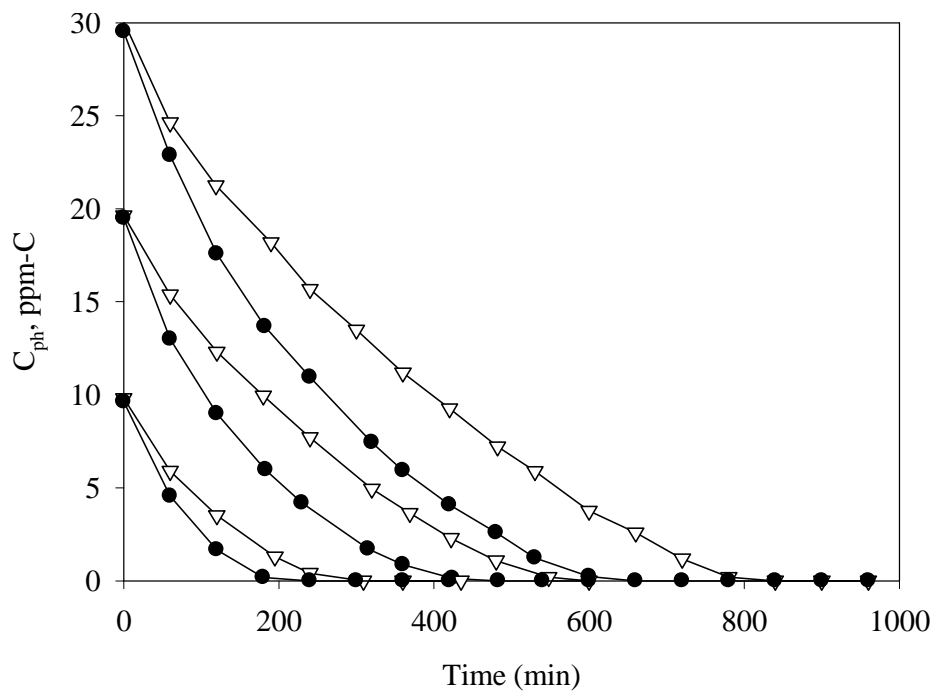
Figure 50 Influence of 5 ppm of ferric ions on the rate of photooxidation of phenol at different initial concentrations. ($\triangledown$) DP P25 (•) DP 25 and 5 ppm Fe^{3+} in solution
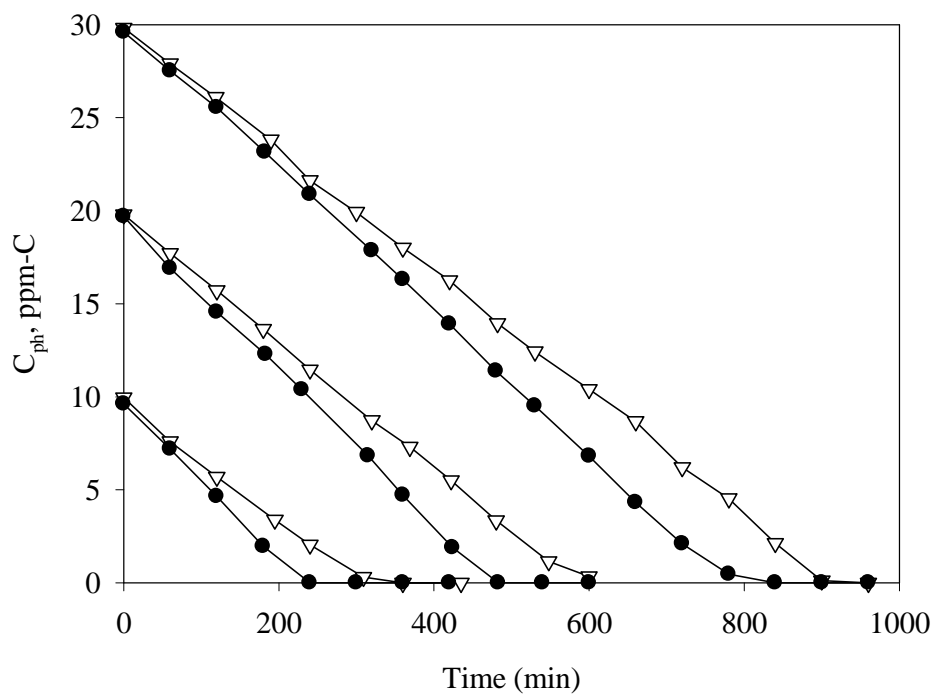
Figure 51 Influence of 5 ppm of ions on the total mineralization of phenol at different initial concentrations. ($\triangledown$) DP 25 (•) DP 25 and 5 ppm Fe^{3+} in solution

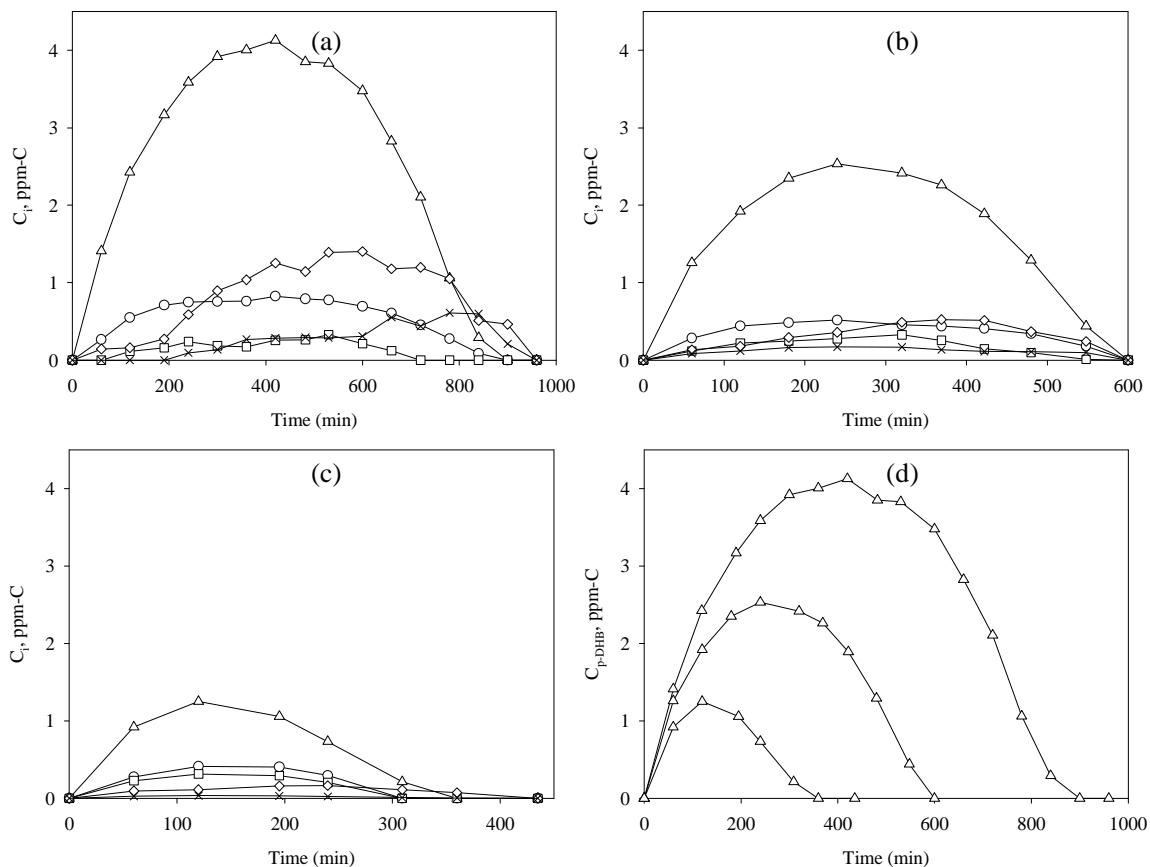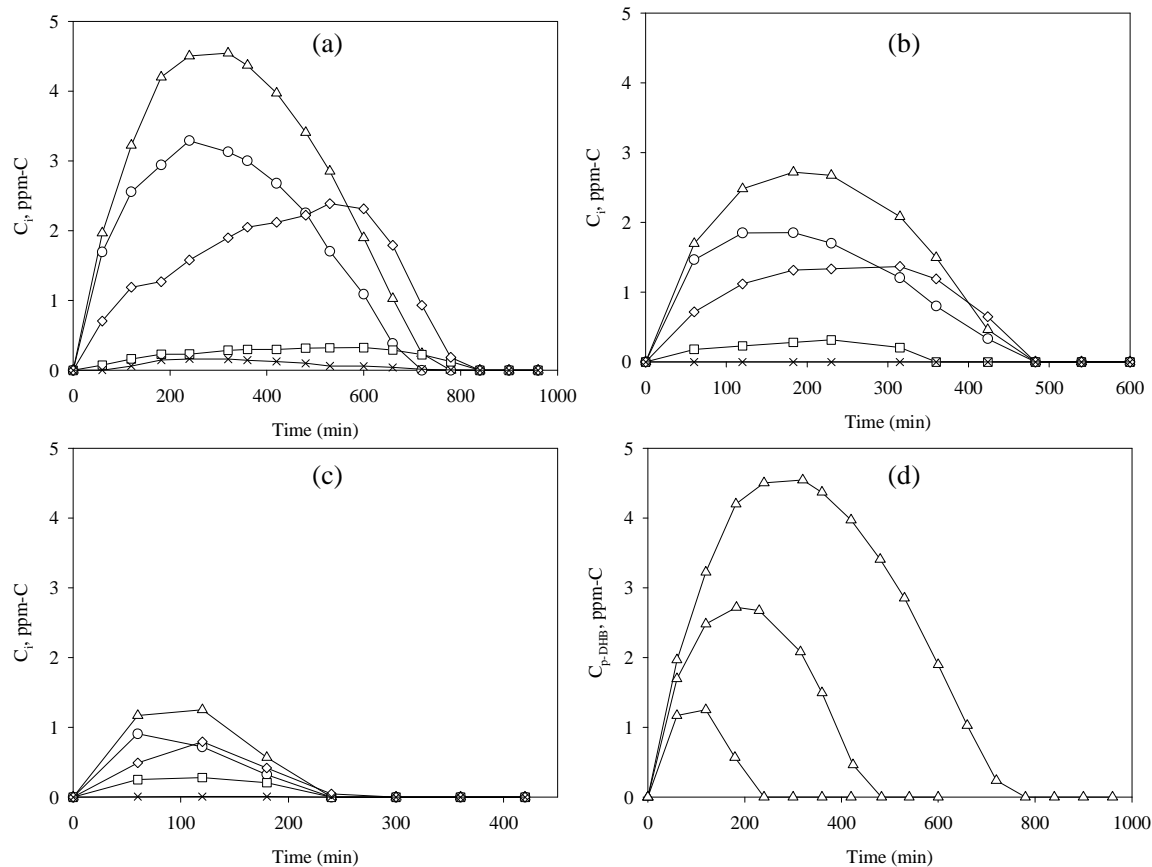**Figure 52** Concentration profiles of phenol photoconversion intermediate species at several initial concentrations on DP 25+5 ppm Fe^{3+} in solution: (Δ) hydroquinone, ($\circ$) catechol, ($\square$) benzoquinone, ($\Diamond$) acetic acid, and ($\times$) formic acid. (a) 30 ppmC, (b) 20 ppmC, (c) 10 ppmC, and (d) comparison of hydroquinone profiles

It is then concluded, that Fe^{3+} species both accelerates the phenol photoconversion and formation-consumption of reaction intermediates with an overall increased degradation rates. This also leads to a faster TOC decay. Furthermore, the influence of iron ions on Sol-Gel Cat photocatalytic conversion performance was also investigated. The observed effects are essentially the same as those observed when DP 25 was employed.

Comparison of phenol and TOC profiles for DP 25 and Sol-Gel Cat, and the influence of Fe^{3+} ions, is reported in Figure 53a and b. It is observed that the catalyst with the lower degradation time was Sol-Gel Cat. This suggests that the iron ions influence on the photocatalytic degradation is not a selective process and its enhancement does not necessarily depend on the TiO_2 material.
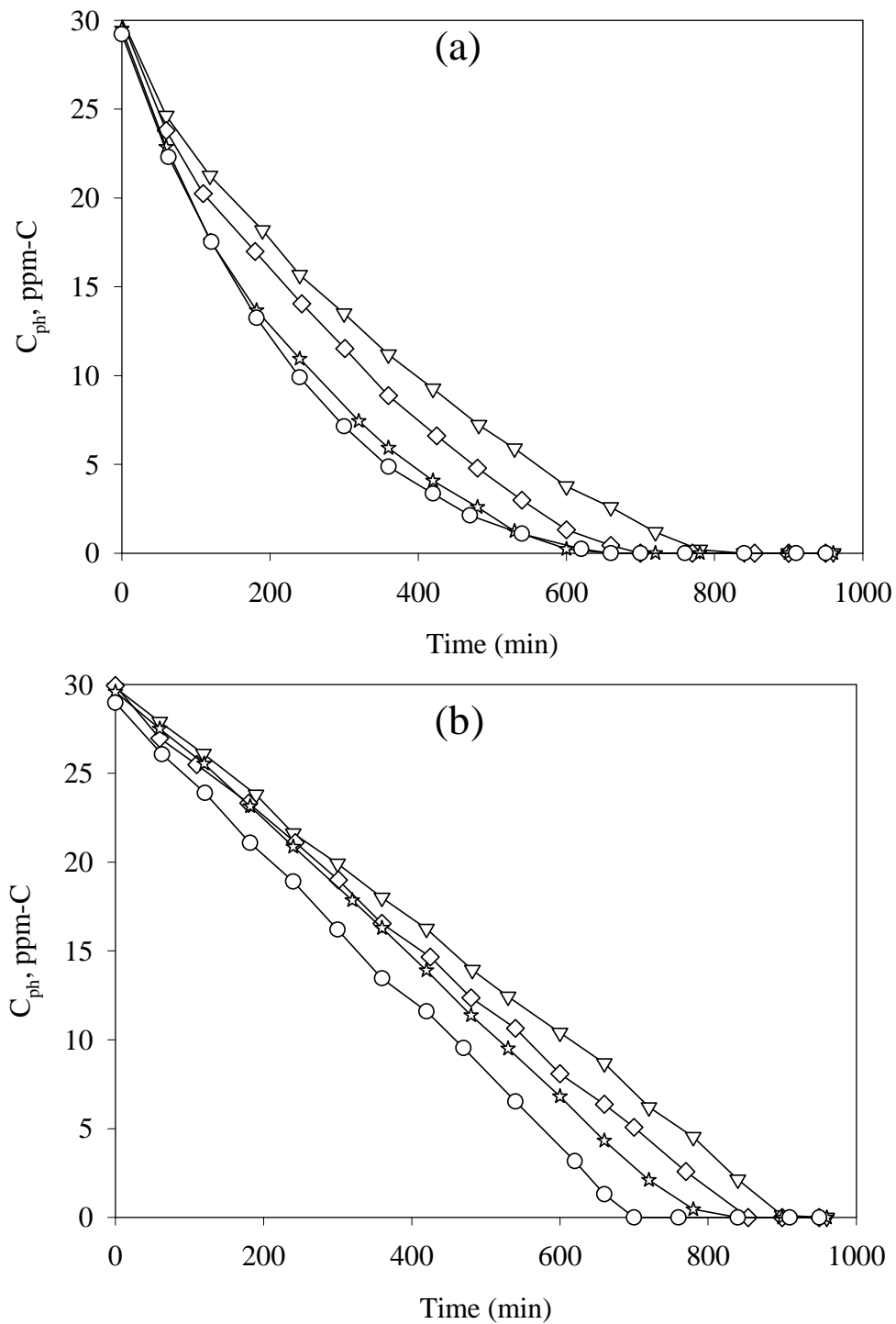
Figure 53 Influence of iron ions on the photocatalytic degradation of phenol (a) phenol and
(b) TOC profiles for ($\triangledown$) DP 25, ($\star$) DP 25+Fe^{3+} in solution, ($\lozenge$) Sol-Gel Cat, and ($\circ$) Sol-
Gel Cat+Fe^{3+} in solution

Ortiz-Gomez 2006 found that Fe^{3+} and Fe^{2+} had a similar influence on the photocatalyst activity. This author also concluded that when ferric ions were used, they were rapidly reduced to ferrous ions once the reaction was initiated. Iron ions were adsorbed onto the catalyst surface with an improvement on photocatalyst activity. Thus; iron ion induced phenol photodegradation appears to be a surface induced phenomenon, where electron transfer from the catalyst conduction band to the electron acceptors, is enhanced. Such reaction mechanism is schematically represented in Figure 54.

The first step is the adsorption of Fe ions onto the TiO_2 surface. When the catalyst is activated with UV light, the adsorbed Fe^{3+} ions are reduced to Fe^{2+} with the photogenerated electron (e^-_{cb}). The second step is the scavenging of the electron from Fe^{2+} by an electron acceptor (e.g. O_2), and re-oxidize it to Fe^{3+}. This mechanism applies when iron is fed as Fe^{2+}. This reduction-oxidation cycle continues throughout the reaction.
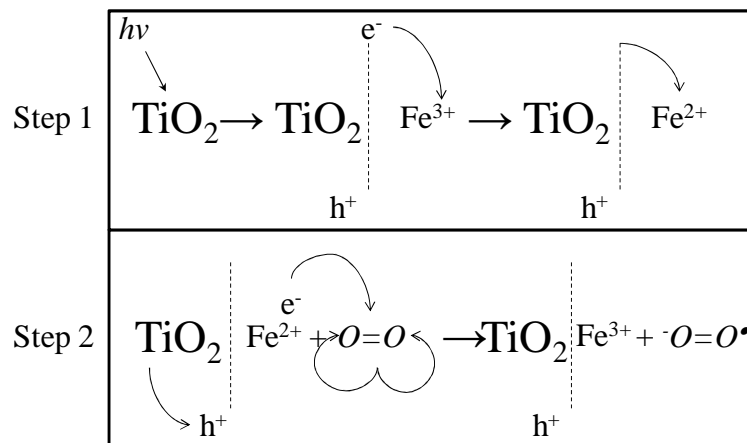
Figure 54 Reduction-oxidation cycle of iron ions on TiO_2 surface. Adapted from Ortiz-Gomez (2006)

While similar results could in principle be obtained by doping the TiO_2 catalysts, the use of iron ions in solution does not require pre-impregnation. Pre-impregnation is a lengthy procedure that may include a long period of drying and calcinations at high temperatures. Arana et al., (2003), for instance, prepared a catalyst containing 0.5% wt of Fe. This Fe-TiO_2 showed an improvement in the oxidation of carboxylic acids. However, the preparation

method described a lengthy procedure that included a 48 hr period of mixing a solution containing Fe ions and TiO_2 catalyst. After these mixings, the catalyst was dried at 393 K for 24 hours and finally calcined at 773 K.

Being acquainted with the previous work developed by Ortiz-Gomez 2006, the objective of the experiments with iron ions in solution in this PhD research were addressed to study the following: a) the Fe ion influence on the photocatalytic activity for different TiO_2 , b) a kinetic model that can be applied to a wide range of TiO_2 materials, c) the calculation of photonic efficiencies.

From the results presented in this chapter, it can be observed that in all cases, three major aromatic intermediates were detected and quantified once the photoreaction was initiated as follows: hydroquinone, catechol and benzoquinone. Hombikat UV-100; however, did not produce catechol, and only negligible amounts of benzoquinone were identified. For most photocatalysts employed, two carboxylic acids were detected; formic and acetic acids. Hombikat UV-100 did not produce acetic acid and Anatase did not form formic acid.

The photocatalysts studied exhibited a rapid reduction of TOC even at the early stages of the reaction. This phenomenon was noticed when Fe ions were used. Thus, there is a quick total mineralization of phenol to CO_2 and water. Therefore at this stage, phenol photoconversion proceeds very rapidly, with phenol forming oxygenated aromatic species and aromatic species, being converted into carboxylic acids, and CO_2. On the other hand, there is also an opportunity for the aromatic intermediates to be oxidized into carboxylic acids and CO_2. Finally, carboxylic acids generated from the oxidation of all aromatics, can be converted into CO_2.

Considering all the above described facts, it can be concluded that the oxidation of phenol can be represented with a "series-parallel" reaction scheme. All these steps are summarized in Figure 55. These results coincide with previous results (Ortiz-Gomez, 2006; Salaices, 2002).
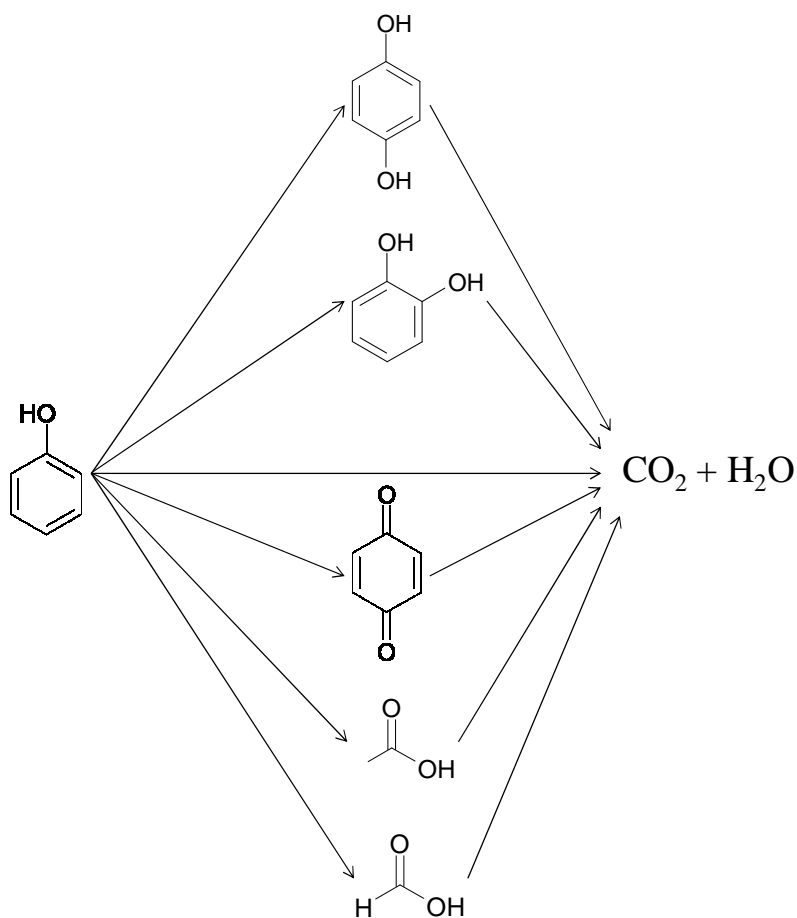
Figure 55 Series-Parallel RN for the photodegradation of phenol involving measurable chemical species

It has to be emphasized that the above reaction scheme applies for all the catalysts studied, and also for the catalyst where iron ions in solution were used. For Hombikat UV-100; however, the step involving the production of catechol and acetic acid from phenol, is not included given these species are not detected experimentally. Similarly, and for the same reasons in the case of Anatase, the formic acid formation steps from phenol are also not considered.

6.4 Oxidation of the Major Intermediates: Hydroquinone, Catechol and, Benzoquinone

Oxidation experiments were performed using the reaction intermediates species observed during the photodegradation of phenol and using the different photocatalysts. These experiments will help decoupling the phenol photoconversion kinetic modeling allowing to

define independently the kinetic parameters for the photoconversion of intermediates, reducing as a result, the number of kinetic parameters involved.

When hydroquinone was employed as a model compound, benzoquinone was produced in all cases, at very low concentrations. Figure 56a reports the concentration profiles for benzoquinone intermediates, while using DP 25. It is shown that catechol was not produced while acetic and formic acids were formed in very low concentrations. This behavior was observed both for various photocatalysts and for iron ions present in solution. Moreover, one can notice in Figure 56b that TOC profile presents a significant reduction during the early stages of photoconversion. Therefore, it is concluded that hydroquinone is simultaneously oxidized to benzoquinone and carboxylic acids, and completely mineralized to CO_2.
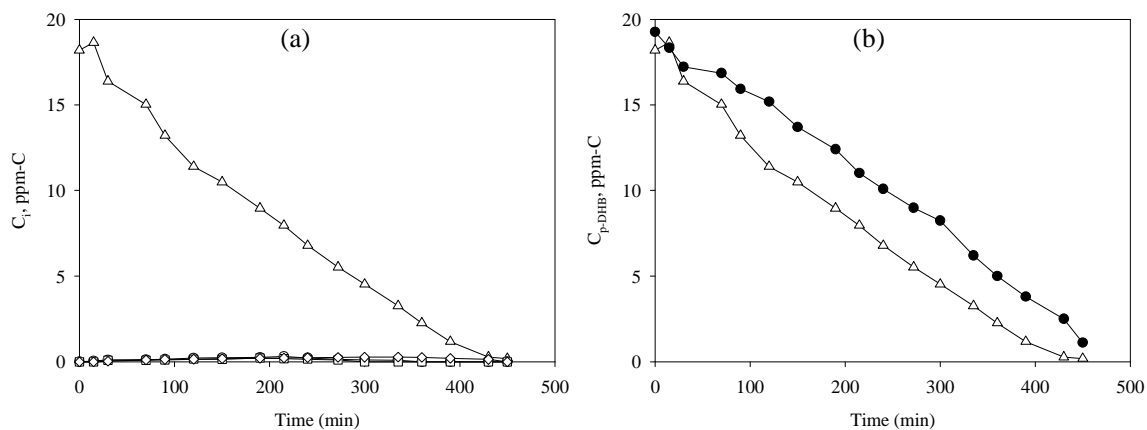
Figure 56 Concentration profiles of hydroquinone photoconversion and its intermediates on DP 25. ($\triangle$) hydroquinone, ($\circ$) benzoquinone, ($\square$) acetic acid and, ($\lozenge$) formic acid ($\bullet$) TOC

Figure 57 reports catechol concentration profiles for 20 ppm of C in catechol using DP 25. It can be observed that hydroquinone is the main aromatic intermediate produced with acetic and formic acids also being formed during catechol photodegradation. Benzoquinone was not found as an intermediate. Hence, one can conclude that catechol is oxidized to hydroquinone and carboxylic acids, and at the same time, it is completely mineralized to CO_2.
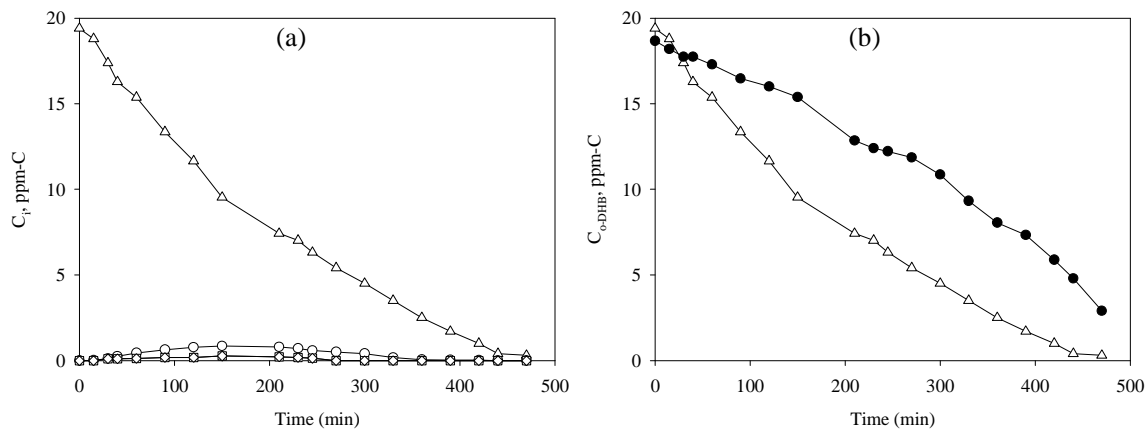
Figure 57 Concentration profiles of catechol photoconversion and its intermediates on DP 25. ($\triangle$) catechol, ($\circ$) hydroquinone, ($\square$) acetic acid and, ($\lozenge$) formic acid ($\bullet$) TOC

Benzoquinone was also used as a model compound under irradiation and in the presence of TiO_2. Figure 58 reports the concentration profiles of benzoquinone and the intermediates produced during the photoreaction on DP 25. One can observe in this figure, that the concentration of benzoquinone decreases rapidly within the first few minutes of reaction time. Similarly, the concentration of hydroquinone increases during the same period, in about the same order of magnitude that benzoquinone is reduced. These results suggest a fast reduction of benzoquinone to hydroquinone. This also can explain the fact that for most of the degradation experiments, benzoquinone is found at very small concentrations, while hydroquinone is always the intermediate compound present at higher concentrations. Again, acetic and formic acids were detected in small concentrations.

From the results presented above, one can hypothesize that during the photocatalytic degradation of benzoquinone, hydroquinone is produced as the major intermediate compound. There is also a decrease of the TOC profiles during the initial irradiation, indicating complete mineralization of benzoquinone and hydroquinone to CO_2, even at these early photoconversion stages.
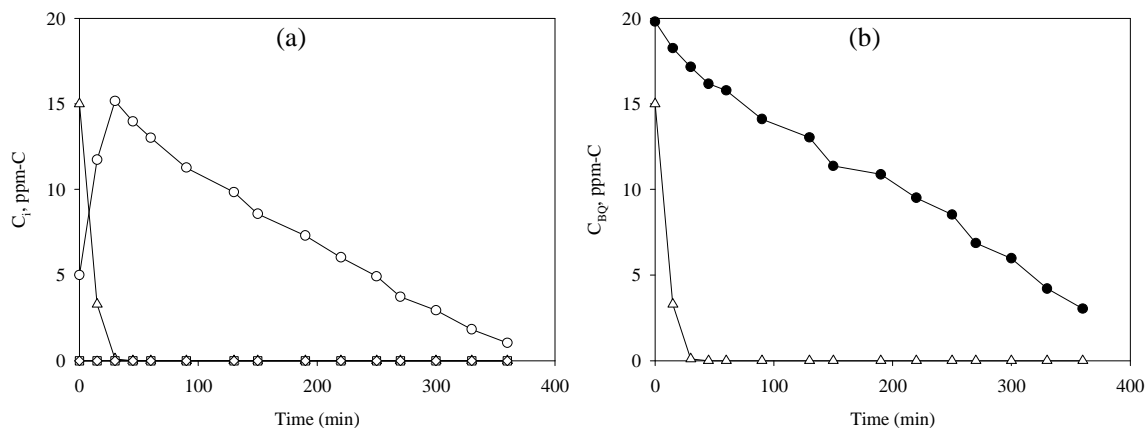
Figure 58 Concentration profiles of photoconversion of benzoquinone and its intermediates on DP 25. ($\triangle$) benzoquinone, ($\circ$) hydroquinone, ($\square$) acetic acid and, ($\lozenge$) formic acid ($\bullet$) TOC

From the experimental results presented in this section a "series-parallel" reaction scheme can also be proposed for hydroquinone, catechol and benzoquinone. Figure 59 summarizes the experimental findings for the photodegradation of the main aromatic intermediate compounds of phenol. In all cases, direct production of CO_2 from the model compound is observed.

Given that hydroquinone, catechol and benzoquinone are intermediates species in the photocatalytic oxidation of phenol, an overall reaction scheme for the photodegradation of phenol can be postulated. This overall reaction scheme has to account for all the detected intermediates.

When proposing an overall reaction scheme for phenol degradation based on the decoupling of the determination of kinetic parameters, it is hypothesized that all the intermediate species behave the same as a model pollutant or as an intermediate. For instance, benzoquinone is an intermediate in the oxidation of phenol for all the catalysts used. Moreover; when benzoquinone is used as a model compound, this forms hydroquinone as the major intermediate compound. It is assumed; then, that benzoquinone is produced from phenol, but at the same time, it produces hydroquinone.
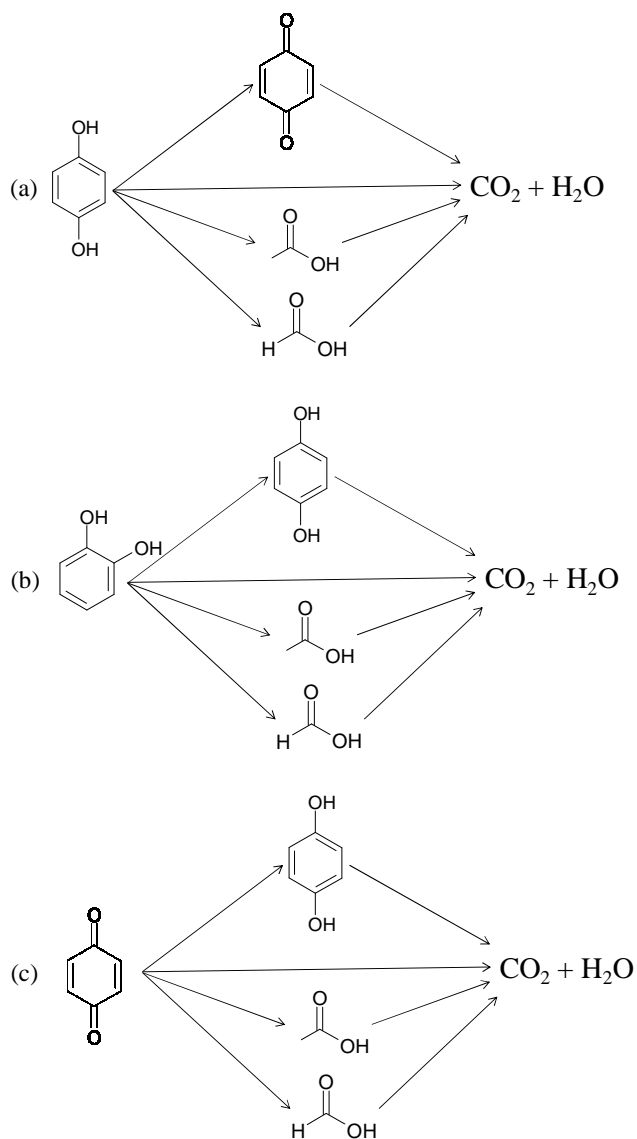
Figure 59 Serial-Parallel RN for the photocatalytic oxidation of (a) hydroquinone, (b) catechol and, (c) benzoquinone

The overall reaction network for the oxidation of phenol on the different TiO_2 catalysts is presented in Figure 60. This reaction scheme consequently applies to all the catalysts used in this study. The dashed arrow represents the step that should not be included for Hombikat UV-100 because catechol is not produced and/or detected when this catalyst was employed. Furthermore, the step showing the benzoquinone from phenol could also be neglected during the kinetic analysis, given that benzoquinone was produced in only very small concentrations only.

A similar general reaction scheme for phenol degradation was presented in previous studies (Ortiz-Gomez, 2006 and Salaices-Arredondo 2002). The main difference between this reaction scheme and the one presented by Ortiz-Gomez (2006) is, that in our study, only those species actually detected and quantified are considered in the reaction network. Ortiz-Gomez (2006) presented all those intermediates that could eventually be formed during phenol photoreaction, even if they were not detected experimentally. By doing so, there is an increased risk of kinetic model over parametrization, without significant gain in the calculation both in the observed chemical species and the related energy efficiencies.
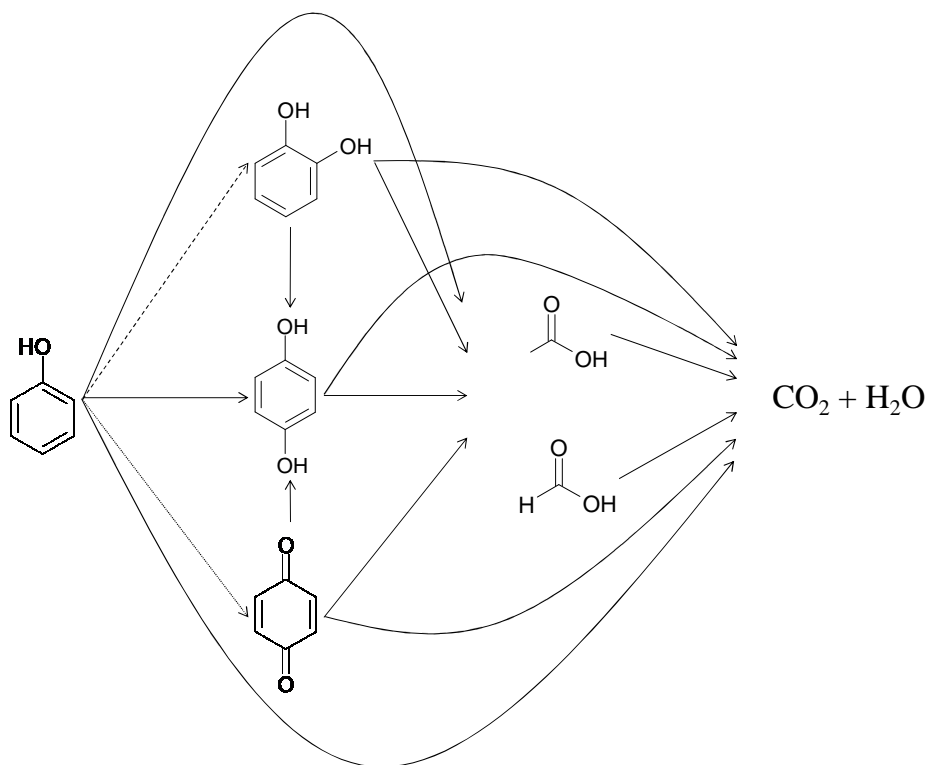
Figure 60 Detailed Series-Parallel RN for the photodegradation of phenol on TiO_2 catalyst

As a result, the proposed reaction mechanism of this PhD Dissertation includes the following:

(a) A single "series-parallel" reaction mechanism that can be applied for the photodegradation of phenol regardless of the catalysts employed. Those species not identified/quantified are not to be included in the reaction scheme.

(b) All the catalysts employed in this study produce the same reaction intermediate species. Hombikat UV-100; however, does not produce catechol as the other photocatalyst tested do.

(c) Acetic and formic acids were the only two carboxylic acids quantified during phenol photoreaction. While it is believed that more carboxylic acids are formed during the photodecomposition, inclusion of these other chemical species will require further study on the intermediate species quantification.

(d) Both, benzoquinone and catechol produce hydroquinone as their major intermediate species. This could explain that hydroquinone was produced in higher amounts during the photocatalytic reactions, in all the catalysts studied. It was also observed that benzoquinone rapidly oxidized to produce high amounts of hydroquinone.

The detailed "Series-Parallel" reaction network presented in Figure 60 was developed by considering the individual photocatalytic conversions of phenol, hydroquinone, catechol and benzoquinone as model pollutants, and their corresponding intermediates species. This overall reaction network incorporates consistently all experimental reaction steps that were proven relevant for the various aromatic pollutants considered in this study.

This overall reaction network was developed under the assumption that all organic contaminants follow the same behaviour when they are intermediate or model compounds. For instance, phenol produces benzoquinone as intermediate compound and when benzoquinone is used as model compound, it produces hydroquinone. Therefore, it is assumed that when benzoquinone is an intermediate, it will produce hydroquinone. This means that regardless of a compound being an intermediate or a model compound, it is expected to produce the same intermediates, assuming all reaction conditions are kept the same.

Based on the above-mentioned observations, Figure 60 is very likely to describe the photoconversion of phenol and its intermediate species.

6.5 Adsorption Isotherms of Phenol and its Intermediates on the Different TiO_2 Catalysts

According to the data reported in the previous sections of this chapter, for most photocatalyst, phenol photodegradation produced hydroquinone, catechol and acetic acid as the major intermediates.

On this basis, in the upcoming Chapter 7 of this thesis, a kinetic model will be developed and established in order to find kinetic parameters for phenol photodegradation. In this kinetic model, the adsorption constants of the different chemical species participating in phenol degradation will be included. Therefore, experimental measurements of the adsorption constants of phenol, hydroquinone, catechol and acetic acid on the different TiO_2 photocatalysts, are also reported in this section.

When measuring the equilibrium adsorption of different chemical species, slurry recirculation rate in the reactor in all the experiments was kept at the same value as for the photodegradation experiments. Figure 61 shows the time needed to reach equilibrium of phenol degradation at a concentration of 30 ppm-C in phenol. From this figure, it can be observed that equilibrium is reached at close to 30 minutes. This experimental finding is in agreement with previous results in the literature where adsorption of phenol on TiO_2 was studied (Bekkouche et al., 2004; Ksibi et al., 2003). At lower concentrations; however, one should expect a decrease in adsorption time.

As a result, and when determining the adsorption isotherm for both phenol and its intermediate photoconversion species, a total conservative time of 60 minutes was used. This secured that the slurry conditions considered were a true representative of the equilibrium liquid phase concentrations on TiO_2.

Figure 62 reports the changes of adsorbed amounts of phenol, hydroquinone, catechol and acetic acid as a function of the equilibrium liquid phase concentrations. Thus, this figure describes the characteristic Langmuir chemisorption isotherms for different phenolic and carboxylic acid species on DP 25. This is consistent with the studies of Robert et al. (2000).

The linear form of the Langmuir equation allows calculating both adsorption constants and the maximum amounts adsorbed. Figure 63 reports this linearization for phenol adsorption on TiO$_2$ DP 25.
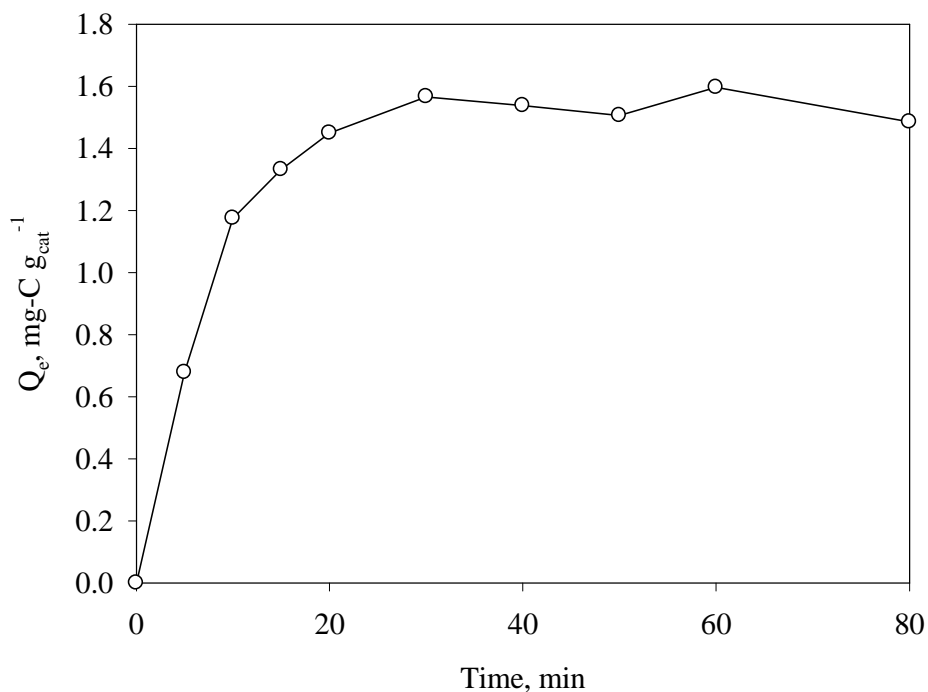
Figure 61 Equilibrium phenol adsorption concentration as a function of time of adsorbed phenol (T = 30 °C and pH = 3.7)

From the results found in Figure 63, K_{ph}^{A} = 0.106 mg-C^{-1} l and Q_{max} = 1.99 mg-C g$_{cat}^{-1}$ values were obtained. Figure 64 shows both Langmuir adsorption predicted values and experimental data.
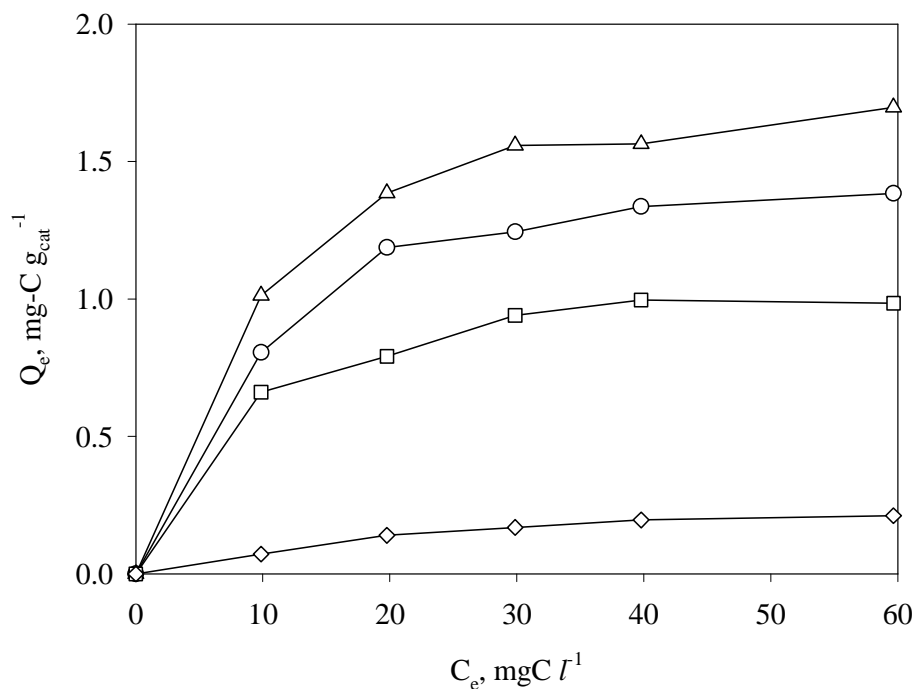
Figure 62 Adsorption isotherm for (Δ) phenol, (○) hydroquinone, (□) catechol and, (◊) acetic acid on TiO_2 DP 25 at 30°C
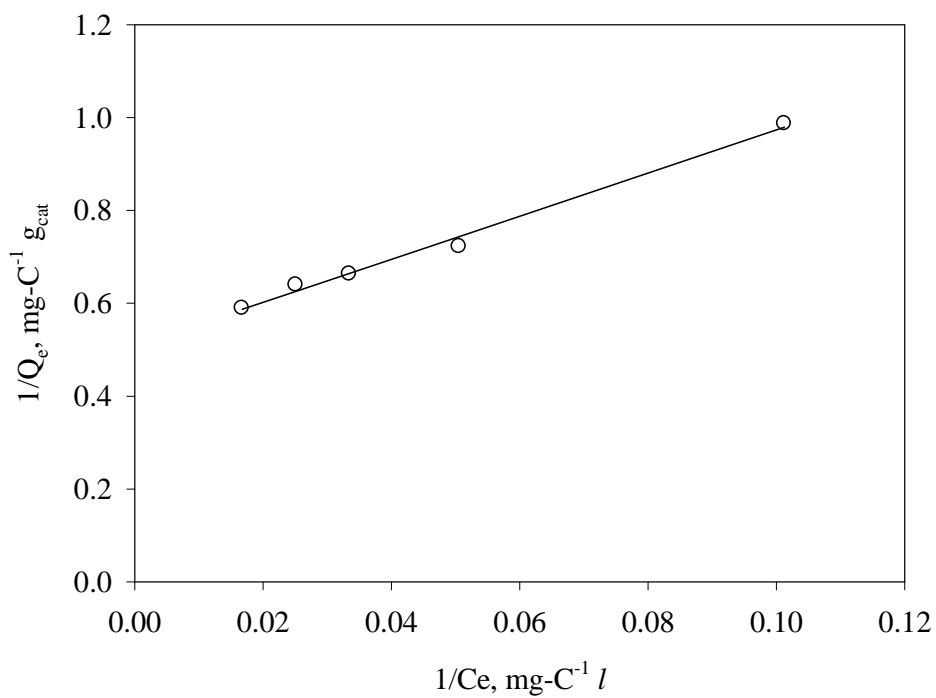
Figure 63 Linear regression for a Langmuir isotherm: adsorption of phenol on TiO_2 DP 25

These results differ from those reported by Bekkouche et al., (2004). These authors found that for phenol, this species adsorbs on TiO_2 DP 25, at approximately Q_{max} =7.10 mg-C (at pH = 3-4). This is considerably higher than the Q_{max} reported in this study. Our result shows that phenol does not have a strong adsorption affinity on DP 25 under the selected photoconversion conditions.

Table 19 reports the adsorption isotherms for the various chemical species studied onto the various TiO_2 catalysts measured experimentally. Adsorption constants for hydroquinone, catechol and acetic acid were not found in the technical literature. Therefore, no comparison could be made for these organic compounds.

From the results presented in the above table, it can be concluded that chemical species adsorption isotherms on the different TiO_2 studied follow the sequence phenol > hydroquinone > catechol > acetic acid. This same trend is applicable for the maximum adsorbed amount per catalyst weight.

It is worth mentioning that when measuring the equilibrium concentrations for acetic acid, several repeats were required and this given the very small quantities involved. It is also observed that the Fe^{3+} ions enhanced the adsorption of all the chemical species on DP 25 and Sol-Gel Cat. This could be assigned that on the catalyst surface, there is a better distribution of charges (Ortiz -Gomez 2006).
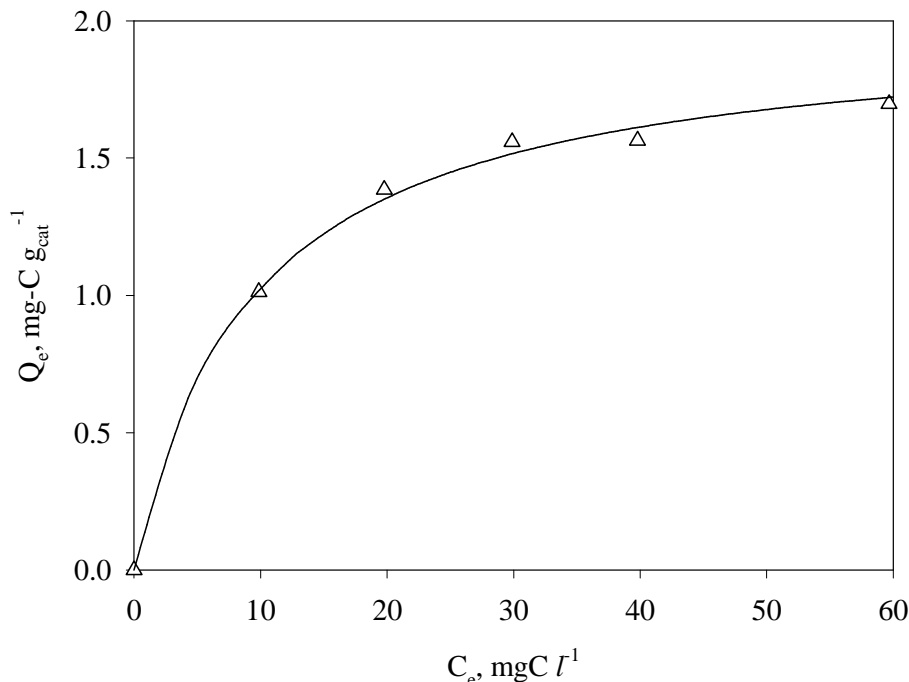
Figure 64 adsorption isotherm of (△) phenol on DP 25 and (——) Langmuir model

Table 19 Adsorption constants and maximal quantities adsorbed for several chemical species on different TiO_2 catalysts

Catalyst	Phenol		Hydroquinone		Catechol		Acetic Acid	
	K^A	Q_{max}	K^A	Q_{max}	K^A	Q_{max}	K^A	Q_{max}
DP 25	0.1097	1.964	0.0947	1.697	0.1389	1.132	0.0209	0.4321
Anatase	0.1768	1.943	0.2134	1.923	0.2342	0.4244	0.1246	0.0747
Hombikat UV-100	0.1532	0.8280	0.1212	0.7720	0.1871	0.1553	0.0785	0.0840
Sol-Gel Cat	0.2088	1.319	0.2121	1.267	0.2168	0.5382	0.0851	0.1650
DP 25+Fe^{3+}	0.1322	2.489	0.1421	2.075	0.1468	0.2147	0.0920	0.0619
Sol-Gel Cat+Fe^{3+}	0.1408	1.749	0.1779	1.794	0.1680	1.290	0.0815	0.0995

K^A is in units of mg-C^{-1} l, Q_{max} in units of mg-C g_{cat}^{-1}

Although the adsorption constants experimentally found in this study will be used in the kinetic modeling, one has to acknowledge that these measurements were done in the dark. Thus, adsorption constants were determined without activation of the photocatalyst by UV light. It was reported that the adsorption constants of organic compounds on the semiconductor surface may be a function of light intensity. Once the TiO_2 is irradiated, its surface may undergo significant changes in electronic properties that may modify adsorption

properties. Xu and Langford (2000) found that K^A measured in the dark is different from the one measured under irradiation. Their results concluded that K^A changes inversely with light intensity. Nonetheless, these authors reported that for radiation intensities above 2.14×10^{-7} einstein s^{-1}, there was no significant change of K^A upon irradiation. In the case of this study, a 15 W lamp was used with a 1.15×10^{-5} einstein s^{-1} emission rate. Thus, it is expected that the reported adsorption constants established under dark conditions for single chemical species, provide a reasonable approximation.

6.6 Conclusions

The Following are the conclusions of this chapter:

(a) Sol-Gel Cat was the photocatalyst that presented the highest phenol photodegradation rates.

(b) Several photocatalyst considered, showed hydroquinone, catechol and/or benzoquinone as mayor aromatic intermediate species. Hombikat UV-100, however, did not form catechol. Most of the catalysts yielded both acetic and formic acids, with acetic acid produced in larger concentrations.

(c) DP 25 and Sol-Gel Cat photoconversion were promoted by Fe^{3+} ions. It appears that this enhancement occurs via an oxidation-reduction cycle of the iron cations adsorbed onto the catalyst surface.

(d) For the various photocatalyst of this study, an overall kinetic reaction scheme, including all the detected species, was proposed. Inter-conversion of intermediates in the reaction scheme was determined experimentally. It was found that benzoquinone rapidly formed hydroquinone within the first few minutes of irradiation. Furthermore, it was found that when catechol was used as a model compound, its major intermediate was hydroquinone.

(e) The different photo catalysts studied showed that phenolic species and carboxylic acid species adsorbed relatively weakly on TiO_2. Slurry samples have to be centrifugated at high speed to get reliable adsorption data. Adsorption isotherms for all chemical species were successfully represented using a Langmuir chemisorption isotherm.

Chapter 7
Results and Discussion Part III: A Unified Kinetic Model for
Phenol Photocatalytic Degradation

7   Introduction

An optimum reactor design is the one that renders a photoreactor with sufficient capacity and minimal dark zones reactor volumes. Availability of a suitable and unified kinetic model will contribute towards the design, the optimization and the process scale up of photoreactor systems.

In this Chapter, a valuable approach for kinetic modeling in photocatalysis is established. This is accomplished via a unified kinetic model which is based on a broadly applicable reaction network (refer to Figure 60). It is highly desirable that this kinetic model should be based on a mechanistic formulation and will be adequate for kinetic modeling using a broad range of TiO_2 based semiconductors.

The approach adopted in this study includes a phenomenological based L-H kinetic, where both reaction and adsorption are accounted for. It is also desirable that this model will be established using rigorous statistical techniques such as cross-correlation coefficients and optimized regressed parameters. This approach may lead to valuable models with acceptable cross-correlation among parameters and narrow parameter spans for the 95% confidence intervals.

The proposed unified model has the structure to be easily adaptable to predict TOC profiles for phenol degradation. This model simplification is consistent with the combination of kinetic model rate equations resulting from the proposed unified model.

7.1   Unified Kinetic Model Using a Langmuir-Hinshelwood Formulation

The reaction rate equations to be reported in this section are based on the reaction network presented in Figure 60 and the L-H reaction rates already described in the literature review.

For the purpose of identifying the kinetic constants involved in the photodegradation process, Figure 65 presents the proposed reaction scheme with the various kinetic constants identified. In this figure, both acetic and formic acids have been lumped into a single pseudo species order to reduce the number of kinetic parameters (Ortiz-Gomez 2006).
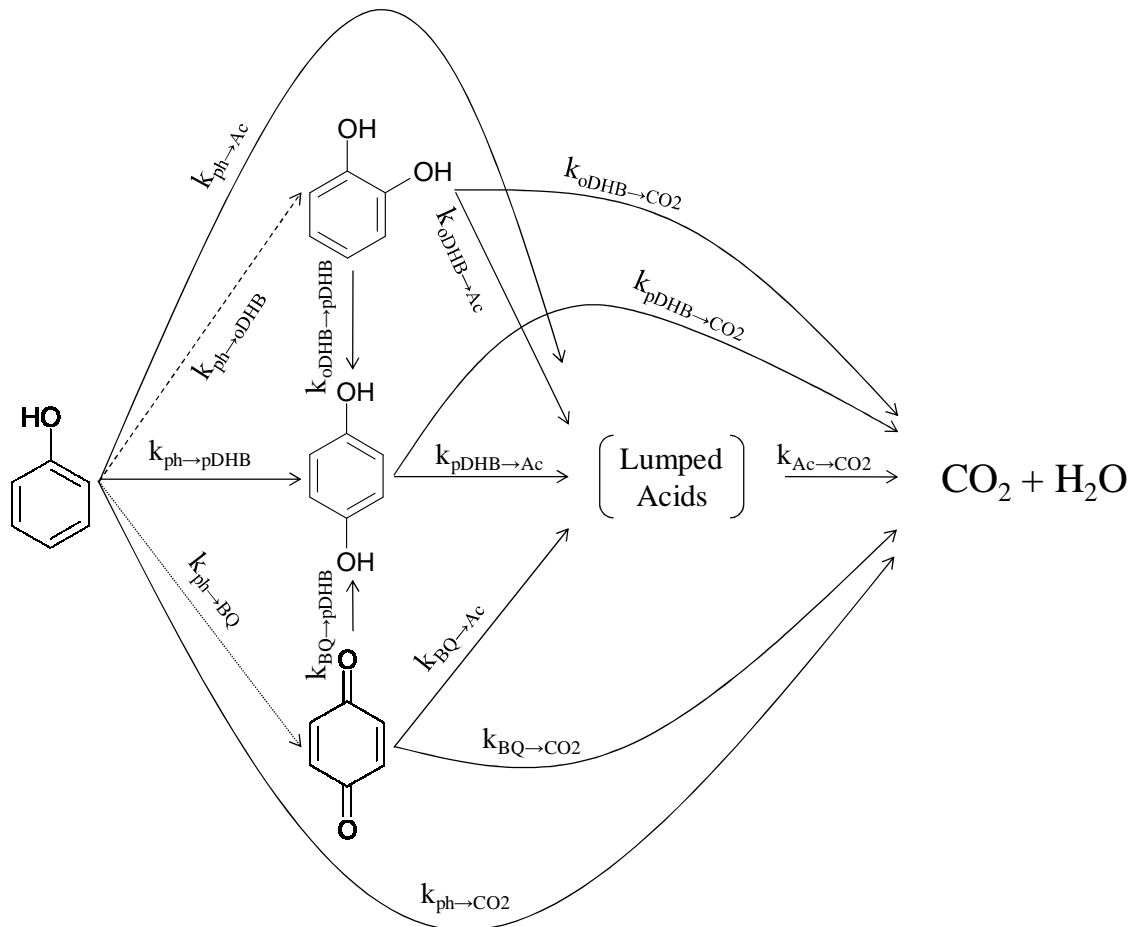
Figure 65 Detailed Series-Parallel RN for the photodegradation of phenol on TiO_2 catalyst

Based on the L-H reaction rate formulation, the rate of reaction for phenol (ph) degradation is given by:

$$\frac{dC_{ph}}{dt} = \frac{-\left(k_{ph-Ac} + k_{ph-oDHB} + k_{ph-pDHB} + k_{ph-BQ} + k_{ph-CO_2}\right)C_{ph}}{\left(1 + K_{ph}^A C_{ph} + K_{oDHB}^A C_{oDHB} + K_{pDHB}^A C_{pDHB} + K_{BQ}^A C_{BQ} + K_{Ac}^A C_{Ac}\right)} \tag{66}$$

where k_{ph-Ac} is a lumped kinetic constant that includes all the kinetic constants for the production of acetic and formic acid from phenol. This kinetic constant is given by:

$$k_{ph-Ac} = k_{ph-acetic} + k_{ph-formic} \tag{67}$$

In the same manner, the term $K^A_{Ac}C_{Ac}$ in the denominator of Eq. (66) involves the adsorption terms for formic and acetic acids as:

$$K^A_{Ac}C_{Ac} = K^A_{acetic}C_{acetic} + K^A_{Acetic}C_{formic} \tag{68}$$

Similar equations can be considered for the other intermediate chemical species. For instance for catechol, denoted as ortho-dihydroxybenzene (oDHB), the rate of reaction is given by:

$$\frac{dC_{oDHB}}{dt} = \frac{k_{ph-oDHB}C_{ph} - (k_{oDHB-Ac} + k_{oDHB-pDHB} + k_{oDHB-CO_2})C_{oDHB}}{(1 + K^A_{ph}C_{ph} + K^A_{oDHB}C_{oDHB} + K^A_{pDHB}C_{pDHB} + K^A_{BQ}C_{BQ} + K^A_{Ac}C_{Ac})} \tag{69}$$

Moreover, the reaction rate equation representing the rate of reaction of hydroquinone or para-dihydroxybenzene (pDHB) can be written as follows:

$$\frac{dC_{pDHB}}{dt} = \frac{k_{ph-pDHB}C_{ph} + k_{oDHB-pDHB}C_{oDHB} + k_{BQ-pDHB}C_{BQ} - (k_{pDHB-Ac} + k_{pDHB-CO_2})C_{pDHB}}{(1 + K^A_{ph}C_{ph} + K^A_{oDHB}C_{oDHB} + K^A_{pDHB}C_{pDHB} + K^A_{BQ}C_{BQ} + K^A_{Ac}C_{Ac})} \tag{70}$$

For benzoquinone (BQ), the reaction rate equation is given by:

$$\frac{dC_{BQ}}{dt} = \frac{k_{ph-BQ}C_{ph} - (k_{BQ-Ac} + k_{BQ-pDHB} + k_{BQ-CO_2})C_{BQ}}{(1 + K^A_{ph}C_{ph} + K^A_{oDHB}C_{oDHB} + K^A_{pDHB}C_{pDHB} + K^A_{BQ}C_{BQ} + K^A_{Ac}C_{Ac})} \tag{71}$$

For carboxylic acids, as they are lumped together into a single chemical pseudo species, the reaction rate equation can be defined as:

$$\frac{dC_{Ac}}{dt} = \frac{k_{ph-Ac}C_{ph} + k_{oDHB-Ac}C_{oDHB} + k_{pDHB-Ac}C_{pDHB} + k_{BQ-Ac}C_{BQ} - k_{Ac-CO2}C_{Ac}}{(1 + K^A_{ph}C_{ph} + K^A_{oDHB}C_{oDHB} + K^A_{pDHB}C_{pDHB} + K^A_{BQ}C_{BQ} + K^A_{Ac}C_{Ac})} \tag{72}$$

Finally, the rate equation for CO_2 formation described as:

$$\frac{dC_{CO_2}}{dt} = \frac{k_{ph-CO2}C_{ph} + k_{oDHB-CO2}C_{oDHB} + k_{pDHB-CO2}C_{pDHB} + k_{BQ-CO2}C_{BQ} + k_{Ac-CO2}C_{Ac}}{\left(1 + K^A_{ph}C_{ph} + K^A_{oDHB}C_{oDHB} + K^A_{pDHB}C_{pDHB} + K^A_{BQ}C_{BQ} + K^A_{Ac}C_{Ac}\right)} \qquad (73)$$

One should mention that $k_{oDHB-Ac}$, $k_{pDHB-Ac}$, k_{BQ-Ac} represent the constants involved in the formation of the lumped acids as explained in Eq. (67).

In summary, Eqs. (66), (69)-(73) represent the net contribution of the various chemical species considered in the reaction network. It should be mentioned that all the described steps in the reaction sequence are supported experimentally. Some of these steps were kept or dropped when optimizing the kinetic parameters for different TiO_2 catalysts. For instance, for most of the photocatalysts, it was found that benzoquinone was formed at very low concentrations. Hence, this compound was considered kinetically insignificant. More about these issues will be reviewed in the parameter optimization section of this chapter.

For the estimation of the kinetic parameters, two built-in MATLAB® subroutines were used: *lsqcurvefit* for the minimization of the objective function and *ode45* for the numerical integration of the differential equations.

7.2   A Unified Kinetic Model for Different TiO_2 Photocatalysts

A L-H based kinetics can be considered a useful approach for modeling the photocatalytic conversion of phenol and its intermediates using different photocatalysts. This model should be established to predict the disappearance of both, reactant and intermediate species at different initial concentrations of phenol (Malato et al. 2009).

On the basis of Eqs. (66) and (69)-(73)) this yields a set of ODEs with a large number of variables and parameters: 14 kinetic constants and 5 adsorption constants. In addition, the mathematical form of the rate equation renders optimized kinetic parameters with a high degree of correlation and large confidence intervals (CI).

Even when the values of the experimental adsorption constants are established independently, a total of 14 kinetic constants still remain to be determined. As a result, most likely the system considered is over-parameterized with many solutions for the optimized

parameters. Therefore, estimation of these kinetic parameters raises numerical issues that need to be addressed.

Chapter 6 reports that phenol, catechol and hydroquinone produced benzoquinone as intermediate and $CO_2 + H_2O$ as final products and this for all the photocatalysts studied. However, the concentration of benzoquinone in every case was rather small. Thus, neglecting this chemical species in the parameter estimation calculation does not significantly affect the final outcome. In this way, the reaction scheme reported in Figure 65 can be simplified into the reaction scheme shown in Figure 66. As a result, the proposed reaction scheme contains 10 parameters only.

This reaction network was successfully applied to all of the TiO_2 photocatalysts of this study. For Hombikat UV-100; however, a special revision of the model was needed since this photocatalyst does not yield catechol. Moreover, one should mention that reaction parameters were obtained using statistical based methods. In this respect, confidence intervals, cross-correlation matrix, and the R^2 correlation coefficient were considered as the major indicators showing the adequacy of selected kinetic network.
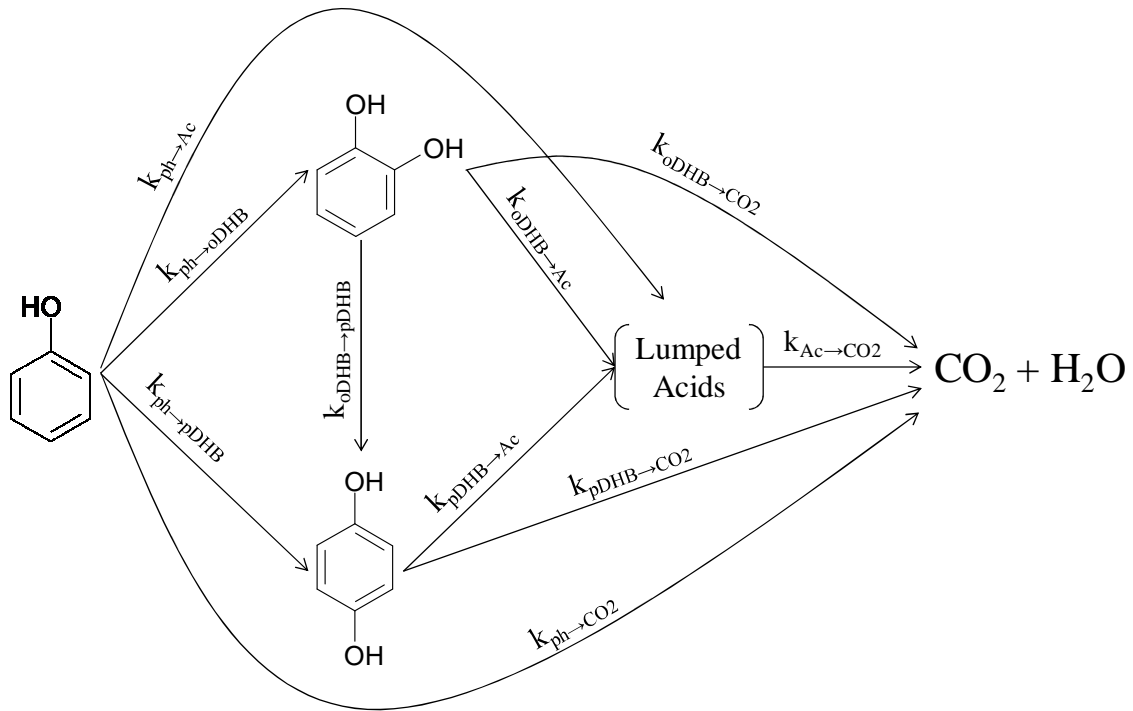
Figure 66 General simplified reaction scheme for phenol photocatalytic degradation

Parameter optimization is a difficult task. One has to compromise in many situations between the number of optimized parameters and the wellness of the fit. As well, having the smallest number of optimized kinetic parameters will mean less cross-correlation among them.

7.2.1   Degussa P25

For Degussa P25 and using the reaction scheme presented in Figure 66, the following set of ODEs is obtained:

a) For phenol:

$$\frac{dC_{ph}}{dt} = \frac{-\left(k_{ph-Ac} + k_{ph-oDHB} + k_{ph-pDHB} + k_{ph-CO_2}\right)C_{ph}}{\left(1 + K_{ph}^A C_{ph} + K_{oDHB}^A C_{oDHB} + K_{pDHB}^A C_{pDHB} + K_{Ac}^A C_{Ac}\right)} \tag{74}$$

b) For catechol:

$$\frac{dC_{oDHB}}{dt} = \frac{k_{ph-oDHB}C_{ph} - \left(k_{oDHB-Ac} + k_{oDHB-pDHB} + k_{oDHB-CO_2}\right)C_{oDHB}}{\left(1 + K_{ph}^A C_{ph} + K_{oDHB}^A C_{oDHB} + K_{pDHB}^A C_{pDHB} + K_{Ac}^A C_{Ac}\right)} \tag{75}$$

c) For hydroquinone:

$$\frac{dC_{pDHB}}{dt} = \frac{k_{ph-pDHB}C_{ph} + k_{oDHB-pDHB}C_{oDHB} - \left(k_{pDHB-Ac} + k_{pDHB-CO_2}\right)C_{pDHB}}{\left(1 + K_{ph}^{A}C_{ph} + K_{oDHB}^{A}C_{oDHB} + K_{pDHB}^{A}C_{pDHB} + K_{Ac}^{A}C_{Ac}\right)}$$ (76)

d) For lumped carboxylic acids:

$$\frac{dC_{Ac}}{dt} = \frac{k_{ph-Ac}C_{ph} + k_{oDHB-Ac}C_{oDHB} + k_{pDHB-Ac}C_{pDHB} - k_{Ac-CO2}C_{CO2}}{\left(1 + K_{ph}^{A}C_{ph} + K_{oDHB}^{A}C_{oDHB} + K_{pDHB}^{A}C_{pDHB} + K_{Ac}^{A}C_{Ac}\right)}$$ (77)

e) For CO_2:

$$\frac{dC_{CO_2}}{dt} = \frac{k_{ph-CO2}C_{ph} + k_{oDHB-CO2}C_{oDHB} + k_{pDHB-CO2}C_{pDHB} + k_{Ac-CO2}C_{Ac}}{\left(1 + K_{ph}^{A}C_{ph} + K_{oDHB}^{A}C_{oDHB} + K_{pDHB}^{A}C_{pDHB} + K_{Ac}^{A}C_{Ac}\right)}$$ (78)

Figure 67 presents the experimental concentration profiles of phenol and its intermediates and the estimated profiles using Eqs. (74)-(78) for 30 ppm-C phenol initial concentration. During the optimization procedure, the kinetic constants were constrained to have positive values only. These are obvious restrictions given kinetic constants can be positive only. Table 20 presents the estimated kinetic constants for this case. Finally, Table 22 reports the cross-correlation matrix of the optimized coefficients.

One should mention that the amount of CO_2 produced during a photoreaction presented in Figure 67 is determined by the difference between the initial phenol concentration (C_{TOC0}) and the concentration given by the TOC analysis at any time. This is expressed in the following equation as:

$$C_{CO_2} = C_{TOC_0} - C_{TOC}$$ (79)

where C_{CO2} is the experimental amount of CO_2 produced during photocatalytic degradation at different reaction times.
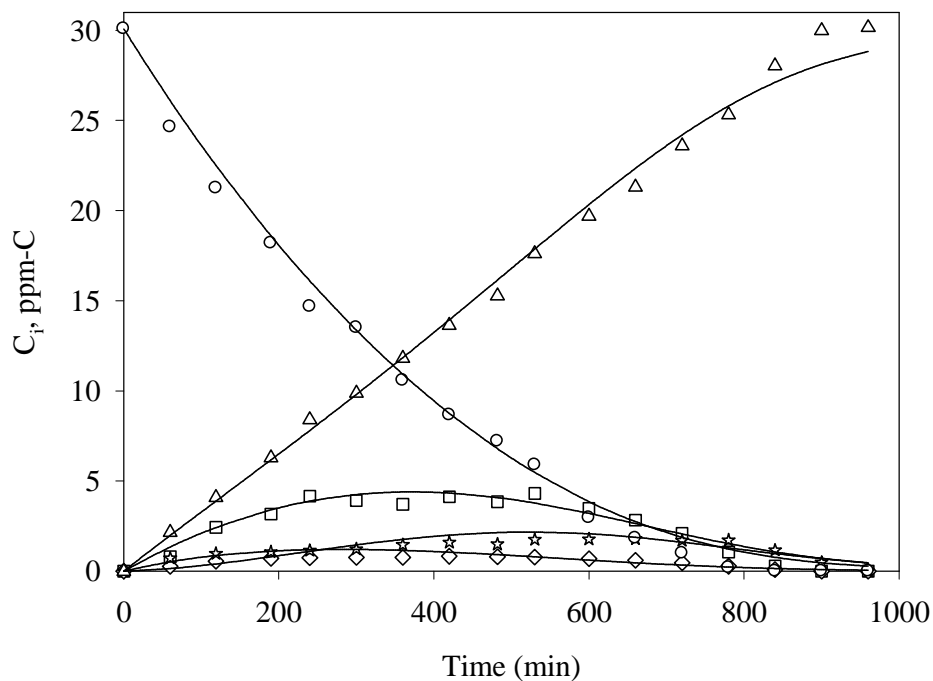
Figure 67 Experimental and estimated concentration profiles for photocatalytic conversion of phenol in DP 25 (○) phenol, (□) hydroquinone, (◊) catechol, (☆) lumped acids, (Δ) CO_2, and (—) model for 30 ppm-C initial concentration in phenol for reaction scheme in Figure 66

Table 20 Estimated parameters for the photoconversion of 30 ppm-C phenol on DP 25 for reaction scheme in Figure 66

Parameter	Symbol	Value	95% CI	STD
k_{ph-Ac}	k_1	1.622×10^{-4}	1.824×10^{-3}	1.127×10^{-3}
$k_{ph-oDHB}$	k_2	1.452×10^{-3}	9.309×10^{-4}	5.571×10^{-4}
$k_{ph-pDHB}$	k_3	3.474×10^{-3}	1.291×10^{-3}	7.975×10^{-4}
k_{ph-CO2}	k_4	4.799×10^{-3}	1.858×10^{-3}	1.148×10^{-3}
$k_{oDHB-pDHB}$	k_5	1.699×10^{-2}	5.445×10^{-2}	3.364×10^{-2}
$k_{oDHB-CO2}$	k_6	2.322×10^{-14}	3.685×10^{-1}	2.277×10^{-1}
$k_{oDHB-Ac}$	k_7	3.422×10^{-14}	3.502×10^{-1}	2.163×10^{-1}
$k_{pDHB-Ac}$	k_8	9.241×10^{-3}	1.268×10^{-1}	7.833×10^{-2}
$k_{pDHB-CO2}$	k_9	3.465×10^{-3}	1.305×10^{-1}	8.064×10^{-2}
k_{Ac-CO2}	k_{10}	1.669×10^{-2}	9.423×10^{-2}	5.822×10^{-2}

Table 21 Cross-correlation coefficients for the optimized parameters of the photoconversion of 30 ppm-C of phenol on DP 25 for reaction scheme in Figure 66

	k_1	k_2	k_3	k_4	k_5	k_6	k_7	k_8	k_9	k_{10}
k_1	1.00									
k_2	-0.13	1.00								
k_3	-0.24	-0.27	1.00							
k_4	-0.75	-0.14	-0.29	1.00						
k_5	0.27	-0.26	-0.74	0.36	1.00					
k_6	0.60	0.06	0.29	-0.82	-0.40	1.00				
k_7	-0.68	0.01	-0.20	0.81	0.26	-0.99	1.00			
k_8	0.62	0.00	0.24	-0.77	-0.31	0.99	-1.00	1.00		
k_9	-0.58	-0.04	-0.28	0.78	0.39	-1.00	0.99	-1.00	1.00	
k_{10}	0.56	0.01	0.27	-0.74	-0.36	0.99	-0.98	0.99	-1.00	1.00

As it can be seen in Figure 67, the model predicts very well the experimental data with a $R^2 =$ 0.997. Nonetheless, cross-correlation coefficients close to ± 1.0 indicate high correlation among the parameters involved in the optimization (El Solh et al. 2003). Table 21 shows a value of -1.00 for the cross-correlation coefficients between $k_{oDHB \to Ac}$ and $k_{pDHBc \to Ac}$, $k_{pDHB \to Ac}$ and $k_{pDHB \to CO2}$, and $k_{pDHB \to CO2}$ and $k_{Ac \to CO2}$. Also, values of 0.99 were obtained for cross correlation coefficients between $k_{oDHB \to Ac}$ and $k_{pDHBc \to CO2}$, $k_{oDHB \to CO2}$ and $k_{pDHBc \to Ac}$, $k_{pDHB \to Ac}$ and $k_{Ac \to CO2}$, and $k_{oDHB \to CO2}$ and $k_{Ac \to CO2}$. It appears that most of these high cross-correlation coefficients occur for kinetic parameters involved in the production/consumption of lumped acids and CO_2.

Thus, from the analysis presented above, it can be concluded that the model reported in Figure 66 is overparametrized and therefore multiple solutions for the kinetic optimized kinetic constants are expected. This can be also confirmed by the large values of the CI obtained in the parameter optimization as reported in Table 20 (e.g. refer to column 4).

A simultaneous optimization was performed for three different initial concentrations of phenol (10, 20, and 30 ppm-C in phenol) with the reaction scheme and the same set of ODEs. This was done in order to find out if the system was overparametrized, regardless of the initial concentration of phenol. Results for the experimental and estimated concentration profiles for this multiple optimization are presented in Figure 68.
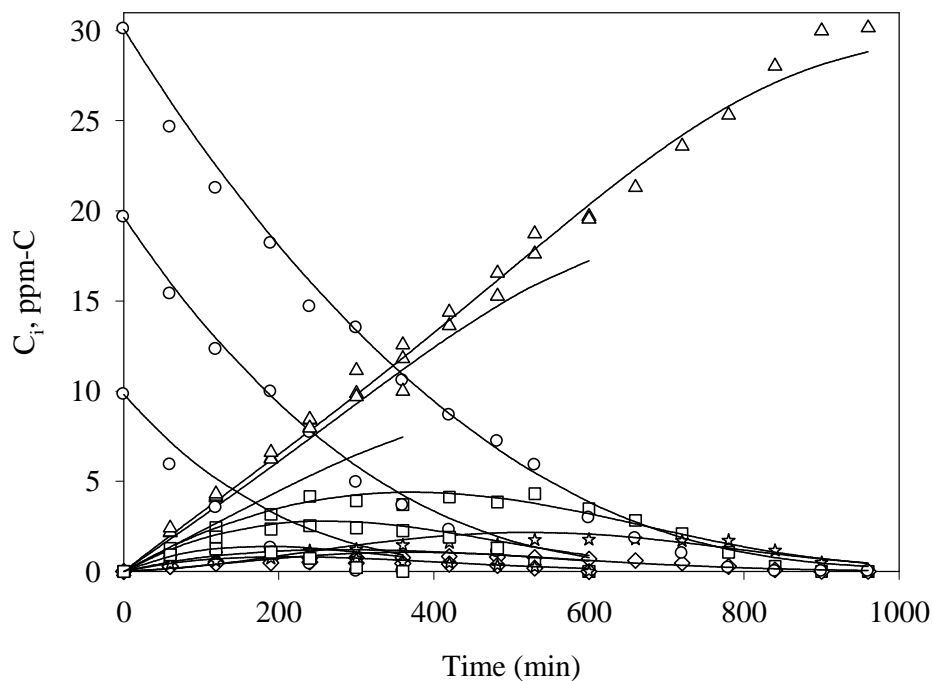
Figure 68 Experimental and estimated concentration profiles for the simultaneous optimization of phenol on DP 25 for 30, 20, and 10 ppm-C initial concentration for the reaction scheme in Figure 66

Table 22 and Table 23 report the kinetic constants and the cross correlation coefficients for the simultaneous kinetic parameter optimization in the case of photocatalytic conversion of phenol. The obtained correlation coefficient was $R^2 = 0.987$. This shows a fairly good fit of the experimental profiles. However, and as suggested by the large value of the CI, the model is likely to present multiple solutions. This is also confirmed with the cross-correlation matrix and the several cross-correlation coefficients close to ± 1.

Analyzing the results of the values for the kinetic constants, it can be noticed that for both the kinetic parameters for 30 ppm-C initial concentration and for the kinetic parameters for 30, 20, and 10 ppm-C initial concentrations. $k_{oDHB \rightarrow CO2}$ and $k_{oDHB \rightarrow Ac}$, representing the formation of CO_2 and lumped acids from catechol respectively, are almost zero with very large CI.

Table 22 Estimated parameters for the simultaneous optimization of 30, 20, and 10 ppm-C in phenol on DP 25 for reaction scheme in Figure 66

Parameter	Symbol	Value	95% CI	STD
k_{ph-Ac}	k_1	3.026×10^{-4}	2.347×10^{-3}	2.651×10^{-3}
$k_{ph-oDHB}$	k_2	1.500×10^{-3}	1.134×10^{-3}	1.281×10^{-4}
$k_{ph-pDHB}$	k_3	3.700×10^{-3}	1.672×10^{-3}	1.889×10^{-4}
k_{ph-CO2}	k_4	4.800×10^{-3}	2.372×10^{-3}	2.679×10^{-3}
$k_{oDHB-pDHB}$	k_5	1.640×10^{-2}	8.431×10^{-2}	9.523×10^{-2}
$k_{oDHB-CO2}$	k_6	4.441×10^{-14}	6.204×10^{-1}	7.008×10^{-1}
$k_{oDHB-Ac}$	k_7	4.441×10^{-14}	5.971×10^{-1}	6.744×10^{-1}
$k_{pDHB-Ac}$	k_8	7.007×10^{-3}	2.288×10^{-1}	2.584×10^{-1}
$k_{pDHB-CO2}$	k_9	7.003×10^{-3}	2.342×10^{-1}	2.645×10^{-1}
k_{Ac-CO2}	k_{10}	1.730×10^{-2}	1.848×10^{-2}	2.201×10^{-1}

Table 23 Cross-correlation coefficients for the optimized parameters in the simultaneous optimization of 30, 20, and 10 ppm-C phenol initial concentration on DP 25 for reaction scheme in Figure 66

	k_1	k_2	k_3	k_4	k_5	k_6	k_7	k_8	k_9	k_{10}
k_1	1.00									
k_2	-0.14	1.00								
k_3	-0.27	-0.23	1.00							
k_4	-0.74	-0.14	-0.30	1.00						
k_5	0.29	-0.30	-0.72	0.34	1.00					
k_6	0.61	0.06	0.25	-0.81	-0.34	1.00				
k_7	-0.68	0.01	-0.16	0.79	0.20	-0.99	1.00			
k_8	0.63	0.00	0.20	-0.76	-0.25	0.99	-1.00	1.00		
k_9	-0.60	-0.03	-0.24	0.77	0.32	-1.00	0.99	-1.00	1.00	
k_{10}	0.58	0.00	0.22	-0.73	-0.30	0.99	-0.99	1.00	-1.00	1.00

Regarding this issue, it is observed experimentally that catechol forms negligible amounts of CO_2 and carboxylic acids and this when compared with phenol and hydroquinone. Therefore, if these two steps are deleted from the reaction network of Figure 66, the reaction scheme presented in Figure 69 is obtained with 8 kinetic constants only.

142

As a result, a next step in the kinetic modeling is to obtain the ODEs for phenol degradation following the reaction scheme reported in Figure 69.
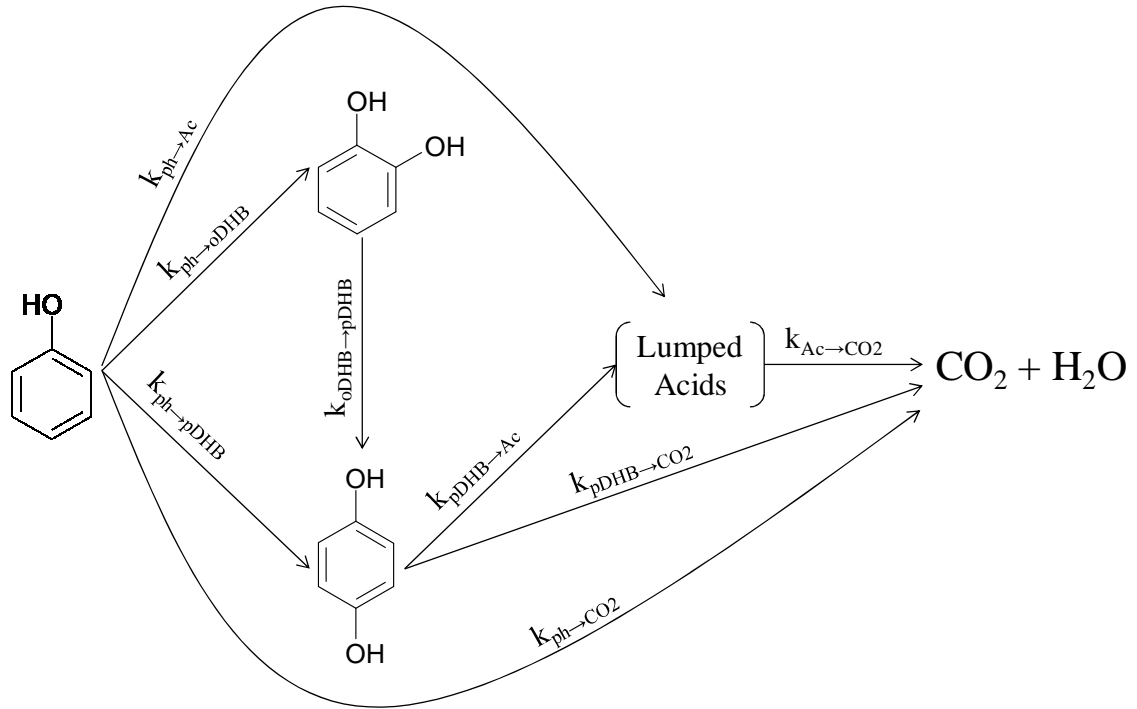
Figure 69 Simplified reaction scheme obtained by dropping off $k_{oDHB \rightarrow CO2}$ and $k_{oDHB \rightarrow Ac}$ for phenol photodegradation on DP 25.

The set of ODEs for this case is presented as follows

a) For phenol:

$$\frac{dC_{ph}}{dt} = \frac{-\left(k_{ph-Ac} + k_{ph-oDHB} + k_{ph-pDHB} + k_{ph-CO_2}\right)C_{ph}}{\left(1 + K_{ph}^A C_{ph} + K_{oDHB}^A C_{oDHB} + K_{pDHB}^A C_{pDHB} + K_{Ac}^A C_{Ac}\right)}$$

(80)

b) For catechol:

$$\frac{dC_{oDHB}}{dt} = \frac{k_{ph-oDHB}C_{ph} - k_{oDHB-pDHB}C_{oDHB}}{\left(1 + K_{ph}^A C_{ph} + K_{oDHB}^A C_{oDHB} + K_{pDHB}^A C_{pDHB} + K_{Ac}^A C_{Ac}\right)}$$

(81)

c) For hydroquinone:

$$\frac{dC_{pDHB}}{dt} = \frac{k_{ph-pDHB}C_{ph} + k_{oDHB-pDHB}C_{oDHB} - \left(k_{pDHB-Ac} + k_{pDHB-CO_2}\right)C_{pDHB}}{\left(1 + K_{ph}^{A}C_{ph} + K_{oDHB}^{A}C_{oDHB} + K_{pDHB}^{A}C_{pDHB} + K_{Ac}^{A}C_{Ac}\right)} \tag{82}$$

d) For lumped carboxylic acids:

$$\frac{dC_{Ac}}{dt} = \frac{k_{ph-Ac}C_{ph} + k_{pDHB-Ac}C_{pDHB} - k_{Ac-CO2}C_{CO2}}{\left(1 + K_{ph}^{A}C_{ph} + K_{oDHB}^{A}C_{oDHB} + K_{pDHB}^{A}C_{pDHB} + K_{Ac}^{A}C_{Ac}\right)} \tag{83}$$

e) For CO_2:

$$\frac{dC_{CO_2}}{dt} = \frac{k_{ph-CO2}C_{ph} + k_{pDHB-CO2}C_{pDHB} + k_{Ac-CO2}C_{Ac}}{\left(1 + K_{ph}^{A}C_{ph} + K_{oDHB}^{A}C_{oDHB} + K_{pDHB}^{A}C_{pDHB} + K_{Ac}^{A}C_{Ac}\right)} \tag{84}$$

Figure 70 reports the experimental and model profiles for 30 ppm-C phenol degradation when the reaction scheme presented in Figure 69 is adopted.

Results for the optimized kinetic constants are presented in Table 24. Table 25 shows the cross-correlation coefficients for this same optimization. It can be noticed that the confidence intervals are now narrower than for the reaction scheme of Figure 66. However, $k_{pDHB-CO2}$ and k_{Ac-CO2} still present large confidence interval values.

Figure 70 Experimental and estimated concentration profiles for ($\circ$) phenol, ($\square$) hydroquinone, ($\Diamond$) catechol, ($\star$) lumped acids, ($\triangle$) CO_2, and (—) model for 30 ppm-C initial concentration in phenol for reaction scheme in Figure 69

Table 24 Estimated parameters for 30 ppm-C phenol on DP 25 for reaction scheme in Figure 69

Parameter	Symbol	Value	95% CI	STD
k_{ph-Ac}	k_1	1.622×10^{-4}	1.038×10^{-3}	6.372×10^{-4}
$k_{ph-oDHB}$	k_2	1.452×10^{-3}	8.171×10^{-4}	5.017×10^{-4}
$k_{ph-pDHB}$	k_3	3.474×10^{-3}	1.003×10^{-3}	6.156×10^{-4}
k_{ph-CO2}	k_4	4.799×10^{-3}	1.039×10^{-3}	6.378×10^{-4}
$k_{oDHB-pDHB}$	k_5	1.699×10^{-2}	1.160×10^{-2}	7.120×10^{-3}
$k_{pDHB-Ac}$	k_6	9.241×10^{-3}	9.353×10^{-3}	5.743×10^{-3}
$k_{pDHB-CO2}$	k_7	3.465×10^{-3}	9.907×10^{-3}	6.083×10^{-3}
k_{Ac-CO2}	k_8	1.669×10^{-2}	1.478×10^{-2}	9.073×10^{-3}

Table 25 Cross-correlation coefficients for the optimized parameters for 30 ppm-C of phenol photoconverted on DP 25 after the reaction scheme in Figure 69

	k_1	k_2	k_3	k_4	k_5	k_6	k_7	k_8
k_1	1.00							
k_2	0.15	1.00						
k_3	-0.27	-0.77	1.00					
k_4	-0.85	-0.13	-0.07	1.00				
k_5	0.18	0.85	-0.79	-0.10	1.00			
k_6	-0.81	-0.23	0.08	0.89	-0.24	1.00		
k_7	0.72	0.24	0.02	-0.90	0.20	-0.98	1.00	
k_8	-0.66	-0.25	0.02	0.81	-0.25	0.95	-0.97	1.00

Furthermore, when the cross-correlation matrix is analyzed, it can be observed that the highest cross-correlation coefficients are those for $k_{pDHB-CO2}$ and k_{Ac-CO2} (-0.97) and for $k_{pDHB-Ac}$ and k_{Ac-CO2} (-0.98).

Therefore, a suitable relationship between $k_{pDHB-CO2}$ and $k_{pDHB-Ac}$ was further considered:

$$R_1 = \frac{k_{pDHB-Ac}}{k_{pDHB-CO2}} \tag{85}$$

This most suitable R_1 ratio was determined as it will be described in the following section. This was achieved performing hydroquinone photodegradation at different levels of initial concentrations (30, 20, and 10 ppm-C).

7.2.1.1 Constrained Relationship: Analysis of Hydroquinone Photodegradation on DP 25

As described in Chapter 6, the photoconversion of hydroquinone produced benzoquinone, two carboxylic acids (oxalic acid and formic acid), CO_2 and H_2O as final products. The concentration of benzoquinone in this case was rather small; therefore, the benzoquinone term was neglected in the parameter optimization.

Moreover and to establish the ratio between the $k_{pDHB-Ac}$ and $k_{pDHB-CO2}$ constants, the simplified reaction network presented in Figure 71 is proposed.
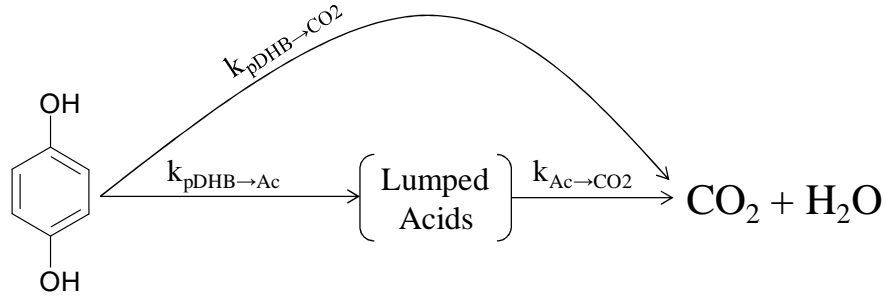
Figure 71 Reaction network for the photo oxidation of hydroquinone

As a result, the following ODEs describing the formation and disappearance of hydroquinone were considered:

a) For hydroquinone:

$$\frac{dC_{pDHB}}{dt} = \frac{-\left(k_{pDHB-Ac} + k_{pDHB-CO_2}\right)C_{pDHB}}{\left(1 + K_{pDHB}^A C_{pDHB} + K_{Ac}^A C_{Ac}\right)}$$

(86)

b) For the lumped carboxylic acids:

$$\frac{dC_{Ac}}{dt} = \frac{k_{pDHB-Ac}C_{pDHB} - k_{Ac-CO2}C_{CO2}}{\left(1 + K_{pDHB}^A C_{pDHB} + K_{Ac}^A C_{Ac}\right)}$$

(87)

Figure 72 reports the experimental and the calculated profiles for the photodegradation of hydroquinone. The values for the estimated kinetic parameters and their confidence intervals are presented in Table 26. In this table, the calculated value of the ratio between $k_{pDHB-AC}$ and $k_{pDHB-CO2}$ is given (refer to Eq. (85))

Thus; and given the independent determination of R ratio, this R value can be used to constrain the estimation of these parameters in the phenol photoconversion reaction system. This constrain helps to avoid reaching, as it will be shown later, inadequate parameter solutions that may arise given the high parameter interactions as a result of high cross-correlation coefficients.
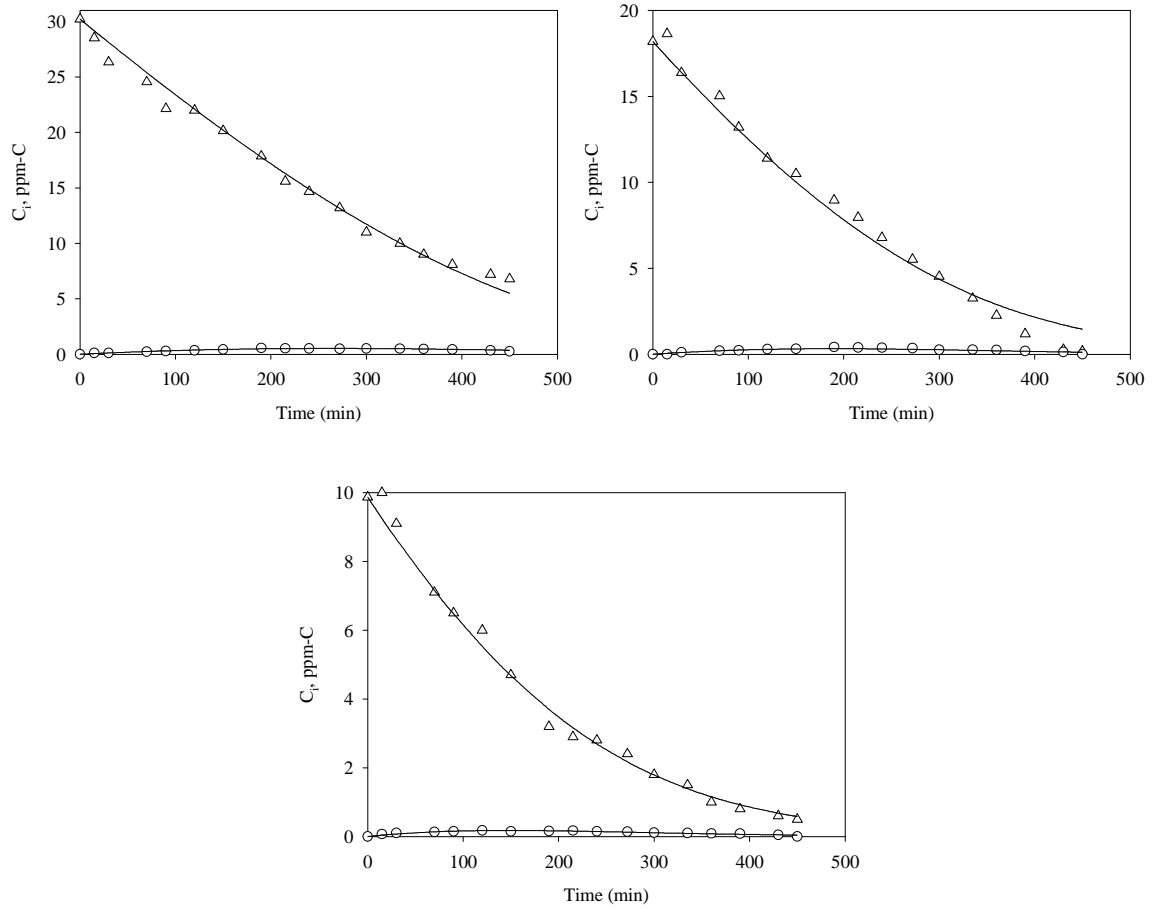
Figure 72 Experimental and estimated profiles for hydroquinone photo-oxidation. (Δ) hydroquinone profiles at different initial concentrations and (○) lumped acids

Table 26 Estimated parameters for the photodegradation of hydroquinone at different initial concentrations

C_{pDHB0}	Parameter	Value (1/min)	95% CI	R
30 ppm-C	$k_{pDHB-AC}$	5.288×10^{-4}	4.947×10^{-4}	
	$k_{pDHB-CO2}$	8.504×10^{-3}	4.5100×10^{-4}	0.062
	k_{AC-CO2}	1.400×10^{-2}	5.895×10^{-4}	
20 ppm-C	$k_{pDHB-AC}$	5.657×10^{-4}	6.630×10^{-5}	
	$k_{pDHB-CO2}$	8.584×10^{-3}	6.451×10^{-4}	0.066
	k_{AC-CO2}	1.447×10^{-2}	2.270×10^{-2}	
10 ppm-C	$k_{pDHB-AC}$	5.617×10^{-4}	1.196×10^{-3}	
	$k_{pDHB-CO2}$	7.699×10^{-3}	1.210×10^{-4}	0.073
	k_{AC-CO2}	1.521×10^{-2}	3.839×10^{-4}	

7.2.1.2 Parameter Estimation for a Simplified Kinetic Model for DP 25

The reaction network reported in Figure 69 and the set of ODEs presented in Eqs. (80)-(84) still contain a large number of kinetic parameters with high cross-correlation coefficients. Thus, estimation of these kinetic parameters brings about numerical issues that need to be addressed.

One should notice that if one considers a 0.067 R ratio relating $k_{pDHB\text{-}AC}$ and $k_{pDHB\text{-}CO2}$ as reported in Table 26, the reaction network remains with seven kinetic parameters only. In this case the ODEs describing changes of various chemical species are the following:

a) For phenol:

$$\frac{dC_{ph}}{dt} = \frac{-\left(k_{ph-Ac} + k_{ph-oDHB} + k_{ph-pDHB} + k_{ph-CO_2}\right)C_{ph}}{\left(1 + K_{ph}^A C_{ph} + K_{oDHB}^A C_{oDHB} + K_{pDHB}^A C_{pDHB} + K_{Ac}^A C_{Ac}\right)} \tag{88}$$

b) For catechol:

$$\frac{dC_{oDHB}}{dt} = \frac{k_{ph-oDHB}C_{ph} - k_{oDHB-pDHB}C_{oDHB}}{\left(1 + K_{ph}^A C_{ph} + K_{oDHB}^A C_{oDHB} + K_{pDHB}^A C_{pDHB} + K_{Ac}^A C_{Ac}\right)} \tag{89}$$

c) For hydroquinone:

$$\frac{dC_{pDHB}}{dt} = \frac{k_{ph-pDHB}C_{ph} + k_{oDHB-pDHB}C_{oDHB} - k_{pDHB-CO_2}(R+1)C_{pDHB}}{\left(1 + K_{ph}^A C_{ph} + K_{oDHB}^A C_{oDHB} + K_{pDHB}^A C_{pDHB} + K_{Ac}^A C_{Ac}\right)} \tag{90}$$

d) For lumped carboxylic acids:

$$\frac{dC_{Ac}}{dt} = \frac{k_{ph-Ac}C_{ph} + R \times k_{pDHB-CO2}C_{pDHB} - k_{Ac-CO2}C_{CO2}}{\left(1 + K_{ph}^A C_{ph} + K_{oDHB}^A C_{oDHB} + K_{pDHB}^A C_{pDHB} + K_{Ac}^A C_{Ac}\right)} \tag{91}$$

e) For CO$_2$:

$$\frac{dC_{CO_2}}{dt} = \frac{k_{ph-CO2}C_{ph} + k_{pDHB-CO2}C_{pDHB} + k_{Ac-CO2}C_{Ac}}{\left(1 + K_{ph}^A C_{ph} + K_{oDHB}^A C_{oDHB} + K_{pDHB}^A C_{pDHB} + K_{Ac}^A C_{Ac}\right)} \tag{92}$$

Results for the model predictions in the photodegradation of 30 ppm-C of phenol using Eqs. (88)-(92) are given in Figure 73. In this calculation, the experimental values for the adsorption constants were used. It can be seen that the fit of the proposed kinetic model is very good both phenol and its intermediate chemical species
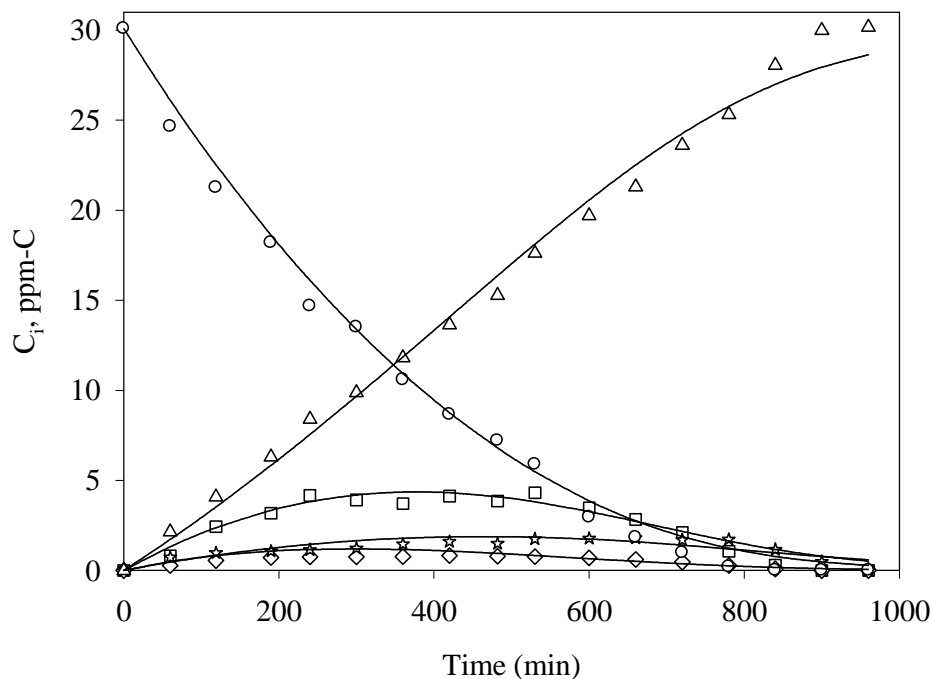
Figure 73 Experimental and estimated concentration profiles for (○) phenol, (□) hydroquinone, (◊) catechol, (☆) lumped acids, (Δ) CO_2, and (—) model for 30 ppm-C initial concentration in phenol for reaction scheme in Figure 69 with the constraint R included in the kinetic model

Moreover; kinetic constants, along with the CI intervals for this case are presented in Table 27. The cross correlation matrix is reported in Table 28.

Table 27 Estimated parameters for 30 ppm-C in phenol on DP 25 for reaction scheme in Figure 69 with the constraint R included in the model

Parameter	Symbol	Value (1/min)	95% CI	STD
k_{ph-Ac}	k_1	1.180×10^{-3}	2.833×10^{-3}	2.252×10^{-4}
$k_{ph-oDHB}$	k_2	1.349×10^{-3}	5.432×10^{-4}	4.842×10^{-4}
$k_{ph-pDHB}$	k_3	3.414×10^{-3}	6.645×10^{-4}	5.923×10^{-4}
k_{ph-CO2}	k_4	3.938×10^{-3}	3.392×10^{-4}	3.027×10^{-4}
$k_{oDHB-pDHB}$	k_5	1.536×10^{-2}	7.565×10^{-2}	6.743×10^{-3}
$k_{pDHB-Ac}$	k_6	8.305×10^{-4}	N/A	N/A
$k_{pDHB-CO2}$	k_7	1.122×10^{-2}	1.388×10^{-3}	1.237×10^{-3}
k_{Ac-CO2}	k_8	6.425×10^{-3}	1.875×10^{-3}	1.671×10^{-3}

Table 28 Cross-correlation coefficients for the optimized parameters of 30 ppm-C of phenol on DP 25 for with the constraint R included in the model

	k_1	k_2	k_3	k_4	k_5	k_7	k_8
k_1	1.00						
k_2	-0.26	1.00					
k_3	-0.10	-0.74	1.00				
k_4	-0.19	0.22	-0.62	1.00			
k_5	-0.20	0.84	-0.78	0.31	1.00		
k_7	-0.46	0.14	0.42	-0.63	-0.08	1.00	
k_8	0.78	-0.30	0.01	-0.25	-0.31	-0.41	1.00

Furthermore, results for the estimation parameters using the data for three different concentrations (30, 20, and 10 ppm-C in phenol) are shown in Figure 74. The estimated rate parameters and their corresponding 95% CI are given in Table 29. Finally, the cross-correlation matrix is presented in Table 30.
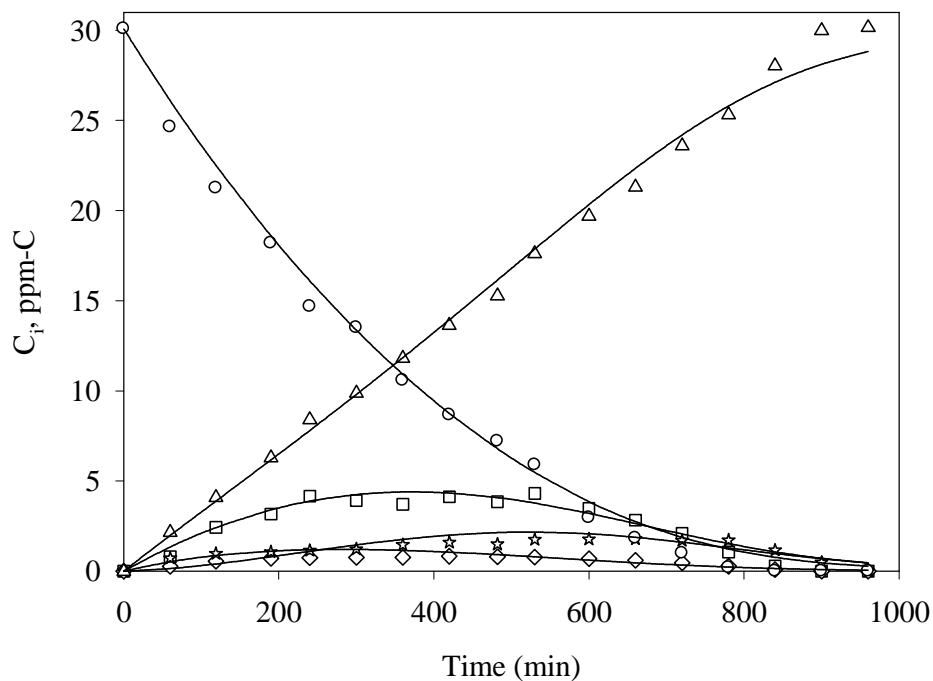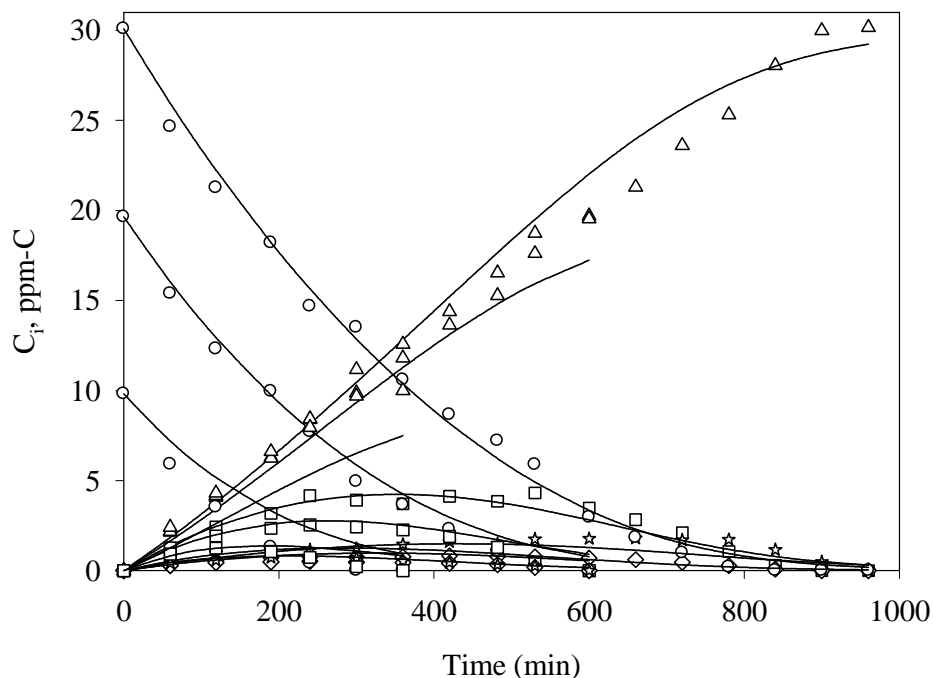
Figure 74 Experimental and estimated concentration profiles for (○) phenol, (□) hydroquinone, (◊) catechol, (☆) lumped acids, (△) CO_2, and (—) model for the simultaneous parameter evaluation of 30, 20, and 10 ppm-C initial concentration in phenol for reaction scheme in Figure 69 with the constraint R included in the kinetic model

Table 29 Estimated parameters for the simultaneous optimization of phenol for 30, 20, and 10 ppm-C in phenol on DP 25 for reaction scheme in Figure 69 with the constraint R included in the model

Parameter	Symbol	Value	95% CI	STD
k_{ph-Ac}	k_1	1.007×10^{-3}	3.848×10^{-4}	4.438×10^{-4}
$k_{ph-oDHB}$	k_2	1.483×10^{-3}	6.931×10^{-4}	7.792×10^{-4}
$k_{ph-pDHB}$	k_3	3.610×10^{-3}	8.697×10^{-4}	1.003×10^{-4}
k_{ph-CO2}	k_4	4.189×10^{-3}	4.641×10^{-4}	5.351×10^{-4}
$k_{oDHB-pDHB}$	k_5	1.595×10^{-2}	9.040×10^{-3}	1.042×10^{-2}
$k_{pDHB-Ac}$	k_6	9.417×10^{-4}	N/A	N/A
$k_{pDHB-CO2}$	k_7	1.273×10^{-2}	1.954×10^{-3}	2.253×10^{-3}
k_{Ac-CO2}	k_8	7.840×10^{-3}	3.190×10^{-3}	3.679×10^{-3}

Table 30 Cross-correlation coefficients for the simultaneous optimization of 30, 20, and 10 ppm-C of phenol on DP 25 for with the constraint R included in the model

	k_1	k_2	k_3	k_4	k_5	k_7	k_8
k_1	1.00						
k_2	-0.28	1.00					
k_3	-0.11	-0.72	1.00				
k_4	-0.19	0.23	-0.64	1.00			
k_5	-0.21	0.84	-0.76	0.31	1.00		
k_7	-0.46	0.14	0.44	-0.63	-0.07	1.00	
k_8	0.77	-0.30	0.00	-0.24	-0.32	-0.40	1.00

From the results presented above, it van be concluded that once the ratio R was included in the kinetic model, the overall correlation between the kinetic parameters was reduced to acceptable levels. In fact, the cross-correlation coefficients presented in Table 28 and Table 30 were significantly lower than the correlations obtained when 10 kinetic constants were optimized. Also, the values for the kinetic constants were calculated with adequate 95% confidence intervals.

Upon inspection of the reconciliation plot presented in Figure 75, a data quality assessment can be made. Firstly, the data presented is not clustered in horizontal bands or vertical lines. Horizontal bands may be the result of changes in the observed conversion caused by an independent variable which is not included in the kinetic model. Vertical lines are also not formed, concluding that the kinetic model is not over-parameterized. Thus, it can be considered that a significant amount of information is included in the parameterized model. (El Solh et al. 2003).
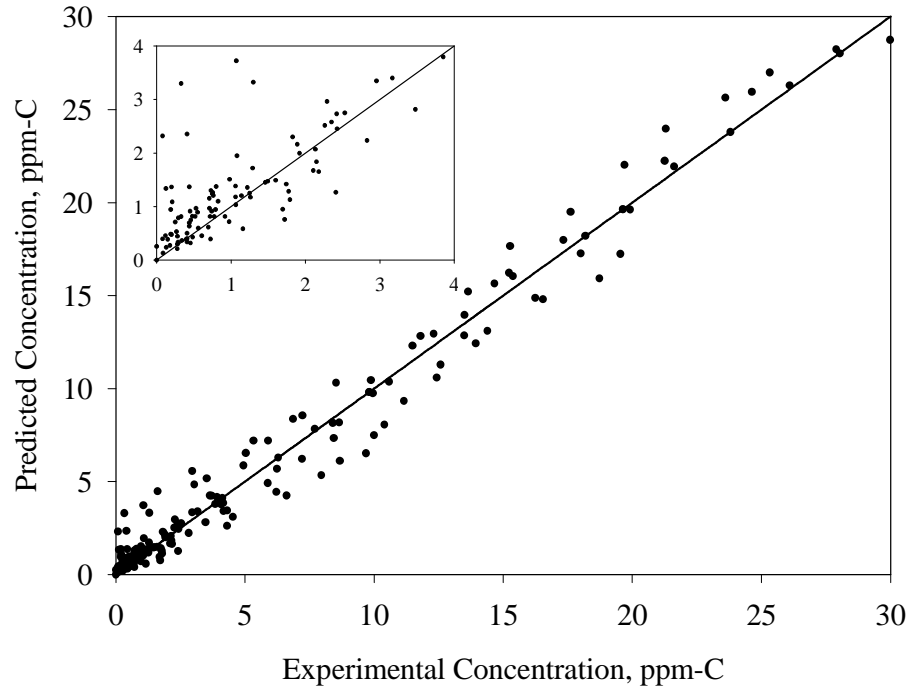
Figure 75 Reconciliation plot showing both the results when seven kinetic parameters are estimated using the DP 25 catalyst. Note: The graph in the left top corner of the figure describes the fitting of the model in the 0-4 ppm chemical species concentration range. The larger graph in the bottom right hand corner described the fitting of the model in the 0-30ppm chemical species concentration range

Figure 75 also shows a zoom-in for the experimental and observed values when smaller concentrations are considered: 0-4 ppm chemical species concentrations. It can be seen that the model gives a good prediction of the experimental data for lower chemical species concentrations. However, data and model predictions for concentrations smaller than 1 ppm-C seem to be more scattered. This scattering is assigned to the fact that experimental measurement of small concentrations is associated with larger errors leading to increased data dispersion.

Finally, the plot for the residuals for the seven kinetic constants optimized model is shown in Figure 76.
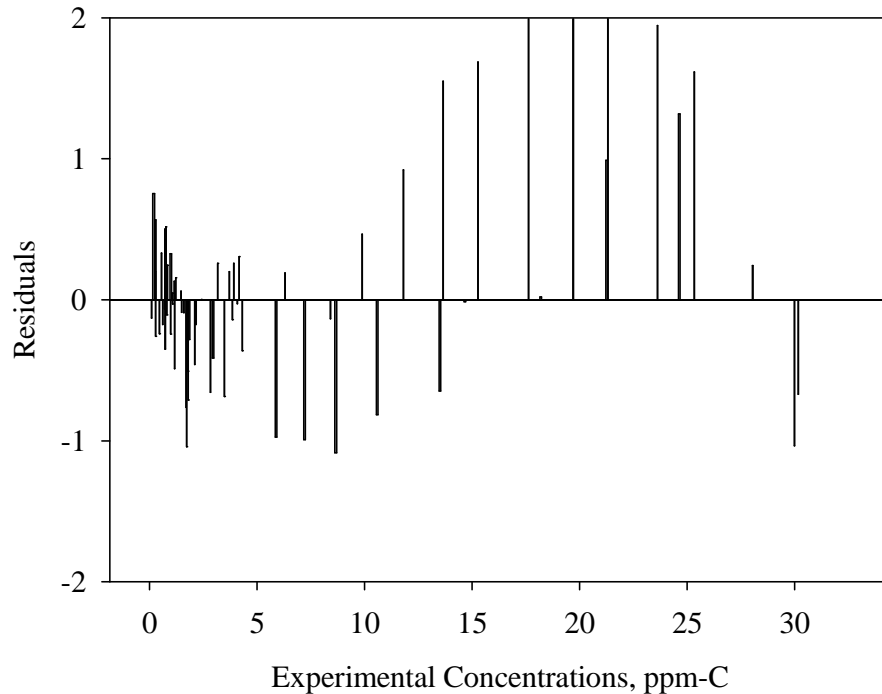
Figure 76: Residuals for the parameter estimation of seven kinetic constants for phenol degradation on DP 25

To summarize; the kinetic model presented in Figure 69 with the set of ODEs shown in Eqs. (88)-(92), includes the constraint R determined for the hydroquinone photodegradation. The R constraint breaks the correlation between $k_{pDHB\text{-}AC}$ and $k_{pDHB\text{-}CO2}$. Including the ratio R in the parameter optimization allows determining seven kinetic constants with adequate 95% confidence intervals. The elements of the cross-correlation matrix show that the parameters are correlated at very moderate levels. These findings allow corroborating the model adequacy by producing concentration estimates consistent with the experimental observations.

It should also be pointed out that like in many non-linear regression problems; the final solution may depend on initial guesses. Therefore, careful selection of initial guesses is a requirement. As well as for any non-linear regression, it is important to verify that a given solution is not simply the location of a local optimum for the objective function. As a result, regression calculations were performed with different initial guesses for the rate constants. Calculations converged to essentially the same solution in all cases with deviations smaller

than 5%. Thus, there is confidence that the set of regressed parameters did not provide a solution converging to a local minimum.

Furthermore, independent experimental determination of the adsorption constants helped to establish a kinetic model with only seven unknown paramenters. Otherwise, the adsorption constants had to be optimized as well. However, simultaneous optimization of the kinetic and adsorption constants renders a kinetic model with 11 parameters. This results in an overparametrized kinetic model. Therefore; and in order to apply the kinetic model proposed adequately, experimental determination of the adsorption constants is strongly recommended.

Regarding suitability of the kinetic model proposed, a significant value of the kinetic model proposed is the prediction of the TOC at various irradiation times. This is an advantage with respect of kinetic models that neglect CO_2 in the modeling. Since the model uses the concentration of the three major intermediates produced during phenol photodegradation, then adding the concentration of the measured organic chemical species should in principle, give the TOC. This additive model prediction is represented in the following equation:

$$TOC_{Model} = C_{ph_{Model}} + C_{pDHB_{Model}} + C_{oDHB_{Model}} + C_{Ac_{Model}} \tag{93}$$

One should mention that the accuracy of the predicted TOC profiles thus depend on the fraction of undetected chemical species. One also expects than in many cases the amount of non-detected species is very small, and a result a TOC model basis on detectable chemical species only is viable. In further sections of this Chapter, more about TOC profiles and kinetic modeling will be discussed. A simplified version of the unified kinetic model, already discussed in Chapter 3, will be presented in Section 7.3. This model is based on the summation of all the reaction rates of phenol and its intermediates species.

Coming back to the original unified kinetic model, for the case of DP 25, the experimental TOC profiles versus the profiles predicted by the kinetic model with seven kinetic constants are depicted in Figure 77. One can observe the successful model fitting, given the close agreement between experimental observations and model predictions.
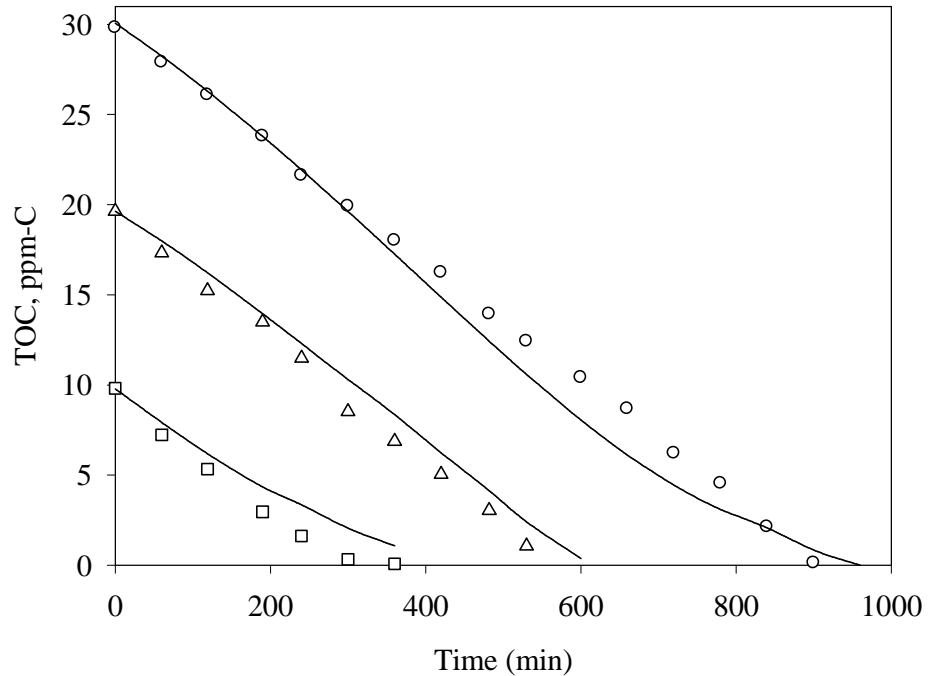
Figure 77 Experimental vs. the predicted TOC for the kinetic model with seven kinetic constants. (○) 30 ppm-C, (△) 20 ppm-C, (□) 10 ppm-C, and (——) model

Reviewing the unified "Series-Parallel" kinetic reaction network already shown in Figure 69 and represented by the ODEs in Eqs. (88)-(92), one should mention that this model includes the following assumptions:

- Hydroquinone and catechol are the two major hydroxylated compounds considered in the kinetic analysis.

- Carboxylic acids are lumped together into a single term to reduce the number of kinetic constants to be determined.

- Catechol is produced from phenol degradation and decomposed to hydroquinone in an isomerization reaction.

- Benzoquinone is not considered in the kinetic analysis. Benzoquinone concentration is considered negligible.

- The adsorption constant associated to the carboxyl acids is considered to be the value obtained for acetic acid.

- Final products of photodegradation, CO_2 and H_2O are not adsorbed onto the catalyst surface.

Regarding kinetic parameter regression, one can apply the same methodology to other TiO_2 photocatalysts of the present study. Before doing this, one has to consider the adapted unified "series-parallel" reaction network that better suits phenol degradation for the various TiO_2 photocatalysts under consideration. With these specifics, the respective set of ODEs can be assembled and the kinetic constants can be assessed using non-linear regression.

In the following sections, the reactions schemes and the kinetic constants for the other TiO_2 considered in this study are reported. The reaction schemes are obtained after testing different kinetic network alternatives based on the unified kinetic model presented in Figure 65

7.2.2 Anatase

For the photocatalysts Anatase, TOC profiles from HPLC results (OC_{inter}) are compared with experimental TOC measurements (refer to Figure 78). Results from this figure suggest that there is still a substantial concentration of other non-identified organic intermediates. Nonetheless; with the experimental TOC measurements, it is possible to approximate the amount of CO_2 produced in the course of the reaction.

Thus, one can notice that the proposed kinetic model simplification using the addition of chemical species fails somewhat for Anatase. This is particularly true towards the end of the irradiation period where carboxylic acids are dominant.
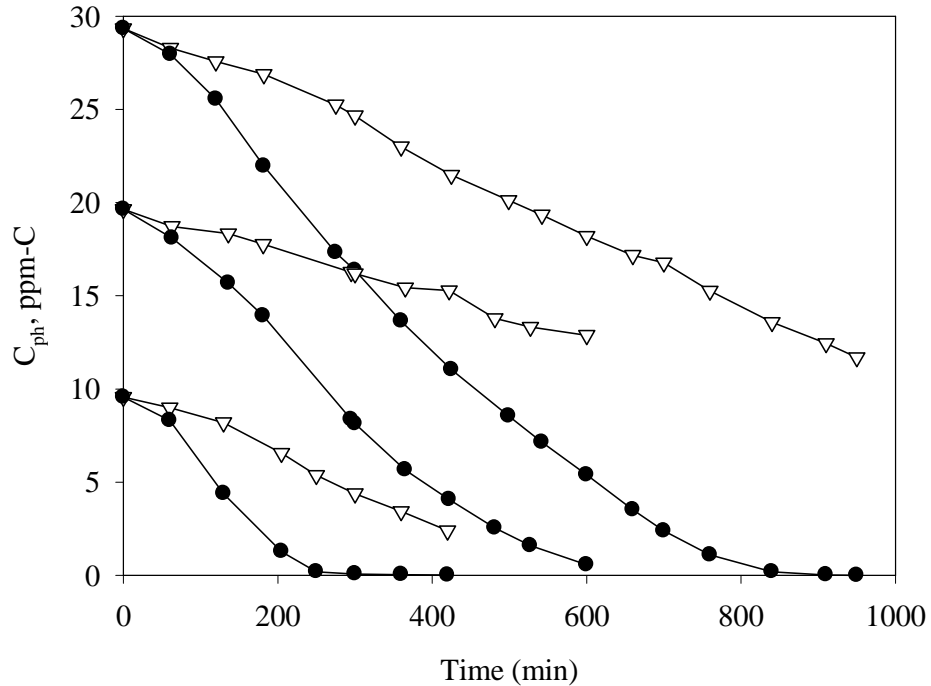
Figure 78 ($\triangledown$) experimental TOC profiles and ($\bullet$) species mass addition of the quantified intermediates for Anatase (OC_{inter})

Thus, the difference between the OC_{Inter} and experimental TOC in Figure 78 can be used to represent the amount of organic carbon contained in the carboxylic acids. OC_{Inter} refer to the concentration of the hydroxylated compounds. Therefore, it was assumed that those intermediates produced and not quantified by the HPLC are carboxylic acids (OC_{AC}) and OC_{AC} was calculated by subtracting OC_{Inter} from TOC as follows:

$$OC_{Ac} = TOC - OC_{Inter} \qquad (94)$$

One should notice that if this OC_{AC} is added to the already lumped concentration of the carboxylic acids, the overall mass balance closes well. This allows applying the kinetic model previously proposed, to any TiO_2 catalysts, regardless of the degree of detection and quantification of the photoconverted intermediates (Ortiz-Gomez 2006).

In the case of Anatase, starting with the unified kinetic model presented in Figure 66, ten kinetic constants were evaluated. From these results, it is found that two kinetic constants are statistically negligible, k_{ph-Ac} and $k_{oDHB-CO2}$. With this first optimization, there is also a high degree of cross-correlation among kinetic parameters.

Based on the previous findings, another optimization is performed for a reaction network with eight kinetic constants. In this case, the kinetic constant that represents the formation of CO_2 from hydroquinone ($k_{pDHB-CO2}$) is smaller compared with the rest of the kinetic constants with very high CI. Also, a high cross-correlation is found between $k_{oDHB-pDHB}$- $k_{pDHB-Ac}$ and $k_{oDHB-pDHB}$- $k_{oDHB-Ac}$. Therefore, two kinetic models are proposed; KM1-Ana-1 and KM2-Ana-1 which are depicted in Figure 79 and Figure 80.

Both reaction networks consist of six kinetic constants. The first one considers that only phenol is directly oxidized to CO_2, while the second one assumes that only hydroquinone is directly decomposed to CO_2 and water.

In order to find the kinetic model that better describes phenol degradation on Anatase, parameter optimization of the kinetic constants need to be performed in both cases. The simultaneous parameter optimization of the kinetic constants in KM1-Ana-1 is presented in Table 31. Also, the cross correlation coefficient matrix is obtained and presented in Table 32.
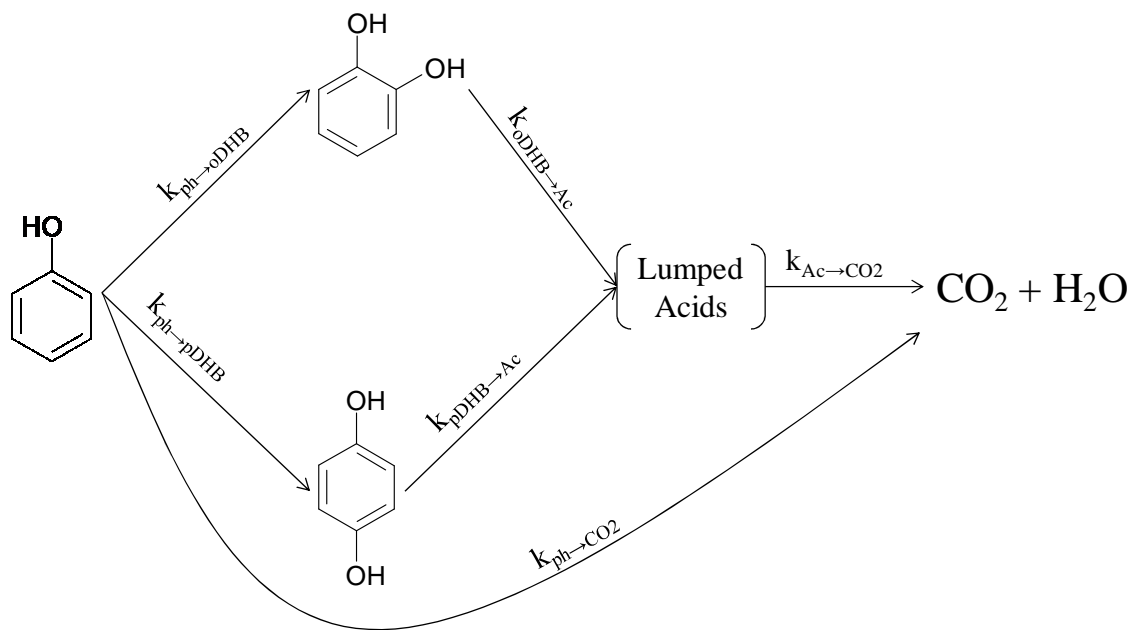
Figure 79 Kinetic network for phenol degradation of Anatase (KM1-Ana1)
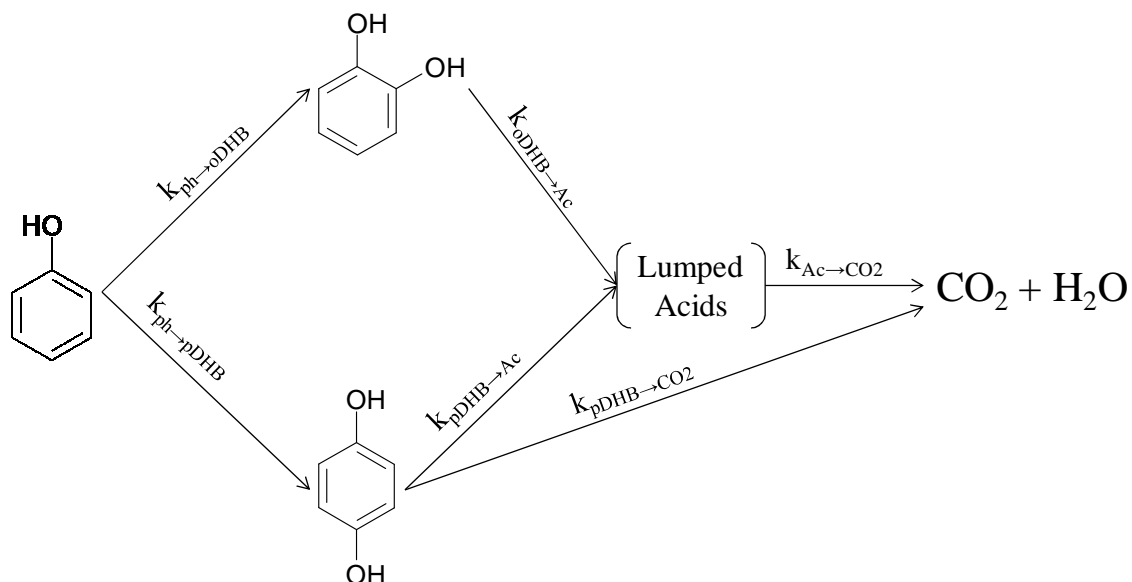
Figure 80 Kinetic network for phenol degradation of Anatase (KM2-Ana1)

Table 31 Estimated parameters for the simultaneous optimization of phenol for 30, 20, and 10 ppm-C in phenol on Anatase for reaction scheme in KM1-Ana-1

Parameter	Symbol	Value	95% CI	STD
$k_{ph-oDHB}$	k_1	1.004×10^{-2}	1.722×10^{-3}	4.606×10^{-4}
$k_{ph-pDHB}$	k_2	8.503×10^{-3}	1.642×10^{-3}	4.392×10^{-4}
k_{ph-CO2}	k_3	4.907×10^{-3}	5.274×10^{-4}	1.411×10^{-4}
$k_{oDHB-Ac}$	k_4	4.508×10^{-2}	9.268×10^{-3}	2.480×10^{-3}
$k_{pDHB-Ac}$	k_5	2.135×10^{-2}	5.098×10^{-3}	1.364×10^{-3}
k_{Ac-CO2}	k_6	4.546×10^{-3}	4.318×10^{-4}	1.155×10^{-4}

Table 32 Cross-correlation coefficients for the simultaneous optimization of 30, 20, and 10 ppm-C of phenol on Anatase for KM1-Ana1

	k_1	k_2	k_3	k_4	k_5	k_6
k_1	1.00					
k_2	-0.83	1.00				
k_3	-0.17	0.03	1.00			
k_4	0.55	-0.65	-0.16	1.00		
k_5	-0.84	0.80	-0.02	-0.69	1.00	
k_6	0.15	0.16	0.80	-0.07	0.02	1.00

For the case of KM2-Ana-1, the optimized kinetic constants are reported in Table 33 for the simultaneous optimization of three different initial phenol concentrations. Likewise, Table 34 reports the cross-correlation coefficients for this optimization.

Table 33: Estimated parameters for the simultaneous optimization of phenol for 30, 20, and 10 ppm-C in phenol on Anatase for reaction scheme in KM2-Ana-1

Parameter	Symbol	Value	95% CI	STD
$k_{ph-oDHB}$	k_1	1.238×10^{-2}	1.136×10^{-3}	3.040×10^{-4}
$k_{ph-pDHB}$	k_2	1.058×10^{-2}	1.052×10^{-3}	2.814×10^{-4}
k_{ph-CO2}	k_3	5.767×10^{-2}	7.527×10^{-3}	2.015×10^{-3}
$k_{oDHB-Ac}$	k_4	5.035×10^{-3}	3.219×10^{-3}	8.613×10^{-4}
$k_{pDHB-Ac}$	k_5	2.229×10^{-2}	3.260×10^{-3}	8.723×10^{-4}
k_{Ac-CO2}	k_6	2.553×10^{-3}	5.741×10^{-4}	1.536×10^{-4}

Table 34: Cross-correlation coefficients for the simultaneous optimization of 30, 20, and 10 ppm-C of phenol on Anatase for KM2-Ana1

	k_1	k_2	k_3	k_4	k_5	k_6
k_1	1.00					
k_2	-0.60	1.00				
k_3	-0.16	-0.14	1.00			
k_4	-0.69	0.64	-0.10	1.00		
k_5	0.52	-0.74	0.20	-0.95	1.00	
k_6	-0.16	0.13	-0.23	0.74	-0.72	1.00

In spite of the fact that both kinetic models fit very well with the experimental data, other aspects have to be considered when selecting the best model for phenol on Anatase. If the matrices of cross-correlation coefficients are compared, it is apparent that the KM2-Ana-1 has higher cross-correlation among the kinetic parameters. For instance, a value of -0.95 is found for the cross-correlation between $k_{pDHB-CO2}$ and $k_{pDHB-Ac}$. Another critical factor in selecting the best kinetic model is the value for the CI. In this respect, KM1-Ana-1 shows the lowest values for the CI giving more credit to its applicability in the kinetic modeling of phenol on Anatase.

One should mention that other different reaction schemes were considered (not shown here) in the context of the present study. However; for KM1-Ana-1, it was found the "series-parallel" model described in Figure 79 was the model leading to the lowest cross-correlation among parameters, smallest CI and better fit to the experimental data. Therefore, KM1-Ana-1 is used to predict the experimental data. Figure 81 compares the experimental values with the model predictions. A good prediction of experimental values can be observed. The reconciliation plot for the optimization and the residuals of the KM1-Ana-1 are presented in Figure 82 and Figure 83 respectively. Thus KM1-Ana-1 provided an excellent case for the "series-parallel" model unified testing.
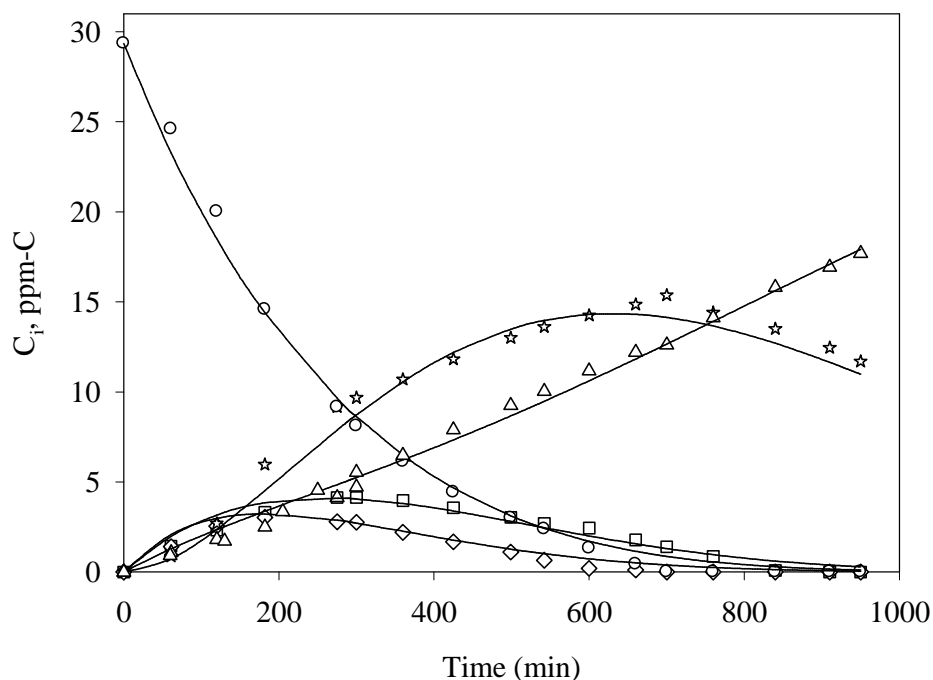
Figure 81 Experimental and estimated concentration profiles for (○) phenol, (□) hydroquinone, (◊) catechol, (☆) lumped acids, (Δ) CO_2, and (—) model for 30 ppm-C initial concentration in phenol for KM1-Ana-1
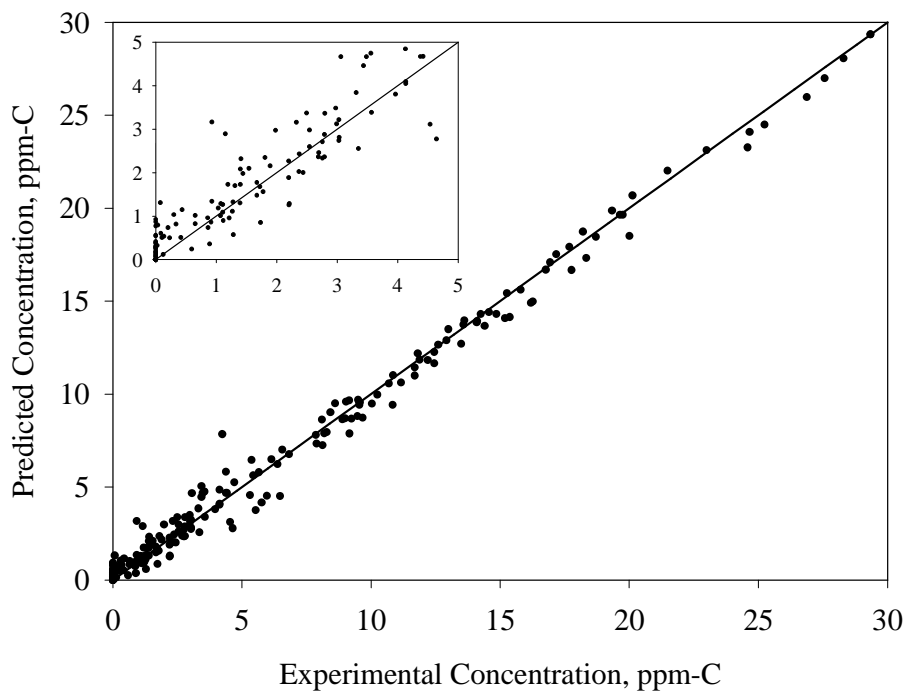
Figure 82 Reconciliation plot showing the results for the KM1-Ana-1 when seven kinetic parameters are estimated using the Anatase catalyst
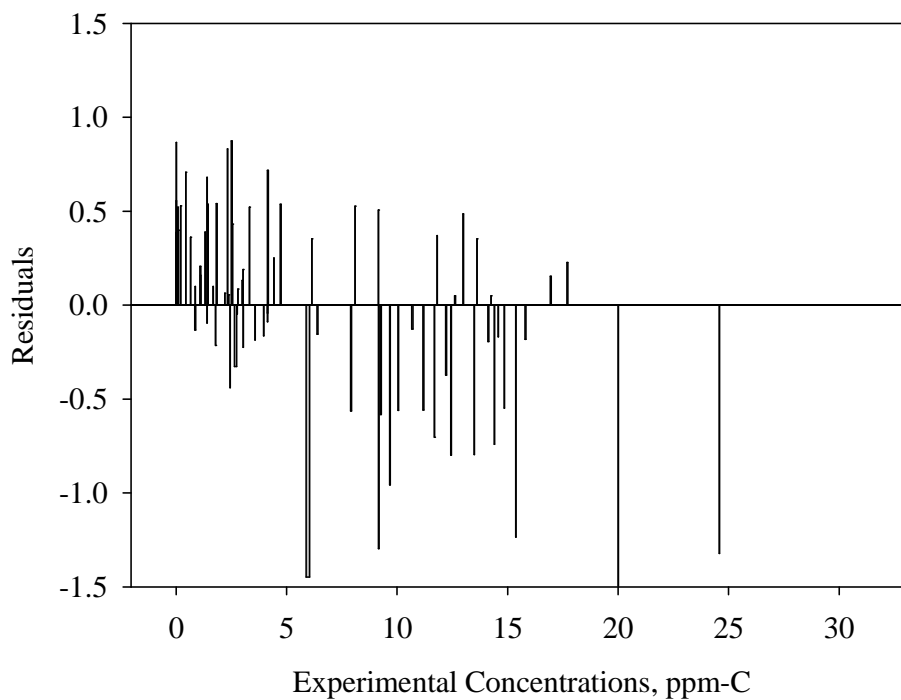
Figure 83 Residuals for the parameter estimation of KM1-Ana-1

7.2.3   Hombikat UV-100

It was found in Chapter 6 of this dissertation that during the photodegradation of phenol on Hombikat UV-100, catechol is not detected as an intermediate species. It was also found that benzoquinone was produced in amounts that cannot be neglected during the kinetic model. Therefore, the unified "Series-Parallel" reaction network reported in Figure 65 has to be adapted with specifics for Hombikat UV-100 as shown in Figure 84.
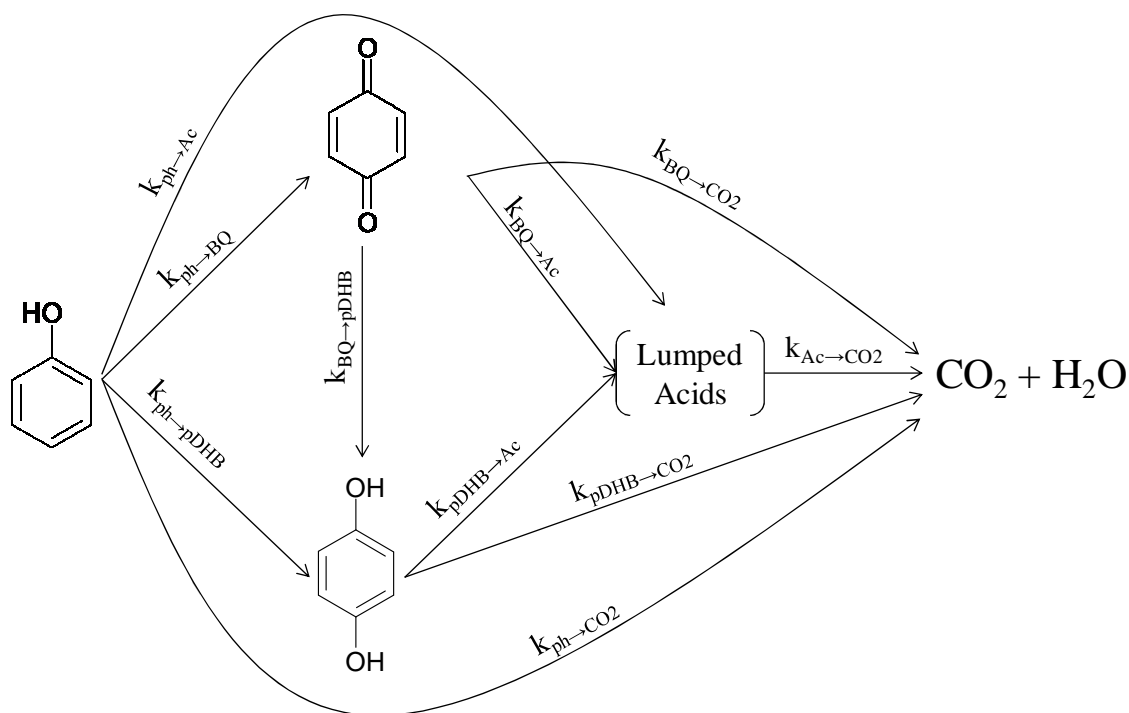
Figure 84 Simplified RN for scenario one in the kinetic modeling of phenol on Hombikat UV-100

One should notice that the reaction network of Figure 84 contains ten kinetic constants, with a kinetic constant representing the formation of hydroquinone from benzoquinone included in the network. Since benzoquinone was formed at small concentrations when compared with hydroquinone; two scenarios are considered in the kinetic modeling for this photocatalyst. The first approach considers benzoquinone as an intermediate, with the rest of the network being close to the one of Figure 84. The second scenario considers benzoquinone in very small concentration and, as a result, Figure 85 is adopted for modeling chemical changes.
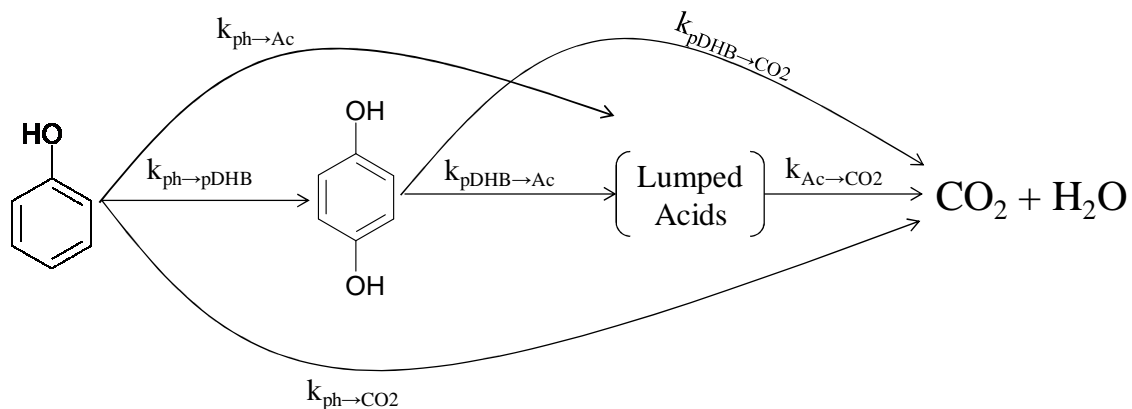
Figure 85 Reaction network for scenario two in the kinetic modeling of phenol on Hombikat UV-100

For the first scenario, and by using experimental data, a simultaneous optimization for the ten kinetic constants is performed. Results from the optimization conclude that three kinetic constants are statistically insignificant: $k_{BQ\text{-}CO2}$, $k_{BQ\text{-}Ac}$, and $k_{pDHB\text{-}CO2}$.

After this first optimization, the reaction network was left with only seven kinetic constants. A second parameter optimization was then performed. With this optimization, a negative value for the lower confidence interval for $k_{ph\text{-}Ac}$ is found. Therefore, this parameter was eliminated from the model. This action reduced the number of parameters to be estimated. Now, with only six kinetic parameters left, the reaction model for Hombikat UV-100 was obtained as reported in Figure 86. This reaction scheme is designated KM1-Hom UV-100.

The optimized values found in this case are reported in Table 35 with their respective 95% CI. Table 36 reports the matrix of cross-correlation coefficients. It is then concluded that the kinetic network presented in Figure 86 accurately describes phenol photodegradation on Hombikat UV-100. Kinetic parameters were obtained with low CI and moderate cross-correlation among parameters. This model considers that benzoquinone only forms hydroquinone. This fact is in agreement with the experimental observations reported in Chapter 6. In this section, it was found that benzoquinone rapidly transforms into hydroquinone once the photoreactor is initiated.
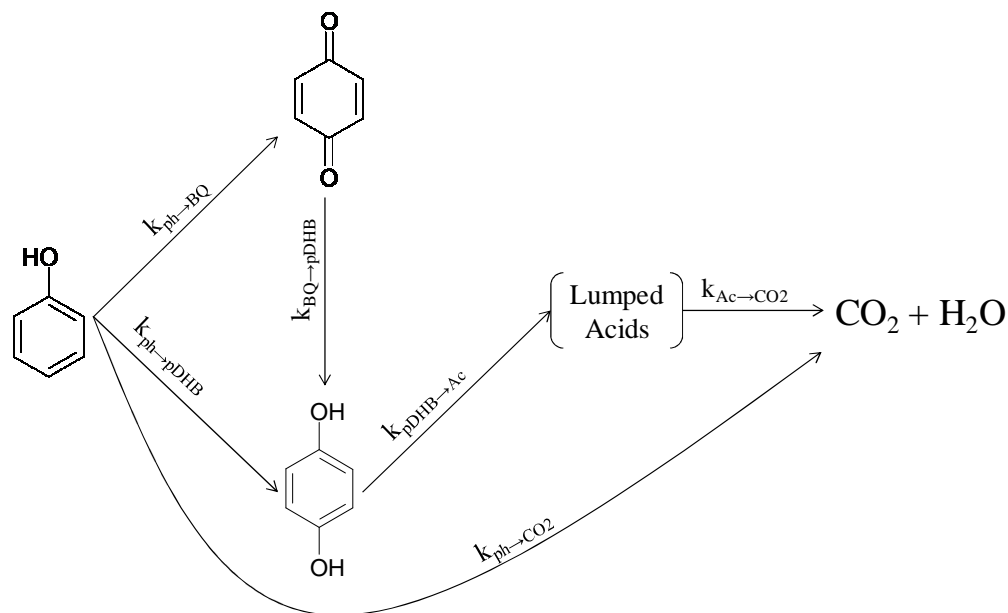
Figure 86 Optimal RN for phenol degradation on Hombikat UV-100. KM1-Hom UV-100

Table 35 Estimated parameters for the simultaneous optimization of phenol for 30, 20, and 10 ppm-C in phenol for the KM1-Hombikat UV-100 network

Parameter	Symbol	Value	95% CI	STD
k_{ph-BQ}	k_1	1.134×10^{-3}	4.774×10^{-4}	1.277×10^{-4}
$k_{ph-pDHB}$	k_2	1.622×10^{-3}	5.616×10^{-4}	1.502×10^{-4}
k_{ph-CO2}	k_3	5.844×10^{-3}	2.411×10^{-4}	6.449×10^{-5}
$k_{BQ-pDHB}$	k_4	1.870×10^{-2}	9.584×10^{-3}	2.654×10^{-3}
$k_{pDHB-Ac}$	k_5	1.487×10^{-2}	2.060×10^{-3}	5.510×10^{-4}
k_{Ac-CO2}	k_6	4.381×10^{-2}	1.325×10^{-2}	3.544×10^{-3}

Table 36 Cross-correlation coefficients for the simultaneous optimization of 30, 20, and 10 ppm-C of phenol for the KM1-Hombikat UV-100 network

	k_1	k_2	k_3	k_4	k_5	k_6
k_1	1.00					
k_2	-0.78	1.00				
k_3	0.15	-0.56	1.00			
k_4	0.87	-0.66	0.24	1.00		
k_5	0.05	0.30	-0.74	-0.15	1.00	
k_6	0.03	0.21	-0.57	0.14	0.22	1.00

In the analysis of the kinetic constants in scenario two (i.e. reaction network in Figure 85), a very small value for the kinetic constant $k_{pDHB\text{-}CO2}$ with very large CI was found. Therefore, this constant was dropped out from the model. A second optimization was performed with only five kinetic constants. In this case, it was found a negative lower CI for the kinetic constant $k_{ph\text{-}Ac}$. Although, at this point there was no high cross-correlation among coefficients, a negative value for the lower CI is enough to consider the kinetic constant negligible. A final optimization was performed with only 4 kinetic constants. The final reaction scheme for scenario two is shown in Figure 87. This reaction scheme is called KM2-Hom UV-100.
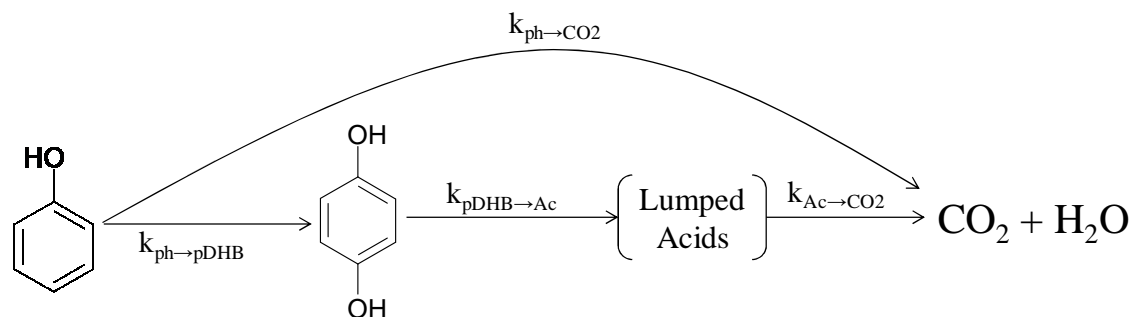
Figure 87: Optimal RN for phenol degradation on Hombikat UV-100. KM2-Hom UV-100

Table 37 and Table 38 report optimized parameters and cross correlation coefficients for KM2-Hombikat UV-100. Comparing KM1 and KM2 for Hombikat, it can be observed that the KM1, with six kinetic parameters presents slightly larger CI values for the optimized parameters. Furthermore, one can notice that both kinetic models present very moderate cross correlation among coefficients.

Table 37 Estimated parameters for the simultaneous optimization of phenol for 30, 20, and 10 ppm-C in phenol for the KM2-Hombikat UV-100

Parameter	Symbol	Value	95% CI	STD
$k_{ph-pDHB}$	k_1	2.337×10^{-3}	2.745×10^{-4}	7.347×10^{-5}
k_{ph-CO2}	k_2	5.953×10^{-3}	2.494×10^{-4}	6.674×10^{-5}
$k_{pDHB-Ac}$	k_3	1.184×10^{-2}	1.839×10^{-3}	4.923×10^{-4}
k_{Ac-CO2}	k_4	2.979×10^{-2}	8.833×10^{-3}	2.364×10^{-3}

Table 38 Cross-correlation coefficients for the simultaneous optimization of 30, 20, and 10 ppm-C of phenol for the KM2-Hombikat UV-100

	k_1	k_2	k_3	k_4
k_1	1.00			
k_2	-0.87	1.00		
k_3	0.69	-0.78	1.00	
k_4	0.49	-0.63	0.22	1.00

Therefore; from a rigorous statistical point of view, KM2-Hombikat UV-100 presented in Figure 87 is the most appropriate reaction scheme for the modeling of phenol on Hombikat UV-100. All intermediate species were included with the only exception of benzoquinone. For KM1 the CIs for the optimized coefficients were a bit larger than KM2.

While for kinetic modeling it is desirable that the optimized kinetic constants present the lowest possible CI, one also has to consider the matching of the model predictions with the experimental observations.

Similarly to these findings, some kinetic models for phenol photodegradation presented in the literature propose that mineralization of any substrate to CO_2 occur through one single intermediate *I*, as follows (Bellobono at al. 2009; Tatti et al, 1997;Rota et al. 1996):

$$S \rightarrow I \rightarrow CO_2 + H_2O \tag{95}$$

where *S* is the organic model compound, phenol in this study and *I* represents all the lumped intermediates generated during the photoreaction. This approach does not require determination of intermediate species because the concentration *I* can be measured from the difference between the TOC profiles and the model compound.

This overall mechanism however, does not account for the complete decomposition of the substrate into CO_2 and H_2O. Complete decomposition of organic molecules such as phenol is apparent from the reduction of TOC shortly after irradiation starts. In our study, this complete decomposition is represented by the kinetic constants $k_{ph\text{-}CO2}$, $k_{o\text{-}DHB\text{-}CO2}$, $k_{p\text{-}DHB\text{-}CO2}$ and $k_{BQ\text{-}CO2}$. For KM2-Hombikat UV-100, only $k_{ph\text{-}CO2}$ was considered significant in the kinetic modeling.

An optimization for phenol degradation considering that phenol and hydroquinone do not undergo complete decomposition (as indicated in Figure 88), was performed. In this case, only three kinetic constants were optimized. Results showed that by not considering direct oxidation, the model profiles predict poorly experimental observations (results not shown here). This provides evidence that phenol and its intermediates undergo direct mineralization to CO_2 and H_2O. Several authors agree with this observation (Zhang et al. 2006; de Lasa et al. 2005; Ortiz-Gomez et al. 2006, 2007 and 2008; Salaices et al. 2001).
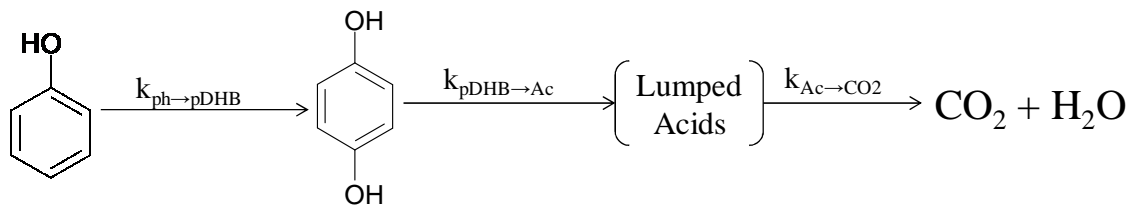
Figure 88 Reaction network for phenol degradation on Hombikat UV-100, direct degradation of phenol into CO_2 is not considered

It is in this respect, difficult to prove that phenol and its intermediates can undergo complete mineralization to produce CO_2. One can; however, envision this situation in the reactor volume regions with high density of photons. Thus; it is concluded from the kinetic model, that neglecting these steps (or kinetic constants) leads to a discrepancy between model and experimental profiles not being adequate for photoreactor simulations, such as Photo-CREC Water II, with significant variation of photon density. Experimental and model predictions for KM1-Hombikat UV-100 are shown in Figure 89. Good agreement between experimental and model profiles is observed.
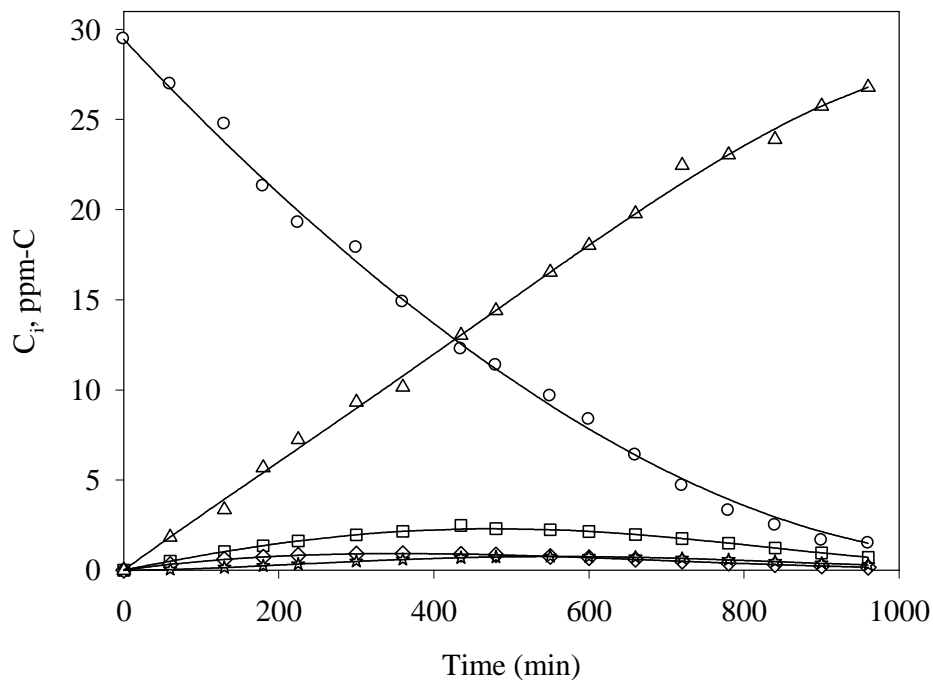
Figure 89 Experimental and estimated concentration profiles for (○) phenol, (□) hydroquinone, (◊) benzoquinone, (☆) lumped acids, (Δ) CO_2, and (——) model for 30 ppm-C initial concentration in phenol for KM1-Hombikat UV-100

7.2.4   Sol-Gel Cat

Again, by starting from the simplified general kinetic model, an optimization is performed for ten kinetic constants. In this first optimization, three kinetic constants were found negligible; $k_{ph\text{-}Ac}$, $k_{oDHB\text{-}CO2}$, and $k_{oDHB\text{-}AC}$. A second optimization of parameters is carried out. Results are reported in Table 39 for the optimized values, while the cross-correlation coefficients are presented in Table 40. The resulting kinetic model, KM-Sol-Gel Cat is shown in Figure 90.

Table 39 Estimated parameters for the simultaneous optimization of phenol for 30, 20, and 10 ppm-C in phenol on Sol-Gel Cat for KM-Sol-Gel Cat

Parameter	Symbol	Value	95% CI	STD
$k_{ph-oDHB}$	k_1	2.656×10^{-3}	1.023×10^{-3}	3.915×10^{-4}
$k_{ph-pDHB}$	k_2	8.319×10^{-3}	1.205×10^{-3}	4.610×10^{-4}
k_{ph-CO2}	k_3	9.202×10^{-3}	6.635×10^{-4}	2.539×10^{-4}
$k_{oDHB-pDHB}$	k_4	2.734×10^{-2}	1.316×10^{-2}	5.036×10^{-3}
$k_{pDHB-Ac}$	k_5	8.918×10^{-3}	2.070×10^{-3}	7.922×10^{-4}
$k_{pDHB-CO2}$	k_6	1.231×10^{-2}	3.284×10^{-3}	1.257×10^{-3}
k_{Ac-CO2}	k_7	1.395×10^{-2}	4.455×10^{-3}	1.705×10^{-3}

Table 40 Cross-correlation coefficients for the simultaneous optimization of 30, 20, and 10 ppm-C of phenol on Sol-Gel Cat for KM-Sol-Gel Cat

	k_1	k_2	k_3	k_4	k_5	k_6	k_7
k_1	1.00						
k_2	-0.75	1.00					
k_3	-0.05	-0.52	1.00				
k_4	0.74	-0.78	0.08	1.00			
k_5	-0.17	-0.16	0.53	-0.12	1.00		
k_6	0.21	0.31	-0.85	0.05	-0.82	1.00	
k_7	-0.24	-0.11	0.55	-0.21	0.84	-0.76	1.00

From the results reported above, low confidence intervals, as well as low cross-correlation in the kinetic parameters, are observed. Therefore, the reaction scheme presented in Figure 90 is found to appropriately predict experimental profiles for phenol and its photoconverted intermediates species on Sol-Gel Cat photocatalyst.
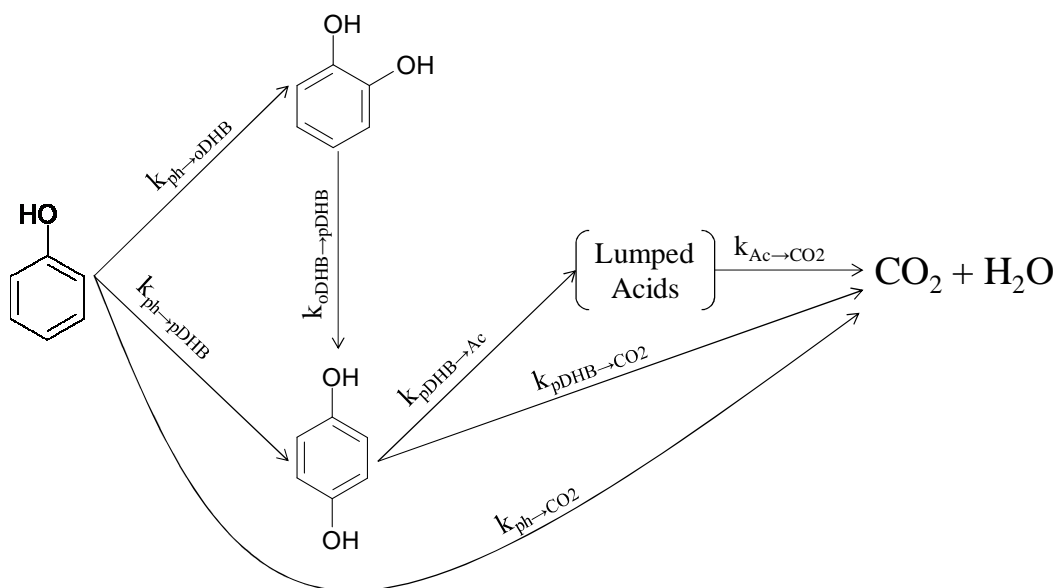
Figure 90 Optimal reaction network for phenol degradation on Sol-Gel Cat: KM-Sol-Gel Cat

7.2.5 Influence of Fe^{3+} ions on the kinetic modeling for DP 25 and Sol-Gel Cat

Lastly, the influence of Fe^{3+} ions on the kinetic model of phenol degradation on DP 25 and Sol-Gel Cat is studied. When Fe^{3+} ions were used in the reacting media, hydroquinone was produced at higher concentrations than when the catalysts were used alone. The objective of this subsection is to analyze the influence of the Fe^{3+} on the kinetic modeling. As done for previous photocatalysts, the kinetic model is based on the simplified reaction scheme with ten kinetic constants. Carboxylic acids are lumped into a single term and also, the difference between experimental TOC and TOC from the intermediate species balance is included in the lumped acids term.

For the case of DP 25+5 ppm Fe^{3+}, the optimum reaction network obtained is presented in Figure 91.This reaction network has seven kinetic parameters, their values are reported in Table 41. Table 42 reports the cross-correlation matrix.
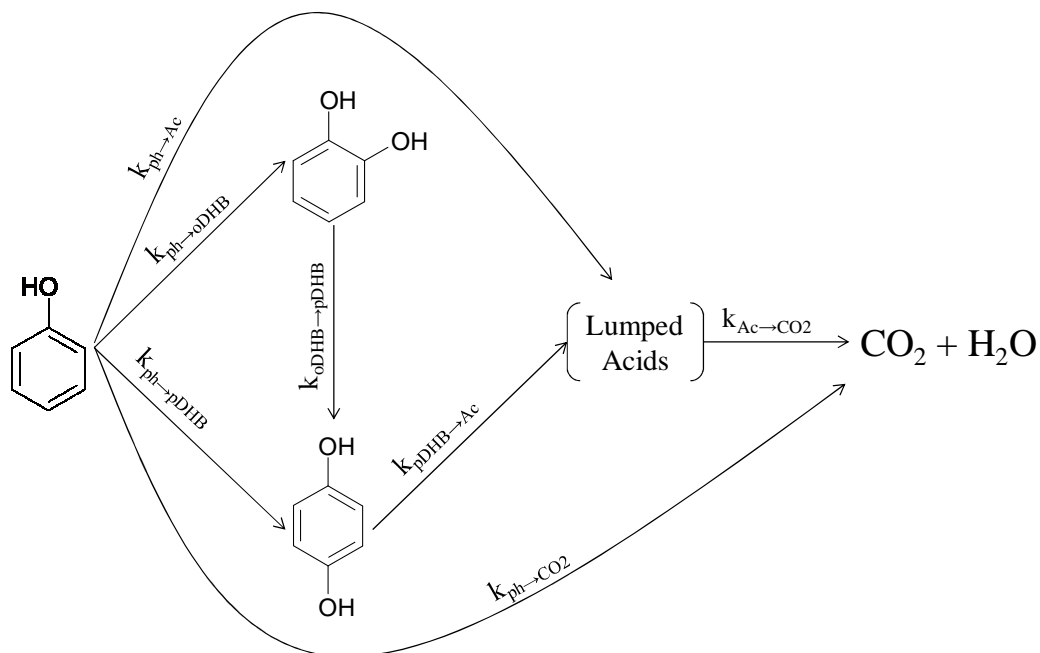
Figure 91 Reaction scheme obtained for the kinetic modeling of phenol degradation on DP 25+5 ppm Fe^{3+}, KM-DP 25+Fe

The low values for the CI and cross-correlation coefficients support the application of the KM-DP 25+Fe for the prediction of experimental profiles of phenol degradation and intermediate species on DP 25 and iron ions in solution.

Table 41 Estimated parameters for the simultaneous optimization of phenol for 30, 20, and 10 ppm-C in phenol on DP 25+Fe^{3+}, KM-DP 25+Fe

Parameter	Symbol	Value	95% CI	STD
k_{ph-Ac}	k_1	7.384×10^{-4}	2.201×10^{-4}	6.052×10^{-5}
$k_{ph-oDHB}$	k_2	5.183×10^{-3}	1.392×10^{-3}	3.693×10^{-4}
$k_{ph-pDHB}$	k_3	6.019×10^{-3}	1.980×10^{-3}	5.253×10^{-4}
k_{ph-CO2}	k_4	7.005×10^{-3}	1.480×10^{-3}	3.927×10^{-4}
$k_{oDHB-pDHB}$	k_5	1.515×10^{-2}	5.263×10^{-3}	1.396×10^{-3}
$k_{pDHB-Ac}$	k_6	2.159×10^{-2}	4.304×10^{-3}	1.142×10^{-3}
k_{Ac-CO2}	k_7	3.516×10^{-2}	8.761×10^{-3}	2.324×10^{-3}

Residual and consolidation plots are not presented in this study for the sake of space. However, it is concluded that the model predicts very well the experimental profiles.

Table 42 Cross-correlation coefficients for the simultaneous optimization of 30, 20, and 10 ppm-C of phenol on DP 25+Fe^{3+}, KM-DP 25+Fe

	k_1	k_2	k_3	k_4	k_5	k_6	k_7
k_1	1.00						
k_2	-0.03	1.00					
k_3	-0.49	-0.58	1.00				
k_4	0.78	0.05	0.10	1.00			
k_5	0.02	0.77	-0.67	0.08	1.00		
k_6	-0.66	0.15	0.45	0.23	-0.07	1.00	
k_7	0.29	0.09	0.04	0.59	-0.08	-0.11	1.00

Kinetic modeling of phenol on Sol-Gel Cat under the influence of iron ions is also performed. If one starts from the general reaction network presented in Figure 66, one finds an "optimum reaction network" as shown in Figure 92.This model only presents 7 kinetic constants. Results for the final optimization are presented in Table 43 and Table 44 respectively.
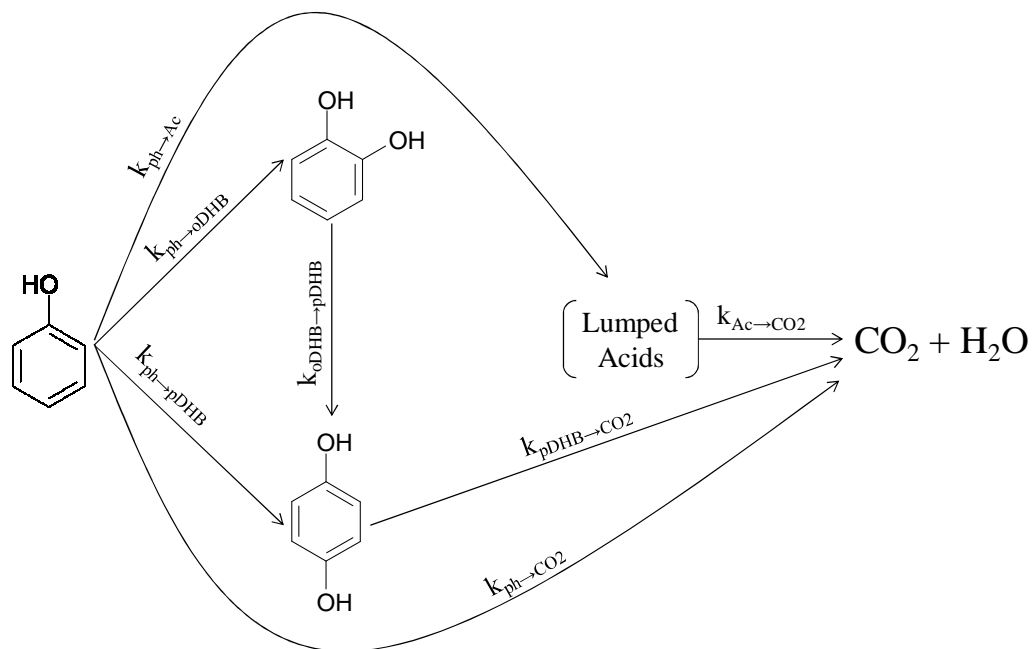
Figure 92 Reaction scheme obtained for the kinetic modeling of phenol degradation on Sol-Gel Cat+5 ppm Fe^{3+}, KM-Sol-Gel Cat+Fe

Table 43 Estimated parameters for the simultaneous optimization of phenol for 30, 20, and 10 ppm-C in phenol on Sol-Gel Cat+Fe^{3+}, KM-Sol-Gel Cat + Fe

Parameter	Symbol	Value	95% CI	STD
k_{ph-Ac}	k_1	2.762×10^{-3}	8.090×10^{-4}	2.144×10^{-4}
$k_{ph-oDHB}$	k_2	5.603×10^{-3}	1.786×10^{-3}	4.734×10^{-4}
$k_{ph-pDHB}$	k_3	6.201×10^{-3}	2.321×10^{-3}	6.152×10^{-4}
k_{ph-CO2}	k_4	6.482×10^{-3}	1.315×10^{-3}	3.586×10^{-4}
$k_{oDHB-pDHB}$	k_5	2.173×10^{-2}	8.819×10^{-3}	2.337×10^{-3}
$k_{pDHB-Ac}$	k_6	2.505×10^{-2}	4.939×10^{-3}	1.309×10^{-3}
k_{Ac-CO2}	k_7	5.585×10^{-3}	3.229×10^{-3}	8.558×10^{-4}

The model proposed for Sol-Gel Cat and Fe ions in solution presented low CI and small cross-correlation among parameters.

Table 44 Cross-correlation coefficients for the simultaneous optimization of 30, 20, and 10 ppm-C of phenol on Sol-Gel Cat+Fe^{3+}, KM-Sol-Gel Cat + Fe

	k_1	k_2	k_3	k_4	k_5	k_6	k_7
k_1	1.00						
k_2	-0.24	1.00					
k_3	-0.03	-0.65	1.00				
k_4	-0.09	0.10	-0.67	1.00			
k_5	-0.19	0.81	-0.71	0.20	1.00		
k_6	-0.26	0.19	0.40	-0.76	-0.03	1.00	
k_7	0.78	-0.34	-0.01	-0.02	-0.33	-0.39	1.00

One should mention that, when DP 25 alone is used in the kinetic modeling of phenol photodegradation, the kinetic constant describing the formation of lumped acids from hydroquinone is considered. This same step is not accounted for when phenol is degraded on DP 25+Fe^{3+}. Both kinetic models are very similar with the only difference being the formation of lumped acids from hydroquinone.

Another variation in the kinetic networks is the constraint found between the formation of CO_2 and lumped acids from hydroquinone for DP 25 alone. For DP 25+Fe, this kinetic constant is statistically negligible. One can notice that there are important differences in the experimental profiles for the various chemical species. DP 25+Fe produced hydroquinone and catechol in larger concentrations and this while compared with the DP 25 alone. These differences result in variations of the proposed kinetic models.

The kinetic model proposed for Sol-Gel Cat does not consider formation of CO_2 or lumped acids from phenol. Additionally, formation of catechol from hydroquinone was not included in the final kinetic network. When iron ions in solutions were used, kinetic constants describing the decomposition of phenol to produce catechol, hydroquinone, carboxylic acids and CO_2 are accounted for.

Differences in the proposed kinetic models indicate that each photocatalyst degrades phenol with somewhat different reaction path, while always complying with the "Series-Parallel" reaction network. It is understood that every photocatalyst is different from one another; having different particle diameters, different surface area, and different crystal composition. Therefore, it is expected that each individual photocatalyst renders different product

distribution with different overall degradation rates. In spite of all this, it appears remarkably significant that all photocatalyst studied proceed with a close "Series-Parallel" reaction network providing the basis for a unified kinetic modeling.

7.3   Simple Version of the Unified Kinetic Model for TOC

Prediction of the evolution of TOC with irradiation time is an operating parameter of great importance for the practical implementation of photocatalytic processes. After all, the engineer in the drinking water purification plant is interested in the irradiation time required to achieve a minimum TOC level. This TOC parameter has also become of great importance because the observed TOC decay displays a zero order for the phenol photoconversion at various initial concentrations (Salaices-Arredondo (2002), Ortiz Gomez (2006)). This zero order is, in fact a consequence, as shown by Eq. (93) and Figure 77 for DP 25, of how the individual chemical species, as given by the Unified Kinetic Model of this study, add up at all times in the process. Moreover, this zero order behavior is a trend consistently observed for all catalyst studied in this thesis. Therefore, this trend provides a most valuable finding for future design and scale up of photocatalytic processes.

In this respect, Figure 93 illustrates the application of the Unified Kinetic Model first presented in Eq. (31) and in Eq.(30) of Chapter 3 for different initial concentrations of phenol on TiO_2. Values for the empirical constants for all the catalysts studied are reported in Table 45 . Initial rates were calculated for the first 60 minutes of irradiation in all cases. Good agreement is found between experimental and model fitting profiles for most of the irradiation time. However, there is a somewhat of a tailing in the TOC model profiles during last hours of irradiation which is not shown by the experimental data.

This data treatment allows TOC degradation to be predicted as a function of initial TOC and irradiation time. It has to be stated that even though the model predicts well the experimental TOC data, the determined kinetic constants are empirical in nature, having a limited physical-chemical meaning. Regarding this TOC based kinetic model for phenol photodegradation, special care has to be taken when numerically determining the empirical constants. Linearization of Eq. (29) allows determining the relationship among constants, and hence, a single solution for the three empirical constants. Otherwise; if the model is applied

without previous linearization, multiple solutions for the optimized parameters may be
obtained.

Table 45 Fitting parameters for the kinetic modeling using TOC profiles

Catalyst	Fitting Parameters			
	Parameter	Value	95% CI	R^2
DP 25	β_1	0.2699	0.0256	
	β_2	7.8110	0.8895	0.995
	β_3	8.1915	0.7759	
Anatase	β_1	0.0044	0.0005	
	β_2	2.2470	0.1693	0.876
	β_3	0.1385	0.0147	
Hombikat UV-100	β_1	0.0047	0.0006	
	β_2	0.5563	0.0853	0.994
	β_3	0.1386	0.0165	
Sol-Gel Cat	β_1	0.0051	0.0012	
	β_2	0.0620	0.0053	0.999
	β_3	0.1407	0.0323	
DP 25+Fe	β_1	0.0010	0.0005	
	β_2	0.0245	0.0145	0.995
	β_3	0.0257	0.0162	
Sol-Gel Cat+Fe	β_1	0.0001	2.9×10^{-5}	
	β_2	0.0170	0.0040	0.965
	β_3	0.0018	0.0006	
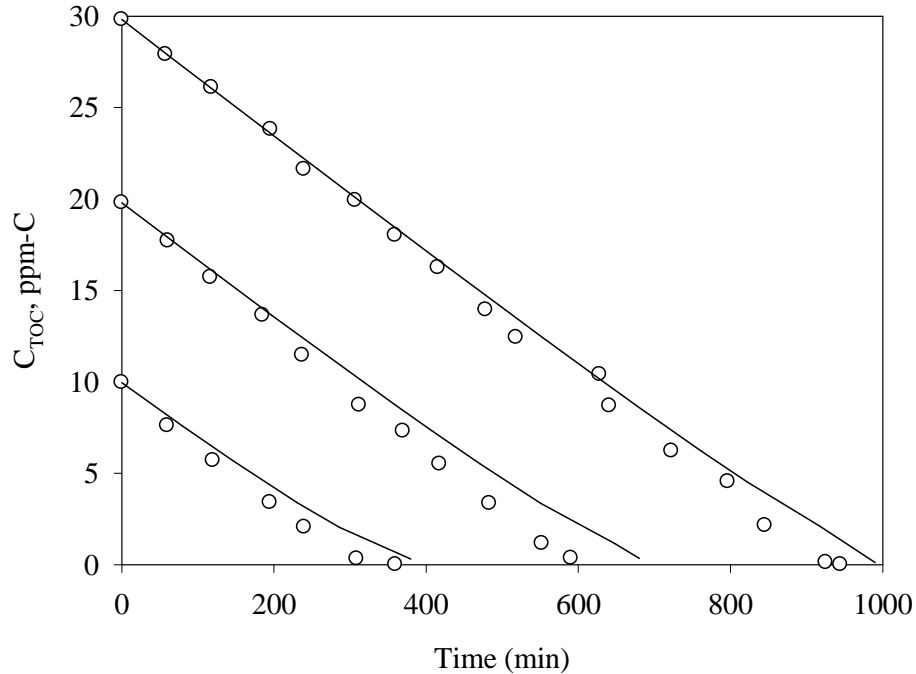
Figure 93 (○) Experimental TOC profiles for phenol degradation on DP 25 vs. (——) model fitting found with Eq. (31)

7.4 Conclusions

From the discussion presented in this chapter, the following conclusions can be stated:

(a) A phenomenological based unified kinetic model is proposed for the obtained experimental observations in phenol photodegradation. This L-H kinetic model is based on a "series-parallel" reaction network. This model is found to be applicable to the various TiO_2 photocatalysts of the present study.

(b) The unified kinetic model requires a number of significant assumptions to be effective, avoiding overparametization. As a result, the unified kinetic model is adapted for each specific photocatalyst under study. For instance; given that some intermediate chemical species are present in very small amounts, they are not included in the kinetic analysis. As well, carboxylic acids are lumped together into a single term in the rate equation.

(c) The proposed unified kinetic model is able to fit the experimental data satisfactorily for the various chemical species resulting from photocatalytic conversion of phenol.

Experimental results are obtained at three different initial concentrations: 30, 20, and 10, ppm-C of phenol. This allows application of the unified kinetic constants for a wide range of phenol concentrations.

(d) A rigorous statistical methodology is adopted for the evaluation of individual kinetic models involved of the unified kinetic model considered. The kinetic parameter selection is based on the correlation coefficients (R^2), smallest 95% CI with the lowest cross-correlation among kinetic parameters and lowest residuals. The adequacy of the final models is further established by analyzing their physical significance. The obtained kinetic constants are always positive within a reasonable range of expected values.

(e) The unified kinetic model involves chemical species adsorption constants. These adsorption constants are determined independently. This allows implementing a kinetic constant regression procedure, where cross-correlation between kinetic constants is considerably reduced.

(f) The unified kinetic model is able to predict TOC at various irradiation times. In order to accomplish this, the addition of various chemical species ODE is considered. This additive approach proves to be valid for the six photocatalysts used in this study.

(g) An empirical kinetic model based on TOC profiles only is capable of predicting TOC profiles concentrations.

Chapter 8
Results and Discussion Part IV: Efficiency Assessment in the Photo-CREC Water II Photoreactor

8   Introduction

The importance of energy efficiency assessments for various reactor configurations has been emphasized in the technical literature in recent years (Serrano et. al. 2009 and 2010; Moreno-Pirajan 2007; Ortiz-Gomez 2006, Salaices-Arredondo 2002). Nonetheless, energy efficiency determination remains an area of challenges given the different variables involved in its calculation. Variables, such as reaction rates, reaction mechanism, kinetic parameters, adsorption constants, light being absorbed by the solid semiconductors, etc.

In this Chapter, the Photochemical Thermodynamic Efficiency Factor (PTEF), first introduced by Serrano and de Lasa (1997), is evaluated in order to obtain the reactor efficiencies for the different TiO_2 photocatalysts. The PTEF determination requires that all the hydroxyl radicals are accounted in the photoconversion of phenol. The hydroxyl radicals, the main species contribution to the photocatalytic conversion, are calculated using the results from the unified kinetic model for every photocatalyst studies. The quantum yield (QY), another very popular efficiency parameter is also computed.

8.1   PTEF Definition

The PTEF was originally proposed by Serrano and de Lasa (Serrano et al. 1997 and 1999). These authors further progressed in energy efficiency assessments providing better reaction networks and enhancing in this manner kinetics and irradiation modeling (Serrano et al. 2009 and 2010). As a result, a more accurate and comprehensive determination of reactor efficiency was provided.

In the present chapter, both the PTEF and the QY are obtained following the same procedure described by the previously mentioned authors. Both, the PTEF, and QY are obtained using the reaction schemes presented in previous Chapter 7 for each photocatalyst employed in phenol photodegradation. This allows the calculation of the total $OH^\bullet$ consumed at various extends of phenol photoconversion, as described by Serrano et al. 2009.

The PTEF considers the ratio between the energy utilized for the formation of $OH^\bullet$ and the energy absorbed by the TiO_2 catalyst as follows:

$$PTEF = \eta_{OH^\bullet} = \frac{Q_{used}}{Q_{abs}} = \frac{-r_{OH^\bullet}.\Delta H_{OH^\bullet}.W_{irr}}{Q_{abs}} \tag{96}$$

with $r_{OH^\bullet}$ being the total reaction rate of $OH^\bullet$ radicals, $\Delta H_{OH^\bullet}$ is the enthalpy of formation of the hydroxyl radical, W_{irr} is the weight or irradiated catalyst, and Q_{abs} is the radiation being absorbed by the different TiO_2 catalysts.

According to Eq. (96), the main parameters to estimate the PTEF are the values of the rate of reaction of the free radical $OH^\bullet$ ($r_{OH^\bullet,T}$) consumption, the enthalpy of $OH^\bullet$ radical formation ($\Delta H_{OH^\bullet}$), and the absorbed photons by the catalyst (Q_{abs}). Absorbed photons were determined as described in Chapter 5, and this for every photocatalyst.

The enthalpy of formation of $OH^\bullet$ was reported to be 98.3 kj/mol (Serrano et al. 2009). Therefore, the remaining variable was the rate of consumption of the hydroxyl radicals. This reaction rate was determined following the same procedure developed by Serrano et al. (2009)

Regarding $r_{OH^\bullet}$, it can be calculated by the following equation:

$$r_{OH^\bullet} = \sum r_{OH^\bullet\, j} = \sum \frac{v_{OH^\bullet j}}{v_{ij}} r_{OH^\bullet\, j} \tag{97}$$

where $r_{OH^\bullet}$, is the total reaction rate for the hydroxyl radical and $r_{OH^\bullet j}$ is the rate of consumption of hydroxyl radical in the step j of the reaction network. r_{ij} is the reaction rate of species i in step j, and is v_{tj} is the stoichiometric coefficient of compound i in step j.

Eq. (97) shows that the total rate of hydroxyl radical consumption can be calculated using an indirect method. This method considers the summation of every single oxidation step in the reaction network. The ratio of the corresponding stoichiometric coefficient is also included in this equation.

Moreover, the rate of consumption of any of the individual steps in the reaction network involving hydroxyl consumption can be written as follows:

$$r_{i,j} = -\frac{V}{W_{irr}}\left\{\frac{dC_{i,j}}{dt}\left(1+K_i^*\right)\right\}\frac{1}{\upsilon_{i,j}}$$

(98)

Therefore, substituting Eq. (98) into (97), $r_{OH\bullet}$ becomes:

$$r_{OH\bullet} = \sum r_{OH\bullet_j} = \sum \frac{\upsilon_{OH\bullet,j}}{\upsilon_{i,j}}r_{i,j} =$$

$$-\sum \frac{\upsilon_{OH\bullet,j}}{\upsilon_{i,j}^2}\left\{\frac{V}{W_{irr}}\left\{\frac{dC_{i,j}}{dt}\left(1+K_i^*\right)\right\}\right\}_j$$

(99)

Where $\left(1+K_i^*\right)$ reflects the influence of adsorption on the catalyst surface as presented in Appendix C.

Furthermore, replacing Eq. (99) in the PTEF definition as shown in Eq. (96) gives,

$$PTEF = \frac{\sum \frac{\upsilon_{OH\bullet,j}}{\upsilon_{i,j}^2}\left\{\frac{V}{W_{irr}}\left\{\frac{dC_{i,j}}{dt}\left(1+K_i^*\right)\right\}\right\}_j \Delta H_{OH\bullet}W_{irr}}{Q_{abs}}$$

(100)

As a result, and considering the relationship of quantum yield and PTEF, the quantum yield can be calculated with the following expression:

$$QY = \frac{PTEF}{\eta_{OH\bullet}}$$

(101)

with $\eta_{OH\bullet}$ assessed at 0.271 mol photon/mol OH$^\bullet$ (Serrano et al. 2009).

8.2 PTEF and QY for DP 25

Determination of the PTEF and QY for the catalysts DP 25 is illustrated in this subsection. The reaction network used for the kinetic modeling of phenol photodegradation on DP 25 is also reported in Figure 94. The applicability of this network for kinetic modeling of the

phenol photodegradation on DP 25 was reported already in the Chapter 7. Figure 94 outlines the various relevant reaction steps involved in the "series-parallel" model as adapted for phenol photodegradation on DP 25. In this figure, step 5 is not considered in the network. This step is an isomerization step not requiring $OH^{\bullet}$ species
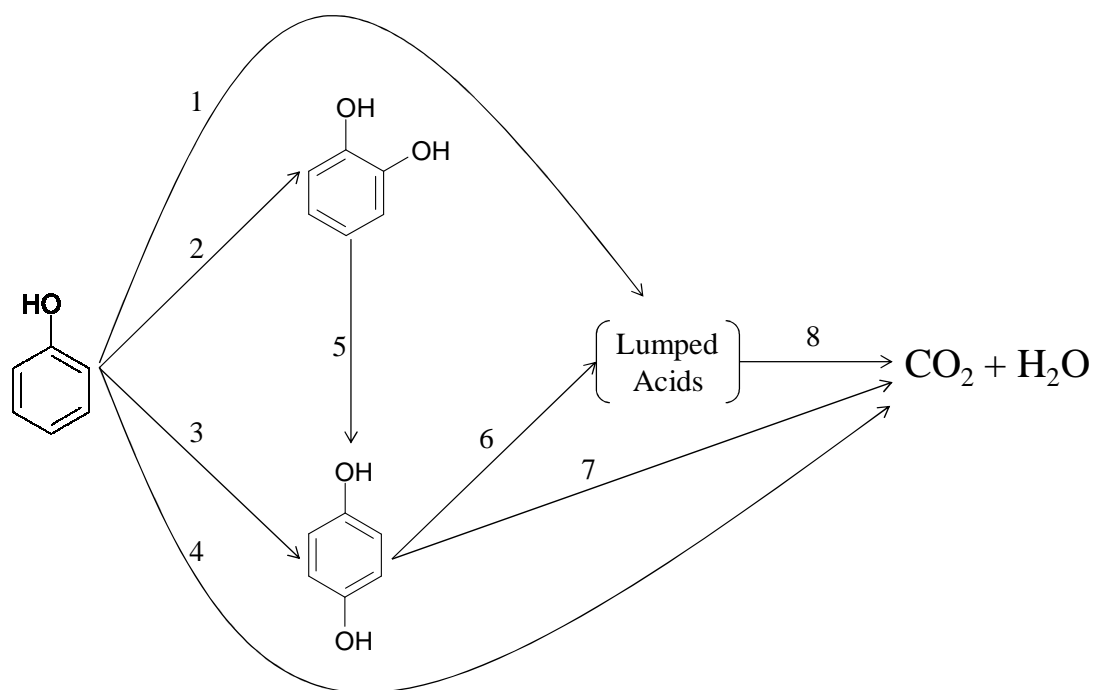
Figure 94 RN for phenol photodegradation on DP 25

It has to be pointed out that the term "lumped acids" in Figure 94 includes all the carboxylic acids. Given that acetic acid is the one present in higher quantities, it is considered to be the species representing carboxylic acid lump in stoichiometric calculations.

Then, the summary of stoichiometric equations for all the reaction steps, shown in Figure 94 is the following:

a) For reaction 1
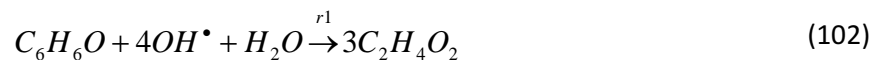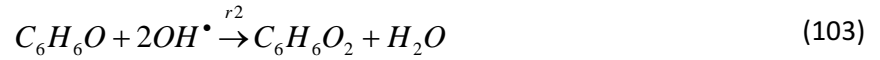
$$C_6H_6O + 4OH^{\bullet} + H_2O \xrightarrow{r1} 3C_2H_4O_2 \tag{102}$$

b) For reaction 2

$$C_6H_6O + 2OH^\bullet \xrightarrow{r2} C_6H_6O_2 + H_2O \tag{103}$$

c) For reaction 3

$$C_6H_6O + 2OH^\bullet \xrightarrow{r3} C_6H_6O_2 + H_2O \tag{104}$$

d) For reaction 4

$$C_6H_6O + 28OH^\bullet \xrightarrow{r4} 6CO_2 + 17H_2O \tag{105}$$

e) For reaction 6

$$C_6H_6O_2 + 2OH^\bullet + 2H_2O \xrightarrow{r6} 3C_2H_4O_2 \tag{106}$$

f) For reaction 7

$$C_6H_6O_2 + 26OH^\bullet \xrightarrow{r7} 6CO_2 + 16H_2O \tag{107}$$
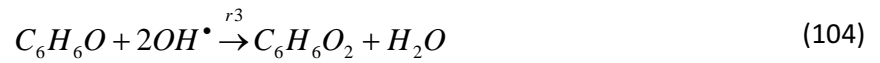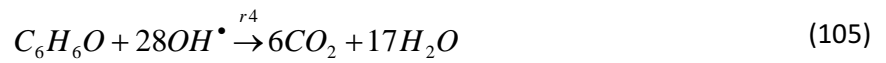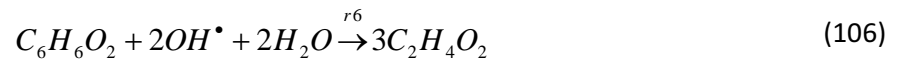
g) For reaction 8
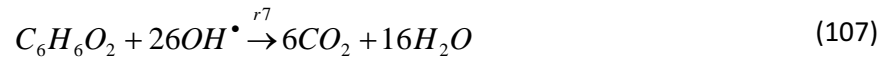
$$C_2H_4O_2 + 8OH^\bullet \xrightarrow{r8} 2CO_2 + 6H_2O \tag{108}$$
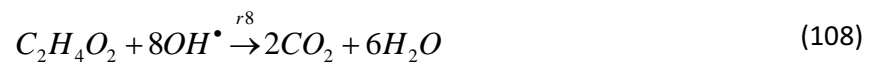
Therefore, the total rate of consumption of $OH^\bullet$ ($r_{OH\bullet}$) can be obtained in terms of consumption of hydroxyl radicals in each step as follows:

$$r_{OH^\bullet} = r_{OH^\bullet,1} + r_{OH^\bullet,2} + r_{OH^\bullet,3} + r_{OH^\bullet,4} + r_{OH^\bullet,6} + r_{OH^\bullet,7} + r_{OH^\bullet,8} \tag{109}$$

where $r_{OH\bullet,i}$ represents the rate of $OH^\bullet$ consumption in reaction i.

In addition, and using the stoichiometric coefficients already reported in Eqs. (102)-(108), it results in:

$$r_{OH\bullet} = 4r_1 + 2r_2 + 2r_3 + 28r_4 + 2r_6 + 26r_7 + 8r_8 \tag{110}$$

Moreover, using the individual rates of reactions defined in Eq. (98), Eq. (110) becomes:

$$r_{OH\bullet} = -\frac{V}{W_{irr}} = \begin{bmatrix} 4\dfrac{dC_{ph,1}}{dt}\left(1+K_{ph}^*\right) + 2\dfrac{dC_{ph,2}}{dt}\left(1+K_{ph}^*\right) + \\[2mm] 2\dfrac{dC_{ph,3}}{dt}\left(1+K_{ph}^*\right) + 28\dfrac{dC_{ph,4}}{dt}\left(1+K_{ph}^*\right) + \\[2mm] 2\dfrac{dC_{p-DHB,6}}{dt}\left(1+K_{p-DHB}^*\right) + 26\dfrac{dC_{p-DHB,7}}{dt}\left(1+K_{p-DHB}^*\right) + \\[2mm] 8\dfrac{dC_{Ac,8}}{dt}\left(1+K_{Ac}^*\right) \end{bmatrix} \tag{111}$$

Therefore, it can be seen that in order to establish the rate of consumption of hydroxyl radicals, as presented in the previous equation, the various rates of change in liquid phase concentrations need to be determined. As shown in Chapter 7, these changes of i chemical species in reaction j can be described using a L-H type rate equation

For example, for the reaction of phenol in reaction 1:

$$\frac{dC_{ph,1}}{dt} = \frac{-k_1 C_{ph}\left(1+K_{ph}^*\right)}{1 + K_{ph}^A C_{ph} + K_{oDHB}^A C_{oDHB} + K_{pDHB}^A C_{pDHB} + K_{Ac}^A C_{Ac}} \tag{112}$$

Then, by substituting the species concentration derivatives for each reaction step, as considered in Eq. (111), it yields:

$$\begin{aligned} r_{OH\bullet} = &-\frac{V}{W_{irr}}((4k_1 + 2k_2 + 2k_3 + 28k_4)C_{ph}(1+K_{ph}^*) + \\ &(2k_6 + 26k_7)C_{p-DHB}(1+K_{p-DHB}^*) + \\ &8k_8 C_{Ac}(1+K_{Ac}^*))/(1 + K_{ph}^A C_{ph} + K_{o-DHB}^A C_{o-DHB} + K_{p-DHB}^A C_{p-DHB} + K_{Ac}^A C_{Ac}) \end{aligned} \tag{113}$$

Finally, substituting Eq. (113) into the definition of PTEF in Eq. (96)

$$PTEF = \frac{-r_{OH} \cdot \Delta H_{OH} \cdot W_{irr}}{Q_{abs}} =$$

$$((4k_1 + 2k_2 + 2k_3 + 28k_4)C_{ph}(1 + K_{ph}^*) +$$

$$(2k_6 + 26k_7)C_{p-DHB}(1 + K_{p-DHB}^*) +$$

$$8k_8 C_{Ac}(1 + K_{Ac}^*))/(1 + K_{ph}^A C_{ph} + K_{o-DHB}^A C_{o-DHB} + K_{p-DHB}^A C_{p-DHB} + K_{Ac}^A C_{Ac})\frac{\Delta H_{OH} \cdot V}{Q_{abs}}$$

(114)

Therefore, one can evaluate the PTEF using Eq. (114), the reaction network presented in Figure 94, the species concentration profiles, the adsorption constants, the reactor volume, and the light absorbed by the TiO_2 DP 25. Once the PTEF is determined, the QY can be calculated using Eq. (101).

The PTEF and QY profiles for phenol photodegradation for a concentration of 30, 20, and 10 ppm-C are shown in Figure 95 and Figure 96 respectively.
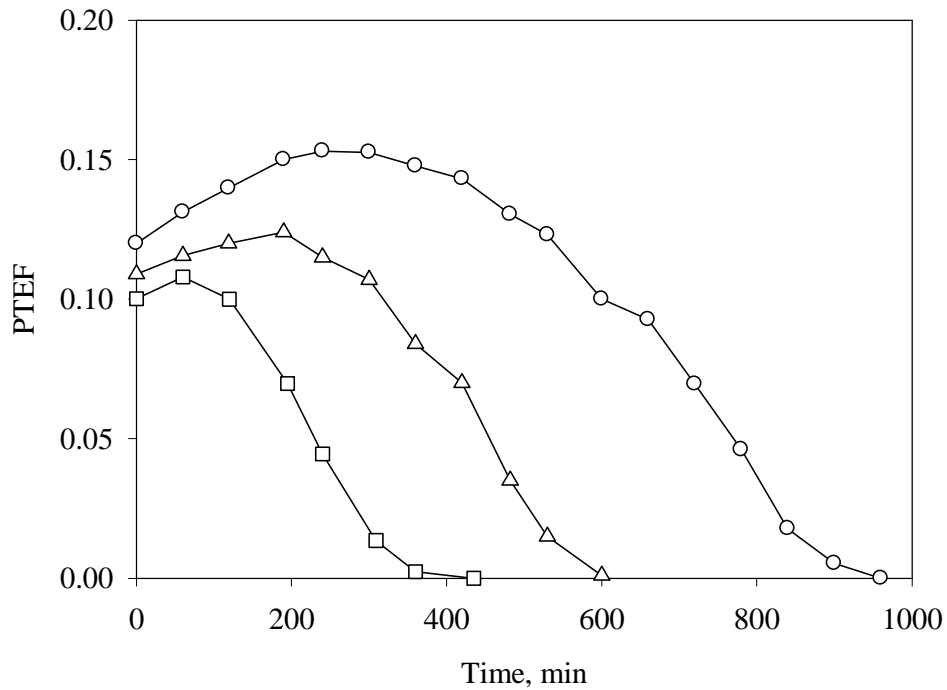
Figure 95 PTEF for phenol degradation on DP 25, (○) 30, (△) 20, and (□) 10 ppm-C_0

Figure 96 QY for phenol degradation on DP 25, (○) 30, (Δ) 20, and (□) 10 ppm-C_0

It can be observed from the above figures that both PTEF and QY display changes with irradiation time. PTEF and QY increase first, reaching a maximum, and then decreasing to zero at the very end of the reaction time. The shape of the curve is the result of the increased intermediate species reactivity and susceptibility due to being further oxidized. When more intermediates are present in the system, the PTEF and QY increase because the OH$^\bullet$ groups are better utilized. This enhanced consumption of hydroxyl radicals continues until the concentration of intermediate species decreases so that no more $OH^\bullet$ reactive radicals are utilized in the system.

8.3 PTEF and QY for all Photocatalysts

Following the same procedure outlined for DP 25, values for PTEF and QY for the rest of the photocatalysts studied were determined. A comparison of all the efficiencies, obtained by the different catalyst, is presented in Figure 97 for PTEF and Figure 98 for QY for an initial concentration of 30 ppm-C.
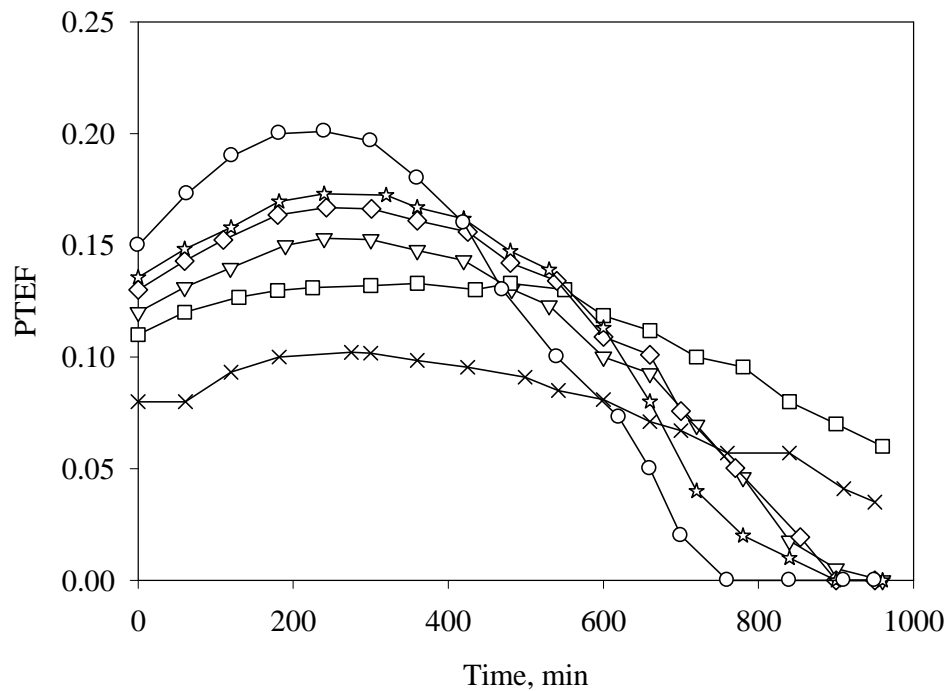
Figure 97 PTEF comparison for (○) Anatase 2+Fe, (☆) DP 25+Fe, (◇) Sol-Gel Cat, (▽) DP 25, (□) Hombikat UV-100, and, (×) Anatase
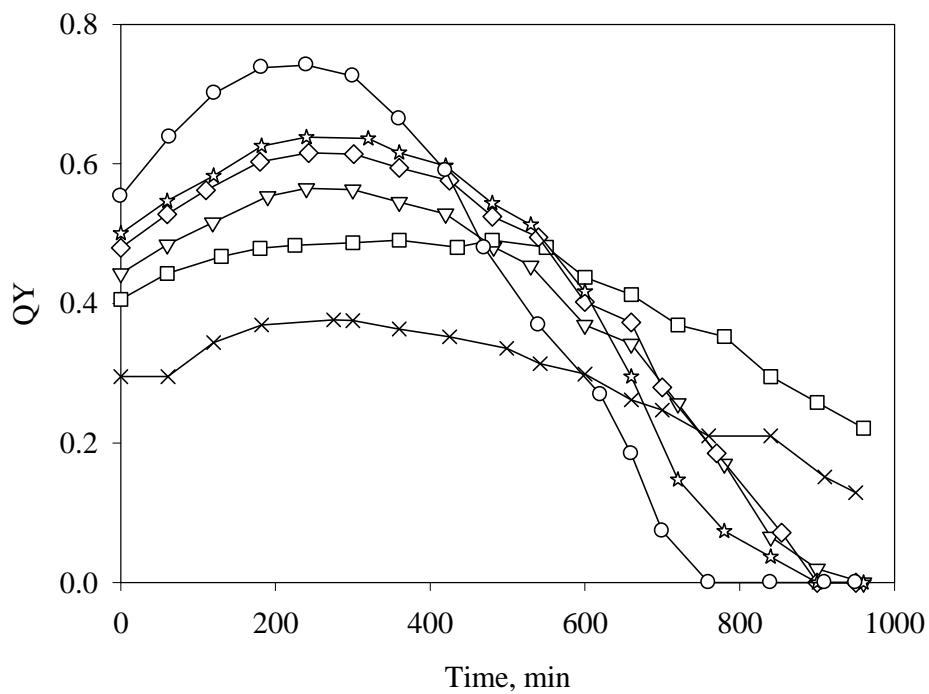
Figure 98 QY comparison for (○) Sol-Gel Cat+Fe, (☆) DP 25+Fe, (◇) Sol-Gel Cat, (▽) DP 25, (□) Hombikat UV-100, and, (×) Anatase

The PTEFs and QYs presented in this section are calculated following a carefully counting of the OH$^\bullet$ radicals consumed at every stage of the photocatalytic conversion. In order to determine the OH$^\bullet$ groups, both stoichiometric and kinetic equations are required. This is obtained for every catalyst by using their respective reaction schemes found in the kinetic modeling section.

The two figures presented above show that at the beginning of the reaction, DP 25+Fe and Sol-Gel Cat+Fe presented the highest efficiencies. Thus, these two photocatalysts display the highest degradation rates with smaller degradation times. For the case of Hombikat and Anatase, it can be observed that the starting PTEF and QY are modest in value vis-a-vis than the other photocatalyst, surpassing them in irradiation times above 800 minutes. This shows that these two semiconductors never reached total mineralization in the 1000 minutes of irradiation time with a therefore relatively modest overall efficiency. It has to be pointed out that the efficiencies determined at every reaction time in the above figures represent instant values. If overall efficiencies are to be obtained, all the values for the efficiencies have to be considered and an average should be established

In this respect, Figure 99 shows an average for the PTEF and QY for the different catalysts at a reaction time of 420 min. Table 46 presents the catalyst notation used in the figure. As expected, the photocatalyst with the largest PTEF values is Sol-Gel Cat+Fe. There is a 10% difference between the most active and less active photocatalysts. This indicates that even though the photocatalyst is still TiO_2, its activity depends on many factors, such as crystal structure, size particle, optical properties, surface area, etc. To summarize the experimental observations it is concluded that the order of catalyst's efficiency is as follows: Sol-Gel Cat+Fe > DP 25+Fe > Sol-Gel Cat > DP 25 > Hombikat > Anatase.

The energy efficiency results presented here are encouraging for the application of photocatalysis for the removal of waste hazardous pollutants given that these results point towards high photocatalytic conversion efficiencies in the Photo-CREC Water II photoreactor. Quantum yields as high as 70% for Sol-Gel Cat+Fe at 300 minutes of irradiation. One would certainly expect that these high efficiencies could also be obtained in a scaled photocatalytic reactor, designed and manufactured using the same principles as for Photo-CREC photoreactors

The methodology for efficiency assessments presented here was established for the complete span of reaction times. In order to implement this methodology, it is necessary to monitor model pollutants as well as the intermediate species concentrations. This allows calculating the OH$^\bullet$ radicals needed for every step in the photoreaction. Nevertheless and to accomplish this, an adequate kinetic modeling of phenol and its intermediate species has to be available. One should also be alert that when calculating PTEF and quantum yields other parameters are needed such as the enthalpy of formation of the hydroxyl radical, and the light absorbed by the different TiO$_2$ catalysts.
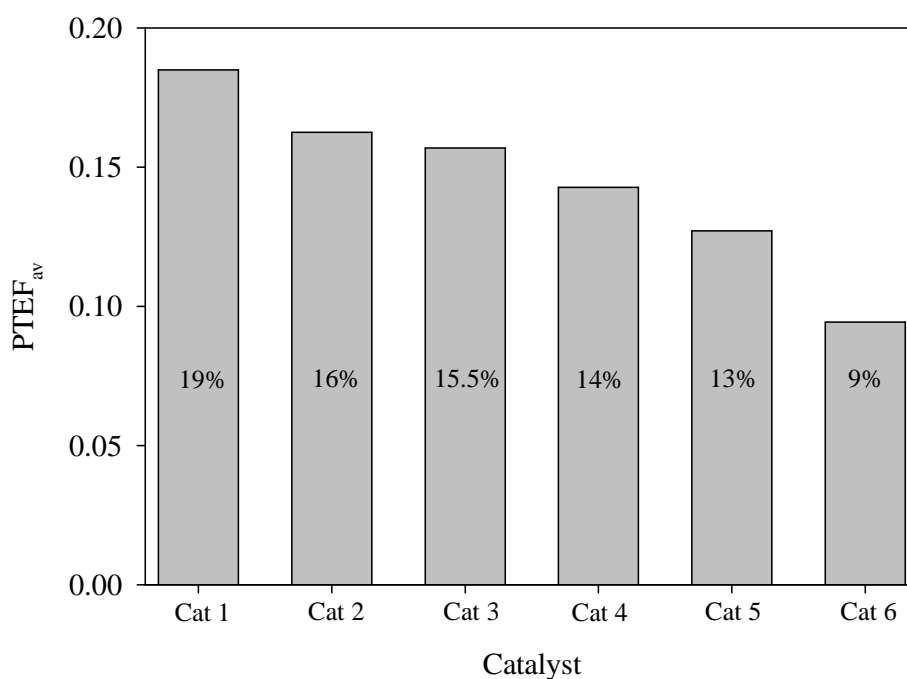
Figure 99 Average PTEF at 420 min of reaction

Table 46 Catalyst notation

Notation	Catalyst
Cat 1	Sol-Gel Cat+Fe^{3+}
Cat 2	DP 25+Fe^{3+}
Cat 3	Sol-Gel Cat
Cat 4	DP 25
Cat 5	Hombikat UV-100
Cat 6	Anatase

8.4 Conclusions

The following are the main conclusions of this chapter:

(a) It is shown that evaluation of reactor efficiencies in a photocatalytic process requires performing macroscopic balances and the radiation absorbed by the photocatalyst. Another alternative is to model the radiation field in order to calculate the LVREA inside the reactor. This can be done with MC simulations.

(b) It is proven that calculation of the PTEF needs the determination of the enthalpy of formation of the hydroxyl radical.

(c) It is shown that PTEF determination for different TiO_2 catalysts employed in this study are established using a unified "series-parallel" reaction network described in Chapter 7 and applicable to all the photocatalysts studied.

(d) It is proven that calculation of the PTEF requires accounting for the total hydroxyl radicals consumed at every reaction time during irradiation, and by all the detected reacting species.

(e) It is demonstrated that Sol-Gel Cat+Fe is the most active photocatalyst leading to a better utilization of produced hydroxyl radicals during the early stages of the photoconversion.

(f) It is proven that the QY for some photocatalyst exceeds at specific irradiation times 70%, case of Sol-Gel Cat+Fe photocatalyst. These high QY values point toward an excellent degree of photon utilization in the Photo-CREC Water-II reactor.

(g) It is shown that these high efficiencies create excellent prospects for the reactor scale up of Photo-CREC-Water II and extensive future use of photocatalysis for water treatment.

Chapter 9
Conclusions and Recommendations

9   Introduction

This chapter reports the main conclusions and contributions of this PhD thesis dissertation. Recommendations for future work are also provided

9.1   Main Contributions

The following represent the most important contributions of the present PhD dissertation.

(a) Sol-Gel Cat-TiO_2 synthesis. This photocatalyst was synthesized in the course of this research. This photocatalyst presented the higher photocatalytic activity of all photocatalyst tested in this dissertation including DP25. Sol-Gel Cat was prepared by mixing a sample containing titanium isopropoxide with a sample containing water. Propanol was used as a solvent. It was found that anatase is the dominant phase of this semiconductor.

(b) Detection of Intermediate Species. Previous studies in our research group utilized HPLC as the main analytical method for detecting and quantifying phenol and intermediate chemical species in the photodegradation of phenol. In this thesis work, the EPA method 8270D was implemented along with a GC-MS system to detect intermediate chemical species. Phenol, hydroquinone, catechol and benzoquinone identities were confirmed using mass spectroscopy. Based on the experimental data, phenol degradation yielded three major aromatic photodegradation intermediates: hydroquinone, catechol and benzoquinone.

(c) Carboxylic Acids. Two major carboxylic acids were detected with an HPLC approach, formic and acetic acid. It was found that for all the catalyst employed in this study, acetic acid was formed always in higher concentrations than formic acid.

(d) Iron Dopant Effect. The effect of iron ions was tested for the two photocatalysts presenting the highest photo-activities (Sol-Gel Cat and DP 25). It was found that 5 ppm of iron increased considerably the activity of these photocatalyst.

(e) Kinetic Model. A phenomenological based unified kinetic model was proposed for the photodegradation of phenol. A Langmuir-Hinshelwood (L-H) model is adopted in the kinetic modeling with both kinetic and adsorption constants being involved.

(f) This L-H kinetic model is based on a "series-parallel" reaction network. This model was found to be applicable to the various TiO_2 photocatalyst of the present study. The proposed unified kinetic model is able to fit the experimental data satisfactorily for the various chemical species resulting from photocatalytic conversion of phenol. Experimental results were obtained at three different initial concentrations: 30, 20, and 10, ppm-C of phenol. This allows application of the proposed kinetic model for a wide range of phenol concentrations.

(g) Kinetic Parameters. The proposed unified kinetic model requires a number of significant assumptions to be effective, avoiding overparametization. As a result, the unified kinetic model was adapted for every photocatalyst in this study. For instance, intermediate chemical species were only included in the "series-parallel" network and kinetic analysis when surpassing detectable levels. As well, carboxylic acids were lumped together into a single term in the rate equation.

(h) Statistical Analysis. A rigorous statistical methodology was adopted for the evaluation of individual kinetic parameters involved in the unified kinetic model. The kinetic parameter selection was based on the correlation coefficients (R^2), smallest 95% CI with the lowest cross-correlation among kinetic parameters and lowest residuals. The adequacy of the regressed parameters was further established by analyzing their physical significance. The obtained kinetic constants were always positive within a reasonable range of expected values.

(i) Adsorption Constants. The proposed unified kinetic model involves chemical species adsorption constants. These adsorption constants were determined independently. This allowed implementing a kinetic constant regression procedure where cross-correlation between kinetic constants is reduced considerably.

(j) TOC. The established unified kinetic model was able to predict TOC at various irradiation times. In order to accomplish this, the addition of various chemical species

in the ODE was considered. This additive approach proves to be valid for the six photocatalysts used in this study.

(k) Spectroradiometric Measurements. Spectrometric measurements in the Photo-CREC Water-II allowed the determination of the evolving irradiation in different TiO_2 slurry media. Other parameters involved in the Macroscopic Radiation Balance were obtained with the help of inner polished and UV-opaque collimators. The MRB allowed determining the total radiation transmission, the non-scattered radiation transmission and the back-scattering radiation exiting the system.

(l) A Monte Carlo Method (MC). A MC based method was employed to simulate the UV radiation field in an annular heterogeneous photoreactor for four different TiO_2 photocatalysts (DP 25, Anatase, Hombikat UV-100 and, Sol-Gel Cat). The MC is an easy to use and easy to apply method. MC is a valuable alternative to circumvent the problems associated with analytical solutions and asymmetric radiation fields.

(m) Phase Function. Narrow backward and forward peaks ($g = -1$ and $g = 1$, respectively) in the H-G phase function are not suitable for MC simulations. On the other hand it was shown that a g value close to zero provides good representation for the experimental LVREA. It was found that for the range $-0.8 < g < 0.8$, differences from MC simulations and experimental values were not very large, less than 10% and this for all cases considered.

(n) Absorption and Scattering Coefficients. A MC method was implemented to determine both the absorption and scattering coefficients. These coefficients were calculated complying with a number of constrains as well as with narrow spans. The only data requirements for this determination were the experimental profiles for the LVREA and the extinction coefficients.

(o) Energy Efficiencies in Slurry Photocatalytic Reactors. Determination of the PTEF and QY is effected for all the time reaction spans during photodegradation. Efficiency calculations consider stoichiometric relationships involving observable chemical species and $OH^\bullet$ radicals. The stoichiometric equations set the number of $OH^\bullet$

radicals required to go through the "Series-Parallel" model interconverting chemical species into others with higher degrees of oxidation.

9.2 Recommendations for Future Work

The following recommendation can be proposed taking into account the results of this dissertation:

(1) Sol-Gel Cat. Given the high activity of Sol-Gel Cat, it is recommended to dope this catalyst with different metal ions to further improve its activity. It is also recommended to continue efforts towards improving the catalyst activity by using dye sensitization, or by using different amounts of adsorbents such as zeolites.

(2) Phase Function. It was found that the H-G phase function provides reliable simulation results of the LVREA. However, most of the phase functions reported in the technical literature only apply for suspended solids in gas media. Therefore, it is suggested to continue work in testing different phase functions in order to find those that might be most suitable for solids suspended in water.

(3) Radiation Studies. Experiments performed in this study were developed by using the same source of light, and therefore the radiative power was a constant variable along the degradation experiments. However, when modeling the kinetics of phenol on TiO_2, it is important to consider the effect of the radiation power. Hence, it is recommended to perform experiments at different radiation intensities so that the LVREA could be included in the kinetic modeling of phenol photodegradation.

(4) Monte Carlo Method. The MC method employed in this study was applied to an annular photoreactor with the radiation source located in the center of the reactor. Nonetheless and given photocatalysis is leaning towards natural sun radiation, simulation of radiation fields that considers external and asymmetric sources of radiation, such in solar irradiated photocatalytic reactors, is recommended.

References

Araña, J.A., Doña-Rodriguez, J.M., González-Diaz, O., Rendóna, E., Herrera-Melián, J.A., Colón, G., Navio, J.A., Pérez-Peña, J., (**2004**) Gas-phase ethanol photocatalytic degradation study with TiO_2 doped with Fe, Pd and Cu. Journal of Molecular Catalysis A: Chemical 215, 153-160.

Ahmed, S., Rasul,M.G., Martens, W.N., Brown, R., Hashib, M.A., (**2011**) Advances in Heterogeneous Photocatalytic Degradation of Phenols and Dyes in Wastewaters: A Review. Water Air and Soil Pollution 215, 3-29.

Ahmed, S., Rasul,M.G., Martens, W.N.,Brown, R., Hashib,M.A., (**2010**) Heterogeneous photocatalytic degradation of phenols in wastewater: A review on current status and developments. Desalination 261, 3-18

Alfano, O.M., Bahnemann, D., Cassano, O.M., Dillert, R., Goslich, R., (**2000**) Photocatalysis in water environments using artificial and solar light. Catalysis Today 58, 199-230.

Andreozzi, R., Caprio, V., Insola, A., Marotta R., (**1999**) Advanced oxidation processes (AOP) for water purification and recovery. Catalysis Today 53, 51-59.

Arana, J., Gonzalez Diaz, O., Dona Rodriguez, J.M., Herrera Melian, J.A., Garriaga I Cabo, C., Perez Pena, J., Carmen Hidalgo, M., Navio-Santos J.A., (**2003**) Role of Fe3+/Fe2+ dopant ions in photocatalytic degradation of carboxylic acids. Journal of Molecular Catalysis A: Chemical 197, 157-171.

Augugliaro, V., Palmisano, L., Schiavello, L.M., (**1991**) Photon absorption by aqueous TiO_2 dispersion contained in a stirred photoreactor. A.I.Ch.E. Journal 37, 1096-1100.

Bahnemann, D., (**2004**) Photocatalytic water treatment: solar energy applications. Solar Energy 77, 445-459.

Bai, L., Wu, Z., Tang, S., Li, M., Xie, P., Wang, S., (**2011**) Study on the phase function in Monte Carlo transmission characteristics of poly-disperses aerosols. Optical Engineering 50, 016002-1-016002-8

Bakardjieva, S., Subrt, J., Stengl, V., Dianez, M.J., Sayagues, M.J., (**2005**) Photoactivity of anatase-rutile TiO_2 nanocrystalline mixtures obtained by heat treatment of homogeneously precipitated anatase. Applied Catalysis B: Environmental 58, 193-202.

Bekkouche, S., Bouhelassa, M. Salah, N.H., Meghlaoui, F.Z., (**2004**) Study of adsorption of phenol on titanium oxide (TiO_2). Desalination 166, 355-362.

Bellobono, I.R., Bianchi, R., de Martini, G., Tozzi, P.M., Bonardi M.L., Groppi, F., Rossi, M., (**2008**) Nonlinear modeling of data in photomineralization kinetics of organic micropollutants by photocatalytic membranes immobilizing titanium dioxide in memrane reactors. Journal of Chemometrics 22, 425-435.

Bellobono, I.R., Scotti, R., D'Arienzo, M., Mrazzoni, F., Bianchi, R., Stanescu, R., Costache, C., Bobirica, L., Cobzaru, G., Tozzi, P.M., Rossi, M., Bonardi, M.L., Groppi, F., Gini, L., (**2009**) Nonlinear Modelling of Kineric Data Obtarined from Photocatalytic Mineralisation of 2,4-Dichlorophenol on a Titanium Dioxide Membrane. International Journal of Photoenergy 631768, 1-10.

Bhatkhande, D.S., Pangarkar, V.G., Beenackers, A.A., (**2001**) Photocatalytic degradation for environmental applications-a review. Journal of Chemical Technology and Biotechnology 77, 102-116.

Binzoni, T., Leung, T. S., Gandijbakhche, A. H., Rufenacht, D., (**2003**) The Use of the Henyey-Greenstein phase function in Monte Carlo simulation in biomedical optics. Physics in Medicine and Biology 51, N313-N322.

Brandi, R. J., Citroni, M. A., Alfano, O. M., Cassano, A. E., (**2003**) Absolute quantum yields in photocatalytic slurry reactors. Chemical Engineering Science 58, 979-985.

Brosillon, S., Lhomme, L., Vallet, C., Bouzaza, A., Wolbert, D., (**2008**) Gas phase photocatalysis and liquid phase photocatalysis: Inderdependence and ingluence of substare concentration and photon flow on degradation reaction kinetics. Applied Catalysis B: Environmental 78, 232-241

Brucato, A., Cassano, A.E., Grisafi, F., Montante,G., Rizzuti, L., Vella, G., (**2006**) Estimating Radiant Fields in Flat Heterogeneous Photoreactors by the Six-Flux Model. AIChE Journal 52, 3882-3890.

Cabrera, M.I., Alfano, O.M., Cassano, A.E., (**1996**) Absorption and Scattering Coefficients of Titanium Dioxide Particles Suspensions in Water. Journal of Physical Chemisty 100, 20043-20050.

Cai, M.F.,Yan, Q.M., Xiao, G.H., Yan, P.S., Xin, J.L., Fang, B.L., (**2003**) Adsorption and photocatalytic degradation of phenol over TiO_2/ACF. The Transactions of Nonferrous Metals Society of China 13, 452-456.

Carvalho, M.G., Farias, T.L., (**1998**) Modelling of Heat Transfer in Radiating and Combusting Systems. Trans IChemE 76, 175-184

Cassano A., Alfano O., (**2000**) Reaction engineering of suspended solid heterogeneous photocatalytic reactors, Catalysis Today 58, 167-197.

Cassano, A.E., Martin, C.A., Brandi, R.J., Alfano, O.M., (**1995**) Photoreactor Analysis and Design: Fundamentals and Applications. Industrial and Engineering Chemistry Research 34, 2155-2201.

Chan, Y.C., Chen, J.N., Lu, M.C., (**2001**) Intermediate inhibition in the heterogeneous UV-catalysis using a TiO_2 suspension system. Chemosphere 45, 29-25.

Changrani, R., Raupp, G. B., (**1999**) Monte Carlo Simulation of the Radiation Field in a Reticulated Foam Photocatalytic Reactor. A.I.Ch.E. Journal 45, 1085-1094.

Chen H.Y., Zahraa, O., Bouchy, M., (**1997**) Inhibition of the adsortpion and photocatalytic degradation of an organic contaminant in an aqueous suspension of TiO_2 by inorganic ions. Journal of Photochemistry and Photobiology A: Cemistry 108, 37-44

Chhor, K., Bocquet, J.F., Cobeau-Justin C., (**2004**) Comparative studies of phenol and salicylic acid photocatalytic degradation: Influence of adsorbed oxygen. Materials Chemistry and Physics 86, 123-131.

Choi, W., (**2006**) Pure and modified TiO_2 photocatalysts and their environmental applications. Catalysis Surveys from Asia 10, 16-28

Chong, M.N, Jin, B., Chow, C.W.K. Saint, C., (**2010**). Recent developments in photocatalytic water treatment technology: A review. Water Research 44, 2997-3027

Colina-Marquez, J., Machucha-Martinez, F., Li Puma, G., (**2009**) Photocatalytic Mineralization of Commercial Herbicides in a Pilot-Scale Solar CPC Reactor: Photoreactor Modeling and Reaction Kinetics Constants Independent of Radiation Field. Environmental Science and Technology 43, 8953-8960.

Colmenares, J.C., Aramendia, M.A., Marinas, A., Marinas, J.M. Urbano, F.J., (**2006**) Synthesis, characterization and photocatalytic activityof different metal-doped titania systems. Applied Catalysis A: General 306, 120-127.

Constantinides, A., Mostoufi, N., (**1999**) Numerical Methods for Chemical Engineers with MATLAB Applications. Prentice Hall PTR, New Jersey, Chapter 7.

de Lasa, H., Serrano Rosales, B., (**2009**) Advances in Chemical Engineering Volume 36: Photocatalytic Technologies. ELSEVIER. Chapter 3, 69-108.

de Lasa, H., Serrano, B., Salaices, M., (**2005**) Photocatalytic Reaction Engineering, Springer: New York.

Diebold, U., (**2003**) The surface science of titanium dioxide. Surface Science Reports 28, 53-229

El Solh, T., Jarosch, K., de Lasa, H., (**2003**). Catalytic Dry Reforming of Methane in a CREC Riser Simulator Kinetic Modeling and Model Discrimination. Industrial and Engineering Chemistry Research 42. 2507-2515.

Enflezos, P., Kalogerakis, N., (**2001**) Applied parameter Estimarion for Chemical Engineers. Marcel Dekker, Inc. New York Basel. Chapters 2,7.

Franch, M.I., Ayllón, J.A., Domènech, X., (**2004**) Fe(III) photocatalyzed degradation of low chain carboxylic acids implications of the iron salt, Applied Catalysis B: Environmental 50, 89-99

Fujishima A., Rao T. N., Tryk D.A., (**2000**) Titanium dioxide photocatalysis, Journal of Photochemistry and Photobiology C: Photochemistry Reviews 1, 1-21.

Fujishima, A., Zhang, X., (**2006**) Titanium dioxide photocatalysis: present situation and future approaches. Comptes Rendus Chimie 9, 750-760

Fujishima, A., Zhanga, X., Trykb, D.A., (**2007**) Heterogeneous photocatalysis: From water photolysis to applications in environmental cleanup. International Journal of Hydrogen Energy 32, 2664-2672

Fujishima,A.,Zhang, X. Tryk, D.A., (**2008**) TiO_2 photocatalysis and related surface phenomena. Surface Science Reports 63, 515-582

Ganoulis, J., (**2009**) Risk Analysis of Water Pollution 2nd Edition. WILEY-VCH. Chapter 1, 1-29

Gaya, U.I., Abdullaha, A.H., (**2008**) Heterogeneous photocatalytic degradation of organic contaminants over titanium dioxide: A review of fundamentals, progress and problems. Journal of Photochemistry and Photobiology C: Photochemistry Reviews 9. 1-12

Gora, A., Toepfer,B, Puddu, V., Li Puma, G., (**2006**) Photocatalytic oxidation of herbicides in single-component and multi-component systems: Reaction kinetics analysis. Applied Catalysis B: Environmental 65, 1-10.

He, Z., Xie, L., Tu, J., Song, S., Lie, W., Liu, Z., Fan, J., Liu, Q., Chen, J., (**2010**) Visible Ligh-Induced Degradation of Phenol over Iodine-Doped Titanium Diozide Modified with Platinum: Role of Platinum and the Reaction Mechanism. Journal of Physical Chemistry C 114, 526-532.

Hernández-Alonso, M.D., Coronado, J.M., Maira, A.J., Soria, J., Loddob, V., Augugliaro, V., (**2002**) Ozone enhanced activity of aqueous titanium dioxide spensions for photocatalytic oxidation of free cyanide ions. Applied Catalysis B: Environmental 39, 257-267

Herrmann, J.M., (**1999**) Heterogeneous photocatalysis: fundamentals and applications to the removal of various types of aqueous pollutants. Catalysis Today 53, 115-129.

Hoffmann, M.R., Scot, T.M., Wonyong, C., Bahnemann, D.W., (**1995**) Environmental Applications of Semiconductor Photocatalysis. Chemical Reviews 95, 69-96.

Imoberdorf, G.E., Taghipour, F., Keshmiri, M., Mohseni, M., (**2008**) Predictive radiation field modeling for fluidized bed photocatalytic reactors. Chemical Engineering Science 63, 4228-4238

Karvinen, S., Lamminmäki, R.J., (**2003**) Preparation and characterization of mesoporous visible-light-active anatase. Solid State Sciences 5, 1159-1166.

Kitano, M., Matsuoka, M., Ueshima, M., Anpo, M., (**2007**) Recent developments in titanium oxide-based photocatalysts. Applied Catalysis A: General 325, 1-14.

Ksibi, M., Zemzemi, A., Boukchina, R., (**2003**) Photocatalytic degradability of substituted phenols over UV irradiated TiO_2. Journal of Photochemistry and Photobiology A: Chemistry 159, 61-70.

Laoufi, N.A., Tassalit, D., Bentahar, F., (**2008**) The degradation of pheol in water solution by TiO_2 photocatalysis in a helical reactor. Global NEST Journal 10, 404-418.

Legrini, O., Oliveros, E., Braun, A.M., (**1993**) Photochemical Processes for Water Treatment. Chemical. Review 93, 671-698.

Li Puma, G., Brucato, A., (**2007**) Dimensionless analysis of slurry photocatalytic reactors using two-flux and six-flux radiation absorption-scattering models. Catalysis Today 122, 78-90.

Linsebigler, A.L., Lu, G., Yates, J.T., (**1995**) Photocatalysis on TiO_2 Surfaces: Principles, Mechanisms, and Selected Results. Chemical Reviews 95, 735-758.

Litter, M.I., (**1999**) Heterogeneous photocatalysis Transition metal ions in photocatalytic systems, Applied Catalysis B: Environmental 23, 89-114.

Litter, M.I., Navío, J.A., (**1996**) Photocatalytic properties of iro-doped titania semiconductors. Journal of Photochemestry and Photobiology A: Chemistry 98, 171-181.

Malato Rodriguez, S., Richter, C., Blanco Galvez, J., Vincent, M., (**1996**) Photocatalytic Degradation of industrial residual Waters. Solar Energy 56, 401-410.

Malato, S., Blanco, J., (**2004**) Photocatalysis. Solar Energy 77, 443-444.

Malato, S., Fernandez-Ibanez, P., Maldonado, M.I., Blanco, J., Gernjak, W., (**2009**) Decontamination and disinfection of water by solar photocatalysis: Recent overview and trends. Catalysis Today 147, 1-59

Martin, C.A., Baltanas, M.A., Cassano, A.E., (**1996**) Photocatalytic reactors II. Quantum efficiencies allowing for scattering effects. An experimental approximation. Journal of Photochemistry and Photobiology A: Chemistry 94, 173-189.

Marugán, J., Van Greiken, R., Alfano, O.A, Cassano, A.E., (**2006**) Optical and Physicochemical Properties of Silica-Supported TiO_2 Photocatalysis. A.I.Ch.E. Journal 52, 2832-2843.

Matthews, R.W., (**1992**) Photocatalytic oxidation of organic contaminants in water: An aid to environmental preservation. Pure and Applied Chemistry 64, 1285-1290.

Mehrvar, M., Anderson,W.A., Moo-Young, M., Reilly,P.M., (**2000**) Non-linear parameter estimation for a dynamic model in photocatalytic reaction engineering. Chemical Engineering Science 55, 4885-4891.

Minero, C., Pelizzetti, E., Malato, S., Blanco, J., (**1996**) Large solar plant photocatalytic water decontamination: Effect of operational parameters. Solar Energy 56, 421-428.

Modest, M. F., Radiative Heat Transfer. Second Edition, Academic Press: California, 2003.

Montoya, J.F., Velasquez, J.A., Salvador, P., (**2009**) The direct-indirect kinetic model in photocatalysis: A reanalysis of phenol and formic acid degradation rate dependence on photon flow and concentration in TiO_2 aqueous dispersions. Applied Catalysis B: Environmental 88, 50-58

Moreira, J., Serrano, B., Ortiz, A., Lasa, H. D., (**2010**). Evaluation of Photon Absorption in an Aqueous TiO_2 Slurry Reactor Using Monte Carlo Simulations and Macroscopic Balance. Industrial and Engineering Chemistry Research 49, 10524-10534.

Moreno-Pirajan, J.C., (**2007**) Solidos porosos. Universidad de los Andes Facultad de Ciencias. Colombia Chapter 7, 243-276.

Mukherjee, P.S., Ray, A.K., (**1999**) Major Challenges in the Design of a Large-Scale Photocatalytic Reactor for Water Treatment. Chemical Engineering and Technology 22, 253-260.

Navarro, P., Sarasa, J., Sierra, D., Esteban, S., Ovelleiro, J.L., (**2005**) Degradation of wine industry wastewaters by photocatalytic advanced oxidation. Water Science and Technology 51, 113-120.

Navio, J.A., Colon, G., Litter, M.I., Bianco, G.N., (**1996**) Synthesis, characterization and photoactivity properties of iron-doped titania semiconductors prepared from TiO_2 and iron(III) acetylacetonate. Journal of Molecular Catalysis A: Cheical 106, 267-276.

Ortiz-Gomez, A., (**2006**) Enhanced Mineralization of Phenol and Other Hydroxulated Compounds in a Photocatalytic Process Assisted with Ferric Ions. PhD Thesis. The University of Western Ontario.

Ortiz-Gomez, A., Serrano-Rosales, B., de Lasa, H., (**2008**) Enhanced mineralization of pheon and other hydroxylated compounds in a photocatalytic process assited with ferric ions. Chemical Engineering Sicience 63, 520-557.

Ortiz-Gomez, A., Serrano-Rosales, B., Salaices, M., de Lasa, H., (**2007**) Photocatalytic Oxidation of Phenol: Reaction Network, Kinetic Modeling, and Parameter Estimation. Industrial and Engineering Chemistry Research 46, 7394-7409.

Pareek, V., (**2005**) Light Intensity Distribution in a Dual-Lamp Photoreactor. International Journal of Chemical Reactor Engineering 3, 1-11.

Pareek, V., Ching, S., Tade, M., Adesina, A.A., (**2008**) Light intensity distribution in heterogeneous photocatalytic reactors. Asia-Pacific Journal of Chemical Engineering 3, 171-201.

Pareek, V.K., Adesina, A.A., (**2004**) Light Intesity Distribution in a Photocatalytic Reactor Using Finite Volume. A.I.Ch.E. Journal 50, 1273-1288.

Pareek, V.K., Cox, S., Adesina, A.A., (**2003**) Light intensity Distribution in Photocatalytic Reactors Using Finite Volume Method. Third International Conference on CFD in the Minerals and Process Industries. CSIRO, Melbourne, Australia. 229-234.

Pasquali, M., Santarelli, F., Porter, J. F., Yue, P.L., (**1996**) Radiative Transfer in Photocatalytic Systems. A.I.Ch.E. Journal 42, 532-537.

Ray, A.K., Chen, D., Li F., (**2000**) Effect of Mass Transfer and Catalyst Layer Thickness on Photocatalytic Reaction, A.I.Ch.E. Journal 46, 1034-1045

Rengifo-Herrera, J.A., Kiwi, J., Pulgarin, C., (**2009**) N, S co-doped and N-doped Degussa P-25 powders with visible light response prepared by mechanical mixing of thiourea and urea. Reactivity towards E. coli inactivation and phenol oxidation. Journal of Photochemistry and Photobiology A: Chemistry 205, 109-115.

Robert, D., Parra, S., Pulgarin, C., Krzton, A., (**2000**) Chemisorption of phenols and acids on TiO_2 surface. Applied Surface Science 167, 51-58.

Romero, R.L., Alfano, O.M., Cassano, A.E., (**1997**) Cylindrical Photocatalytic Reactors. Radiation Absorption and Scattering Effects Produced by Suspended Fine Particles in an Annular Space. Industrial and Engineering Chemistry Research 36, 3094-3109.

Romero, R.L., Alfano, O.M., Cassano, A.E., (**2003**) Radiation Field in an Annular, Slurry Photocatalytic Reactor. 2. Model and Experiments. Industrial and Engineering Chemistry Research 42, 2479-2488.

Rota, F., Cavassi, M., Niego, D., Gorlani, R., Vianelli, L., Tatti, L.,Bruzzi, P., Moroni, A., Bellobono, I.R., (**1996**) Mathematical Modelling of Photomineralization of Phenols in Aqueous Solution, by Photocatalytic Membranes Immobilizsing Titanium Dioxide. Chemesphere 33, 2159-2173.

Salaices, M., Serrano, B., de Lasa, H., (**2001**) Photo-catalytic conversion of organic pollutants. Extinction coefficients and quantum efficiencies. Industrial and Engineering Chemistry Research 40, 5455-5464.

Salaices, M., Serrano, B., de Lasa, H., (**2002**) Experimental Evaluation of Photon absorption in an aqueous TiO_2 Slurry reactor. Chemical Engineering Journal 90, 219-229

Salaices, M., Serrano, B., de Lasa, H.I., (**2004**) Photocatalytic conversion of phenolic compounds in slurry reactors. Chemical Engineering Science 59, 3-15.

Salaices-Arredondo, M., (**2002**) Photocatalysis in Slurry Reactors Radiation Transmission and Kinetic Modeling. PhD Thesis. The University of Western Ontario.

Satuf, M. L., Brandi, R. J., Cassano, A.E., Alfano, O.M., (**2005**) Experimental Method to evaluate the Optical Properties of Aqueous Titanium Dioxide Suspensions. Industrial and Engenieerng Chemistry Research 44, 6643-6649.

Schiavello, M., Augugliaro, V., Palmisano, L., (**1991**) An experimental method for the determination of the photon Low reflected and adsorbed by aqueous dispersions containing polycrystalline solids in heterogeneous photocatalysis. Journal of Catalysis 127, 332–341.

Selvam, K., Muruganandham, M., Muthuvel, I., Swaminathan, M., (**2007**) The influence of inorganic oxidants and metal ions on semiconductor sensitized photodegradation of 4-fluorophenol. Chemical Engineering Journal 128, 51-57

Serrano, B., de Lasa, H., (**1997**) Photocatalytic Degradation of Water Organic Pollutants. Kinetic Modeling and Energy Efficiency. Industrial and Engineering Chemistry Research 36, 4705-4711.

Serrano, B., de Lasa, H., (**1999**) Photocatalytic Degradation of Water Organic Poluttants. Pollutant Reactivity and Kinetic Modeling. Chemical Engineering Science 54, 3063-3069.

Serrano, B., Ortiz, A., Moreira, J. de Lasa, H.I., (**2009**) Energy Efficiency in Photocatalytic Reactors for the Full Span of Reaction Times. Industrial and Engineering Chemistry Research 48, 9864-9876.

Serrano, B., Ortiz, A., Moreira, J. de Lasa, H.I., (**2010**) Photocatalytic Thermodynamic Efficiency Factors. Practical Limits in Photocatalytic Reactors. Industrial and Engineering Chemistry Research 49, 6824-6833.

Sivalingam, G., Priya, M.H., Madras, G., (**2004**) Kinetics of the photodegradation of substituted phenols by solution combustion synthesized TiO_2. Applied Catalysis B: Environmental 51, 67-76.

Sobczynski, A., Duczmal, L., Zmudzinski, W., (**2004**) Phenol destruction by photocatalysis on TiO_2: an attempt to solve the reaction mechanism. Journal of Molecular Catalysis A: Chemical 213, 225-230.

Sun, L., Bolton, J.R., (**1996**) Determination of quantum yield for the photochemical generation of hydroxyl radicals in TiO_2 suspensions. Journal of Physical Chemistry 100, 4127-4134.

Tatti, L., Niego, D., Rota, F., Bruzzi, P., Moroni., Bellobono, I.R., (**1997**) Mathematical Modelling of Pilot-Plant Photomineralization of Chlrorophenols in Aqueous Solution, by Photocatalytic Membranes Immobilizing Titanium Dioxide. Chemosphere 34, 41-49.

Thiruvenkatachari, A., Vigneswaran, S., Moon, I.S., (**2008**) A review on UV/TiO_2 photocatalytic oxidation process. Korean Journal of Chemical Engineering 25, 64-72.

Toepfer, B., Gora, A., Li Puma, G., (**2006**) Photocatalytic Oxidation of multicomponents solutions of herbicides: Reaction kinetics analysis with explicit photon absorption effects. Applied Catalysis B: Environmental 68, 171-180.

Trillas, M., Pujol, M., Domenech. X., (**1992**) Phonel Photodegradation over Titanium Dioxide. Journal of Chemical Technology and Biotechnology 55, 85-90

Tryba, B., Morawski, A.W., Inagaki, M., Toyada, M., (**2006**) The kinetics of phenol decompsition under UV irradiation with and without H_2O_2 on TiO_2, Fe-TiO_2 and Fe-C-TiO_2 photocatalysts. Applied Catalysis B: Environmental 63, 215-221.

Vidal A., (**1998**) Developments in Solar Photocatalysis for water Purification. Chemosphere 36, 2593-2606.

Vinu, R., Madras, G., (**2010**) Environmental remediation by photocatalysis. Journal of the Indian Institute of Science 90,189-230.

Wang, Z., Cai, W., Hong, X., Zhao, X., Xu, F., Cai, C., (**2005**) Photocatalytic degradation of phenol in aqueous nitrogen-doped TiO_2 suspensions with various light sources. Applied Catalysis B: Environmental 57, 223-231.

Wilke, K., and Breuer H.D., (**1999**) The infuence of transition metal doping on the physical and photocatalytic properties of titania. Journal of Photochemistry and Photobiology A: Chemistry 121, 49-53.

Wolfrum, E.J., Turchi, C.S., (**1992**) Comments on reactor dynamics in the evaluation of photocatalytic oxidation kinetics. Journal of Catalysis 136, 626–628

Xu, Y., Langford, C.J., (**2000**) Variation of Langmuir adsorption determined for TiO_2-photocatalyzes degradation of acetophenone under different light intensities. Journal of Photochemistry and Photobiology A: Chemisty 133, 67-71.

Yokota, T., Cesur, S., Suzuki, H., Baba, H., Takahata, Y., (**1999**) Anisotropic Scattering Model for the Estimation of Light Absorption Rates in Photoreactor with Heterogeneous Medium. Journal of Chemical Engineering of Japan 32, 314-321.

Zaleska, A., (**2008**) Doped-TiO_2: A Review. Recent Patents on Engineering 2, 157-164.

Zhang, L., Kanki, T., Sano, N., Toyoda, A., (**2006**) Pathways and Kinetics on Photocatalytic Destriction of Aqueous Phenol. Envronmental Monitoring and Assessment 115, 395-403.

Zhou, J., Zhang, Y., Zhao, X.S., Ray, A.K., (**2006**) Photodegradation of Benzoic Acid over Metal-Doped TiO_2. Industrial and Engineering Chemistry Research 45, 3503-3511.

Appendices

Appendix A: Determination of direction cosines

Figure A-1 is the key to find the direction cosines (i.e. converting spherical to Cartesian coordinates).
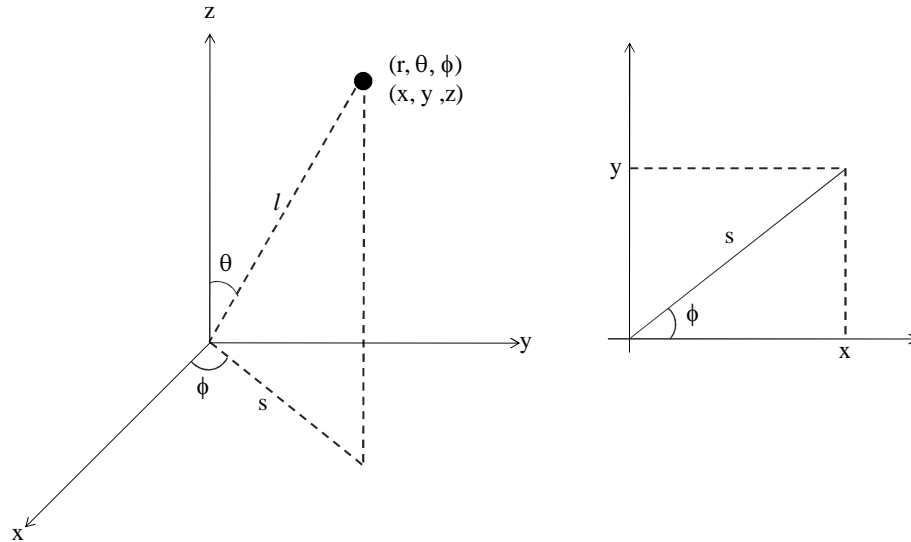

Figure A-1: Cartesian and cylindrical coordinates representation

The right side of the figure shows the xy-plane from the picture on the left. By the Pythagorean Theorem:

$$
\begin{aligned}
s &= \sqrt{x^2 + y^2} = l\sin(\theta) \\
x &= s\cos(\phi) = l\sin(\theta)\cos(\phi) \\
y &= s\sin(\phi) = l\sin(\theta)\sin(\phi) \\
z &= l\cos(\theta)
\end{aligned}
\qquad \text{Eq. A-1}
$$

Thus, the direction cosines will be given by:

$$
\begin{aligned}
e_x &= \sin(\theta)\cos(\phi) \\
e_y &= \sin(\theta)\sin(\phi) \\
e_z &= \cos(\theta)
\end{aligned}
\qquad \text{Eq. A-2}
$$

Appendix B: Detection of Aromatic Intermediates by GC/MS

As explained in the experimental section, detection of aromatic compounds were done by using a variation of the EPA method 8270D, with the preparation technique 3580 on an Agilent 19091z-205 350 max HP-1 capillary column of 50 m x 200 μm x 0.5 μm nominal was used. When a 1 μl sample treated with the 8270D EPA method was injected in the equipment, the chromatogram presented in Figure A-2 was obtained. This chromatogram was obtained for an experiment with an initial concentration of 20 ppm C in phenol after three hours of irradiation.
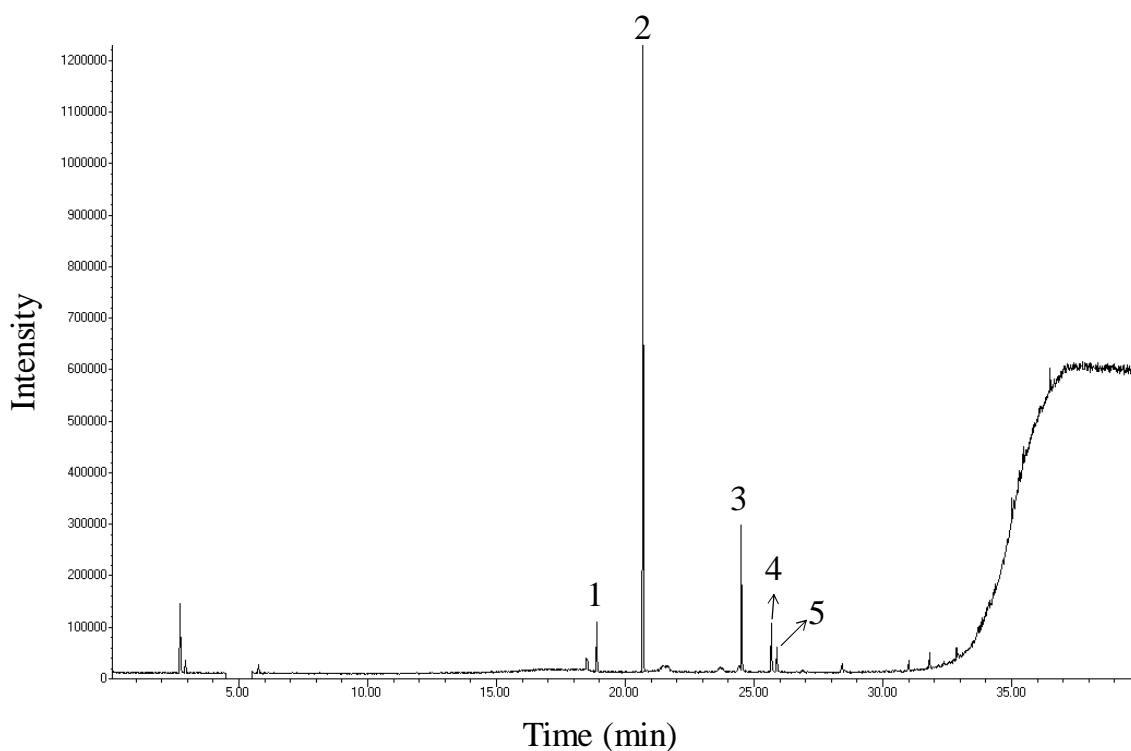

Figure A-2 Mass chromatogram for a sample obtained by the 8270 method

In the Figure, the components enumerated are the intermediates most likely to be phenol sub products. Information about this detected intermediates are given in Table A-1. In the table, the number of the component, retention time and the probability match given by the GC/Ms is presented.

Table A-1 Identification of the intermediate aromatic components in phenol degradation using DP 25 catalyst

Component	Retention time (min)	Match (%)
1. Benzoquinone	18.890	89.6
2. Phenol	20.96	96.7
3. 1,2 – Benzenodiol	54.515	94.5
4. Hydroquinone	25.655	91.8
5. Resorcinol	25.878	90.7

In figures Figure A-3 to Figure A-7, the mass spectrums of the components found in Figure A-2 are indicated as letter a. These figures also present the comparison between the spectrum of the pure components and the ones obtained in the injection, indicated as b. Lastly, these figures report the netter match found in the NIST/EPA/NIH Mass Spectral Library on the Enhanced ChemStation G1701DA version D.00.00.38, indicated as letter c.
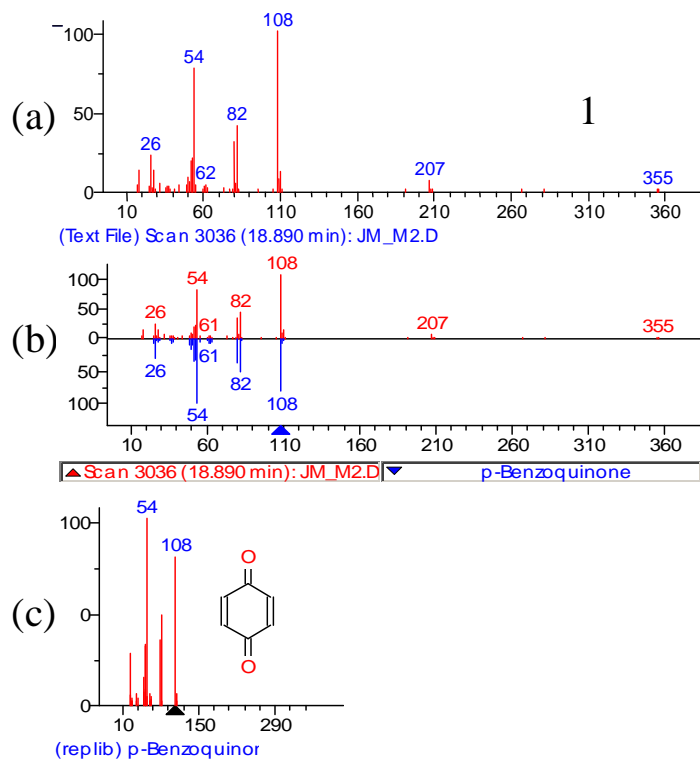
Figure A-3 Mass spectrum for component 1, Benzoquinone
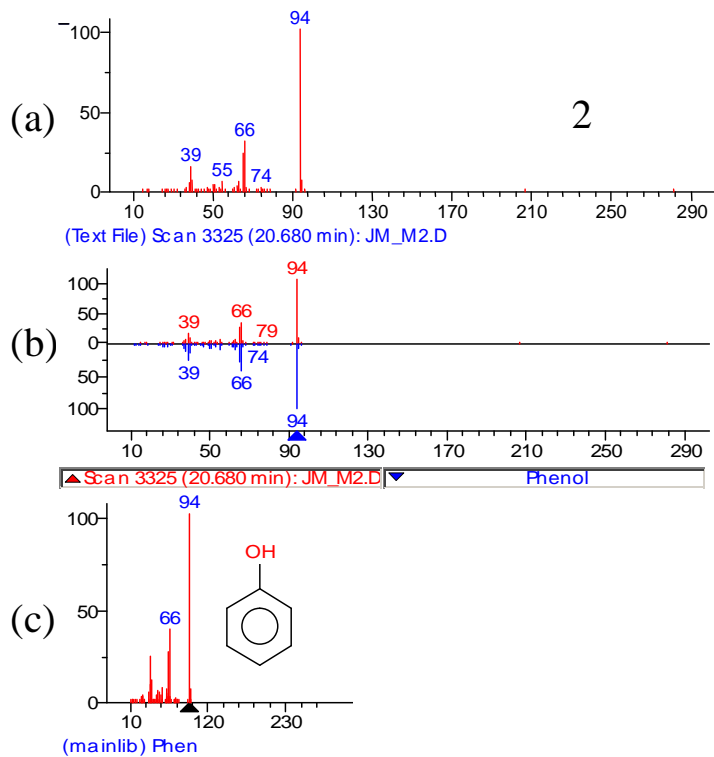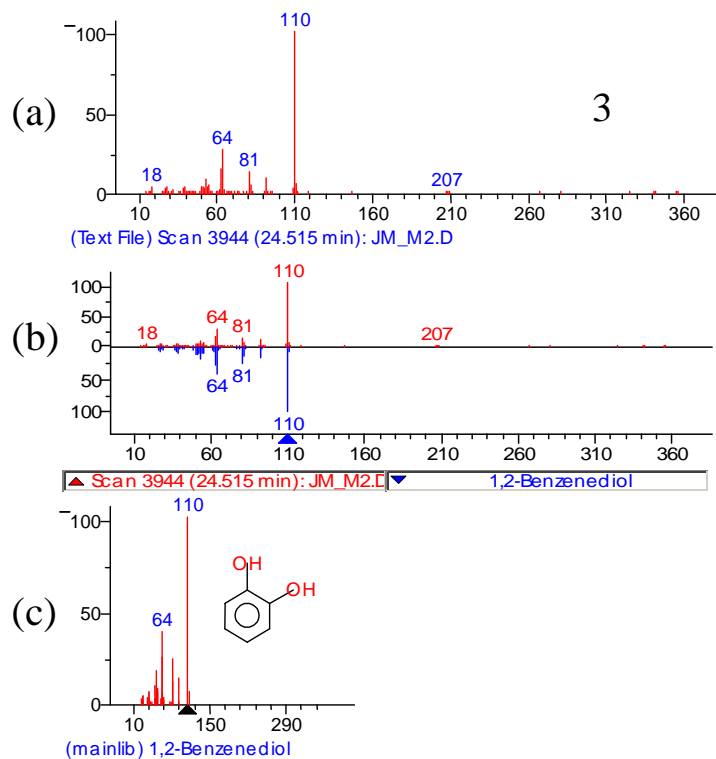

Figure A-4: Mass spectrum for component 2, Phenol

209

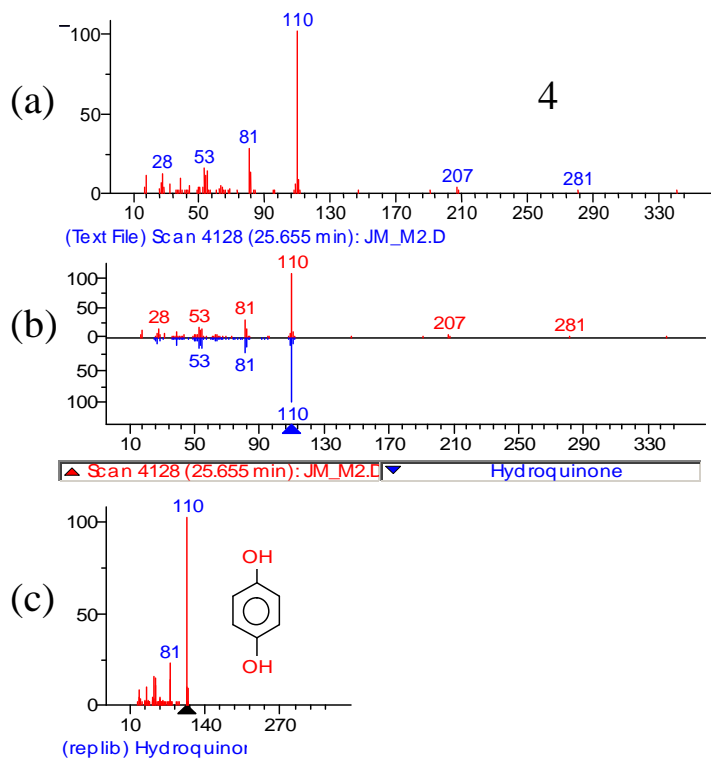**Figure A-5** Mass spectrum for component 3, 1,2-Benzenodil

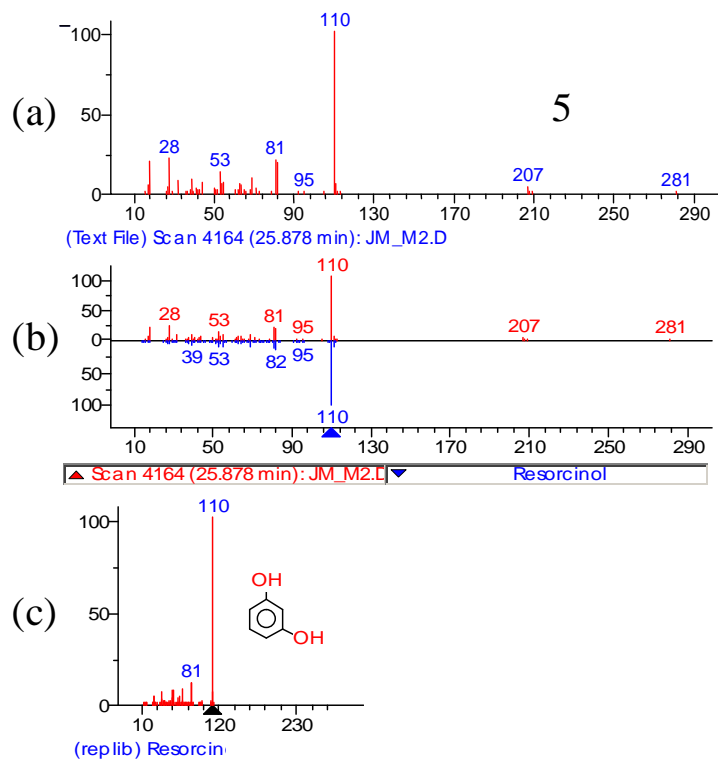**Figure A-6** Mass spectrum for component 4, Hydroquinone

Figure A-7 Mass spectrum for component 5, Resorcinol

Appendix C: Derivation of Equations for K_i^* calculation

An expression can be provided to calculate the total reaction rate for "i" species, accounting for the species fractions distributed in both liquid and adsorbed phases:

$$N_{i,T} = N_{i,L} + N_{i,ads}$$

Eq. A-3

where N_i is in moles.

These amounts of "i" species, distributed in the liquid and adsorbed phases, can be expressed as concentrations in each of the phases as follows:

$$\frac{N_{i,T}}{V} = \frac{N_{i,L}}{V} + \frac{N_{i,ads}}{V}$$

Eq. A-4

$$N_{i,ads} = Wq_i \text{ and } C_{i,T} = C_i + \frac{Wq_i}{V}$$

Eq. A-5

Furthermore analytical differentiation of Eq. A-5 leads to the reaction rate of the compound "i" in the step "j" as,

$$\frac{dC_{i,T}}{dt} = \frac{dC_i}{dt} + \frac{W}{V}\frac{dq_i}{dt}$$

Eq. A-6

If one assumes adsorption equilibrium between phases in equation as

$$q_i = \frac{K_i q_m C_i}{1 + \sum_{j=1}^{n} K_j C_j}$$

Eq. A-7

In this respect, one can notice that $q_i = q_i(C_i)$ and $C_i = C_i(t)$ and as a result the total derivative of q_i is given as,

$$\frac{dq_i}{dt} = \sum_{j=1}^{n} \frac{\partial q_i}{\partial C_j}\frac{dC_j}{dt}$$

Eq. A-8

Thus to evaluate the total derivative as in Eq. A-8 one has to establish the $\dfrac{\partial q_i}{\partial C_i}$ partial derivatives,

$$\frac{\partial q_i}{\partial C_i} = \frac{K_i q_m + q_m \sum\limits_{j,j\neq i} K_i K_j C_j}{\left(1+\sum\limits_{j=1}^{n} K_j C_j\right)^2}$$

Eq. A-9

And for $i \neq j$

$$\frac{\partial q_i}{\partial C_j} = \frac{-K_j K_i q_m C_i}{\left(1+\sum\limits_{j=1}^{n} K_j C_j\right)^2}$$

Eq. A-10

Substituting these partial derivatives in the total concentration change of the "i" species it yields:

$$\frac{dC_{i,T}}{dt} = \frac{dC_i}{dt} + \frac{W}{V}\frac{dq_i}{dt}$$

Eq. A-11

$$\frac{dC_{i,T}}{dt} =$$
$$\frac{dC_i}{dt} + \frac{W}{V\left(1+\sum\limits_{j=1}^{n} K_j C_j\right)^2}\left\{\left(K_i q_m + q_m \sum\limits_{j,j\neq i} K_i K_j C_j\right)\frac{dC_i}{dt} - \sum\limits_{j,j\neq i} K_j K_i q_m C_i \frac{dC_j}{dt}\right\}$$

Eq. A-12

Also,

$$\frac{dC_{i,T}}{dt} =$$
$$\frac{dC_i}{dt} + \frac{W}{V\left(1+\sum\limits_{j=1}^{n} K_j C_j\right)^2}\left\{\left(K_i q_m + q_m \sum\limits_{j,j\neq i} K_i K_j C_j\right)\frac{dC_i}{dt} - \sum\limits_{j,j\neq i} K_j K_i q_m C_i \frac{dC_j}{dt}\frac{dC_i}{dt}\frac{dt}{dC_i}\right\}$$

Eq. A-13

$$\frac{dC_{i,T}}{dt} =$$

$$\frac{dC_i}{dt} + \frac{W}{V\left(1+\sum_{j=1}^{n}K_jC_j\right)^2}\left\{\left(K_iq_m + q_m\sum_{j,j\neq i}K_iK_jC_j\right)\frac{dC_i}{dt} - \sum_{j,j\neq i}K_jK_iq_mC_i\frac{dC_j}{dt}\frac{dC_i}{dt}\frac{dt}{dC_i}\right\} \qquad \text{Eq. A-14}$$

$$\frac{dC_{i,T}}{dt} = \frac{dC_i}{dt}\left\{1 + K_i^*\right\} \qquad \text{Eq. A-15}$$

Where

$$K_i^* = \frac{W}{V\left(1+\sum_{j=1}^{n}K_jC_j\right)^2}\left\{\left(K_iq_m + q_m\sum_{j,j\neq i}K_iK_jC_j\right) - K_jK_iq_mC_i\frac{dC_j}{dC_i}\right\} \qquad \text{Eq. A-16}$$

In the present study where reacting species are phenol (ph), o-DHB, and p-DHB, it results,

$$q_{ph} = \frac{K_{ph}q_mC_{ph}}{1 + K_{ph}C_{ph} + K_{o-DHB}C_{o-DHB} + K_{p-DHB}C_{p-DHB}} \qquad \text{Eq. A-17}$$

$$\frac{dq_{ph}}{dt} = \frac{\partial q_{ph}}{\partial C_{ph}}\frac{dC_{ph}}{dt} + \frac{\partial q_{ph}}{\partial C_{o-DHB}}\frac{dC_{o-DHB}}{dt} + \frac{\partial q_{ph}}{\partial C_{p-DHB}}\frac{dC_{p-DHB}}{dt} \qquad \text{Eq. A-18}$$

$$\frac{\partial q_{ph}}{\partial C_{ph}} = \frac{K_{ph}q_m + K_{o-DHB}K_{ph}q_mC_{o-DHB} + K_{p-DHB}K_{ph}q_mC_{p-DHB}}{\left(1 + K_{ph}C_{ph} + K_{o-DHB}C_{o-DHB} + K_{p-DHB}C_{p-DHB}\right)^2} \qquad \text{Eq. A-19}$$

$$\frac{\partial q_{ph}}{\partial C_{o-DHB}} = \frac{-K_{o-DHB}K_{ph}q_mC_{ph}}{\left(1 + K_{ph}C_{ph} + K_{o-DHB}C_{o-DHB} + K_{p-DHB}C_{p-DHB}\right)^2} \qquad \text{Eq. A-20}$$

$$\frac{\partial q_{ph}}{\partial C_{p-DHB}} = \frac{-K_{p-DHB}K_{ph}q_m C_{ph}}{\left(1 + K_{ph}C_{ph} + K_{o-DHB}C_{o-DHB} + K_{p-DHB}C_{p-DHB}\right)^2} \qquad \text{Eq. A-21}$$

If $\text{denom} = 1 + K_{ph}C_{ph} + K_{o-DHB}C_{o-DHB} + K_{p-DHB}C_{p-DHB}$

Replacing equations Eq. A-19, Eq. A-20, and Eq. A-21 in Eq. A-18, it results,

$$\frac{dC_{ph,T}}{dt} = \frac{dC_{ph}}{dt} + \frac{W}{V}\frac{dC_{ph}}{dt}\left\{ \begin{array}{l} \left[\dfrac{K_{ph}q_m + K_{o-DHB}K_{ph}q_m C_{o-DHB} + K_{p-DHB}K_{ph}q_m C_{p-DHB}}{(denom)^2}\right] \\[3ex] + \left[\dfrac{-K_{o-DHB}K_{ph}q_m C_{ph}}{(denom)^2}\right]\dfrac{dC_{o-DHB}}{dC_{ph}} \\[3ex] + \left[\dfrac{-K_{p-DHB}K_{ph}q_m C_{ph}}{(denom)^2}\right]\dfrac{dC_{p-DHB}}{dC_{ph}} \\[3ex] \left[\dfrac{-K_{Ac}K_{ph}q_m C_{ph}}{(denom)^2}\right]\dfrac{dC_{Ac}}{dC_{ph}} \end{array} \right\} \qquad \text{Eq. A-22}$$

or

$$\frac{dC_{ph,T}}{dt} = \frac{dC_{ph}}{dt}\left\{1 + K_{ph}^*\right\} \qquad \text{Eq. A-23}$$

where

$$K_{ph}^* = \frac{W}{V}\left\{ \begin{array}{l} \left[\dfrac{K_{ph}q_m + K_{o-DHB}K_{ph}q_m C_{o-DHB} + K_{p-DHB}K_{ph}q_m C_{p-DHB}}{(denom)^2}\right] \\[3ex] + \left[\dfrac{-K_{o-DHB}K_{ph}q_m C_{ph}}{(denom)^2}\right]\dfrac{dC_{o-DHB}}{dC_{ph}} + \left[\dfrac{-K_{p-DHB}K_{ph}q_m C_{ph}}{(denom)^2}\right]\dfrac{dC_{p-DHB}}{dC_{ph}} \\[3ex] + \left[\dfrac{-K_{Ac}K_{ph}q_m C_{ph}}{(denom)^2}\right]\dfrac{dC_{Ac}}{dC_{ph}} \end{array} \right\} \qquad \text{Eq. A-24}$$

Using a similar approach one can also show that,

$$\frac{dC_{o-DHB,T}}{dt} = \frac{dC_{o-DHB}}{dt}\left\{1 + K_{o-DHB}^*\right\} \qquad \text{Eq. A-25}$$

where:

$$K_{o-DHB}^* = \frac{W}{V}\left\{\begin{array}{l} \left[\dfrac{K_{o-DHB}q_m + K_{o-DHB}K_{ph}q_mC_{ph} + K_{p-DHB}K_{o-DHB}q_mC_{p-DHB}}{(denom)^2}\right] \\[3mm] + \left[\dfrac{-K_{o-DHB}K_{ph}q_mC_{o-DHB}}{(denom)^2}\right]\dfrac{dC_{ph}}{dC_{o-DHB}} + \left[\dfrac{-K_{p-DHB}K_{o-DHB}q_mC_{o-DHB}}{(denom)^2}\right]\dfrac{dC_{p-DHB}}{dC_{o-DHB}} \\[3mm] + \left[\dfrac{-K_{Ac}K_{o-DHB}q_mC_{o-DHB}}{(denom)^2}\right]\dfrac{dC_{Ac}}{dC_{o-DHB}} \end{array}\right\} \qquad \text{Eq. A-26}$$

and

$$\frac{dC_{p-DHB,T}}{dt} = \frac{dC_{p-DHB}}{dt}\left\{1 + K_{p-DHB}^*\right\} \qquad \text{Eq. A-27}$$

where

$$K_{p-DHB}^* = \frac{W}{V}\left\{\begin{array}{l} \left[\dfrac{K_{p-DHB}q_m + K_{p-DHB}K_{ph}q_mC_{ph} + K_{p-DHB}K_{o-DHB}q_mC_{o-DHB}}{(denom)^2}\right] \\[3mm] + \left[\dfrac{-K_{p-DHB}K_{ph}q_mC_{p-DHB}}{(denom)^2}\right]\dfrac{dC_{ph}}{dC_{p-DHB}} + \left[\dfrac{-K_{p-DHB}K_{o-DHB}q_mC_{p-DHB}}{(denom)^2}\right]\dfrac{dC_{o-DHB}}{dC_{p-DHB}} \\[3mm] + \left[\dfrac{-K_{Ac}K_{p-DHB}q_mC_{p-DHB}}{(denom)^2}\right]\dfrac{dC_{Ac}}{dC_{p-DHB}} \end{array}\right\} \qquad \text{Eq. A-28}$$

And finally for carboxylic acids:

$$\frac{dC_{Ac,T}}{dt} = \frac{dC_{Ac}}{dt}\left\{1 + K_{Ac}^*\right\} \qquad \text{Eq. A-29}$$

where:

$$K_{Ac}^* = \frac{W}{V}\left\{\begin{array}{l} \left[\dfrac{K_{Ac}q_m + K_{Ac}K_{ph}q_mC_{ph} + K_{Ac}K_{p-DHB}q_mC_{p-DHB}}{(denom)^2}\right] \\[3mm] + \left[\dfrac{-K_{Ac}K_{ph}q_mC_{Ac}}{(denom)^2}\right]\dfrac{dC_{ph}}{dC_{Ac}} + \left[\dfrac{-K_{p-DHB}K_{Ac}q_mC_{Ac}}{(denom)^2}\right]\dfrac{dC_{p-DHB}}{dC_{Ac}} \\[3mm] + \left[\dfrac{-K_{Ac}K_{o-DHB}q_mC_{Ac}}{(denom)^2}\right]\dfrac{dC_{o-DHB}}{dC_{Ac}} \end{array}\right\} \qquad \text{Eq. A-30}$$

<div align="center">

Curriculum Vitae

Jesus Moreira del Rio

</div>

Post-Secondary Education

2006-2011   Doctor of Philosophy in Chemical Engineering
The University of Western Ontario, London ON Canada

2000-2006   Bachelor of Chemical Engineering
Universidad Autónoma de Zacatecas, México.

Honors and Awards

May 2010   Best Conference Presentation in Session, Sarnia Research Bridges Symposium.

May 2010   Nominated for the Teaching Assistant Award, The University of Western Ontario.

May 2009   Nominated for the Teaching Assistant Award, The University of Western Ontario.

May 2008   Recipient, Teaching Assistant Award in the Division of Physical Sciences, The University of Western Ontario

September 2006-August 2011   *Full Scholarship for International PhD studies* (5 years). Sponsored by the Federal Government of Mexico through the National Council of Science and Technology (CONACYT).

September 2006-Semptember 2011   Faculty of Graduate Studies Scholarship. The University of Western Ontario.

2006   Dean's Honours List with a GPA of 96/100. University of Zacatecas, Mexico.

Work Experience

2010-Present   Instructor, Teaching Assistant Training Program
The University of Western Ontario. Teaching Support Centre.

2006-2011   Research Assistant.
The University of Western Ontario.

2006-2010   Teaching Assistant.
The University of Western Ontario.

Publications:

International peer-reviewed publications
1. Moreira, J., Serrano, B., Ortiz, A., Lasa, H., **(2011)**. TiO_2 Absorption and Scattering Coefficients Using Monte Carlo Method and Macroscopic Balances in a Photo-CREC Unit. Accepted for Publication in the Chemical Engineering Science. Impact Factor: 2.136.
2. Moreira, J., Serrano, B., Ortiz, A., Lasa, H., **(2010)**. Evaluation of Photon Absorption in an Aqueous TiO_2 Slurry Reactor Using Monte Carlo Simulations and Macroscopic Balance. Industrial and Engineering Chemistry Research 49, 10524-10534. Impact Factor: 1.75.
3. Serrano, B., Ortiz, A., Moreira, J. de Lasa, H.I., **(2010)**. Photocatalytic Thermodynamic Efficiency Factors. Practical Limits in Photocatalytic Reactors. Industrial and Engineering Chemistry Research 49, 6824-6833. Impact Factor: 1.75.
4. Serrano, B., Ortiz, A., Moreira, J., de Lasa, H.I., **(2009)**. Energy Efficiency in Photocatalytic Reactors for the Full Span of Reaction Times. Industrial and Engineering Chemistry Research 48, 9864-9876. Impact Factor: 1.75.

Refereed Proceedings
1. Aaron Ortiz Gomez, Benito Serrano Rosales, Jesus Moreira del Rio and Hugo de Lasa. "Mineralization of Phenol in an Improved Photocatalytic Process Assisted with Ferric Ions: Reaction Network and Kinetic Modeling," in *Advances in Chemical Engineering*: Photocatalytic Technologies Vol. 26, page 69-110. Elsevier, October **2009**.
2. Jesus Moreira, Benito Serrano, Aaron Ortiz, Hugo de Lasa. "Determination of the Absorption and Scattering Coefficients for TiO_2 Using Monte Carlo Simulations and Macroscopic Balances". **2011** *AIChE Annual Meeting: Minneapolis*, MN, USA. Accepted as Oral Presentation.
3. Jesus Moreira, Benito Serrano, Aaron Ortiz, Hugo de Lasa. "Evaluation of Photon Absorption Parameters in an Aqueous Photocatalytic Slurry Reactor Using Monte Carlo Simulations and Macroscopic Balances". *The 21st International Symposium on Chemical Reaction Engineering*. June 13th-16th, **2010**, Philadelphia, PA, USA. Accepted as Oral Presentation.
4. Serrano, B., Ortiz, A., Moreira, J. de Lasa, H.I. "Photocatalytic Reactor Efficiency Factor for the Complete Span of Reaction Times," 2009 *AIChE Annual Meeting*: Nashville, TN, USA, November **2009**.
5. Jesus Moreira del Rio, A. Ortiz-Gomez, H. de Lasa, B. Serrano Rosales. "Photocatalytic Reactor Efficiency Factor for the Complete Span of reaction times," 8th *World Congress of Chemical Engineering*, Montreal QC. Canada, August **2009**. Oral Presentation
6. Benito Serrano Rosales, Jesus Moreira del Rio**,** Miguel Salaices Arredondo, Aaron Ortiz Gomez and Hugo de Lasa. "An Estimation of the Efficiency in a Photocatalytic Reactor," *Engineering Conference International*, *Water Treatment and Reuse II*, Tomar, Portugal, February, **2007**.